Università degli Studi di Trento

Dipartimento di Fisica

PhD Thesis – XXIV cycle

Silicon nanocrystals: from bio-imager to erbium sensitizer

Supervisor:

Prof. Lorenzo Pavesi

Candidate:

Nikola Prtljaga

March 2012

Table of Contents

Introduction

When trying to define a scientific research, most usual definition is: search for knowledge in which foundations stands curiosity and human urge to understand the world that surrounds him. Even if, the main driving force that pushed us towards the discovery of the world might be the plain curiosity, from the sole beginning there have been some more practical aspects involved in the research activity. Very often a deeper understanding of natural phenomena was awarded by possibility of their manipulation in the way to bring more extensive benefits and match more precisely needs of a human society than in the form of their natural occurrence.

A good example of the application oriented scientific research is the research on the semiconductors that brought us the silicon technology. Even though, it was founded on the merely need to increase a computational power, its development changed the world in a unique way, reaching far further than its original applications had foreseen.

As the title of this thesis reveals, the final goal of the work that is going to be presented in following, are the possible applications of a particular material platform. Or more precisely, applicability of that specific material platform in reaching the desired level of performance required by a particular application. In order to assess its suitability and possible benefits, a profound understanding of the underlying physics becomes essential in its evaluation.

But before entering in the details regarding the specific physical aspects inherent to different applications, it is desirable to explain the motivation that stands behind the choice of silicon as a preferred material and, more importantly, why to use it in the form of nanocrystals.

I. Silicon

Silicon (Si) is a very common chemical element classified as tetravalent metalloid. Interestingly, it is one of the most abundant elements found on the Earth. In fact, it is the eight most abundant by mass in whole universe and the second most abundant in the Earth's crust [1].It is very rarely found as a pure element, but rather often in a form of different silicates.

Although, silicon is readily available in the form of silicates it seems that a very few organisms actually require it. It has been proposed that silicon could act as ultra trace nutrition element in higher organism animals but its exact biological function is still under debate [2]. It is known however, that is used by some simple organism (diatoms, radiolarian etc.) to construct their skeletons or by some advanced plants to construct specific cellular parts [3].

Having in mind that the life has developed in a silicon rich environment, it is not surprising that a very low toxicity has been observed for humans. As an example of negative impact of silicon on human health, usually is cited silicosis which is more related to the mechanical properties of silicate dust than to chemical properties of silicon itself [4]. However, it has been demonstrated a role of chemical activity of silicon based radicals in its development [5,6].

A part from this particular case of negative impact, silicon remains to be one of the less toxic and one of the most bio-compatible inorganic elements, making it a material of choice for a variety of biological applications.

Most of the silicon that is used in industrial purposes is used in a form of its natural occurrence, with a very little processing and usually without purification into its elemental form. Typically, silicon is used in a form of a sand or clay, for production of building blocks or different types of ceramics and cements. For other types of usages such as production of steel and different aluminum alloys, a more pure form is required.

A very small percentage of silicon is actually purified in an extremely pure form required by semiconductor industry. However, the economic importance of this small fraction on global economy is simple enormous. Whole information and communication technology would have developed very differently without availability of silicon.

Yet, the real semiconductor era begin with the proof of bipolar transistor effect in another element, germanium [7]. In the beginning of its development, semiconductor industry was far away from the general use of silicon as a semiconductor material. Other materials such as germanium and III-V compounds were much more appealing due to a higher electron mobility and easier processing at the time [8].

On the other hand, a big advantage of silicon (and germanium) respect to III-V compounds was that one has to deal with only one kind of the atoms (being elemental semiconductors) which eliminates various kinds of lattice defects and guarantees a good lattice thermal conductivity. Respect to germanium, silicon has a larger band-gap (0.7 eV respect to 1.12 eV) making it more suitable for power applications. However, germanium didn't have to be as much pure as silicon to be successfully employed as semiconductor material. Only after the invention of the Siemens process for production of high purity poly-silicon, silicon started to be usable as semiconductor material for transistor applications [8].

The main impact that turn everything towards the silicon was the discovery of the passivation action of silicon dioxide (reduction of the surface states), which became a basis of the metal-oxide-semiconductor (MOS) technology. The silicon dioxide proved to be far much stable than the germanium one. In addition, silicon dioxide acts as well as an excellent insulator and effective mask during the device manufacturing, allowing for introduction of planar interconnects and monolithic integration which is base of large scale integration (VSLI) [9,10].

Advanced MOS technology and very large scale integration (VSLI) both based on extraordinary properties of silicon and silicon dioxide interface, opened the way for cost-effective digital technology, which then in turn opened the way for necessary mass market of silicon technology. Any technological solution that could exploit this advanced silicon manufacturing, could count on cost-effectiveness and mass production and, consequently, on wide availability and reach.

II. Silicon photonics

One of the key features of silicon that made it a number one semiconductor material was a monolithic integration made possible by solving the problem of electrical connections by passing from the wire bonding to the metal evaporated planar interconnects. Today, the interconnects problem of a different kind pushes the silicon technology again in a new direction.

In the past, performance scaling described by Moore's law [11] has been accomplished mostly through the size feature decrease and clock frequency increase. But both are expected to run into some fundamental physical barriers [12].

As for the feature size decrease, silicon complementary metal-oxide-semiconductor (CMOS) process scaling is expected to continue at its current pace as the fundamental barriers such as gate oxide thickness, Si-Si bond length, space occupation of electron wave function are not imminent [8]. Moreover, there are already in use successfully some of the technological solutions (high k-gate materials) in order to mitigate some of them [13].

The situation is different for the clock frequency issue. With clock frequency rise, the transistor leakage current and resistance-capacitance (RC) delays in signal transmission increases, leading to excess power consumption, heat and noise production, undercutting the gains that increased frequency might provide [12].

One of the solutions to this issue is breaking up the tasks into many concurrent operations and distributing these across many small processing units, or in other words a passage to a parallel computing. However, this new approach brings also the new technological challenges. In order for this new computing scheme to work efficiently, a high-speed interconnects are needed to move the data rapidly [12].

It has become increasingly difficult for conventional copper based electrical interconnect to satisfy the design requirements of delay, power, bandwidth, and delay uncertainty. One promising solution to this issue could be optical interconnects [14]. On the other hand, introducing optical interconnects into VLSI architectures requires compatibility with CMOS technology [15]. That requirement could be satisfied if we use silicon as a material platform and CMOS technology as a processing technology for production of optical elements. And this is exactly what the silicon photonics is all about.

A big drawback of silicon photonics is inexistence of efficient silicon based laser [16].Silicon is an indirect band-gap material, and is not naturally capable of efficient radiative recombination. While, in direct band-gap materials (GaAs and InP, for example) radiative recombination occurs rapidly and efficiently via a simple two-particle process, in

indirect band-gap material an additional third particle must be involved to carry away the excess momentum, which results in slow optical transition rates.

On the other hand, major non-radiative processes such as Auger recombination, in which an electron (or hole) is excited to a higher energy level by absorbing the released energy from an electron–hole recombination, and free-carrier absorption (FCA) where the free electrons in the conduction band can jump to higher energy levels by absorbing photons, have much shorter lifetimes than those of radiative recombination in silicon, resulting in an extremely poor light emission.

Although, fundamentally limited as a gain material due to indirect band-gap and low mobility, silicon still could be used as a very good substrate having good thermal conductivity, advanced fabrication possibilities, low optical losses, good optical quality of native oxide and large refractive index difference between Si-SiO_2 [16]. These silicon properties were used for the demonstration of hybrid silicon laser [17–19] and epitaxial lasers on silicon [20–22]. Yet, satisfactory solution still hasn't been found. In the case of hybrid approach, monolithic integration is not achieved and instead bonding technology is used [23–25], impacting negatively on price and reliability of hybrid active devices [16]. As for the epitaxial lasers, reliability of compound semiconductor lasers remains a big issue [16],while for the Ge-on-Si laser, electrical pumping remains still to be demonstrated [22,26].

In spite of its inherent limitations as gain material, optical gain and even lasing has been demonstrated in bulk silicon by exploiting the stimulated Raman scattering [27–29]. However, the big drawback of silicon Raman laser is that it is intrinsically optically pumped and not suitable as photonic solution for the interconnect problem.

Aside from the silicon Raman laser, there have been other successful approaches that lead to the demonstration of optical gain in silicon [30–32]. One particularly interesting route is by using the silicon nanocrystals (Si-nc).

III. Silicon nanocrystals

The zero-dimensional semiconductor systems are very peculiar material system displaying properties that lay somewhere in between the molecular and bulk materials. To be considered as zero-dimensional, semiconductor material has to be reduced to a nanometer dimensions and in this form is usually referred to as semiconductor quantum dot (or nanocrystal, nanoparticle etc.) [33]. They are frequently but not necessarily, dispersed in the host matrix, glass or crystalline material. In the case when the band-gap of the surrounding matrix is wider than the embedded semiconductor quantum dot, dot behaves as a potential well for the carriers generated in it.

Quantum dots maintain their absorption properties similar to bulk material up to very small dimensions (typically hundreds of atoms) [33,34]. After the photon absorption, an electron/hole is promoted to valence/conduction band. However, due to restricted size of the dot, electrostatic Coulomb attractive interaction between formed carriers is efficient and immediate resulting in the formation of the bound state called exciton. Exciton size can be easily calculated in different semiconductors using the Bohr theory of atoms and for the bulk silicon its radius is approximately 5 nm [35].

When the semiconductor dot's dimensions are smaller than the Bohr exciton radius, the system is considered to be in a "strong" confinement region [33]. At the length scale where "strong" confinement is achieved, quantum effects become appreciable in defining the material properties and thus the name quantum dots.

The influence of quantum confinement on the optical properties of semiconductor nanocrystals has been intensively investigated in recent years [33]. The main manifestation of quantum size effect is a high-energy shift of the luminescence band and an enhancement of the spontaneous emission rate (easily obtained in quantum-mechanical description of a "particle in box").

In direct band-gap semiconductors both absorption and emission are governed by the fundamental direct gap. Therefore most properties of nanocrystals can be predicted by relatively simple effective-mass calculations based on known parameters of the band edge states. In fact, spectroscopic studies have revealed an increase of the band-gap and the oscillator strength with decreasing size and an atomic-like discrete character of the electronic states in excellent agreement with theoretical predictions [33].

On the other hand, silicon is indirect band-gap material and the same theoretical modeling is not applicable in this case [36–42]. Nevertheless, the electronic band structure of silicon (Si) crystals is significantly modified when the size is reduced to below the exciton Bohr radius (~4.9 nm) of bulk silicon due to the quantum size effect. However, when decreasing the size of nanocrystals a surface becomes an important aspect in material properties determination [43]. This is especially expressed in silicon case, a material widely known for its sensitivity to a surface passivation state [44]. An example of this sensitivity is given by the size dependent quantum yield of resulting PL in silicon nanocrystals even in the high quality samples [45,46].

In general the properties of Si nanocrystals can be controlled by the size, shape, surface termination, etc. Silicon nanocrystals can be prepared by various methods and their properties are slightly different depending on the preparation procedure because of different defect density, different degree of interaction between nanocrystals, different surface termination, etc.

Spatial confinement shifts the energy of the electronic states to higher values in a similar way in both direct and indirect band-gap nanocrystals [33]. In indirect band gap semiconductors (silicon) the optical transitions are allowed only if phonons are absorbed or emitted to conserve the crystal momentum.

Several approaches have been proposed towards improving the efficiency of light emission from silicon based structures. All of them were based on the lifting of the lattice periodicity inducing an uncertainty in the k-space and therefore altering the indirect nature of this material. The spatial confinement of electrons and holes inside a nanocrystal increases the uncertainty of their crystal momentum (Heisenberg uncertainty principle), thus allowing optical transitions in which phonons are not involved [38,47].

The recent advances of nanotechnology has allowed the traditional phonon-selection rule in indirect band-gap materials to be relaxed by achieving quantum confinement and localization of excitons in a nanometer-scale crystalline structure [48]. In this way, the defect recombination of excitons has been greatly suppressed by their localization in silicon nanocrystals, leading to improved light emission [45] and optical gain (in the visible) [49–51]

respect to the bulk silicon. As well, an electroluminescence by bipolar injection has been demonstrated in the same material system [52].

Although silicon nanocrystals have high PL yield with respect to bulk silicon [45,46], they maintain they indirect band-gap nature [47]. The appearance of optical transitions which occur without phonon assistance does not imply their direct nature neither: the exciton recombination has a final probability to proceed either by zero-phohon or phonon assisted process. The relative strength of different optical transitions are a function of silicon nanocrystal size [38,47]

Silicon nanocrystals are of particular interest as a gain material because they have a potential to lead to a demonstration of silicon quantum dot laser [16], exploiting all advantages that quantum dots lasers offer respect to conventional lasers (low threshold and temperature dependence, high modulation bandwidth) [53].

On the other hand, strong detrimental effects and difficult control of nanocrystal fabrication at the nanoscale, makes the realization of quantum dot silicon-based laser rather challenging. The local concentration of carriers in nanocrystals due to the spatial confinement is very high and this can lead to a variety of nonlinear phenomena and irreversible processes of which the most prominent is Auger recombination of carriers in nanocrystals [54,55].

In this work, it will be considered the nanocrystals which diameter is limited to less than 10 nm because quantum size effects start to play a role below this size. Above this size, silicon nanocrystals can be regarded as bulk.

The nanocrystals of different surface termination will be considered although the majority of silicon nanocrystal samples discussed will be oxygen (O) or hydrogen (H) terminated. The properties of O-terminated and hydrogen (H)-terminated Si nanocrystals are qualitatively similar in the size range considered in this work (around 3 nm) but quantitatively there are some differences. The advantage of H-terminated Si nanocrystals is that almost all theoretical calculations are made on them and thus understanding experimentally obtained phenomena is easier. On the other hand, they are not always stable and H-terminated surface could be easily oxidized.

IV. Er^{3+} sensitization by silicon nanocrystals

A relaxed crystal momentum-conservation achieved through quantum confinement of excitons [38,47], increases the radiative recombination rate in silicon nanocrystals, leading to increased photoluminescence. Nevertheless, the radiative recombination maintains its indirect character up to very small silicon nanoparticle sizes [38,47]. Practically this means that, even at room temperature, decay times of PL remain quite long, of the order of few microseconds [44,56].This unusually long decay time for semiconductor, allows for an easy engineering of the non-radiative recombination in this material system [57].

The discovery of the sensitizing action of silicon nanoclusters (Si-ncl) on erbium ions (Er^{3+}) [58], offered, yet, another way towards achievement of monolithically integrated silicon laser. In this scheme, absorbing specie (sensitizer, in this case silicon nanocluster) is excited easily by very efficient pump photon absorption or electrical excitation. Consequently, the

excited sensitizer relaxes giving its energy non-radiative manner to an erbium ion [59,60], avoiding the limitations of erbium excitation process and improving overall material performance.

CMOS process compatibility combined with convenient light emission in the third telecom window (1.5 μm) has been considered as a particular advantage of this approach [16]. Not to mention that erbium doped amplifiers are already widely used in current long-haul optical telecommunications systems [61]. In spite of promising initial reports of optical gain [62] and efficient electrical excitation [63], the laser action in this material still haven't been demonstrated.

There is consensus in the literature that the principle reason obstructing the achievement of the optical gain in this material is a very low fraction of sensitized erbium ions although there is still ongoing dispute of the reasons standing at the origin of observed behavior [64–67].

V. Thesis outline

The work in this thesis is inserted in the context of possible applications of silicon nanocrystals, regarding the thematic previously discussed. Most of the work that is going to be presented is of experimental nature while smaller part consists of modeling and numerical simulations of specific photonic devices and natural phenomena.

In the first chapter possible application of silicon nanocrystals as bio-imaging agent is investigated by employing colloidal dispersion of individual Si-nc where surface properties could be controlled to a great extent. By using a suitable functionalization scheme, the impact of the surface on the light emitting properties can be minimized, producing samples where quantum confinement effects become dominant in light emitting properties. The control of surface properties allows an efficient elimination of surface quenching centers, resulting in high quantum yield (~30 %) nanoparticles.

This fairly simple system allows, for detailed study of some classical phenomena such as MIE scattering of small scatterers and their impact on the light emitting capabilities of such ensemble. The big advantage is that measured scattering properties could be compared with computer simulations. The agglomeration impact on light emitting performance of this system is established and alternative approach to mitigate this phenomenon is individuated and tested. Once optimized, interfacing this system with biological systems for bio-imaging and drug delivery purposes becomes quite straightforward.

The second chapter examines the silicon nanocrystals as a gain material. Since the demonstration of optical amplification in low dimensional silicon (Si-nanocrystals) [49], considerable research efforts have been devoted to understand the basic mechanisms driving the photoluminescence properties of this system. The work presented in this chapter concerns the study of a zero phonon (direct) optical transition as a possible source of optical amplification in this material system. To this scope, investigation of the dynamics of the system on a nanosecond time-scale and under high excitation conditions has been employed.

Additional insight on ultrafast dynamics has been obtained by using optical cavities. To this end optically active free-standing micro-disk resonators have been fabricated. In this

case the photoluminescence of silicon nanocrystals (Si-nc) is coupled to whispering gallery modes (WGM) of the resonator. Extensive characterization of photoluminescence properties from the cavity-embedded Si-ncs is presented. Finally, sub-nanosecond emission dynamics of cavity coupled Si-nc emission from a single micro-disk resonator is explored.

In chapter 3, a study of Er^{3+}-doped Silicon-Rich-Oxide (SRO) materials and Er^{3+}-doped SRO based devices is presented. As mentioned previously, this material opens the route towards compact, waveguide amplifiers and lasers in telecom band and allows for the possibility of electrical injection schemes, which are not realizable in standard erbium amplifiers. Unfortunately, a number of gain limiting factors have been identified in this material plaguing the performance of light emitting/amplifying devices based on it. Therefore, before the realization of working devices, an understanding of the energy transfer physics becomes compulsory.

In the first part of the third chapter, the energy transfer mechanism is analyzed and to that end two types of samples were considered: μm thick Er^{3+}-doped SRO films suitable for optically pumped amplifiers and tens of nm thin Er^{3+}-doped SRO films suitable for electrically pumped amplifiers and lasers. By employing extensive optical, electrical and structural characterization a pressing drawback in this material has been identified and possible remedy to low performance of Er^{3+} doped SRO devices has been proposed. Considering a set of optimized samples, quantitative optical experiments are reported. By means of pump& probe experiments an internal gain has been measured in optically pumped Er^{3+}-doped SRO active waveguide, measured values being still too low for a working device.

In order to achieve an electrical pumping of erbium doped SRO a novel structures based on slot waveguides have been proposed, modeled and manufactured. Moreover, a preliminary result of their performance is also presented.

In the conclusion, some future perspective and possibilities for different lines of research are discussed.

Chapter 1.1
Silicon nanocrystals as bio-imaging agent

1.1. Introduction

A number of different drawbacks have been identified for organic fluorescent dyes commonly employed in bio-imaging such as: overlap of excitation and emission band, short lifetimes, narrow excitation spectral bands, photobleaching etc. [68,69]. Diverse alternatives have been proposed to organic dyes in order to mitigate these detrimental effects: organic based nanoparticles [70], carbon nanotubes [71], golden nanoparticles [72] and semiconductor quantum dots [73]. However, the need for additional molecular tagging [70], some concerns about their biodegradability [72,74], the toxicity of their by-products [75], the phototoxicity [76] or the toxicity due to their structural properties [77] severely limit their actual use.

On the other hand, silicon is a common trace element in biological systems and is naturally absorbed and extracted by a number of different tissues [78]. The same is valid as well for nanostructured silicon (Si-nc for example) [79], making silicon a perfect candidate for imaging applications from the point of view of biocompatibility [80]and biodegradability [79].

In order to achieve the low detection limits needed for *in vivo* imaging, emission in the near-infrared (700 nm – 1000 nm) is generally preferred [68,81]. Unfortunately, near infrared (NIR) fluorescent dyes possess very low quantum yields [82]. Although, silicon in its bulk form is a very poor light emitter, porous silicon [83] shows that nanocrystalline silicon acts as an efficient NIR light emitter [84].

While quantum confinement and exciton localization are generally considered as responsible for the improved light emission of Si-nc [38], the Si-nc surface rules the emission properties [85]. In fact, Si-nc lack long term photoluminescence (PL) stability in air or aqueous solutions due to a rapid and efficient surface oxidation [86].

For the sake of successful appliance of Si-nc in biological environment, oxidation process has to be controlled. By appropriate Si-nc surface functionalization with organic molecules, improved stability to oxidation could be achieved [69,86,87]. The oxidation process should not be suppressed completely as it offers an easy and straightforward way for achieving biodegradability. However, Si-nc shouldbe brightly luminescent and tolerate

contacts with water and oxygen in the experimental time-scale which, for cell studies, is in the range of a few days.

In addition, for cell and *in vivo* applications Si-nc must be targeted to specific action sites, requiring a sort of "interfacing" with biological environment. In this case, the Si-nc coating should be tailored and the optimum size established taking into account mechanisms allowing biological barriers to be crossed [88,89].

Designing of a suitable interface is a very difficult task, due to the complexity of biological systems. Therefore, various empirical strategies are being employed. Nevertheless, preparation of water-dispersible Si-nc which maintain size-dependent photoluminescence (PL) has proven to be difficult [90].A promising way towards producing of luminescent hydrophilic Si-nc is obtained by grafting of carboxyl-terminated alkenes to Si-nc surface [90], leaving them still reasonable exposed to water and solutes [91].

While, medium sized (≈100 nm) silicon nanostructures, with intrinsic near-infrared luminescence, offer additional advantage as a drug delivery system [79], dimensions of the order of a few nanometers (i.e. comparable to proteins) appear desirable for some applications such as *in vivo* imaging [92].In this case, the surface coating should also be designed to avoid small particle aggregation into larger structures [90]. Stabilization by physisorption of organic molecules avoids further reaction steps which may affect the PL emission of Si nanostructures.

The temporal evolution of PL of Si-nc in aqueous environment still lacks a complete description, while stability of Si-nc and safe targeting to action sites remain unresolved questions, explaining why this material system is still not routinely applied in spite of its seemingly superior physical properties.

In this chapter, it will be presented a study of evolution of luminescence of functionalized Si-nc in water suspension with or without presence of various surfactants in order to investigate physical coating as a strategy to improve their stability. Special attention is given towards the understanding of processes that govern the time evolution of PL of this system on different timescales. The experimental conditions required for the stable Si-nc aqueous suspensions are individuated, and surfactant effects on light emission are investigated.

1.2. Hydrophilic silicon nanocrystals

Si-nc are produced in toluene/ethanol mixture by sonication of just etched porous silicon (see **Figure 1**and section II of Appendix to Chapter 1 for additional info). Thus, as-prepared luminescent Si-nc are hydrophobic(hydrogen terminated) [86]. Hence, it is necessary to modify their surface to a hydrophilic state to make them compatible with an aqueous environment. Although, the surface modification into an hydrophilic state could be achieved by simply leaving the Si-nc immersed in water where oxidation slowly takes place [79], a more controlled approach is preferred.

In order to achieve a suitable surface modification, a photochemical hydrosilylation of the hydrogen passivated Si-nc surface by undecylenic acid was used (see section II of Appendix to Chapter 1) [93]. This process will be referred to, as Si-nc functionalization, in the

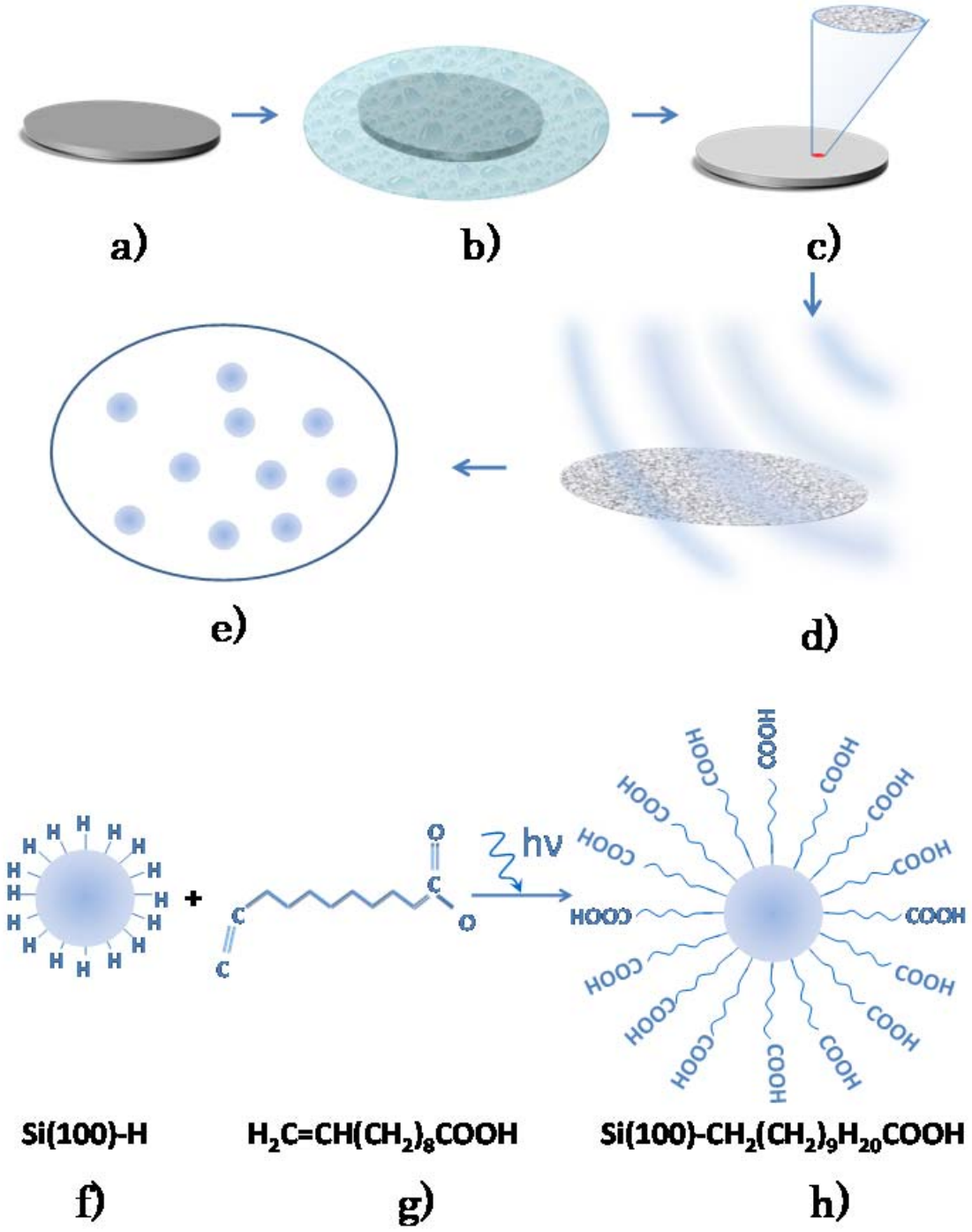

Figure 1 *- A silicon wafer (**a**) was electrochemically etched in HF/ethanol solution (**b**) to produce the porous silicon (**c**). Porous silicon was then sonicated (**d**) in toluene/ethanol solution to obtain Si-nc (**e**). The carboxyl-acid-terminated monolayer on the surface of the Si-nc–COOH (**h**) was achieved through the photochemical hydrosilylation of undecylenic acid (**g**) with a hydrogen-terminated Si(100) surface (**f**) of Si-nc.*

following. After functionalization, Si-nc are carboxylic terminated (Si-nc-COOH, see also section II, VI and VIII of Appendix to Chapter 1) and they can be easily suspended both in

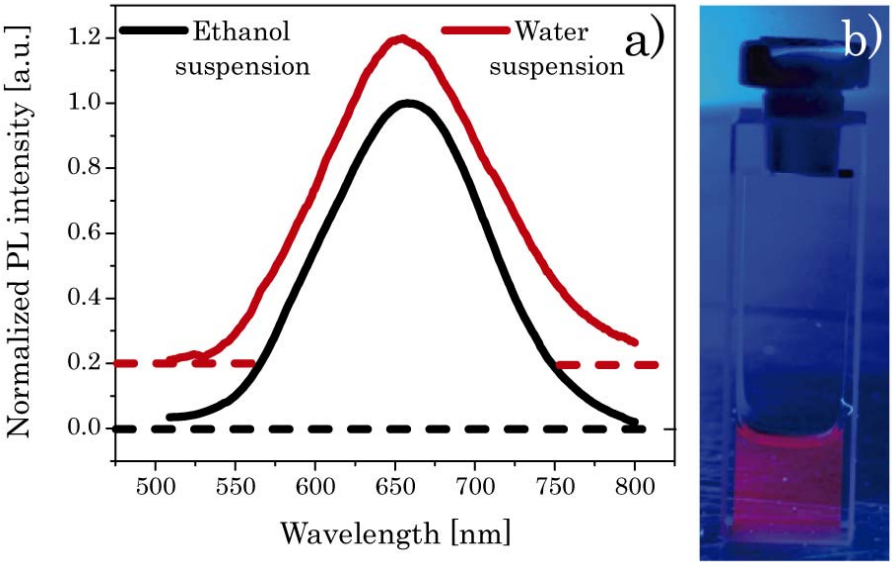

Figure 2 *- (**a**) Normalized PL spectra of functionalized Si-nc–COOH in ethanol (black line, down) and water (red line, up) suspension. PL spectrum of functionalized Si-nc–COOH in water suspension is offset along the y axis by 0.2 for clarity, dashed line corresponding to zero. No visible spectral deformation could be observed for different suspensions. The excitation is at 361 nm. (**b**) Red photoluminescence from the Si-nc–COOH suspended in ethanol under illumination from UV lamp.*

ethanol and in water, producing luminescent suspensions (**Figure 2b**).

Conversely, it was not possible to dilute or re-suspend non-grafted Si-nc in aqueous solutions, as the Si-nc either aggregated or were physisorbed on the vessel. In addition the luminescence of non-functionalized Si-nc (hydrogen terminated, Si-np-H) is completely quenched in water (on timescale where no significant oxidation occurs) and ethanol.

This method is used instead of oxidation by water exposure for a number of reasons:

- Carboxylic termination allows for straightforward coupling with different chemical and biological species [94,95];
- It is fast (modification of surface lasts less than 2 hours, see section II of Appendix to Chapter 1);
- The process is controlled whilst water exposure is difficult to control [96]. Water exposure does not yield always the stoichiometric oxide shell on the surface of the Si-nc and exactchemical nature of the resulting native oxide is poorly controlled leading to easy creation of sub-oxides [97]. In order to achieve a proper surface oxidation a more elaborate oxidation procedure is usually employed [94,96,98,99] ;
- Sub-oxides creation is not desirable as they are usually related with occurrence of efficient luminescence quenching centers [79,100].
- Fully oxygenated surface may influence the optical properties of Si-nc dramatically [43,101–103] while the impact of Si-C bond on optical properties of Si-nc seems to be rather moderate [104]. Moreover, the impact of -COOH functional group could be mitigated by usage of longer alkyl chain [105,106] achieving as well better suspension stability [106].

The functionalised Si-nc were further characterized by means of transmission electron microscopy (TEM), Fourier transform infrared spectroscopy (FTIR), atomic force microscopy (AFM) and X-ray photoelectron spectroscopy (XPS) confirming carboxyl capping of the produced nanocrystals (see Appendix to Chapter 1).

1.3. Short time-scale evolution of PL of Si-nc-COOH

Freshly prepared Si-nc-COOH suspended in ethanol show a broad red luminescence band (see**Figure 2a**), which peaks at around 640 nm and is about120 nm wide. The red photoluminescence is the first indicator that the PL that is observed could be due to quantum confinement effects (QCE) since the defect band associated with oxide defects is usually situated more towards the blue part of the visible spectrum [44,107,108]. The hydrosilylation is essential to produce a stable dispersion as can be seen from the **Figure 2b**. In addition, the PL of functionalized Si-nc is not quenched in ethanol [86] (**Figure 2a** and **Figure 2b**) further confirming that the surface of the particles is partially coated and, therefore, hardly accessible to dissolved species.

Once, the Si-nc-COOH are suspended in water, their PL lineshape and peak position do not change with respect to what observed for ethanol suspension on short timescales (hours, during which no significant oxidation occurs **Figure 2a**). Nevertheless, a rapid decrease of their PL intensity is observed immediately after suspension in water (**Figure 3a**). This also points to a QCE nature of the emission, since emission due to interface states show a quite different behavior when the nanocrystals are immersed in water [100].

In water suspension, the PL intensity of Si-nc-COOH decreases up to approximately 50% of its initial value in a time span of 10-15 minutes and then stabilizes (**Figure 3a**). What is interesting is that during the same time, the absorbance increases rapidly and stabilizes, too (**Figure 3a**). The opposite trends between emission intensity and absorbance prove that these are not caused by a decrease of the Si-nc concentration (e.g. due to Si-nc precipitation).

In order to get some more insight on these phenomena and the origin of PL, time resolved photoluminescence measurements were performed on the Si-nc-COOH suspended in water after PL stabilization. As it is commonly observed for Si-nc, the luminescence decay lineshape is a stretched exponential function [109]:

$$I(\tau) = I_0 * \exp[-(\tau / \tau_0)^{\beta}] \quad (1)$$

Where **I(t)** is the PL intensity, **β** is a stretching parameter and **τ_0** is a temporal parameter which for **β**=1 corresponds to the mean luminescence lifetime given by **τ**. The results of fitting the experimental data with the stretched exponential are reported in **Figure 3b** (see also **Figure 14** from section IX in Appendix to Chapter 1).

The time decay of the functionalized Si-nc-COOH is in the microsecond range. Microsecond long lifetimes are compatible with the results of other studies where the emission is attributed to quantum confinement [38,44,56,110]. On the other hand, radiative recombination due to oxide defects is fast with typical decay time of order of the nanoseconds [44,107,108].

QCE origin of PL is further confirmed by the strong wavelength dependence of the

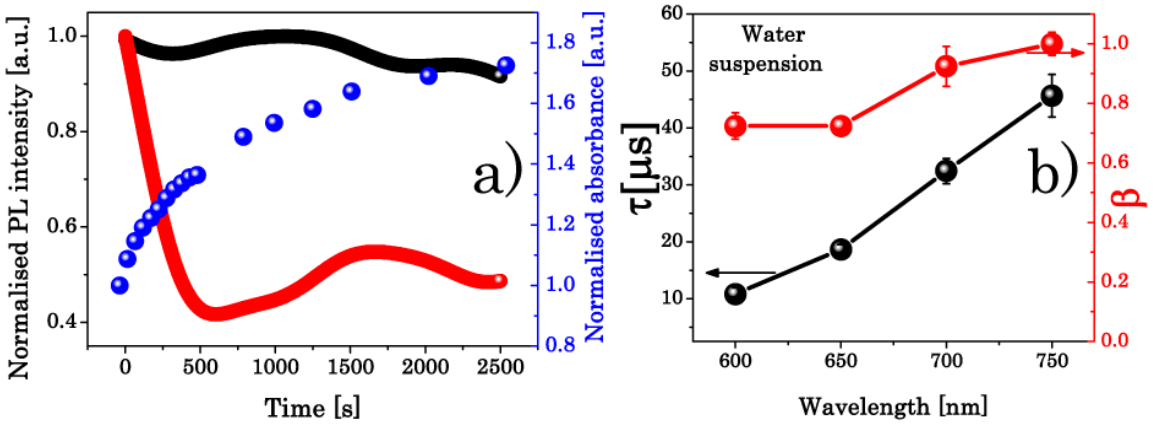

Figure 3 *– (**a**) Time evolution of PL (full red spheres) and absorbance (full blue spheres) of functionalized Si-nc–COOH in water suspension upon UV excitation (361 nm). Both curves are normalized to the initial value of the PL intensity and of the absorbance, respectively. The long-term oscillations are due to a convective motion of heated solvent in the illuminated part, causing the small discrepancy in the dynamics of the PL and of the absorbance in the water suspension. To show this effect the PL evolution of Si-nc–COOH in ethanol suspension (black full spheres) is also reported. (**b**) Stretched exponential fit parameters obtained from the fit of decay curves of functionalized Si-nc–COOH in water after the photoluminescence intensity stabilization (see panel (**a**)). Decay curves are obtained by integrating a 90 nm wide spectral window. Excitation is at 355 nm.*

time decays (**Figure 3b** and **Figure 14** from section IX in Appendix to Chapter 1). In the case of QCE origin of PL, the time decay constants will be size dependent and it will get shorter for the smaller sizes of the Si-nc due to the increase of the radiative rates as the Si-nc size decreases [38,44,56,110,111]. As the emission of the single silicon nanoparticle has been proven to be very narrow even at the room temperature [112–114], the broad PL band typically observed from the Si-nc ensemble, is attributed to a broad size distribution (see also section V of Appendix to Chapter 1)where each emission wavelength is characteristic of a given size [44].

In other words, if the time decay of the PL band is spectrally analyzed, in the case of QCE origin of PL, it will show a time decay which is shorter towards the smaller wavelengths (higher energies, smaller sizes, see **Figure 3b** and **Figure 14** from section IX in Appendix to Chapter 1). The microsecond long time decay which gradually shortens towards the lower wavelength is unique signature of the ensemble of luminescence quantum dots which maintain their indirect band-gap character (silicon) and where the quantum confinement influence on PL properties is dominant [111].

These observations imply also a high crystalline quality of the Si-nc-COOH [110] in accordance with what observed from TEM and XPS (see section V and VIII of Appendix to Chapter 1). Furthermore, the high values of the dispersion parameter **β** (**Figure 3b** and **Figure 14** from section IX in Appendix to Chapter 1) suggest that the Si-nc are isolated and no inter-dot hopping occurs [115]. The time decays of the functionalized Si-nc-COOH in water and ethanol suspension remain stable and it is not changing on short timescales (hours).

For Si-nc-COOH in ethanol suspension a quantum yield with value of 30% is found, which agrees well with the values found in the literature on similar systems [45,116]

confirming a good quality of produced Si-nc-COOH. From the quantum yield and the values for absorption cross-section of Si-nc found in the literature [117], the concentration of functionalized Si-nc-COOH in ethanol suspension was estimated to be approximately 10^{13} nc/cm^3 (see section XI in Appendix to Chapter 1). In the case of the Si-nc-COOH in water suspension, quantum yield measurements become unreliable (experimental error rises from 5 % in ethanol suspension up to almost 20 % for suspension in water) due to fluctuations of both the emission and the absorption (**Figure 3a**).

Let us discuss now the origin of the temporal dependence of the emission and absorption observed in water suspension. The PL of Si-nc-COOH in ethanol suspension remains stable, even after long illumination (**Figure 3a**), while the initial fast temporal decrease of the PL of Si-nc-COOH in water suspension does not depend on illumination. Indeed, experiments where the laser excitation was turned off and on, demonstrate a decrease of the PL which is independent on the presence and the absence of the laser light, i.e. the decay continues even in the absence of illumination and the PL intensity is not recovered by turning off the illumination.

Combining these observations with the unchanging PL lineshape and time decays, we can safely discard photobleaching (or light stimulated surface chemical reactions) as the cause of emission decrease of Si-nc-COOH in aqueous ambient. As well, change in the dielectric constant of the surrounding medium between different suspensions (refractive index of ethanol $\mathbf{n}$ = 1.36 [118] and water $\mathbf{n}$ = 1.33 [119] at $\boldsymbol{\lambda}$ = 640 nm) is not enough to explain the considerable differences in PL and absorbance in these two solvents.

Since the water and ethanol suspensions were produced by dissolution of the same amount of starting Si-nc-COOH, the concentration of the Si-nc-COOH in both suspensions is expected to be approximately the same. Thus, the increased absorbance in water suspension cannot be due to an increase of the electronic absorption of Si-nc-COOH (moreover nor PL lineshape change nor lifetime variations were observed).

One possible cause to such behaviour could be an increased scattering of light due to aggregate creation. During the surface functionalization step poly-acrylic coating could be created [106], favoring a large aggregates creation [120]. However, in this case same behavior would be observed for both suspensions and formed the aggregates would be visible under TEM imaging [120].

On the other hand, increased scattering of light could be caused by the speeding-up of the agglomeration of Si-nc-COOH in water. In this case, a creation of small agglomerates of functionalized Si-nc-COOH in water due to polar repulsion as for micelle formation has to be postulated.

In fact, the surface of Si-nc-COOH is only partially coated by the undecylenic acid [121]. Moreover, the functionalizing molecule introduces an alkyl chain, which imparts a partially hydrophobic character to the coated Si-nc-COOH. This could yield small dynamic dominions of Si-nc-COOH in the strongly polar water.

Since, neither the suspension becomes opaque to an eye nor filtration over 200 nm filters changes the PL dynamic of the suspension and, moreover, the extinction saturates at values presented in **Figure 3a**, the formation of relatively small agglomerates of Si-nc is expected (sizes lower than 200 nm).

A qualitative estimate of this increased absorbance can be done by using the theory of

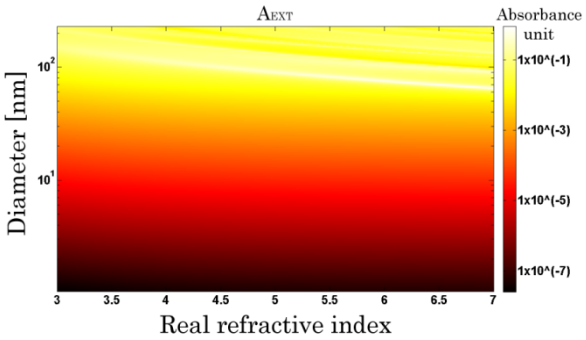

Figure 4 *- Semi-log 2D maps of the absorbance due to scattering* A_{ext} *as a function of the real part of the refractive index (x axis) and Si-nc-COOH's cluster size (y axis). Wavelength of the incident light is fixed to 361 nm. The imaginary part of the refractive index is assumed to be zero.*

Mie scattering of small scatterers [122].In order to calculate the Mie scattering from the Si-nc-COOH, crude approximations were employed: a single size and spherical shape for the single isolated Si-nc-COOH and spherical large clusters of agglomerated compact Si-nc-COOH were assumed.

The calculations were done with a non-commercial software based on classic Bohren and Huffman MIE (BHMIE) algorithm [123] for Mie scattering from a sphere in a medium [124]. For the medium, the refractive indexes of water at 25°C and at the excitation wavelength were used.

In the case of a wavelength scan, the refractive index of the medium was accordingly corrected. Since the refractive index of the Si-nc-COOH is not known (literature reports only average refractive indexes of the Si-nc embedded in a given matrix), a scan over a range of refractive indices was done including that of the bulk silicon at the suitable wavelength [125].

Figure 4 shows the results of Mie scattering calculations where the absorbance (due to extinction) A_{ext} is reported at the wavelength of the excitation laser light for different cluster sizes. The absorbance is normalized to the value of Si-nc-COOH concentration which in this case scales as the inverse of the volume of the nanoparticles (assumption of spherical clusters).

A number density of $n_0 = 10^{13}$ cm^{-3} (see section XI of Appendix to Chapter 1) and a particle diameter of $d_0 = 4$ nm were assumed. From TEM imaging and AFM measurements a bit larger values of the average size of Si-nc-COOH have been found (see section V and VII of Appendix to Chapter 1). Moreover, in case of the AFM measurements, the measured larger values could be as well due to the surface coating since AFM probes only the surface of the nanoparticles.

However, as seen from FTIR and XPS (see section VI and VIII of Appendix to Chapter 1) a partial oxidation of Si-nc-COOH have occurred meaning that, most probably, the produced Si-nc-COOH have a core/shell configuration with large crystalline silicon core covered by a thin silicon dioxide shell. Unfortunately, due to the limited spatial resolution of TEM, this cannot be directly tested by imaging of silicon nanoparticles. However, as shown previously, the PL in these samples is due to QCE and, as such, could be directly related with the Si-nc core size. Si-nc core size of approximately $d_0 = 3$ nm could be deduced from the peak of PL [44,96,126].

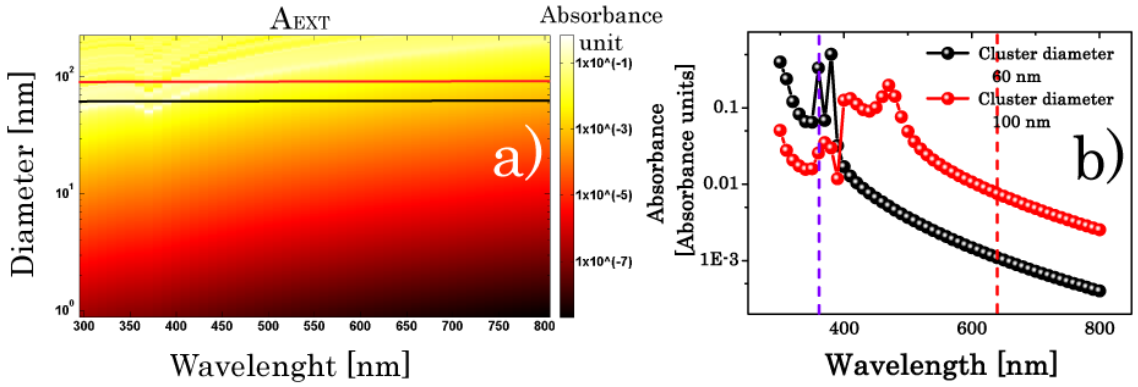

Figure 5 *– (**a**) Semi-log 2D maps of the absorbance due to scattering as a function of wavelength of the emitted light (x axis) and Si-nc-COOH's cluster size (y axis). Values and wavelength dependence of the real part of the refractive index of Si-nc-COOH are assumed to be the same as those of bulk silicon* [125]*. Imaginary part of the refractive index is assumed to be zero. Two solid horizontal lines (black and red) represent cluster sizes (60 nm – solid black line and 100 nm – solid red line) for which semi-log plots in part b of the same figure have been generated. (**b**) Semi-log plot of the absorbance as a function of wavelength of the emitted light for two different cluster sizes with diameter: 60 nm (full black spheres) and 100 nm (full red spheres). Vertical dashed lines represent excitation wavelength (violet) and PL peak wavelength (red).*

As the refractive index difference between ethanol, water and silicon dioxide shell is quite small, a main scattering contribution is coming from the silicon core. However, the shell contribution should not be completely disregarded [127]. As the calculation of the exact scattering amplitudes of complex core/shell particles are quite cumbersome [127], shell contribution was taken into account in an empirical way by assuming a slightly bigger average size of the silicon nanoparticles ($d_0 = 4$ nm).

As can be observed from **Figure 4**, there is a very steep increase of absorbance with increased Si-nc-COOH agglomerate size due to the increased scattering, for all the values of refractive index considered. The interference pattern observed at large cluster sizes and large refractive indices is due to the assumption of a monodisperse population of nanoparticles. As TEM images show (see section V of Appendix to Chapter 1), there is a size distribution of the Si-nc-COOH which will eventually wash out the interference pattern without offsetting significantly the absorbance values found [127].

To infer whether the agglomeration affects also the intensity and lineshape of the emission, the spectral dependence of absorbance due to Mie scattering was calculated as well. The refractive index of bulk silicon at the absorption wavelength was assumed [125].

From **Figure 5** it can be seen that the computed absorbances are significantly smaller than those found at the excitation wavelength. In addition, absorbance tends to decrease with increased wavelength. It is interesting to note that the wavelength dependence of absorbance weakens with increased cluster size (see **Figure 5b)**.

The ratio of the absorbance value at the emission wavelength, with respect to the value at the excitation wavelength, increases from 0.3% for a 60 nm diameter cluster to 27 % for a 100 nm diameter cluster (**Figure 5b)**. However, no PL quenching and spectral deformation of the PL band has been observed in the experiment, confirming that we are dealing with rather small aggregates.

Agglomeration has been also confirmed by dynamic light scattering (DLS) and zeta potential measurements (see section X of Appendix to Chapter 1). For the aqueous suspension of Si-nc-COOH a typical cluster sizes of 100 nm was found. Small discrepancies with simulation are due to the approximations considered in the calculations. Moreover, the surface charge revealed by zeta potential measurements is too low for stable suspension of nanoparticles.

If the concentrated ethanol Si-nc-COOH is sonicated immediately before transferring to water, a smaller (than for a non-sonicated suspension) increase in the absorbance of the water suspension is observed (~20 % more than in equally diluted ethanol suspension). However, if the sonicated concentrated ethanol suspension is left at rest for one week before transfer to water, the absorbance shows the same trend as in **Figure 3a**.

This implies that agglomeration occurs as well in ethanol, though to a lesser extent than in water. Agglomerates in ethanol suspension should be much smaller since absorbance does not change. This was confirmed by DLS measurements (see section X of Appendix to Chapter 1).

It is interesting to note that, despite agglomeration, the high value in the β coefficient measured by TR PL indicates that the nanocrystals are not interconnected in the agglomerates.

1.4. Short time-scale evolution of PL of Si-nc-COOH in the presence of the surfactants

As shown in previous section, the chemical coating alone is not sufficient to prevent a limited agglomeration of produced Si-nc-COOH in aqueous environments. In order to address this issue without compromising desirable PL properties of Si-nc-COOH by further chemical reaction, a physical coating has been considered. In particular, in order to decrease the Si-nc-COOH agglomeration in water, surfactants were used.

The surfactants have been already used previously to impart hydrophilic character to hydrogen terminated hydrophobic surface of porous silicon and porous silicon powder [86,128–131]. If the agglomeration of the coated Si-nc-COOH is driven by a partially hydrophobic character of an alkyl chain of the functionalizing molecule, physisorption of the surfactant molecules should be able to decrease [129,130].

Moreover, by using polar surfactants, Si-nc-COOH suspension could be electrostatically stabilized decreasing agglomeration phenomenon [132]. In addition, surface charging of Si-nc-COOH by physisorption of polar molecules could facilitate the cellular uptake of nanoparticles [89,133].

Two different surfactants were tested, differing in their ionicity: sodium dodecyl (SDS - anionic) and cetyl trimethylammonium bromide (CTAB - cationic). They are representatives of two different ionicity classes and have been already well characterized in literature [131]. The control sample was an aqueous suspension.

In the presence of CTAB [1 ml, the critical micelle concentration (CMC)] [134], a significant blue shift and quenching of the emission is observed already after few minutes

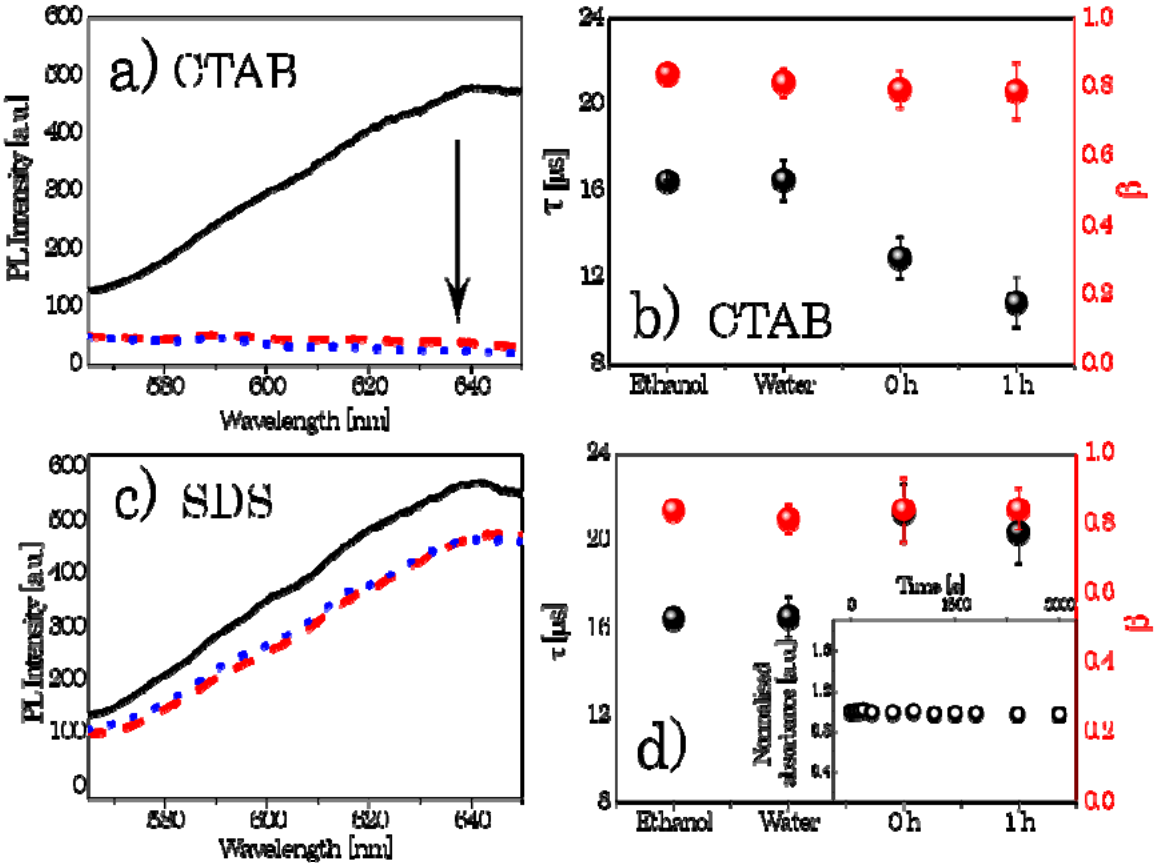

Figure 6 *– (**a**) PL spectra of functionalized Si-nc-COOH in water suspension (solid black line), immediately after adding the cationic surfactant CTAB (dashed red line) and one hour later (dotted blue line). Significant quenching of PL signal could be observed (indicated by the black arrow). (**b**) Stretched exponential fit parameters obtained from the fit of the 580 – 640 nm integrated decay curves of functionalized Si-nc-COOH in concentrated ethanol suspension (diluted ethanol suspension shows the same values), water suspension (control sample) and in water suspension with added cationic surfactant CTAB in different time intervals (immediately after adding and 1 hour later). (**c**) PL spectra of functionalized Si-nc-COOH in water suspension (solid black line), immediately after adding of the anionic surfactant SDS (dashed red line) and one hour later (dotted blue line). (**d**) Stretched exponential fit parameters obtained from the fit of 580 – 640 nm integrated decay curves of functionalized Si-nc-COOH in concentrated ethanol suspension (diluted ethanol suspension shows the same values), water suspension (control sample) and in water suspension with added anionic surfactant SDS in different time intervals (immediately after and after 1 hour). (**Inset**) Time evolution of absorbance (empty black circles) of functionalized Si-nc-COOH in water suspension with SDS in CMC. Curve is normalized to initial value of absorbance. Note that due to the streak camera used to measure the time decay and the time integrated spectra, the wavelength interval of the measurements is limited. Pulsed UV excitation was used (λ_{exc} = 355 nm, 6 ns, 10 Hz) in all cases.*

(**Figure 6a**). Concurrently, the lifetime decreases while the β parameter stays constant (**Figure 6b**). These data can be interpreted as due to a quick hydroxylation and oxidation of Si-nc [131].

In the presence of SDS (7-10 mM, the CMC) [135], a slight decrease but no lineshapechange are observed while the lifetime increases and β-parameter stays constant (**Figure 6c** and **Figure 6d**). The small decrease of the PL intensity can be due to the lengthening of the lifetime, i. e. to a decrease of the emission rate. It is important to notice that the absorbance of the suspension remains constant (**Figure 6d Inset**) indicating that no agglomeration occurs.

In the literature, there is no clear consensus on the mechanism and action of the anionic surfactant SDS, as there have been contradicting experimentally reports [128,131]. What becomes clear from our data is that SDS influences directly the PL lifetime of Si-nc-COOH. Since the lifetime is lengthened while the intensity is decreased, it looks that the overall effect is a lengthening of the radiative lifetime while the non-radiative lifetime is mostly unchanged. Thus, no further surface passivation occurs while most probably an electrostatic (Stark-like) separation in the electron-hole wave-function causes the increase of the lifetime [136]. The electrostatic surface field might be due to the presence of the negatively charged group of adsorbed SDS molecules.

1.5. Long time-scale evolution of PL of Si-nc-COOH

What it have been discussed up to now is the short time-scale (hours) of PL evolution of Si-nc-COOH. As shown in **Figure 2** and **Figure 3a,** apart from the initial loss of intensity, the PL is stable both in intensity and color. This should allow to use Si-nc-COOH as imaging probes, since their emission properties are maintained in a period much longer than typical renal clearance time for the nanoparticles of their size [92].

However, if Si-nc-COOH are to be used as an imaging probe (for *in vivo* and cell studies), they have to maintain their light properties in arc of a few days. Moreover, they should also undergo spontaneous dissolution in order to maintain their biodegradability (once internalized inside of the cell they escape renal clearance and bile excretion mechanism) [81]. In addition it would be desirable that they could be conserved once produced, in order to facilitate their distribution.

On a longer time scale (days), ethanol or aqueous suspensions show quite different behavior (**Figure 7**)[1]. While PL of Si-nc-COOH in ethanol remains stable with time (up to a few months, not shown in the **Figure 7**), a constant blue shift of PL emission and a decrease of the PL intensity are observed for Si-nc-COOH in water.

The same PL evolution is observed as well even when SDS is added to the suspension (**Figure 8**).

This behaviour is attributed to a slow oxidation of Si-nc, which causes a decrease of the Si-nc-COOH core that is, in turn, reflected in a blue shift in the Si-nc-COOH emission [129]. In the case of interface PL activation during the oxidation in water, quite different behavior is observed [100].

The residual oxidation of the Si-nc-COOH is difficult to overcome by improving the

[1] Photographs were taken by E. Rigo.

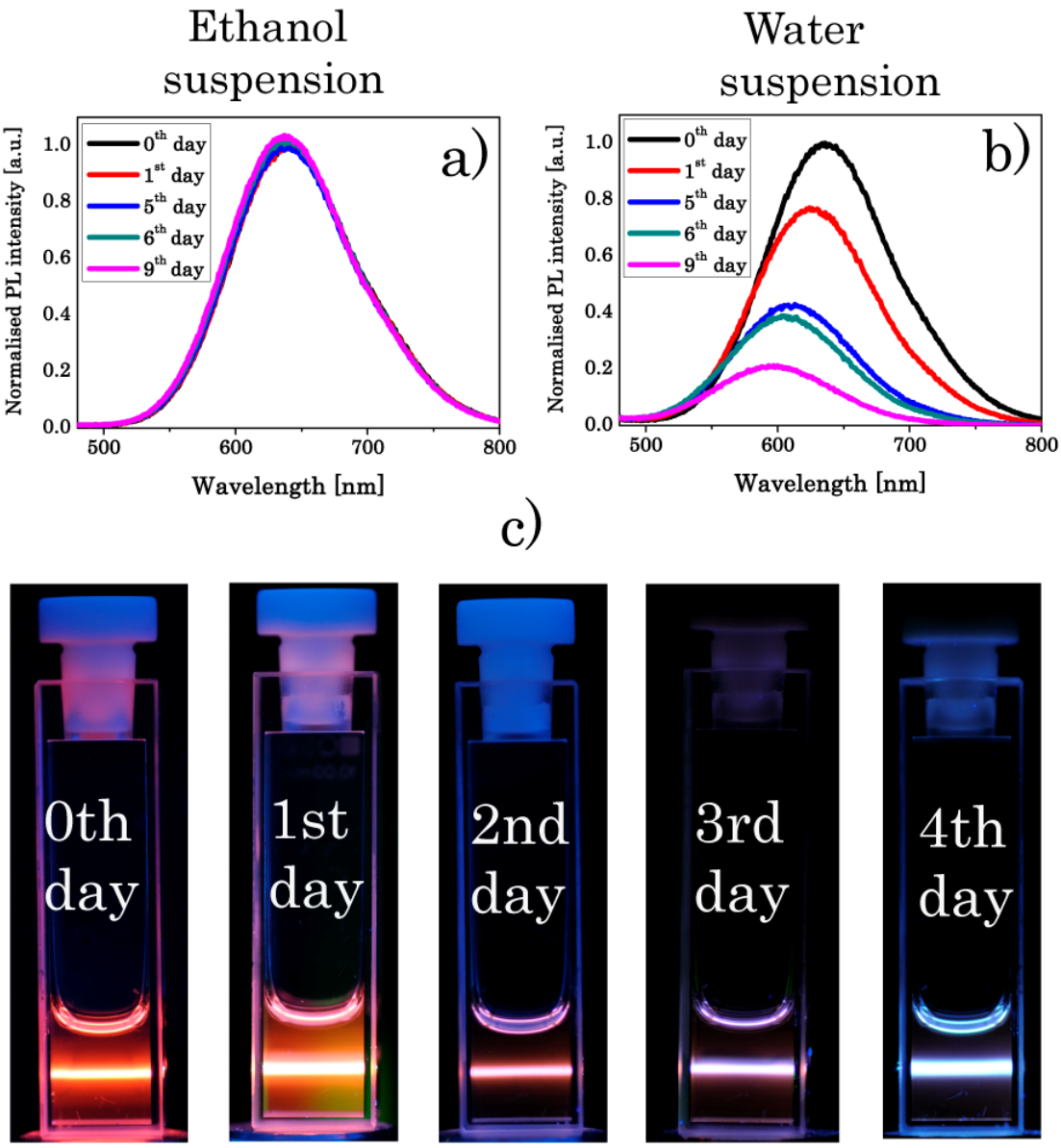

Figure 7 *- Time evolution of the PL of functionalized Si-nc–COOH on a long timescale (days) in different suspensions: (**a**) in ethanol suspension. PL is not quenched by ethanol and remains stable over a long time. (**b**) In water suspension. Blue-shift of emission peak and decrease of PL intensity with time could be noticed. All spectra are normalized to the initial PL intensity after stabilization in their respective suspensions. (**c**)[1] Photographs of diluted suspension of Si-nc-COOH in water during the first five days of their exposure. Change in emission color could be observed Excitation was provided by UV laser (355 nm).*

degree of functionalization [121]. However, improved resistance to oxidation would most certainly decrease biodegradability of such nanoparticles [79].

In particular, when SDS is added, a slight increase in the PL intensity after one day with respect to a bare aqueous suspension is observed (**Figure 8a**). Moreover, the absorbance of suspension with added SDS decreases while aqueous solution maintains values of absorbance from previous day. This is caused by the lower degree of agglomeration in the presence of the anionic surfactant. However, as the peak wavelength follows the trend as the

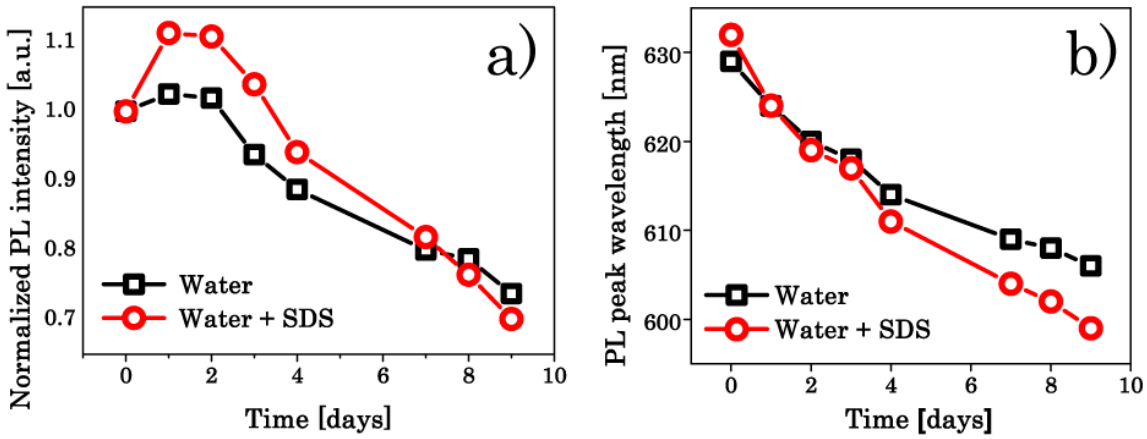

Figure 8 *- PL intensity (**a**) and peak wavelength (**b**) with time (days) of functionalized Si-nc–COOH in water suspension (black empty squares) and in water suspension with SDS added (10 mM, red empty circles). Excitation was at 350 nm. PL intensities are normalized to initial PL intensity after stabilization of the respective suspensions.*

control samples (**Figure 8b**) it becomes clear that SDS is not effective in increasing the degree of protection of Si-nc to the residual oxidation; meaning that is not interfering with the Si-nc-COOH biodegradability process.

1.6. Conclusions and future perspectives

Si-nc-COOH have a great potential in bio-imaging and offer a promising alternative to commonly used fluorescence dyes. Summarizing, in this chapter it was shown that a highly luminescent Si-nc can be prepared by sonication of porous silicon. Their solubility in polar solvents (such as ethanol or water that is omnipresent in biological ambient) is achieved by surface functionalization with undecylenic acid trough a light driven hydrosilylation reaction, without interfering with their intrinsic light emitting properties.

The obtained nanoparticles show a high assembly quantum yield (~30%), as required from bio-imaging agent and very stable PL characteristics in the ethanol suspension allowing for easy storage.

On the other hand, the behavior of functionalized Si-nc-COOH was found to be quite different in water suspension. In particular, it was demonstrated that limited agglomeration occurs on nanoscale, being present even in ethanol suspension. Increased scattering of light by dynamic agglomeration, undermines the optical performance of Si-nc-COOH, emphasizing the necessity for improved coating process.

As the more complete surface coverage by functionalizing molecules is rather challenging to achieve from the chemical point of view, the effect of surfactants as a physical coating was explored to decrease agglomeration.

Two different types of polar surfactants (cationic: CTAB and anionic: SDS) were employed. In the case of CTAB a negative influence due to a rapid increase in the oxidation process was found, while SDS showed to be effective in decreasing of agglomeration.

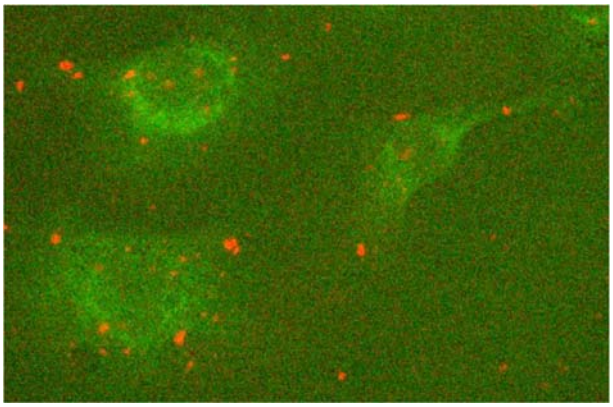

Figure 9 *– Fluorescence microscope image of SKOV 3 cells incubated for 30 minutes with water suspension of Si-nc-COOH in the presence of DCA.*

Moreover, the presence of SDS, while being effective in decreasing of the agglomeration, does not interfere with the oxidation process, maintaining the biodegradability of Si-nc-COOH. Nevertheless, if Si-nc are to be considered as a bio-imaging agent and substitution to a fluorescent dyes, there are a number of key issues that have to been dealt with, before their successful applications in field of fluorescent labeling.

In particular, apart from their stability in water, Si-nc would have to maintain their PL properties in a wide range of biological environments (not always of aqueous nature [137]) with a possibly very different pH values [93]. Moreover, a cellular uptake of these nanoparticles is still to be demonstrated [133]. In addition, surfactants such as SDS do not allow for their straightforward usage in cell or *in vivo* imaging due to their inherent toxicity [138]. As a consequence, other more bio-compatible surfactants would have to be individuated.

In order to exploit fully the potential of this new material platform for *in vivo* imaging, excitation trough one of the tissue transparency windows would have to be achieved [81,139,140]. while the possibility of multichannel [141] and/or multimodal imaging would be highly preferable [142,143].Additionally, the feasibility of targeting specific biological sites remains to be largely unexplored [144,145]. And lastly, low cytotoxicity of these nanoparticles would have to be confirmed [146]

Using the present work as a departure point, some of these aspects have been explored by mu colleagues E. Froner, E. D'Amato and S. Larcheri under supervision of Prof. Marina Scarpa and in collaboration with Fondazione Bruno Kessler (FBK).

In particular, it was successfully demonstrated the possibility of excitation of previously described nanoparticles by two-photon absorption with the excitation in the first tissue transmission window. It has been confirmed that Si-nc-COOH maintain their desirable PL properties in a range of pH values (6-9) similar to the physiological ones.

A more suitable surfactant (from the point of view biocompatibility), sodium deoxycholate monohydrate (DCA) has been identified with an overall performance identical to SDS (in the terms of agglomeration decrease and biodegradability deterioration). In humans, DCA is synthesized in the liver, secreted into bile, and delivered to the small intestine, where its micelles function as fatty acid carriers. Using these improvements in the physical coating, bio-imaging on living cells (*in vitro*) was demonstrated (**Figure 9**).

Appendix to Chapter 1

I. Porous Silicon formation[2]

All chemicals were purchased from SIGMA-ALDRICH and employed without further purification. Photoluminescent porous silicon (p-Si) layers were formed by galvano-static anodization (80 mA*cm^{-2} for 5 minutes) of 1 cm^2 chips of boron-doped p-type Si (100) oriented wafer (10-20 Ωcm resistivity, University Wafer) in a 1:2 v/v solution of 48% HF and absolute ethanol (Fluka).

II. Si-nc suspension preparation[2]

A Schlenk flask containing undecylenic acid (0.7 M) in toluene/ethanol mixture (1:1) was outgassed under argon for 30 min to remove the dissolved oxygen. One freshly prepared p-Si chip was then transferred into this Schlenk flask and sonicated with UNISET AC2 (Emmegi) ultrasonic bath under white light (ELC bulb 250 W) irradiation for 30 min with continuous argon bubbling. An argon atmosphere was used during the whole procedure. After sonication, the silicon chip was removed and the suspension of nanoparticles was stirred for 1 hour under argon flux and illumination.

After reaction, a clear solution of COOH-terminated nanoparticles was obtained. Luminescent particle suspension was filtered through a 0.2 μm syringe filter (Sartorius Minisart SRP25) and, then, the solvent was removed under reduced pressure with a Rotor-Vapor (Heidolph). The resulting material was redispersed in ethanol containing HCl (1 mM). Purification from undecylenic acid and residual solvents was performed by filtration cycles over Vivaspin 15 concentrators (Sartorius) with molecular weight cut-off (MWCO) 100.000. The retentate was collected after each cycle and the filter was rinsed with pure ethanol + 1 mM HCl. This process was repeated five times. As a result, an ethanol suspension of concentrated COOH-terminated silicon nanocrystals (Si-nc-COOH) was obtained.

III. Dispersion of Si-nc in water and organic solvent[2]

Aqueous suspension of Si-nc-COOH was obtained by re-suspending Si-nc-COOH (50 μl) in a volume of bi-distilled water (950 μl, nominal 15-18 MΩ cm MILLIPORE) and shaking for few second. Aqueous solutions of Si-nc-COOH in the presence of surfactants were obtained by diluting Si-nc-COOH (50 μl, ethanol suspension) in the aqueous solution (950 μl) containing 4-(2-hydroxyethyl)-1-piperazineethanesulfonic acid (HEPES,10 mM) at pH 7.00 in the presence of sodium dodecyl (SDS, 10 mM) or of cetyl trimethylammonium bromide (CTAB, 1 mM).

---

[2] Sample preparation was done by E. D'Amato and E. Froner

IV. PL characterization

Time resolved photoluminescence (TR–PL) measurements were performed using as an excitation source the third harmonic (355 nm, 6 ns pulse width, 10 Hz repetition rate) of a Neodymium doped yttrium aluminium garnet (Nd:YAG) laser with a photon flux of approximately 10^{25} photons $s^{-1}cm^{-2}$ on the sample.

As detection system, a CCD Streak camera interfaced with a spectrometer (10 ns of time resolution and 1 nm of spectral one) was used. Continuous wave photoluminescence (CW PL) measurements were done by a Cary Eclipse (VARIAN) fluorometer with an excitation wavelength of 350 nm.

The quantum yield measurements were performed using the 361 nm excitation line of a SpectraPhysics UV-extended Argon ion laser. A SOPRA monochromator interfaced with a visible photo multiplier tube (PMT) was used in detection (spectral resolution was 1 nm). The laser power was determined using an Ophir power meter calibrated at 365 nm. As reference source for a quantum yield measurements a red LED (MV5052 produced by Fairchild semiconductors) was used. The exact procedure for the quantum yield measurements can be found in Ref. [147].

All PL measurements were performed at room temperature and corrected for the spectral response of the detecting instruments. All solutions were contained in quartz cuvettes of 1 cm path length. The photos of Si-nc were taken by using as an excitation source UV lamp or UV laser.

V. Electron microscopy[3]

Silicon nanocrystal morphology and size distribution were evaluated by Transmission Electron Microscopy (TEM) and Selected-Area Electron Diffraction (SAED) using a Philips CM12 TEM/STEM microscope, operated at an accelerating voltage of 120 kV and provided with a W filament. The chemical composition analysis was performed using Energy-Dispersive X-ray Spectroscopy (EDXS) with a Falcon multichannel and Edax Sutw sapphire detector (C/U).

The samples were prepared by deposition at room temperature of solution of Si-nc-COOH in ethanol on a holey Cu grid with carbon film.

The TEM image of silicon nanocrystals along with the histogram of their size distribution is presented in **Figure 10a**. No physical aggregates have been observed. Due to low image contrast, organic surface layer could not be seen.

The histogram of their size distribution (**Figure 10b**) is calculated from a survey of several regions of the sample. The mean particle diameter and the standard deviation are 6.4 nm and 1.8 nm, respectively. SAED analysis confirms the good crystalline nature of the silicon nanocrystals showing the typical cubic structure of silicon (**Figure 10c**).

---

[3]Electron microscopy was done byProf. S. Gialanella and S. Larcheri

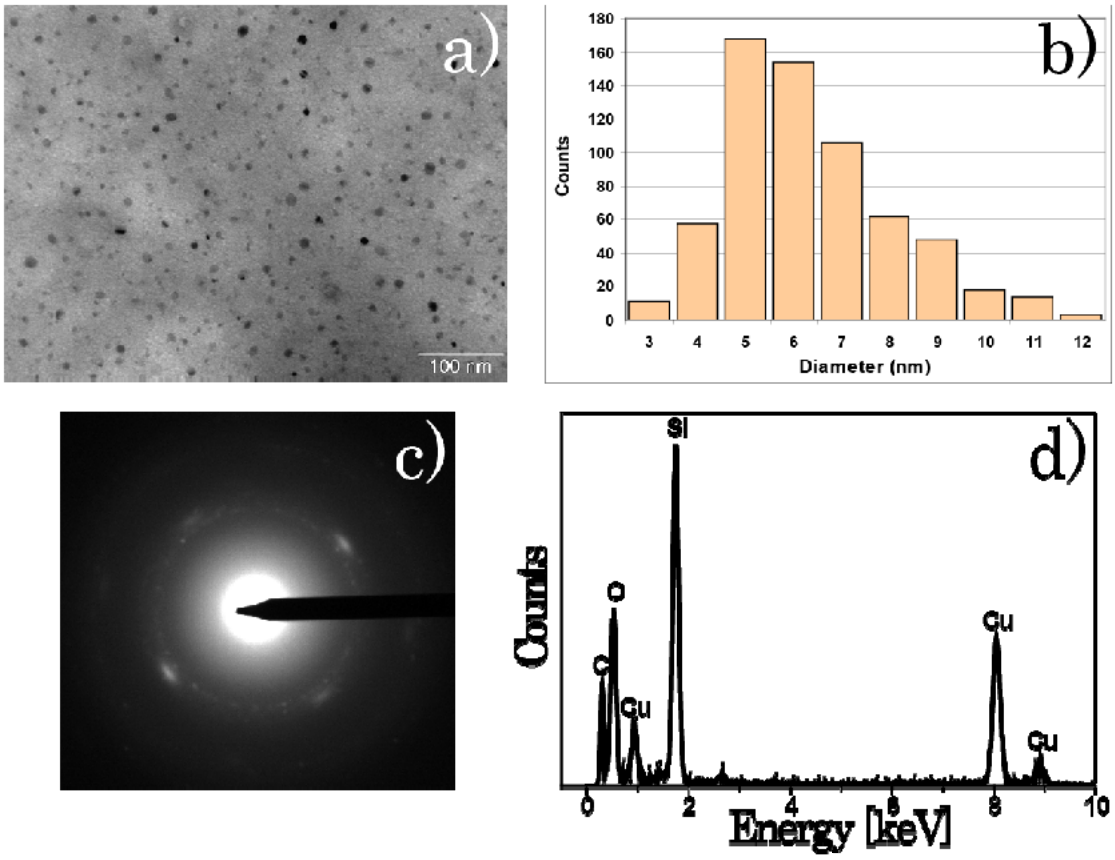

***Figure 10** – (**a**) TEM image of functionalized Si-nc-COOH. (**b**) Histogram of size distribution of Si-nc-COOH. (**c**) SAED analysis of Si-nc-COOH. (**d**) EDXS elemental analysis of nanoparticles observed.*

The elemental analysis by means of EDXS confirms that nanoparticles observed consist mostly of silicon (**Figure 10d**). However, a strong oxygen peak is also observable, indicating that initial oxidation of particles has occurred. Other elemental peaks that can be observed in the **Figure 10d** are due to the TEM grid used.

VI. FTIR

FTIR spectra were acquired in transmission mode by a Vertex V70 spectrophotometer (BRUKER) equipped with a globar MIR source and DLaTGS detector (with KBr windows). FTIR spectroscopy was performed over an extended wave-number range (500-4000 cm^{-1}) to examine both the possible reaction of COOH end group with the hydrogenated silicon surface and the degree of surface oxidation after reaction. For these measurements, about 200 µl of an ethanolic Si-nc solution were deposited, drop by drop, onto a ZnSe support ad left to dry under vacuum. Clean ZnSe support was used as baseline.

In **Figure 11**is reported the FTIR spectra of ethanol (**Figure 11a**), undecylenic acid (**Figure 11b**) and functionalized Si-nc-COOH (**Figure 11c**). In all three cases peaks due to C-H_x stretching in spectral region between 3000 cm^{-1} and 2800 cm^{-1} are clearly visible. As well, strong peak at 1710 cm^{-1} due to C=O bond could be observed in both **Figure 11b** and **Figure 11c** indicating the presence of undecylenic acid in samples with functionalized Si-nc-COOH.

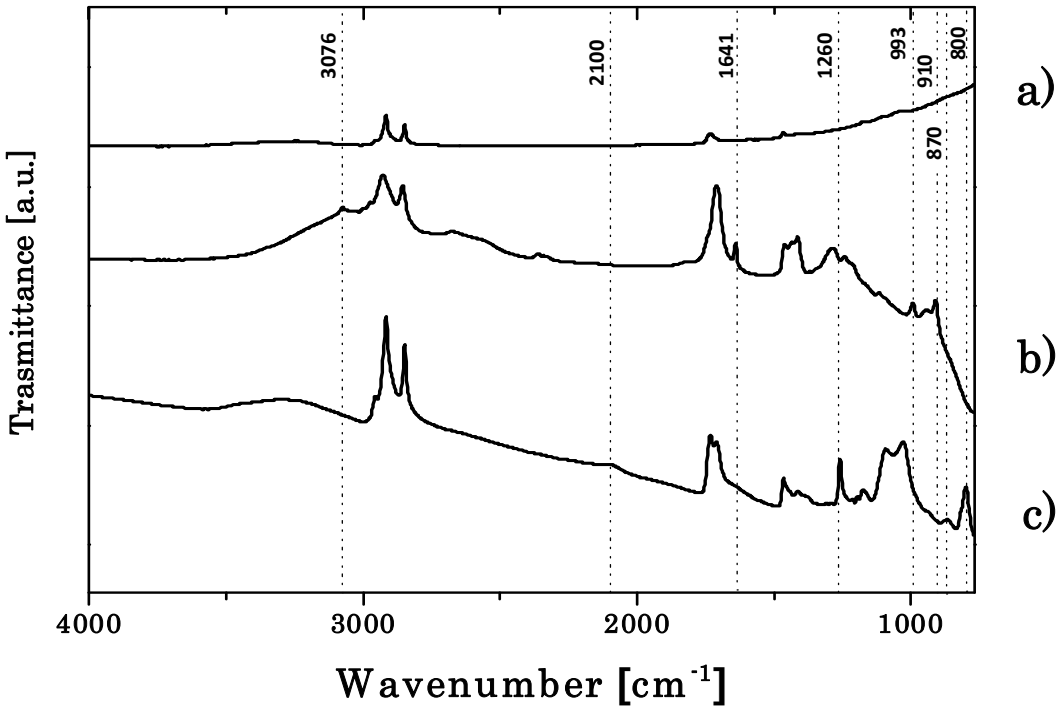

Figure 11 *- FTIR spectra of: (**a**) ethanol, (**b**) undecylenic acid and (**c**) functionalized Si-nc-COOH. All spectra are corrected for respective baselines.*

Moreover, four small peaks at 3076, 1641, 993 and 910 cm^{-1} corresponding to C=C bonds of undecylenic acid (**Figure 11b**) disappear in **Figure 11c** while two new peaks at 1259 and 800 cm^{-1} due to Si-C bond appear (**Figure 11c**).

This indicates alkyl termination of Si-nc surface after functionalization by covalent bonding of undecylenic acid to Si-nc surface [99,148,149].Two pronounced peaks at 1000 and 1100 cm^{-1} together with a broad peak at 3250 cm^{-1} (-OH stretching), are the signs of the presence of oxide on Si-nc-COOH surface [148–150], a common problem in hydrosilylation [129]. Weak absorption peaks due to hydrogen-terminated Si(100)-H surface are also visible at 2100 and 870 cm^{-1} (**Figure 11c**) [148]. This clearly demonstrates that the substitution of surface H atoms is incomplete and proceeds by covalent bonding of C atoms and partial oxidation of Si-nc-COOH surface.

VII. AFM[4]

The AFM measurements were done using the Solver P-47 (NT-MDT) equipped with SFC090SEMI head in non-contact mode. The samples were prepared by diluting the

[4]AFM measurements were done by R. Dallapiccola and E. D'Amato

concentrated ethanol solution of Si-nc-COOH by hundred times in ethanol or deionised water. 2µl of diluted solution was deposited on clean mica substrate and dried in air. Measurements were performed in air.

In **Figure 12a** is reported typical AFM image of Si-nc-COOH diluted in ethanol deposited on mica substrate. Vertical cross-section across the space indicated by the red line in **Figure 12a** is reported in **Figure 12b**. AFM imaging was repeated in several regions of the samples for both solutions. Values of Si-nc-COOH size found agree well with what observed with TEM images (see section V of Appendix to Chapter 1).

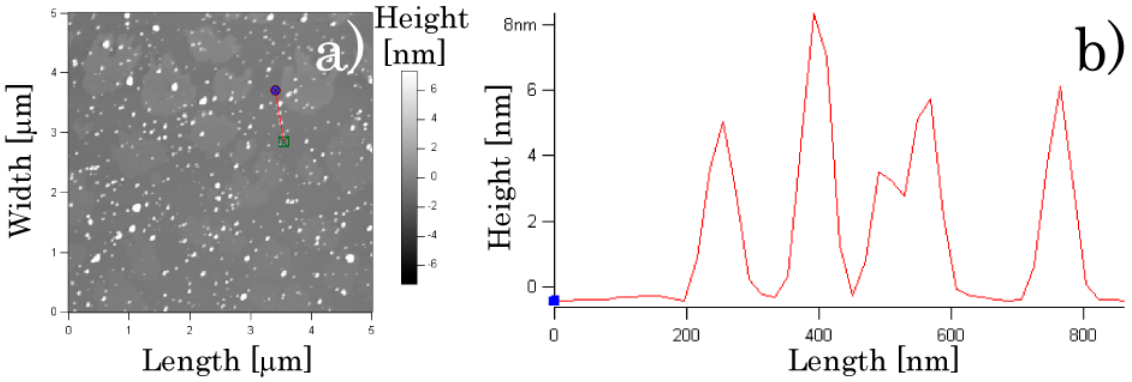

***Figure 12** – (**a**) AFM image of Si-nc-COOH diluted in ethanol and deposited on clean mica substrate. b) Vertical cross-section across the space indicated by the thin red line in part a).*

VIII. XPS[5]

X-ray Photoelectron Spectroscopy (XPS) measurements of Si-nc-COOH were carried out on a Scienta ESCA 200 instrument equipped with a hemispherical analyser and a monochromatic Al K (1486.6 eV) X-ray source. The emission angle between the analyser axis and the sample surface was 90°, corresponding to a sampling depth of approximately 10 nm. Quantification of relative elemental percentage was obtained, after Shirley background subtraction, by using the integrated area of the deconvoluted core lines together with atomic sensitivity factors. The Si-nc-COOH were deposited from the concentrated ethanol solution, drop by drop on a flat, clean gold surface. The solvent was left to evaporate in a fume cupboard equipped with dust filters and then inserted into the XPS high-vacuum chamber.

The XPS survey spectrum is shown together with atomic percentage (**Figure 13a**). The Au signal was absent in the sample area were Si-nc-COOH were present, indicating that only the Si-nc-COOH layer was sampled. Only peaks corresponding to C, O, and Si were observed, matching the elemental composition of the undecenoic acid-grafted Si-nc.A ratio C/O of about 2.9 indicated that oxygen was partly due to Si oxidation which was confirmed by the Si 2p spectrum (**Figure 13b**) where combined composition of SiAOH and SiO2 (S2and S3

[5]XPS measurements were done by C. Potrich.

components respectively in **Figure 13b**) was present. Si oxidation was expected since all Si-nc-COOH manipulations were made under ambient atmosphere, after the functionalization step.

C 1s %	O 1s %	Si 2p %
58.3	20.2	21.6

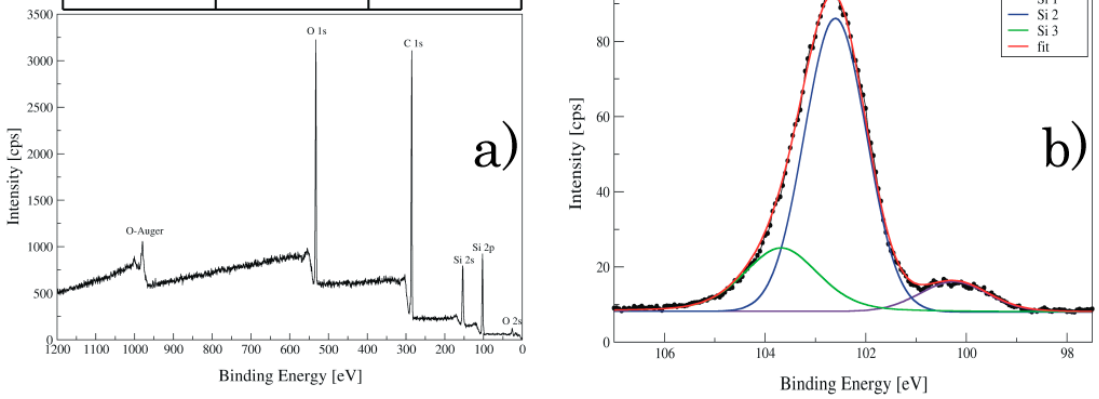

Figure 13 *– (**a**) The XPS survey spectrum together with atomic percentage of Si-nc-COOH (**b**) Si 2p spectrum. Raw data are indicated by black full circles, Si 1 component corresponding to by violet line, Si 2 component corresponding to by blue line, Si 3 component corresponding to by green line and fit by red line.*

IX. Time resolved PL measurements in ethanol suspension

The sample was 1ml of concentrated suspension of Si-nc-COOH in ethanol (approx. 20 times more respect to concentration used for other experiments). The data were fitted with a stretched exponential function (see section1.3 of Chapter 1) [109].

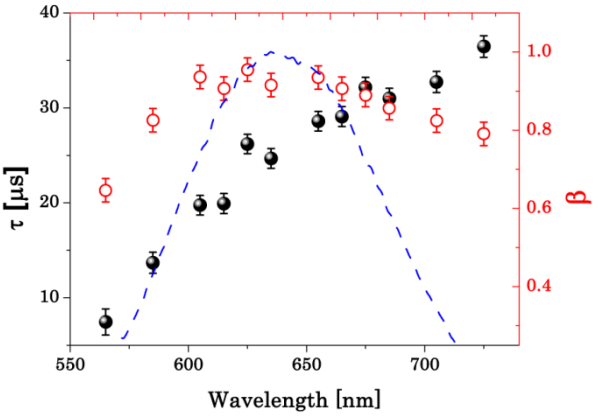

Figure 14 *- Results of the fit of decay curves of concentrated functionalized Si-nc-COOH in ethanol suspension with stretched exponential function (black spheres for mean decay lifetime **τ** and empty red circles for stretching parameter **β**). Decay curves are obtained by integrating 20 nm wide spectral windows. The points are not equidistant due to partial overlap of different spectral acquisition windows. Excitation is at 355 nm.*

The results of fitting the experimental data with the stretched exponential are reported in **Figure 14**. The time decay of the functionalized Si-nc-COOH was found to be in microsecond range. Moreover, strong wavelength dependence of the time decays, with a decrease towards lower wavelengths was observed.

X. DLS and Zeta potential

DLS and Zeta potential measurements were performed using Zetasizer Nano ZS of Malvern Instruments. Diluted ethanol suspension was prepared by suspending 200 µl of concentrated Si-nc-COOH ethanol suspension in a 1ml of pure ethanol. Aqueous suspension of Si-nc-COOH was obtained by re-suspending 200 µl of concentrated Si-nc-COOH ethanol suspension in a 1ml deionidized water of (nominal 15-18 MΩ cm MILLIPORE) containing 4-(2-hydroxyethyl)-1-piperazineethanesulfonic acid (HEPES,10 mM) at pH 7.00 and shaking for few second. In order to study the surfactants effect, to aqueous suspensions 10 mM of SDS was added. Note that higher concentration of Si-nc-COOH was used in these experiments (respect to PL measurements and numerical simulations), as in the case of lower concentration, signal was beyond instrument detection limit.

In the undiluted concentrated ethanol suspension a value of approximately 10 nm for the agglomerate size was found. The very same value was found as well in the diluted ethanol suspension. On contrary, in water suspension cluster size evolved quickly from 60 nm immediately after addition, to value of 100 nm where it stabilized. Interestingly this value decreased to the average size of 80 nm after one day of incubation in deionized water.

In the presence of the SDS agglomerate size in the water suspension decreases to a value of approximately 30 nm.

Zeta potential was measured only in water suspension of Si-nc-COOH, as in other samples the signal was too low for reliable determination. The value found is -23.1 mV. This value is lower than what expected of stable suspension [132].

XI. Si.nc-COOH concentration determination

The Si-nc-COOH concentration in aqueous suspension has been estimated from the data obtained for Si-nc-COOH concentration in ethanol suspension, by means of optical measurements. The concentration has been calculated from the experimental data by using the absorption cross-section value for Si-nc reported in the literature [117]. The top view schematics of the incidence light geometry on the sample, is presented in **Figure 15a**, while the actual rear view of the measurement is presented in the photo in **Figure 15b.**

Symbols in the **Figure 15a** stand for:

$\mathbf{P_0}$ - incidence laser power on the sample;

$\mathbf{P_{ac}}$ – light power absorbed by cuvette and solvent only;

$\mathbf{P_a}$ – light power absorbed by Si-nc-COOH;

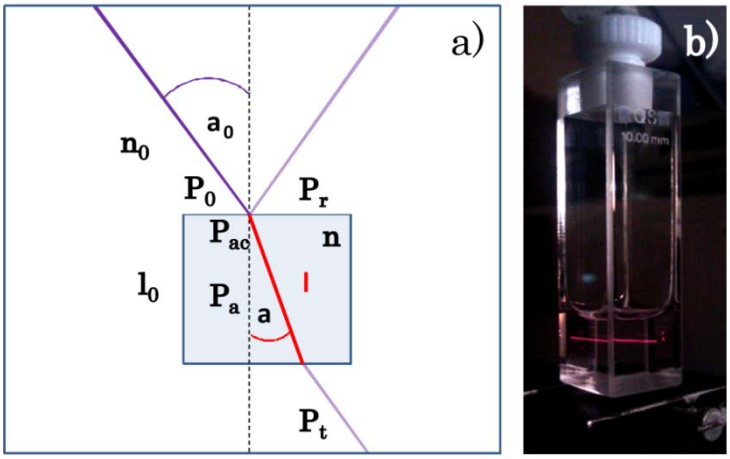

Figure 15 *- (**a**) Top view schematic representation of the excitation light incidence geometry. (**b**) Photo of the sample.*

P_t - transmitted light power;

P_r - reflected light power;

n_0 - refractive index of air (taken to be: $n_0 = 1$);

n - refractive index of ethanol (taken to be: $n = 1.36$);

α_0 - light incidence angle in the air ($\alpha_0 = 48°$);

α- angle between light beam and normal direction (dashed black line, **Figure 15a)** in the suspension;

l_0 - length of cuvette ($l_0 = 1$ cm);

l - length of optical path of light beam inside of cuvette.

Assuming that the Si-nc concentration in the suspension is sufficiently low, influence of the Si-nc, on the real part of suspension's refractive index could be neglected and the solvent refractive index could be used instead. From the Snell law of refraction:

$$n_0 * \sin\alpha_0 = n * \sin\alpha \tag{2}$$

and Pythagoras's theorem:

$$\cos\alpha = \frac{l_0}{l} \tag{3}$$

optical path of the light beam inside of the sample could be found as:

$$l = l_0 * \left\{\cos\left[\arcsin\left(n_0 * \sin\alpha_0 * n^{-1}\right)\right]\right\}^{-1} \tag{4}$$

Also, if the Si-nc concentration is sufficiently low and light loss mechanism is considered to be completely due to absorption from the Si-nc, (disregarding the scattering contribution of Si-nc, etc.), Beer-Lambert's law can be written as:

$$P_t = P_0` * \exp\left(-\sigma_{Si-nc} * n_{Si-nc} * l\right) \tag{5}$$

Where

$$P_0` = P_0 - P_{ac} - P_r \tag{6}$$

And $\sigma_{Si\text{-}nc}$ is Si-nc absorption cross section taken from the literature [117] ($\sigma_{Si\text{-}nc} = 5*10^{-15}$ cm^2, taken for the excitation energy of 3.53 eV and detection energy of 1.94 eV. This detection energy coincides with the peak of PL band of fresh Si-nc prepared by our method) while $n_{Si\text{-}nc}$ is the density of Si-nc in suspension.

Combining the Eq. (4) and (5) and after some algebra, concentration of Si-nc could be expressed as:

$$n_{Si-nc} = \ln\left[P_0` * \left(P_0` - P_a\right)^{-1}\right] * \left(\sigma_{Si-nc} * l_0 * \left\{\cos\left[\arcsin\left(n_0 * \sin\alpha_0 * n^{-1}\right)\right]\right\}^{-1}\right)^{-1} \tag{7}$$

There are a number of processes that could limit the accuracy of the results obtained from Eq. (7). The most important sources of experimental errors are:

- an accurate measurement of incident laser power;
- scattering contribution of Si-nc;
- an error in determination of the real part of suspension's refractive index;
- the absorption cross section for Si-nc taken from literature [117];
- convective motion of illuminated suspension.

In order to account for this effect, all the measurements were repeated several times and mean values were taken.

However, the samples we are working with are prepared in different manner from those used for absorption cross section determination in Ref. [117]. As well, the excitation energy we are using in these experiment is slightly different (3.43 eV respect to 3.53 eV in Ref. [117]) and broad distribution of sizes and consequently somewhat different absorption cross sections are present in our samples. As all of these effects are difficult to be accounted for, in order to be conservative in experimental error estimate, it is reported only the order of magnitude of the estimated concentration.

Chapter 2
Silicon nanocrystals as gain medium

2.1. Introduction to material properties

2.1.1. Photoluminescence in a silicon nanocrystal's ensemble

The discovery of efficient light emission from porous silicon [83] suggested that some of the problems associated with the silicon indirect band gap nature could be overcome by the localization of the excitons in a strong confining potential (e.g. by placing them inside of the nanocrystals). The PL origin from the nano-structured silicon was initially attributed to transitions between confined electron and hole states modified by quantum confined effects (QCE) [83,117,151]. However, it became clear soon, that the interface states could as well contribute significantly to the PL emission [43,152].

One of the main difficulties when dealing with the silicon nanocrystals is that most of the experiments are carried out on rather large ensembles with significant size dispersion (see for example section V of Appendix to Chapter 1). Fabrication techniques currently employed still lack the maturity and control, common to the production of quantum dots made out from compound, III-V or II-VI group semiconductor materials.

As a consequence, the interpretation of the experimental data is difficult due to the associated inhomogeneous broadening [112–114] and various collective effects [52,115,153–159]. Additional complications arise, as nanocrystal's surface conditions are poorly controlled across the ensemble [44].

As an example of the complexity this leads to, even in the interpretation of the basic properties, it could be considered a PL decay time of silicon nanocrystals. PL decay time in Si-nc's ensemble is described by the stretched exponential function [109,115]. Evidently, the deviation from the single exponential behavior could be due to various reasons. It was proposed recently that a certain amount of "stretching" (deviation from the single exponential decay) behavior is intrinsic to the indirect band-gap quantum dots [160], whereas other contribution could not be disregarded neither.

The most often considered are: a distribution of the nanocrystal's sizes (and hence, a distribution of the recombination rates [56,111]), nanocrystal shape [161,162], nanocrystal

surrounding [41,103,163–165], disorder and strain [36,166,167], intensity intermittency (so-called "blinking") [168], quenching center distribution [169,170], inter - nanocrystal transport [153,159,171,172], modification of the local density of optical states [114,173,174] etc.

Obviously, the poor fabrication control, the uncertainty on the surface conditions and the limited applicability of the theoretical tools, make the analysis of the properties of a silicon nanocrystal's ensemble a challenging task [44]. Unfortunately, none of these aspects is alleviated when stimulated emission is considered.

2.1.2. Optical amplification in silicon nanocrystals

Since the demonstration of the optical gain [49], significant attention has been focused on the optical amplification process in silicon nanocrystals. This is not surprising, as this was the first silicon based system in general, where optical amplification has been demonstrated. Additional attractiveness to this approach was given by its simplicity, CMOS compatibility [57] and the possibility of electrical excitation [52,175].

Secondly, Si-ncs provide a straightforward route towards realization of a silicon quantum dot laser [53]. In addition, a few other improvements with respect to bulk silicon have been named such as: lower non-radiative recombination rate (due to exciton localization), size controlled emission (due to QCE), lower carrier absorption (emission is moved towards visible), better radiative emission efficiency (due to k-conservation rule breaking), and better light extraction (smaller refractive index mismatch between SRO and air) [57].

Along with the previously mentioned advantages regarding the silicon nanocrystals as gain medium, a few downsides have been identified as well. For example, although, it is referred to as a CMOS compatible approach, a word of caution is needed. Manufacturing process of silicon nanocrystals embedded in silicon dioxide begins with the deposition of the film of non-stochiometric "silicon rich oxide" by one of the different deposition methods (sputtering, chemical vapor deposition, silicon ion implantation etc.). This material is referred to as a "silicon rich oxide" (SRO or SiO_x, where $x < 2$) because it contains an excess of silicon atoms with respect to stochiometric silicon dioxide (SiO_2).

Silicon nanocrystals formation then proceeds by thermally driven phase separation where excess silicon atoms separate from initial dielectric matrix, agglomerate and create nanometer size silicon nanoparticles embedded in pure stochiometric SiO_2. Phase separation and consequently, silicon nanoparticles size, density and crystallinity degree can be controlled by adjusting the "silicon excess", temperature and duration of thermal treatment. In order to induce the Si-nc nucleation, high temperature (usually in excess of 1000°C) are necessary [176], meaning that Si-ncs have to be implemented in the beginning of the CMOS process, limiting compatibility with additional processing steps.

Unfortunately, this is not the only drawback when optical amplification with silicon nanocrystals is considered. The wavelength range of the optical amplification in silicon nanocrystals lies well beyond telecom wavelengths [49,177] while electrical pumping still lacks maturity [52,175].

Nevertheless, up to date, there have been numerous reports of optical amplification in Si-nc based materials produced by different methods [50,177–180]. Regardless to the particular production technique used, when the optical gain is detected, a set of similar PL characteristics is observed. The optical amplification is present only in a very fast PL component (on a nanosecond or shorter time scale) while only optical losses are exhibited in slow component (μs time scale) which is due to indirect band-gap recombination. Additionally, the gain band is always blue shifted respect to the excitonic one [181].

Although, significant amount of time has passed since the first optical gain observation, the laser action demonstration is still eluding, as similar issues to spontaneous emission case are encountered. Even though, on the first sight, stimulated emission in the quantum dot system (e.g. silicon nanocrystals) should be fairly simple to achieve, the situation is greatly complicated by the surface effects [43] and the collective phenomena [156,182]. This is also the principal reason why the origin of the optical gain has not been established yet [57]. At the present, it is still not clear whether the fast component associated with the optical gain is intrinsic to Si-nc or it is due to specific surface conditions. Quite similar debate remains open on the origin of spontaneous emission in the same system.

The gain in silicon nanocrystals has been traditionally associated with a surface termination of Si-nc, in particular with an Si=O double bond for which optical excitation causes a large lattice relaxation of the Si=O bond [152,183] like in the silanone molecule. Until recent optical gain demonstration in silicon nanocrystals embedded in silicon nitride [184], it was generally accepted that oxide is needed for the gain observation [181]. Nevertheless, the optical amplification has been again associated with the exciton localization on the surface states [49,184].

The surface origin of optical amplification is favored for a number of reasons. As in the case of bulk silicon, high values of free [185] (confined [186,187]) carrier absorption will prevent the net gain observation [188,189]. In addition, due to ground level degeneracy of excitons in Si-nc, optical gain is expected only in multi-excitonic regime, where it has to compete with a very efficient Auger mechanism [185].

These aspects have been recently re-examined in a few theoretical studies [190–192]. Overall conclusion is that optical amplification could be achieved in indirect band-gap transitions, in spite above mentioned effects, even in the bulk silicon, if certain conditions are met (e.g. low temperature).

2.1.3. Direct band-gap recombination in silicon nanocrystals and surface tailoring

Somewhat different strategy has been employed in germanium [22] (indirect band-gap material as well). In the case of germanium, the direct band-gap recombination was exploited [193]. Unfortunately, the same strategy is not directly applicable to silicon, due to the higher energy difference between Γ and X conduction bands valley extremes (large energy depth of X valley) [194].

In very small silicon nanocrystals (smaller than 2 nm) direct band-gap transitions are expected to become dominant optical transitions due to QCE [47]. There have been a number of reports claiming to observe direct band-gap transitions in colloidal systems [195–197]. However, practical implementations for achieving this type of emission in small

nanocrystals remain to be very challenging, especially in the case of nanocrystals embedded in silicon oxide matrix (CMOS compatible approach), due to influence of surface oxidation on the PL properties of Si-nc [43,101].

This led to an opposite approach where silicon nanocrystal's surface is tailored in order to get efficient and fast direct-like photoluminescence [198]. Moreover, it was proposed that surface properties could be as well used to suppress some of the non-radiative processes such as Auger recombination [199].

All the same, in this chapter the attention will be focused on the embedded samples guaranteeing monolithic integration and full CMOS process compatibility. Interestingly, it has been demonstrated that a zero-phonon PL emission could be experimentally observed even in fully oxidized embedded silicon nanocrystals [200]. Moreover, this emission has been observed in the nanocrystals with sizes greater than 2 nm.

2.1.4. Zero-phonon emission in silicon nanocrystals

When the size of the Si-nc is changed (in the regime where the Si-nc radius is smaller than Bohr exciton radius in bulk silicon [201]), its electronic band structure is heavily influenced by QCE [38,202]. Most of the experimental and the theoretical works in the field focused on the features related to the indirect band-gap (Γ-X transitions, 1.12 eV of in case of bulk silicon), while less attention has been dedicated to a direct band-gap (Γ-Γ transitions), as these electronic states lay much higher in energy (3.32 eV of energy separation in bulk silicon) [194].

Naturally, these higher energy conduction/valence band states are also influenced by quantum confinement [202]. Interestingly, due to their complex nature, influence of QCE is markedly different for these states. Contrary to the indirect band-gap behavior, the QCE lead to decrease and red-shift of direct band-gap with increased confinement [203–206]. The amount of the direct band-gap decrease (and indirect band-gap increase) is not sufficient to make the silicon nanocrystals direct band-gap material, at least up to very small sizes [47,205]. The direct band-gap optical transitions in silicon are practically inhibited by a very efficient intra-band relaxation of carriers which thermalize to the minimum of the conduction/valence band [207].

In silicon nanocrystals, due to finite size and QCE, energy levels are more separated. Depending on the Si-nc size, this energy spacing might become bigger than the typical phonon energy [42,205]. Under these conditions, hot carrier thermalization should proceed mainly by multi-phonon emission [42,205,208]. If the multi-phonon emission remains the main cooling mechanism, the so called "phonon bottleneck" is likely to occur [208]. Effectively this means that cooling rate of carriers in Si-nc will be much slower than in bulk silicon [206], leading to increased efficiency of direct radiative transitions [200].

On the other hand, knowing that the energy spacing between hole levels is smaller than those for electrons [205] and having in mind that the Si-nc's are embedded in silicon dioxide, other processes such as vibronic coupling [209] or Auger cooling mechanism [210] may contribute to thermalization and decrease efficiency of direct radiative transitions.

Owing to the relaxation of the k-conservation rule [47], oscillator strength of direct transitions will become stronger as the Si-nc size is decreasing [205,206]. The radiative

lifetimes for these transitions have been calculated and values in the nanoseconds range (depending on Si-nc size) are found [206]. This means that the efficiency and observation possibility of these transitions is limited only by the non-radiative processes.

The Auger recombination is expected to increase rapidly in the smaller nanocrystals [211], leading to multi-exciton lifetimes shorter than 100 ps [212] influencing the carrier population in the higher energy states. However, the re-excitation of carriers will enhance the carrier density with excess of energy respect to minimum of the band [200]. Therefore, zero-phonon recombination will be enhanced through a sort of carrier "recycling" [213] leading also to apparent lengthening of the direct PL decay time on the order of 100 ps (multi-exciton recombination lifetime in Si-nc) [200,214].

Contrary to the slow exciton band [117,215], Auger recombination is actually beneficial for the observation of zero-phonon PL coming from non-equilibrium hot carriers [200]. Without the mechanism of the Auger recycling, the typical decay time of zero-phonon PL is expected to be in picosecond range [216–219]. The reason for that is that hot carriers easily undergo an efficient surface state capture.

The presence of oxygen related bonds on the surface of silicon nanocrystals induce a significant perturbation of the Si-nc excited state [40,220], influencing heavily subsequent radiative recombination [43,101]. However, in the case of silicon nanocrystals embedded in silicon dioxide matrix, at least partial surface oxidation of Si-nc is simply inevitable. Surface perturbation of core states is significantly smaller if the oxide shell is complete [96,221].

During the nucleation process large strain build-up is expected to occur on the interface between Si-nc and matrix [222–224], governed by initial strain profile in the as-deposited film [225,226]. Moreover, in case of certain deposition techniques, such as Plasma Enhanced Chemical Vapor Deposition (PECVD), used for the deposition of the samples under study, even at large annealing temperature complete phase separation is not achieved [225–227]. This leads to faulty matrix and increased disorder.

For the Si-nc embedded in silicon dioxide matrix, significant influence on PL properties is coming from the strain and disorder induced by the surrounding matrix [36,41,167]. This often leads to the creation of undesirable trapping centers (e.g. silicon dangling bonds). In order, to decrease the number of trapping centers, samples used in this work were passivated with hydrogen [85]. Unfortunately, silicon-hydrogen bonds could be disassociated under long exposure time to high intensity UV irradiation [85,228] and surface capture could be reactivated. This may lead to the PL intensity degradation after very long UV light exposure.

2.1.5. Optical amplification by zero-phonon recombination

Quite recently, it has been shown that that the emission band of zero-phonon PL in silicon nanocrystals could provide with a stimulated emission and transient gain under femtosecond optical pump [229]. In the same work sub-picosecond lifetime for the stimulated emission was observed.

The work presented in this chapter will be centered on the search for stimulated zero-phonon emission in of silicon nanocrystals embedded in a silicon dioxide matrix produced by CMOS compatible approach (PECVD). In the first part of this chapter, spectroscopy study of

the used material will be presented and experimental conditions under which zero-phonon emission could be observed will be explored. In the second part Si-nc will be placed in an optical cavity. Firstly, the optical properties of the cavity embedded Si-nc will be thoroughly characterized and afterwards, the optical cavity will be exploited in the study of the ultrafast emission dynamics.

Evidently, based on the results presented in Ref. [229] the stimulated emission may be expected only in pulsed regime and in a very short time after the initial excitation. That means that even if the laser action is achieved, CW operation of such laser would be extremely challenging. Nevertheless, even the pulsed operation would be very interesting in light of the extremely high bit rates needed for the data transmission. Based on the stimulated lifetime reported in Ref. [229] modulator free pulsed laser operation with a bit-rate in excess of 1 Tbit/s should be possible.

2.2. Continuous-wave photoluminescence measurements of thin silicon-rich oxide films

2.2.1. Low excitation photon flux photoluminescence measurements

Samples used in this study were produced in FBK clean-room facilities in a standard CMOS line[6] (for more details on the fabrications procedure see section I of Appendix to Chapter 2). Detailed description of the samples fabrication procedure can be found as well in Ref. [230].

Shortly, thin films (200 nm) of silicon-rich oxide (SRO) were deposited on top of the crystalline silicon wafer by plasma enhanced chemical vapor deposition (PECVD) technique. Afterwards, samples were annealed at high temperature in nitrogen atmosphere, in order to induce a phase separation and a silicon nanocrystal nucleation and growth. In addition, thewsilicon nanocrystal surface was passivated with hydrogen in order to reduce the number of dangling bonds and boost the emission intensity [56,85].

Typical PL spectrum coming from the samples under continuous-wave (CW) excitation is reported in **Figure 16** (for more details on the experimental conditions see section II of Appendix to Chapter 2). The broad, Gaussian-like PL band (115 nm wide, see Inset of **Figure 16**) could be observed indicating a fairly broad size distribution of the silicon nanocrystals present in the samples, typical to the deposition technique used (PECVD) [44,227].

At low excitation photon fluxes (~10^{15}-10^{16} ph./(cm^2 x s)) the PL band peaks at approximately 820 nm (~1.5 eV) corresponding to an average diameter of silicon nanocrystals of 3.5 nm, if the QCE are considered to be responsible for observed PL [200]. This is reasonable assumption considering the spectral position of PL band, as the oxide defect emission is usually situated higher in energy (> 2.25 eV) [43].

---

[6]Samples deposition was performed by M. Ghulinyan and under supervision of G. Pucker of FBK-APP.

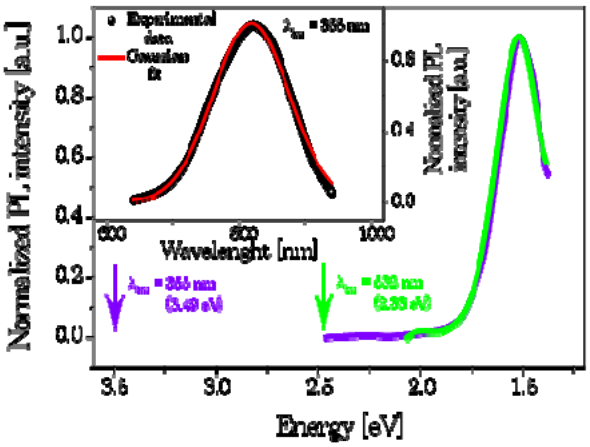

Figure 16 *– Normalized PL spectra of silicon-rich thin films under CW excitation. Violet solid line represents spectrum under UV excitation (355 nm or 3.49 eV, indicated by the violet arrow, excitation photon flux of* $\Phi = 6.8 \times 10^{15}$ *ph.*cm^{-2}*s^{-1}). PL spectrum under visible excitation (532 nm or 2.33 eV, green arrow, excitation photon flux of* $\Phi = 1.4 \times 10^{16}$ *ph.*cm^{-2} *s^{-1}) corresponds to the green solid line. (**Inset**): Normalized PL spectrum under UV excitation (empty black circles, the same excitation conditions as in main figure) and the best fit by a Gaussian function (red solid line) yielding a width of* $w = 115 \pm 1$ *nm and peak wavelength* $\lambda_{peak} = 820 \pm 1$ *nm.*

The PL band does not shift, nor changes the shape, when the excitation wavelength is changed from UV (355 nm) to green (532 nm) (see **Figure 16**). This indicates a good phase separation where the population of very small nanocrystals or silicon amorphous nanoclusters could be considered negligible. As could be seen in **Figure 16**, there is no visible difference between the two spectra obtained under two different excitations wavelengths. Therefore, in the following, for technical reasons, excitation wavelength of 532 nm will be mostly used for CW PL experiments.

It is important to underline that under UV excitation (355 nm), another PL band at higher energies (> 2.25 eV) is not present. As mentioned previously, PL band at those emission energies is usually attributed to the oxide defect [43,100]. The lack of it, points out to a good quality of samples and well passivated nanocrystals.

2.2.2. High excitation photon flux (μ-PL) measurements

In order to study the dependence of the PL intensity on the photon flux under CW excitation a μ-PL setup was used. It consists of confocal Zeiss microscope equipped with 100x objective. As an excitation source was used CW diode pumped solid state (DPSS) laser emitting at 532 nm, while the photoluminescence signal was detected with a visible CCD camera (Andor). Excitation light and PL signal were both perpendicular to the sample surface. More details on the experimental conditions and the experimental setup used can be found in section III of Appendix to Chapter 2.

In the **Figure 17a** is reported the PL intensity dependence on the excitation photon flux of the thin SRO films. In order to quantify this dependence, the experimental data were

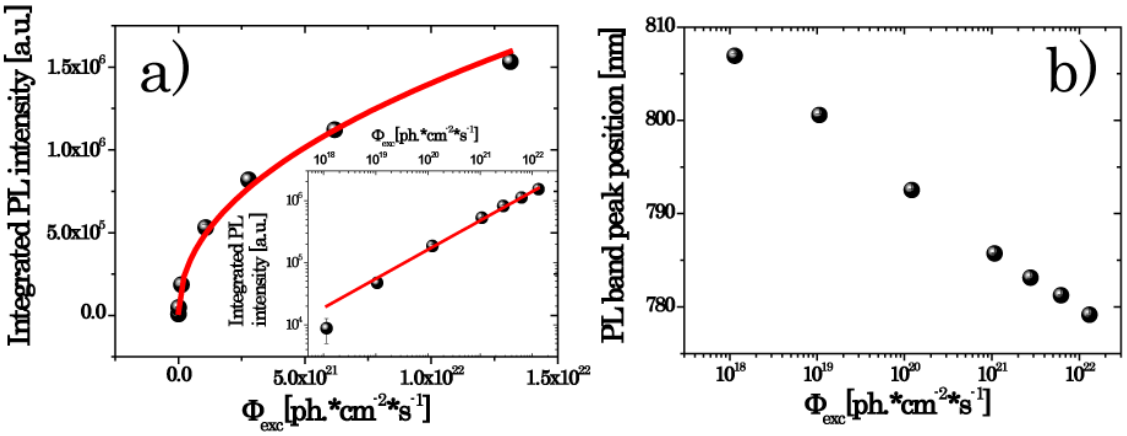

Figure 17 *- (**a**) PL intensity dependence on excitation photon flux (black spheres, λ_{exc} = 532 nm) of thin SRO films. Red solid line is the best fit of experimental data with an allometric function leading to a power law coefficient **b** = 0.47 ± 0.01. Excitation photon flux was varied between the values of Φ = 1.14 x 10^{18} ph.*cm^{-2}*s^{-1} and Φ = 1.3 x 10^{22} ph.*cm^{-2}*s^{-1}. (**Inset**): Log-log plot of the same experimental data (black spheres) as in the main figure together with an allometric function fit (red solid line). (**b**) Semi-log plot of PL band peak position shift with increased excitation photon flux (black spheres, λ_{exc} = 532 nm). PL band is shifting towards the shorter wavelengths with increased excitation photon flux. The excitation photon flux variation is the same as in panel (**a**).*

fitted with an allometric function (see **Figure 17a**). The allometric function is defined as:

$$I(\Phi) = a * \Phi^{b} \tag{8}$$

Where **I(Φ)** is a PL intensity as a function of excitation photon flux, **Φ** is excitation photon flux, **a** is a constant (allometric coefficient) and **b** is an allometric exponent (scaling exponent or power law coefficient). By fitting the experimental data with this function, the power law dependence of PL intensity on excitation photon flux could be extracted.

The PL intensity of studied samples evolved sub-linearly with increased excitation photon flux, with a power law coefficient equal to **b** = 0.47 ± 0.01. A low value of power law coefficient points out to a presence of an efficient non-radiative recombination mechanism. The most common non-radiative recombination mechanism present in silicon nanocrystals under high excitation photon fluxes is the Auger recombination [54].

Strong Auger recombination will lead to a saturation of PL when the multi-exciton regime is reached [117,215]. When the saturation is reached, the allometric function fitting is not applicable anymore, and more elaborated analysis based on rate equation modeling should be employed [117,171].

As could be seen in **Figure 17a**, the allometric function still fits the data satisfactorily, meaning that a full saturation of PL has not been reached, yet. However, in the case when the Auger recombination is the dominant non-radiative recombination mechanism present (in the range of the excitation photon flux values where full saturation of PL hasn't been reached), the power coefficient of 2/3 is expected [54].

As the free carrier absorption is unlikely to be effective in thin films as the ones under study [231,232], additional non-radiative recombination channel is most likely to be due to inter-nanocrystals transport [159,171].

Interestingly, under intense excitation photon flux, the peak position of PL band is blue-shifting with respect to its low excitation photon flux value (see **Figure 16** and **Figure 17b**). As the photoluminescence from thin films is collected perpendicularly to the sample surface in a non-waveguiding configuration, absorption due to free (confined) carrier absorption [232] and various non-linear processes [231] could be safely excluded as driving mechanisms to the observed behavior.

As shown in **Figure 16**, the PL band of the samples under study is fairly broad, corresponding to a significant size dispersion of silicon nanocrystals and consequently it implies a dispersion in absorption cross-sections and radiative lifetimes [56,117]. This means that for a larger Si-nc (with larger absorption cross-section and longer radiative lifetimes) is easier to reach a multi-exciton regime and undergo a saturation due to Auger recombination [117,215], leading to apparent blue-shift of photoluminescence band.

This effect should be even more pronounced in the case of inter-nanocrystal transport where it seems that at least, in the case of the tunneling mechanism of transport, there exists a preferential direction of exciton transport from the smaller nanocrystals towards the larger ones [155–157,159]. However, as discussed previously for the PL dependence on excitation photon flux (**Figure 17**), PL saturation (even of fraction of silicon nanocrystals) seems to be highly unlikely under the used excitation conditions.

On the other hand, inter-nanocrystal transport itself, could lead to a PL peak shift [156,159]. This effect should be even more pronounced under high excitation photon fluxes where there is a high probability of having two nearby nanocrystals [153,171,233].

Regardless, of the exact mechanism for the observed blue-shift, the data presented in **Figure 17b,** show that the amount of the blue-shift is getting almost exponentially smaller with the excitation photon flux increase.

By extrapolating the data from **Figure 17b,** it could be seen that is very unlikely that the PL peak position would shift further than 750 nm even under extreme pumping conditions (by pulsed laser for example, with the excitation photon fluxes of the order ~10^{25} ph.*cm^{-2}*s^{-1}). Thus, the observed blue-shift of the PL would not influence the findings presented inthe following sections.

We have also checked the uniformity of the PL emission. On the wafer a good uniformity with less than 10% variation in the PL intensity has been observed.

2.3. Time resolved photoluminescence measurements of thin silicon-rich oxide films

2.3.1. Low repetition rate excitation

In order to study the dynamics of the PL coming from the thin SRO films, time resolved measurements have to be performed. To that end, samples are excited by intense laser pulses of a short temporal duration (~6 ns in present case, more details on experimental conditions and experimental setup could be found in section IV of Appendix to Chapter 2).

The PL decay times of silicon nanocrystals could be described by a stretched exponential function (see also section 1.3 of Chapter 1 and section 2.1.1 of Introduction to Chapter 2) [109]. The time traces obtained from the TR PL measurements were fitted with a stretched exponential function. Mean lifetimes τ and stretching parameters β were extracted (spectral dependence of the fitting parameters is reported in **Figure 18a**. A strong spectral dependence of the photoluminescence decay could be observed). As discussed previously (see section 1.3 of Chapter 1 and section IX of Appendix to Chapter 1), this is an indicator of a good crystallinity of produced silicon nanocrystals [110] and quantum confinement origin of observed PL [38].

The stretching parameters found (see **Figure 18a**) are consistently lower than those reported on colloidal samples in Chapter 1 (see for example **Figure 14**). Low values of the stretching parameter β indicate to a possibility of inter-nanocrystal transport [115], in accordance with what was concluded in the previous section from the PL intensity dependence on excitation photon flux under CW excitation.

The TR PL measurements performed on the microsecond time scale do not provide information on the ultrafast emission dynamics. On the μs timescale the emission recombination is completely dominated by the slow indirect band-gap recombination as the carriers have already undergone the cooling process and single exciton regime has been reached.

In the case of QCE origin of PL, PL lifetimes of the order of hundreds of μs have been reported [56,162]. By using the low repetition rate excitation (10 Hz in present case), one permits a full relaxation of the system between subsequent laser pulses. Spectral resolution of the detection setup was set to 1 nm, while temporal resolution was varied. For the study of the sub-nanosecond part of the luminescence decay temporal resolution of 18 ns was used, while 9 μs of temporal resolution was used in other cases.

The initial part of the PL dynamics (on the ns time scale) is reported in the **Figure 18b**. The steep rise of the PL intensity upon the laser pulse arrival is followed by a fast decay which slows down quite rapidly. What becomes clear from **Figure 18b** is that that there are two photoluminescence dynamics contributing to PL emission. The first component is due to a very fast relaxation process, being present only in the first initial moments after the pulse arrival, while the second one is much slower (~μs) and can be identified as indirect band-gap recombination which full decay is reported in **Figure 18a**.

The initial fast contribution can be fitted very well with a Gaussian function giving the 18 ns of full width at half maximum (FWHM). Gaussian time decay is not physical and it

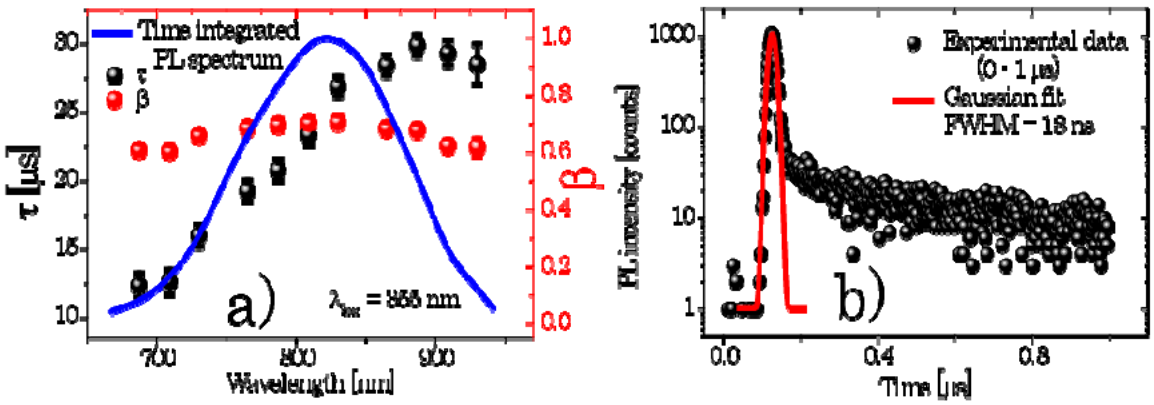

Figure 18 *– (**a**) Spectral dependence of the PL time decay of thin SRO films. Time decay photoluminescent traces were fitted with stretched exponential functions, the fitting parameters are reported. Time constant* ***τ*** *is given by the black spheres. A strong wavelength dependence of the time constant could be observed. On the contrary, stretching parameter* ***β*** *(red spheres) shows only a weak dependence on the emission wavelength. Time integrated PL spectrum under the same pulsed UV excitation (355 nm, 6 ns pulses, 10 Hz repetition rate) is reported as well (blue solid line). Excitation photon flux was* ***Φ*** *= 4.9 x 10^{24} ph.*cm^{-2}*s^{-1}. Decay curves are obtained by integrating 20 nm wide spectral windows. (**b**) The semi-log plot of the first μs of the PL time decay of thin SRO films (black spheres). The initial PL contribution can be fitted well with a Gaussian function (solid red line) giving the value of FWHM equal to 18 ns. Time trace was obtained by the integration of a 10 nm wide spectral window centered at 640 nm. Pulsed UV pump excitation (355 nm, 6 ns pulses, 10 Hz repetition rate) was used with the excitation photon flux of* ***Φ*** *= 4.9 x 10^{24} ph.*cm^{-2}*s^{-1}.*

means that a photoluminescence emission responsible for the fast initial contribution is decaying faster than the time resolution used (~18 ns) and, very probably, on timescale even shorter than the laser pulse duration (~6 ns).

It is obvious that additional information on the time decay of the fast contribution cannot be obtained in the present configuration, as the ultimate time resolution is set by the laser pulse duration (~6 ns) which is a value very close to the overall time resolution value used (~18 ns). Under these conditions, only an upper limit of 18 ns, for the time decay of the fast component could be set.

The fast PL band decay on the nanosecond scale is very often associated with defect emission from the silicon-dioxide matrix or oxidized silicon nanocrystals surface. It is not associated with zero-phonon emission [54,107,200]. In the case of defect emission, the decay times of the order of tens of ns have been reported [54,107,200]. In that case, a fast rise of photoluminescence should be followed by a long decaying tail on the ns scale which is not observed (see **Figure 18b**), as the fast contribution consists only of the fast Gaussian-like shape. However, as seen in **Figure 18b**, a strong contribution of the slow band may hinder a fast decaying tail on ns scale.

In order to elucidate more on the origin of the fast contribution, the spectral dependence of the different contributions is considered. In **Figure 19a** PL spectra of thin SRO films under different excitation and at different time scales are reported. It can be seen that

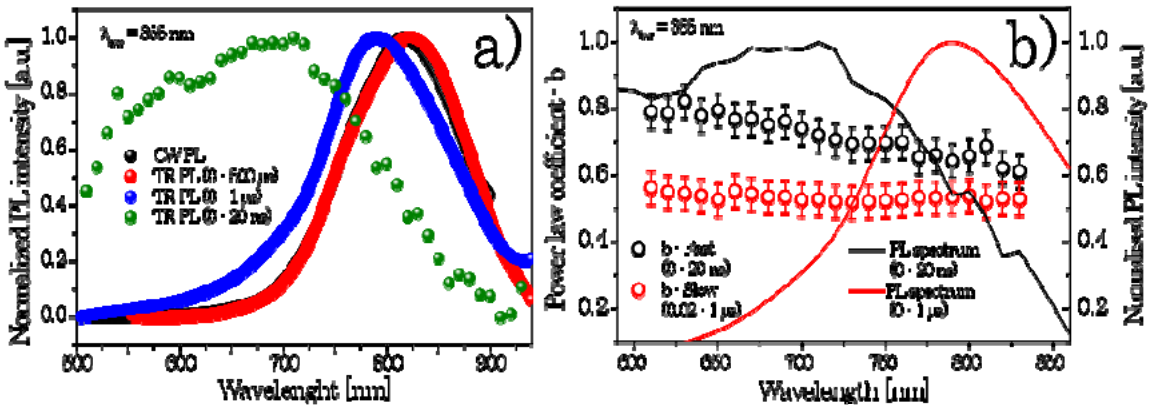

Figure 19 *– (**a**) PL spectra of SRO thin films under different excitations. PL spectrum under CW UV excitation (355 nm, excitation photon flux* Φ *= 6.8 x* 10^{15} *ph.*cm*$^{-2}$**s*$^{-1}$*), is given by empty black circles, while all other spectra are obtained under pulsed UV excitation (355 nm, 6 ns pulses, 10 Hz repetition rate and excitation photon flux* Φ *= 4.9 x* 10^{24} *ph.*cm*$^{-2}$**s*$^{-1}$*). Time integrated PL spectrum is represented with empty red circles, PL spectrum of the first µs of the time decay with empty blue circles and PL spectrum of the fast contribution (first 20 ns of the time decay) with green spheres. (**b**) Spectral dependence of power law coefficients of the fast PL band (empty black circles) and the first µs of the slow PL band without fast contribution (empty red circles) in the spectral region of mutual overlap of the two PL bands. Spectrum of the fast PL band is indicated with black spheres and the spectrum of first µs of slow PL (including the fast contribution) is represented by red solid line. Pulsed UV excitation was used (355 nm, 6 ns pulse duration, 10 Hz of repetition rate). Excitation photon flux was varied between values of* Φ *= 6 x* 10^{22} *ph.*cm*$^{-2}$**s*$^{-1}$ *and* Φ *= 6.5 x* 10^{24} *ph.*cm*$^{-2}$**s*$^{-1}$*. Power law coefficients were acquired by fitting the experimental data with allometric function. Experimental data were obtained by integrating the 10 nm wide spectral windows.*

time integrated PL spectrum under pulsed excitation and spectrum obtained under CW PL are practically identical.

On the other hand, if the PL spectrum of the first µs (time window used in **Figure 18b**) after the laser pulse arrival is plotted, differences arise. The PL band in this case is slightly blue-shifted (790 nm) with respect to the position of the time integrated spectrum (820 nm). In addition, the PL band is clearly asymmetric, with long tail on the blue side and small shoulder like feature as well. These characteristics are more common to the rise of a new PL band which might be identified as the previously mentioned fast contribution in a **Figure 18b**.

To evidence it more clearly, the spectral dependence of only the fast PL contribution is reported in **Figure 19a**. The fast PL component features a very broad PL band with a completely different spectral distribution with respect to the slow component. The fast PL band peaks at approximately 650 nm. It is important to underline that the fast PL band decreases abruptly for wavelengths shorter than 550 nm at odds with what expected from emission coming from defects [54,107,200]. Although the small contribution from the defects on the blue side of the fast PL band in the present conditions cannot be completely disregarded, it becomes clear that the main PL contribution is of a different origin.

Interestingly, the position of the fast PL band coincides with the spectral region where usually optical gain is reported [50,177,184,229].

A fast contribution under pulsed excitation pumping in the red (> 600 nm) has been previously reported. It was attributed to stimulated emission [177,180] or to efficient initial carrier relaxation driven by an Auger process [54,55].

In order to distinguish between the two cases, the power dependence of the fast PL contribution on the excitation photon flux must be considered. It is instructive as well, to compare the power dependence of the fast PL band with that of the slow PL band. In **Figure 19b**, the spectral dependences of power law coefficients for fast and slow PL bands are both reported.

When comparing the power dependencies of two PL contributions, a certain care has to be taken. If only power dependence of the time integrated PL is considered (in conditions where PL saturation is not reached [117,215]), the values found correspond to those obtained under CW excitation. However, if the mechanism of inter-nanocrystal is present transport on the long time scale (trapping – de-trapping mechanisms [115], or dipole-dipole type of interaction [234]) the power dependence of the initial part of the slow decay should differ with respect to time integrated or CW case.

In the **Figure 19b** only the power dependence of the first μs of slow PL is reported. This should not be influenced by these effects.

Spectrally flat values of approximately $\mathbf{b} = 0.55 \pm 0.05$ for power law coefficients of the slow component were found. These values are very close to the 2/3 value expected from the Auger dominated PL process. Slightly lower values could be due to presence of fast inter-nanocrystal transport [155,157,159] or, most probably, to the onset of PL saturation [117,215]. Moreover, the values found are slightly higher than those found in the case of the CW excitation, indicating that in the samples under study, there might be as well traces of inter-nanocrystals transport on the longer time scale.

On the other hand, the values of the power law coefficient for the fast component exceed 2/3 in a broad spectral range, indicating that the PL decay of the fast band is not due to Auger recombination, nor is Auger limited [54]. It can be seen that a high value of $\mathbf{b} = 0.8$ is achieved on the peak of the fast PL and decreases down to the values of slow band on the red side where the fast contribution is disappearing. High values of the power law coefficient imply as well that the fast PL we observe is not due to defect emission. Defect emission is correlated with a presence of a large number of non-radiative centers causing the low power law coefficient.

Although the fast PL band does not show super-linear behavior in the range of excitation photon fluxes used, its origin could be tentatively ascribed to stimulated emission (originating on the surface or core states) [177,229].

However, if the fast PL band is coming from the core states of silicon nanocrystals, high values of the power law coefficient could be observed even in the absence of the stimulated emission [218,235]. Thus, in order to investigate further the nature of the fast PL band and to what degree stimulated emission contributes to it, additional experiments are needed.

2.3.2. High repetition rate excitation

To get more insight into the origin of the fast PL band, an extensive knowledge of its dynamics becomes essential. The main limiting factor in the previous experiments was the lack of time-resolution due to the laser pulse duration. The natural way to overcome this obstacle is to use, simply, shorter laser pulses.

As shown previously, the ultrafast dynamics seems to be of importance only in the initial moments after the pulsed excitation, when the multi-exciton regime is achieved. From what reported in **Figure 18b**, it seems unlikely that this regime would be maintained for times longer than 10ns. Thus, it would be desirable to study the system in the multi-exciton regime only. The PL coming from the single exciton recombination on this timescale acts only as a background. Due to thermal effects and, possible, sample degradation, it is very difficult to maintain the system in multi exciton regime in CW mode.

In addition, and more importantly, the ultrafast dynamics cannot be studied in the steady state regime. Therefore, the most opportune excitation would be the pulsed excitation with sub-ns pulse duration and with the repetition rate low enough to allow to the system to relax in a single exciton regime (~10 ns). To this purpose quasi-CW frequency doubled Ti:Saphire laser was used, emitting at 385 nm with 2 ps pulses and with 82 MHz of repetition rate (12 ns between subsequent pulses, see section IV of Appendix to Chapter 2 for more details on experimental conditions). PL signal was excited and collected under 45° by a streak camera (1 nm of spectral resolution and 22 ps of temporal one).

In the **Figure 20** the time–integrated spectrum under picosecond pulsed excitation is reported. The small modulations that are present in the PL spectrum are the interference fringes, as the PL was collected under 45° increasing slightly the optical path of light in the sample. However, this still cannot be considered as a waveguiding configuration, avoiding the experimental artifacts that it may lead to [236].

The PL band appears to be quite broad and asymmetric with a long tail reaching the blue side. If compared to the PL spectra obtained under low repetition rate excitation (see **Figure 20**), it can be seen that, apart from the interference fringes, the red side of the PL band corresponds very well to the time integrated spectrum (see also **Figure 16** and **Figure 19**), while the blue side coincides well with the spectrum obtained by integrating over the first 1 μs (see also **Figure 19**). Analogously to the low repetition case, the long tail on the blue side could be associated with a rise of a new PL band.

The fact that PL band is broader and corresponds to a sum of the spectra obtained on different timescale under low repetition rate excitation, is a consequence of the different type of excitation used (quasi-CW), allowing for simultaneous visualization of the different PL mechanisms which usually act on different timescales.

The fast PL component is more clearly visualized in the PL spectrum integrated over the first ns after the laser pulse arrival (see **Figure 20b**). In this case the slow PL component acts only as a background. The slow PL band is centered at approximately 810 nm while the fast PL band can be seen at around 600nm (see **Figure 20b**) The slow band is slightly broader than in case of CW pumping most probably due to mechanisms of inter-nanocrystal transport [159] and the fact that the system is not allowed to relax completely between the subsequent excitations.

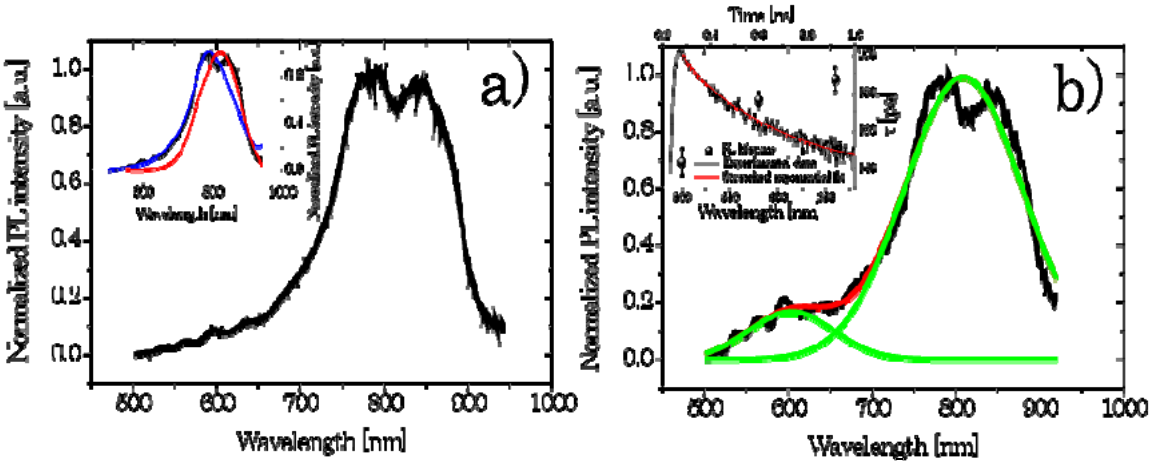

Figure 20 *– (**a**)Normalized time integrated PL spectrum of thin SRO films under quasi-CW excitation (385 nm, 2 ps pulse width, 82 MHz repetition rate) with an excitation photon flux* Φ *= 2.88 x* 10^{25} *ph.*cm*$^{-2}$**s*$^{-1}$*. PL signal was excited and collected under 45°. Small modulations present in the PL spectrum are due to interference fringes. (**Inset**): Normalized time integrated PL spectrum under quasi-CW excitation (black solid line) compared with the PL spectra obtained with low repetition rate excitation on different time scales: integrated over 500 μs (red solid line) and 1 μs (blue solid line). The excitation photon flux for quasi-CW excitation was* Φ *= 2.88 x* 10^{25} *ph.*cm*$^{-2}$**s*$^{-1}$ *while in case of low repetition rate excitation photon flux of* Φ *= 4.9 x* 10^{24} *ph.*cm*$^{-2}$**s*$^{-1}$ *was used. (**b**) Normalized PL spectrum of the thin SRO films under quasi CW-excitation (385 nm, 2 ps pulse width, 82 MHz repetition rate) with the excitation photon flux* Φ *= 2.88 x* 10^{25} *ph.*cm*$^{-2}$**s*$^{-1}$*,integrated over the 1 ns after the laser pulse arrival (black solid line). PL signal was excited and collected under 45°. Small modulations present in the PL spectrum are due to interference fringes. Double Gaussian fit of the two PL bands (green solid lines) together with their sum (red solid line) are presented as well. Gaussian fit yields width* w *= 101 ± 3 nm and peak wavelength* λ_{center} *= 604 ± 2 nm for the fast PL band and width* w *= 141 ± 1 nm and the central wavelength* λ_{center} *= 809 ± 1 nm for the slow band. (**Inset**): The time trace of the zero-phonon PL band (black solid line) showing the multi-exponential nature of the PL decay. Time trace was acquired at* λ *= 580 nm. The best fit with stretched exponential function is indicated with red solid line. Spectral dependence of the time decays of the fast PL band is reported as well (black spheres). Time decay traces were fitted with stretched exponential function and mean decay time extracted has been plotted. Stretching parameter* β *was found to have values of approximately 0.7 in all cases considered. Time traces were obtained by integration over 90 nm wide spectral windows. Temporal resolution of the detection system was 22 ps.*

The mutual position of the two bands corresponds extremely well to what expected from the zero-phonon (fast) and the phonon assisted (slow) PL band in a strong quantum confinement regime for the Si-nc of this size, confirming the core states as an origin of the fast PL band [200]. To confirm this, the time decay of the fast PL component was studied.

Time decay was found to be multi-exponential in nature, in agreement with a zero-phonon origin of PL (see **Figure 20b Inset**) [200,219]. In order to quantify it, the time traces were fitted with the stretched exponential function [109]. The values of approximately 160 ps were found (see **Figure 20b Inset**) consistent again with the zero-phonon origin of fast

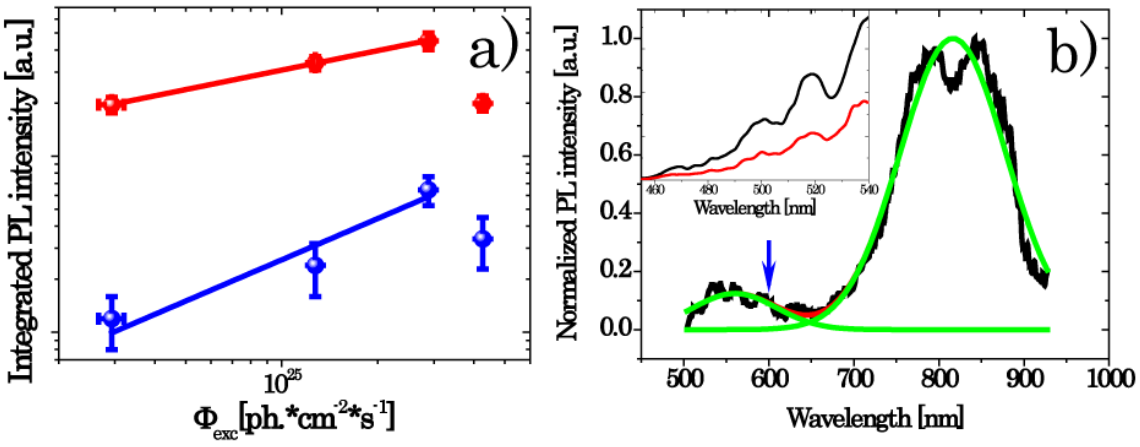

Figure 21 *– (**a**) Power dependence of the PL intensity of the zero-phonon PL band (blue spheres) and phonon-assisted PL band (red spheres) under quasi-CW excitation (385 nm, 2 ps pulse width, 82 MHz repetition rate) with the excitation photon flux varied in the range between* $\Phi = 2.93 \times 10^{24}$ *ph.*cm^{-2}*s^{-1} and* $\Phi = 4.27 \times 10^{25}$ *ph.*cm^{-2}*s^{-1}. Solid lines of the corresponding colors are the best fit with allometric function of the experimental data obtained (in range of excitation photon fluxes where sample degradation does not occur). (**b**) Normalized PL spectrum of the thin SRO film under quasi-CW excitation (black solid line) at the value of excitation photon flux* $\Phi = 4.27 \times 10^{25}$ *ph.*cm^{-2}*s^{-1} (represented by fourth, most right point in the panel (**a**)) where the degradation of the sample PL intensity does occurs. Double Gaussian fit of the two PL bands (green solid lines) together with their sum (red solid line) is presented as well. Gaussian fit yield width* $w = 98 \pm 4$ *nm and peak wavelength* $\lambda_{center} = 560 \pm 2$ *nm for the zero-phonon PL band and width* $w = 125 \pm 1$ *nm and the central wavelength* $\lambda_{center} = 817 \pm 1$ *nm for the phonon-assisted PL band. After the illumination (at this value of excitation photon flux), zero-phonon PL band blue-shifts by approximately 40 nm from the initial position at lower photon fluxes (indicated by a blue arrow). (**Inset**): The blue side of the PL spectrum of fast PL band under quasi-CW excitation and extremely high excitation photon flux* $\Phi = 7.2 \times 10^{25}$ *ph.*cm^{-2}*s^{-1}. The spectrum of fresh previously non-illuminated thin film (black solid line) is reported together with the spectrum of the same film after 5 minutes of illumination (red solid lines). PL intensity loss is clearly visible.*

PL [200,217,219]. The stretching parameters β showed values of around 0.7 in all cases, without any spectral dependence. Although, the stretching parameter didn't show any kind of spectral dependence, weak wavelength dependence in the lifetime was found in agreement with what previously reported for the zero-phonon photoluminescence [219]. Thus the fast PL component could be identified as a zero-phonon emission that is originating from the core states of silicon nanocrystals.

This is the first time that the zero-phonon emission has been observed in samples made in CMOS compatible approach (PECVD). Moreover, for the first time this type of emission was identified in hydrogen passivated silicon nanocrystals. Thanks to the specific type of excitation used, this is as well the first time that the zero-phonon emission can be observed in the time-integrated PL spectrum (see **Figure 20**).

In order to investigate to what degree stimulated emission contributes to the zero-phonon emission, the power dependence of PL intensity on excitation photon flux was

studied, in a restricted range of excitation photon fluxes (see **Figure 21a**). The choice of the lower values of the excitation photon flux was given by the necessity of having a value of excitation photon flux high enough to bring the system in the multi-exciton regime and distinguish the fast PL band from the slow background. On the other hand, the maximum value of the excitation photon flux was limited by PL intensity loss and sample degradation. The values of excitation photon flux are sparse, in order to minimize influence of possible short term power fluctuation of the excitation source.

For the power dependence of the phonon-assisted PL band a value of power law coefficient **b** = 0.37 ± 0.07 was found in close agreement with measurements under CW excitation (see **Figure 17**). The zero-phonon PL band showed a value of power law coefficient **b** = 0.8 ± 0.2 the same value found with low repetition rate measurements (see **Figure 19b**). This value, although larger than 2/3 [54], is still sub-linear, meaning that stimulated emission is not the dominant contribution in the zero-phonon emission. This is further supported by the lifetime measurements.

Time decay of the zero-phonon emission does not show any kind of variation with the excitation photon flux which would be expected in the case of stimulated emission presence. Thus, it can be concluded that or the optical gain coefficient has a very low value, not detectable in present case, or the stimulated emission is effective only on timescale shorter than the detection system temporal resolution (< 22 ps).

Interestingly, it was found that at an approximate photon flux of $\Phi = 4.27 \times 10^{25}$ ph.*cm^{-2}*s^{-1} a sudden degradation of the sample occurs, with a loss of intensity of both PL bands, effect being slightly more pronounced on the phonon-assisted PL band (see **Figure 21a**). This makes the zero-phonon PL band more pronounced in the overall spectrum after PL intensity loss (see **Figure 21b**).

Loss of the PL intensity is most probably related to the activation of non-radiative centers under the high photon flux excitation conditions. As the fast PL band blue-shifts for a 40 nm after the PL intensity loss (**Figure 21b**), there is a possibility that photoluminescent oxide defects are being created as well. If the oxide defects are being created and activated, together with a loss of PL intensity of the zero-phonon picoseconds band situated at 600 nm, a new band on ns scale should rise at the wavelengths lower than 500 nm [54,107,200] .

In order to explore further this scenario, the blue side of zero-phonon PL was monitored while exposing the sample to a very high photon flux of $\Phi = 7.2 \times 10^{25}$ ph.*cm^{-2}*s^{-1} in order to accelerate the degradation process (see **Figure 21**). It can be observed that only intensity of the zero-phonon emission lowers without a rise of a new PL band on ns scale.

That implies that only non-radiative centers similar to Pb centers (silicon dangling bonds) are activated [85,237,238]. On the other hand, the lifetime of the zero-phonon PL band does not change, neither the stretching parameter **β,** nor the spectral dependence of the lifetimes. Therefore, activation of the non-radiative centers removes effectively the silicon nanocrystal affected from the emission process, as the PL lifetime remains unchanged.

As a possible mechanism behind the PL loss intensity, dissociation of the hydrogen bond is proposed [85]. During the phase separation process and silicon nanocrystal growth, a large strain builds up on the interface between silicon nanocrystal and surrounding matrix leading to the creation of an amorphous shell [222]. Under these conditions, it may occur that not all bonds of interface silicon atoms are saturated [85]. The unsaturated bonds of silicon atoms are called silicon dangling bonds and act as an extremely efficient quenchers of

PL [85]. The thin SRO films used in this study are passivated with hydrogen in order to reduce the number of silicon dangling bonds and enhance the photoluminescence [56,85].

Unfortunately, the hydrogen bond could be dissociated under UV illumination when the photon energy exceeds the bond energy [85]. Similar mechanism of surface hydrogen substitution was used in the preparation of colloidal samples described in the first chapter. This process will be obviously enhanced under the high photon flux excitation, as in present case. This however, does not explain the threshold like behavior of the degradation process nor sample PL stability under lower excitation photon flux.

Recently, it was demonstrated that hydrogen substitution with alkyl chains is much more effective when the silicon nanocrystals are in excited state [239,240]. Moreover, the dependence of the reaction efficiency on the silicon nanocrystal size has been observed, with smaller nanocrystals being more prone to hydrogen substitution [241].

Therefore, the possible scenario behind the PL intensity loss could be the following: when the multi-exciton regime is achieved, activation energy for hydrogen surface bond dissociation may be lowered, making it more susceptible to UV induced dissociation [240].

Once the excitation photon flux threshold is reached (strong multi-exciton regime) hydrogen bonds easily dissociate and silicon dangling bonds reactivate again. Silicon dangling bond presence leads to a strong perturbation of nanocrystal excited state and exciton localization on it, quenching the emission. In embedded samples (as used in this study), no further passivation is possible due to oxidation [237] or Si-C bond creation [239] and PL intensity loss is permanent.

Obviously, as the PL persist even after the degradation occurred, only a fraction of Si-nc is influenced, as well as only the fraction of nanocrystals is effectively hydrogen passivated. Thus, the PL intensity loss mechanism proposed is identical to excited state hydrosilylation, just dissociation occurs not because of carbon atom binding on the hydrogen bond when the nanocrystal is in excited state, but due to absorption of an additional UV photon, explaining the high photon flux needed and threshold like behavior.

If this is the case, Si-nc size dependence of the dissociation should be maintained as in the case of the hydrosilylation, with small Si-nc being more prone to reaction [241]. In the case of the zero-phonon emission influenced by QCE, emission from the smaller Si-nc is dominating the *red side* of the zero-phonon band. Any deactivation of the smaller Si-nc, would lead to PL intensity loss of zero-phonon band and its apparent *blue shift* as actually observed (see **Figure 21b**). Once activated, silicon dangling bonds would influence as well the phonon-assisted band, causing its intensity loss and *red shift* (as contribution of smaller Si-nc is decreased) (see **Figure 21**). Moreover, as the number of the smaller Si-nc contributing to PL emission is decreasing, size dispersion of emitting Si-nc should get narrower as well, leading to a narrowing of the both PL bands as observed (see **Figure 20b** and **Figure 21**).

Clearly, to confirm proposed mechanism of the PL intensity loss further experiments are needed, and previous discussion should be considered only as a tentative description of the phenomenon. The main goal of this work is the study of the zero-phonon emission and not the mechanisms behind its intensity loss, although the understanding of the physics behind would be most certainly beneficial in a view of material optimization. For the moment, the knowledge of the experimental conditions under which the sample degradation is avoided and zero-phonon emission is visible, is sufficient.

Regardless, of the exact mechanism of PL intensity loss origin, this imposes a limit on the study of the zero-phonon emission and stimulated emission in the bulk samples. It still remains unclear to what degree stimulated emission of the zero-phonon transition is present in the samples, as no lifetime shortening nor super-linear behavior was observed. Blue shift under intense excitation has been explained in the frame of surface state activation and not stimulated emission.

In order to get additional information on the possible presence of the stimulated emission in the samples under the study, more elaborated experimental techniques are needed.

2.4. Introduction to whispering-gallery-modes resonators

2.4.1. Gain measurements techniques

In comparison to the case of compound semiconductor quantum dots, where there is clear and unequivocal observations of stimulated emission (marked for example, by a sudden super-linear increase of PL intensity with pumping power in a narrow wavelength range), in the case of silicon nanocrystals, the signatures of stimulated emission have been extracted from fairly elaborate and complicated experiments [49], and the results have shown significant specimen-to-specimen variation [180,242].

In all of these reports [49,50,180,184,229], the optical gain has been measured using techniques that exploit the light amplification due to single passage of light in gain medium, examples being: pump & probe technique [243] and Variable Stripe Length (VSL) [244] in which case spontaneous emission acts as a probe signal. Unfortunately, these gain analyzing techniques are easily susceptible to experimental artifacts if the optical gain values are low, and special care is needed in the data interpretation [236,245].

Additionally, a special care is needed even when considering simple PL coming from the bulk samples, as it was demonstrated that under certain experimental conditions PL intensity may show super-linear increase with the pump power, even in the absence of stimulated emission [235,246].

The most certain way to demonstrate the stimulated emission is to make a laser. To that end, an optical cavity is needed. Even if the threshold conditions for laser action are not reached, optical cavities will allow detecting even small changes in the emission properties, providing with valuable insight on the processes influencing PL emission.

In this chapter, usual gain measurements techniques represented by pump-&probe or VSL have been replaced by a different experimental approach. In particular, an optical cavity was used for the study of the zero-phonon PL. The PL emission has been studied in the conditions where the enhancement of the stimulated emission is expected, and where positive feedback needed for the laser oscillations to occur, could be provided.

Note that the samples with nominally the same silicon excess and, consequently, equal Si-nc distribution (size, density) will be used in this work.

2.4.2. Whispering-gallery modes resonators

The simplest light confining system is an optical resonator or optical micro-cavity. Optical micro-cavities confine light to small volumes by its resonant recirculation. As the circulation path is finite, after a single pass light will interfere with itself and, if the interference is constructive, a resonant cavity mode will be formed. An ideal cavity would confine light indefinitely (that is, without loss) and would have well defined resonant modes [247].

Deviation from this ideal condition is described by the cavity quality factor (**Q** factor) which is proportional to the confinement time in units of the optical period or, as well, it can be thought as a number of passages that light makes inside of the optical resonator before being lost. If the resonator is made out of gain providing material, the increased number of passages will increase drastically the sensibility with respect to single-pass gain measurements techniques [247].

In this work, a particular class of optical resonators is used, constituted of spherical dielectric structures, where optical rays are totally internally reflected by the surface itself. The circular optical modes in such resonators, frequently dubbed as whispering-gallery modes (WGMs), can be understood as closed circular beams supported by total internal reflections from boundaries of the resonators [248]. The peculiar name of such structures derives from the analysis of echoes effects of acoustic waves in the dome of St. Paul cathedral (London) by Lord Rayleigh, at the beginning of last century [249].

When the reflecting boundary has high index contrast, and radius of curvature exceeds several wavelengths, the radiative losses, similar to bending losses of a waveguide, become very small, and the quality factor **Q** becomes limited only by the material attenuation and by the scattering caused by geometrical imperfections (for example, surface roughness) [248].

Another, important property of the WGM resonators is that the frequency spacing of adjacent resonant modes (free spectral range - FSR) as well as their position, is a function of a size, with increased spacing for the smaller resonators. Obviously, as the size of the micro-resonator decreases, confinement is lost and quality factor decreases as well [247,248].

Whispering gallery mode (WGM) resonators have raised a lot of interest mainly due to the easiness of fabrication, which relaxes the ultra-high resolution process needed to create for example photonic crystal cavities with similar properties [250,251]. Fabrication restrictions are particularly relaxed in the case of planar WGM resonators (micro-rings and micro-disks) which can be micro-fabricated onto wafer substrates using conventional integrated-circuit deposition and etching techniques, assuring circuit integration and cost-effective mass-manufacturing [252,253].

This is the reason why the planar WGM resonators have been widely used for characterization of Si-nc ensembles by probing their non-linear properties [231], loss-mechanisms [187], inter-nanocrystal transport [171], and emission linewidth [114] among others.

However, until now planar WGM resonators haven't been used for a study of the ultrafast PL dynamics in Si-nc ensemble. The second part of this chapter will concern with detailed characterization of active micro-disc resonators. Before passing to the time-resolved

measurements under high excitation photon flux conditions, the influence of the optical cavity on light emitting properties of Si-nc ensemble under CW excitation will be established.

Finally, the properties of zero-phonon emission from cavity embedded silicon nanocrystals will be addressed.

2.5. Active micro-disk production

The micro-disk resonators have been made by etching thin SRO films (more details on the exact procedure can be found in the section I of Appendix to Chapter 2). Produced micro-disk resonators consist of the SRO disk that lays on a silicon pedestal in order to separate it from the silicon substrate (see **Figure 22b**).

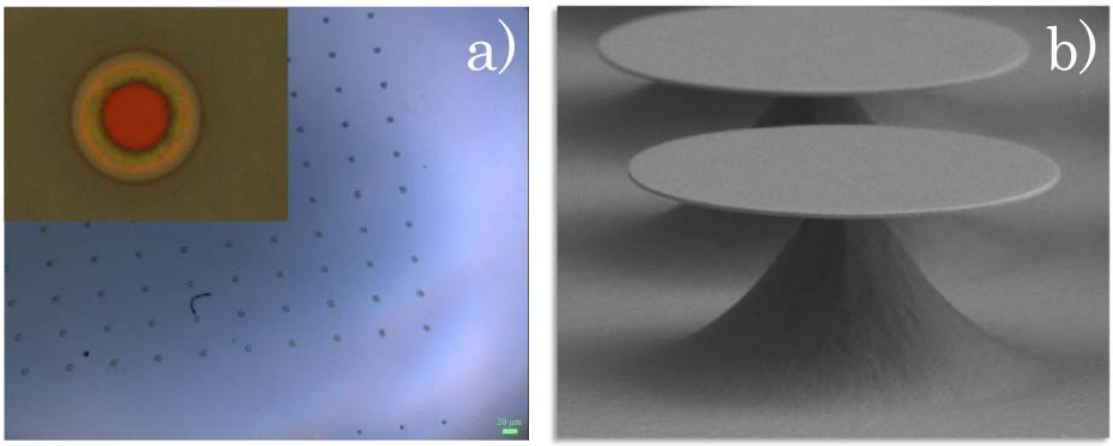

***Figure 22** – (**a**) Microscope image of the field of micro-disks with diameter of 7 μm under 10x magnification. The field of micro-disk resonators consists of a square matrix with 10 micro-disks in every column and row. The distance between neighboring discs is approximately 50 μm. (**Inset**): Top microscope image of a single micro-disk resonator under 100x magnification. The red inner circle is the silicon pedestal visible trough the transparent SRO layer. (**b**) SEM image of the micro-disk resonators.*

Freestanding geometry in which the micro-disk resonator is separated from silicon substrate and suspended in air is of crucial importance in order to achieve a good confinement in silicon-rich oxide material (refractive index of silicon rich oxide varies between values of 1.5 and 1.8 depending on the exact silicon excess and wavelength).

Of equal importance is to create a micrometric size separation between the resonator and the silicon substrate, otherwise the light will tend to leak towards the substrate jeopardizing the functionality of the optical resonator.

The micro-disk resonators are arranged in a square matrix (see **Figure 22a**) with 10 micro-disks in every column and row. The distance between neighboring micro-discs is approximately 50 μm.

When a large number of resonators are excited simultaneously through a large excitation spot over the micro-disk array, the observed WGM resonant spectrum is

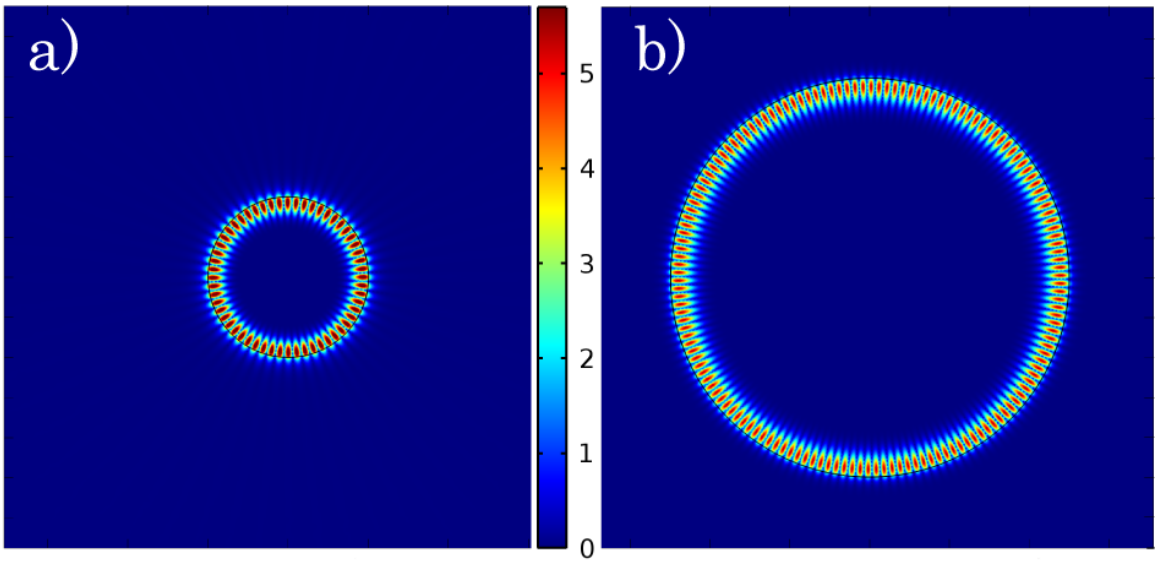

Figure 23 *– Distribution of electric field modulus for the 1st radial TE family in the micro-disk resonators of: (**a**) 4 μm diameter and (**b**) 10 μm diameter. Electric field distributions have been obtained by commercial FEM solver in 2D. For the micro-disks material real refractive index of* ***n*** *= 1.69 was used while imaginary part of refractive index was set to zero (transparent material). The air was used as a surrounding ambient with the real part of refractive index set to* ***n*** *= 1. The imaginary part of refractive index was again set to zero. Micro-disk surface was modeled as perfectly smooth (no scattering contribution was considered). Silicon pedestal was not accounted for.*

characterized with a low quality factors [254]. These are attributed to an inhomogeneous broadening of peaks due to the slight dispersion of micro-disk diameters within the excited area [230].

However, even when the excitation spot is well focused on a single micro-disk resonator, under high excitation conditions, the same inhomogeneous broadening may appear in a closely spaced micro-disk resonators. The reason is that under high excitation conditions, the nearby micro-disks are excited as well by scattered excitation light. Their PL signal will be detected trough the collection optics as the field of view of the collection optics is usually wider than excitation spot itself.

Closely packed samples consisting of a square matrix of 100 by 100 micro-disks (see **Figure 22b)** were studied as well. However, due to the presence of inhomogeneous broadening and the thermal interpretation of experimental data became increasingly difficult. This approach has been abandoned, and low-density samples have been employed instead.

Therefore, in this chapter only the results obtained on the low-density (in terms of micro-disks spacing) samples will be reported.

In **Figure 23** the electric field distributions for two micro-disk resonators of different sizes are reported. It can be observed that the electric field outside of the micro-disk is decreasing with increased size, diminishing the radiative losses and, hence, making the light detection more difficult in agreement with what recently experimentally observed [255]. This is also reflected in the higher Q values from the bigger resonators.

For this study micro-disks of 7 μm of diameter were chosen. Micro-disk resonators of this diameter show quality factors high enough (~10^3) to boost PL emission with still sufficient radiative losses for easy detection. This choice was done having in mind, the phonon-assisted part of PL emission (centered at 800 nm) which can be easily observed under the CW excitation. Thus, quality of fabrication process and the overall quality of the optical cavity can be easily established.

However, the chosen size of the micro-disc resonator might not be the most appropriate for the observation of the zero-phonon emission which in present case is situated around 600 nm (silicon nanocrystals with an average size of 3.5 nm and slow emission band situated around 800 nm [200], see also **Figure 20b**).

Radiative losses of the micro-disk resonator show strong dependence on both micro-disk size and emission wavelength [255]. For a given size, radiative losses are expected to decrease rapidly going towards shorter emission wavelengths. This may limit the observation of the WGM resonant spectrum shadowed by the uncoupled fraction of emitted light.

There are other disadvantages of the large resonators with a stronger confinement for the particular experimental scheme used, the far field detection. One of those is the free spectral range (FSR) which is a spectral separation between different resonant WGM modes.

The FSR should be large enough to distinguish different resonant modes even under conditions where only modest spectral resolution of the setup is at disposition. This is important in order to increase the overall sensibility of the detection instruments as the emission intensities are very low.

2.6. Continuous-wave photoluminescence measurements of active micro-disk resonators

2.6.1. Top excitation - top collection configuration

When active micro-disk resonators are being produced, silicon-rich oxide film passes through additional processing steps with respect to thin SRO films (see section I of Appendix to Chapter 2). It is possible, although unlikely, that some of these additional processing steps might influence the light-emitting properties of the used active material.

Therefore, a series of measurements is performed, in order to check, the good quality of the produced optical resonators. CW PL measurements have been done in the top excitation – top collection configuration (see **Figure 24**) exploiting the experimental setup described in section III of Appendix to Chapter 2).

Top excitation – top collection configuration is used because it mimics the emission conditions of un-patterned thin films. As pointed out previously, micro-disc resonators are planar optical cavities confining light only in two dimensions (horizontal plain). Thus, the light emitted in vertical direction is representative of the active materials and should be the same as in un-patterned film. By characterizing the PL properties of the vertically emitted light coming from the micro-disc resonator, it can be established if the additional processing steps have influenced the active material.

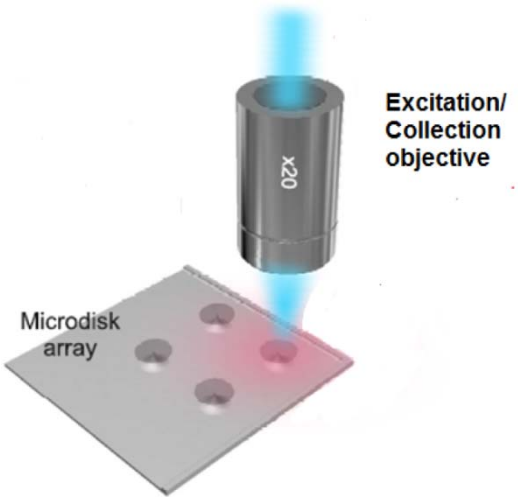

Figure 24 *– Scheme of the top excitation – top collection configuration for the CW μ-PL measurements on the active micro-disc resonators. The single active micro-disc is excited vertically by a laser beam and the PL signal is collected in backscattering. Afterwards, the PL signal is separated from the excitation beam with a dichroic mirror and directed towards the detection instruments.*

With the experimental setup described in section III of Appendix to Chapter 2, it was possible to characterize not only, the different single micro-disks across the sample, but as well the different regions of the same micro-disk (see **Figure 25**). In this way the uniformity of the active material could be checked.

In the **Figure 25** the characterization for a single micro-disk resonator in the top excitation-top collection configuration on different regions is reported. In particular, it was monitored the PL intensity dependence and PL band peak shift on the excitation photon flux (see **Figure 25** and **Figure 26**).

In **Figure 25** the PL intensity dependence on the excitation photon flux is reported. The experimental data are fitted accurately with the allometric function showing no signs of PL saturation [117,215]. The values of the power law coefficient obtained on the different parts of the micro-disk resonator are quite similar (Spot 1 – **b** = 0.45 ± 0.01, Spot 2 – **b** = 0.46 ± 0.01, Spot 3 – **b** = 0.43 ± 0.01, see **Figure 25**) and comparable with that obtained on thin SRO films before micro-disk definition (see **Figure 17**).

Moreover, the PL band peak position shifts in the approximately same manner in all three cases (see **Figure 26**). The values of these shifts are very similar in magnitude to thin SRO films under same conditions (see **Figure 17**). Therefore, it can be concluded that the additional steps needed to produce active micro-disk resonators, do not impact negatively on the PL properties of the active material. The only difference with respect to thin films is due to the presence of optical cavity.

It should be noted, that WGM's could be observed in this configuration too. Although they are weak due to a very high background of un-coupled light (see **Figure 26**). The resonant modes were less pronounced in the case of larger resonators in agreement with what discussed in section 2.5 (not shown). As the coupled light tends to escape the resonator in the horizontal plain [232], the only way to observe the resonant modes in vertical plain is due to the scattering from the surface roughness on the edge of the optical resonator.

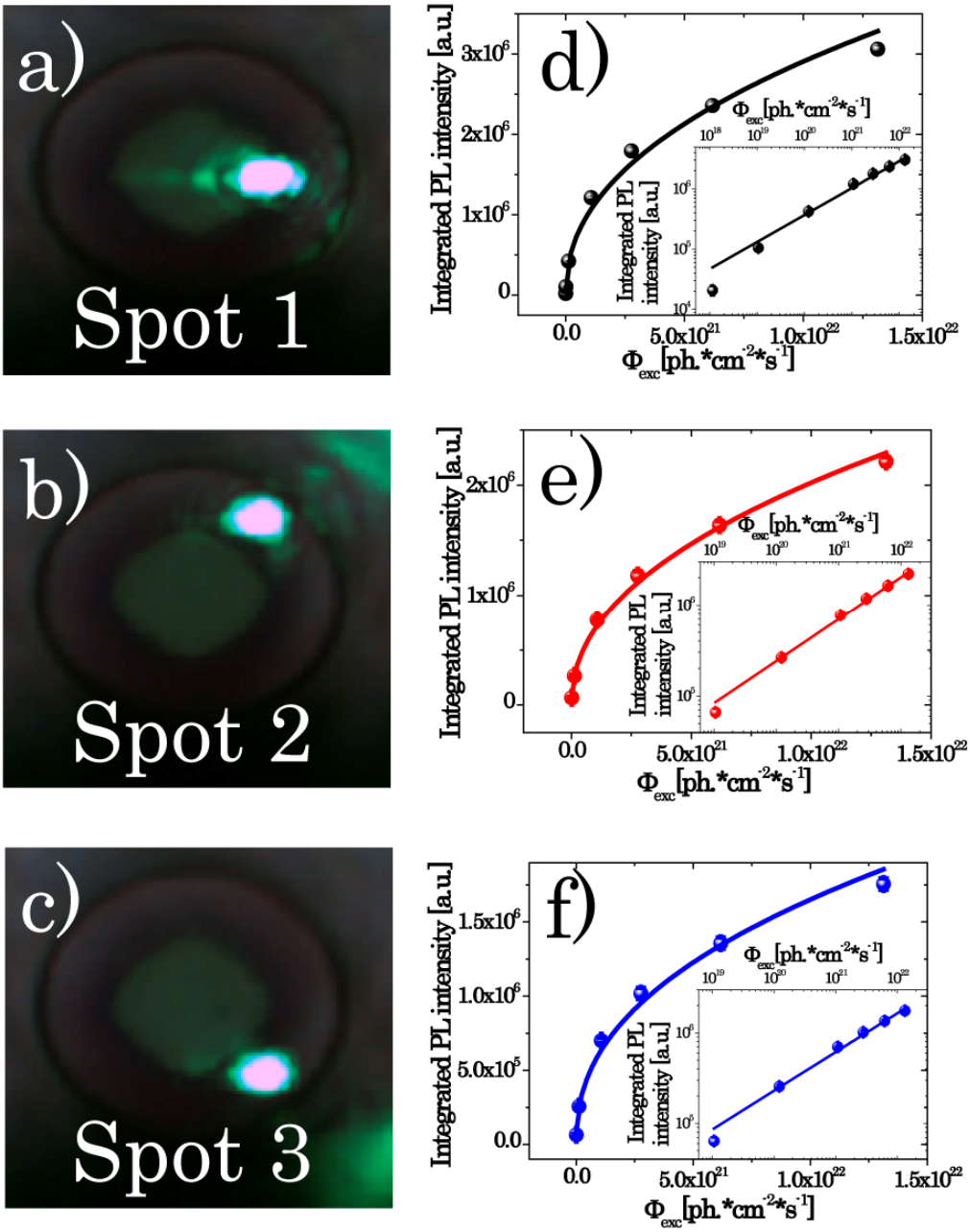

Figure 25 *– (**a-c**) Microscope images of the laser excitation spot at different regions of the same micro-disk resonator. (**d-f**) PL intensity dependence on the excitation photon flux (spheres of the corresponding color). Panel (**d**) corresponds to Spot 1, panel (**e**) to Spot 2 and panel (**f**) to Spot 3. Solid lines of corresponding color are the best fits with allometric function giving power law coefficients* $b = 0.45 \pm 0.01$ *(Spot 1),* $b = 0.46 \pm 0.01$ *(Spot 2) and* $b = 0.43 \pm 0.01$ *(Spot 3). (**Insets**): Log-log plots of panel (**d-f**). Excitation wavelength used was* $\lambda_{exc} = 532$ *nm and excitation photon flux was varied from value of* $\Phi = 1.14 \times 10^{18}$ *ph.*cm^{-2}*s^{-1} to* $\Phi = 1.3 \times 10^{22}$ *ph.*cm^{-2}*s^{-1}.*

Scattering contribution is a very strong function of the emission wavelength [122,123,127] (see as well **Figure 5**). Hence, a very strong spectral dependence of the values of the quality factors is expected (when measuring in a different experimental configuration described in the next section). As it will be shown in the next section, this is not the case meaning that scattering is not a dominant loss mechanism in the optical resonator.

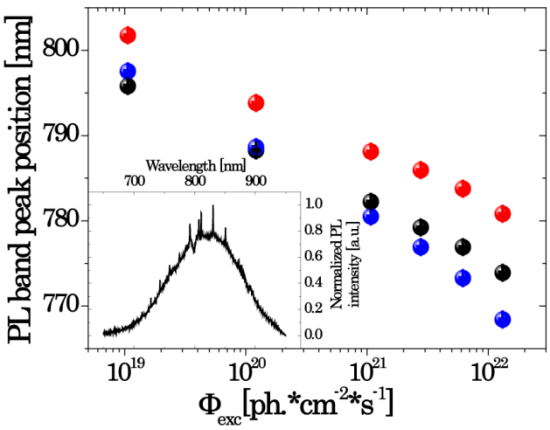

Figure 26 *- Semi-log plot of the PL band peak position shift with the excitation photon flux, for different position of the laser excitation spot on the same micro-disc resonator (black spheres for Spot 1 in* ***Figure 25*** *, red spheres for Spot 2 in* ***Figure 25****, blue spheres for Spot 3 in* ***Figure 25****). In all three cases, PL band is shifting towards the shorter wavelengths with increased excitation photon flux. The excitation photon flux was varied from* $\Phi = 1.14 \times 10^{18}$ *ph.*cm^{-2}*s^{-1} to* $\Phi = 1.3 \times 10^{22}$ *ph.*cm^{-2}*s^{-1} and the excitation wavelength was* $\lambda_{exc} = 532$ *nm. (**Inset**): PL spectrum of active micro-disc resonator of 7 µm obtained perpendicularly to the micro-disc plane. Small whispering-gallery modes features could be observed on the high background coming from the un-coupled light.*

Nevertheless, scattering contribution which can be tentatively defined as a fraction of PL intensity in the resonant mode with respect to the uncoupled background (Purcell effect has been disregarded in this crude estimate [114]) should be more pronounced on the blue side when collecting PL signal perpendicularly to the micro-disk surface. As it can be seen in **Figure 26** this is not the case neither. This means that there is an additional physical mechanism compensating for the increased scattering with decreased emission wavelength.

In the present case, this is most likely to be a decrease in the overlap between the resonant mode and the resonator edge surface with shorter emission wavelength. Or in other words, reduced radiative bending losses of the optical resonator for the emission wavelengths on the blue side of the PL band [255].

2.6.2. Top excitation - edge collection configuration

Once the micro-disk resonators are produced and the quality of the active material has been checked, the influence of the cavity on the optical properties of silicon nanocrystal ensemble has to be established. It is also desirable to determine the optimum experimental conditions for observation of whispering-gallery modes prior to the time-resolved measurements and zero-phonon emission observation.

When dealing with the time resolved measurements the PL signal acquired is usually significantly lower than in the case of continuous-wave measurements. Thus, firstly active micro-disks resonators have been characterized with CW PL measurements. To that end a different experimental configuration has been used.

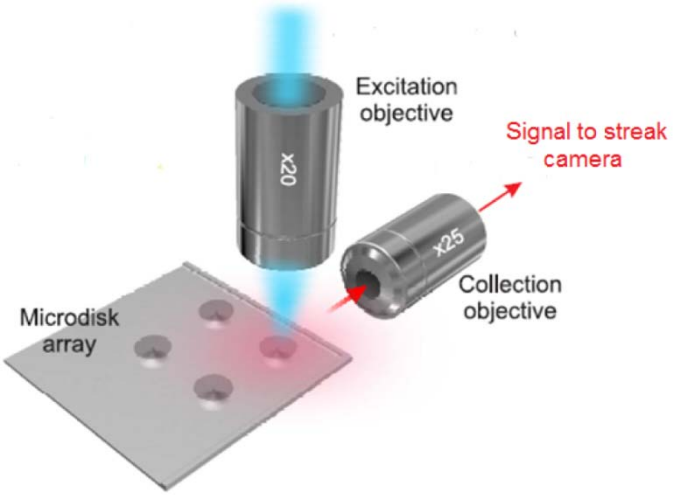

***Figure 27** - Scheme of the top excitation – edge collection configuration for the CW μ-PL measurements on the active micro-disc resonators. The same configuration was also used for TR PL μ-PL measurements. The single active micro-disc is excited vertically by a laser beam and the PL signal is collected in the horizontal plane through the collection objective and directed towards the detecting instrument.*

The micro-disk resonators are planar cavities, exhibiting the light confinement only in the horizontal plain. In order, to study the effect of the cavity, emitted light has to be collected in the same plane [232]. To that purpose another configuration for μ-PL measurements has to be used. Scheme of this new configuration is reported in the **Figure 27** (for more details on experimental setup used and experimental conditions see section V of Appendix to Chapter 2).

In this configuration, PL is excited perpendicularly as in previous case (see section 2.6.1 of Chapter 2), while the PL signal is collected in the horizontal plane with another objective (see **Figure 27**). Confined light will tend to escape the resonator in the horizontal plain and radiative loss will be collected with far field detection. Obviously, the overall sensitivity of detection will be a strong function of the radiative losses of the micro-disk resonator.

The degree of the light confinement and consequent optical losses will depend also on the polarization of the emitted light. This is well represented in **Figure 28** where the PL spectra with different polarization filtering are reported. It can be seen, that in all three cases of polarization filtering (Un-polarized, TE or TM polarization) the effect of the optical cavity is visible through the creation of narrow emission peaks in the PL spectrum.

The TM modes for these dimensions of the micro-disk resonator (7 μm diameter, 200 nm of thickness) are weakly supported. In fact, the PL spectra show small, broad modulations on the un-coupled background which correspond to one weakly coupled radial family (**Figure 28b**). Most of the light observed in TM polarization is uncoupled, and acts as an effective background hindering the clear observation of the cavity peaks (**Figure 28a**). On the other hand, in TE polarization the effect of the optical cavity is more clearly pronounced. The cavity peaks are well visible while the background level of uncoupled light is fairly low. Thus, for closer inspection of the cavity effects, the study in the TE polarization is more convenient as the cavity peaks are well pronounced and the level of un-coupled background light is lower for un-polarized and TM polarized detection.

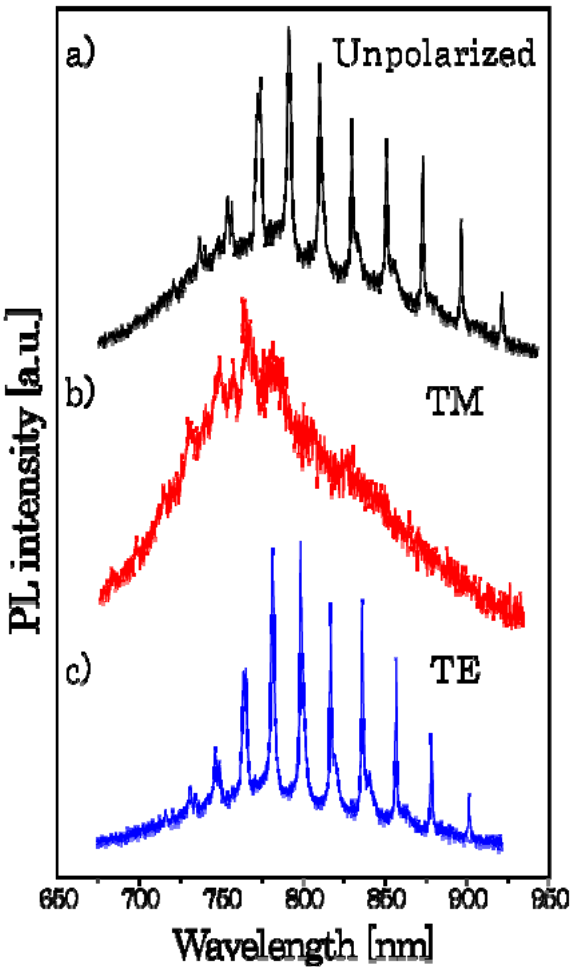

Figure 28 *– PL spectra of the micro-disk resonators of 7 μm of diameter (**a**) unpolarized (black solid line) (**b**) in TM polarization (red solid line) (**c**) and in TE polarization (blue solid line). Excitation wavelength was* λ_{exc} *= 532 nm with the excitation photon flux* $\Phi = 1.5 \times 10^{21}$ *ph.*cm^{-2}*s^{-1}.*

In the TE polarization, the different peaks are fairly separated allowing for their easy identification. In fact, by closer observation of **Figure 28c** contribution from the two different TE radial families could be observed. In **Figure 29** the distributions of electric field modulus for these two radial TE families are reported. It can be seen that the electric field distributions are quite different as well as the radiative losses, explaining for the differences in the mode intensity observed in PL spectrum.

By comparing the experimental data with the simulations, it is possible to identify the observed peaks in PL spectrum with the corresponding TE radial family. Moreover, it is possible to identify azimuthal mode number for the different modes of the same radial family as shown in **Figure 30**. It can be seen that the 1st TE radial family is more pronounced in the PL spectrum at least on the red side of the PL spectrum (λ > 750 nm, see **Figure 30**)) suffering higher radiative bending losses (**Figure 29**), with visible whispering-gallery modes having the azimuthal number between 28 and 38 (see **Figure 30**).

In the **Figure 31** the quality factor as experimentally measured for the first two TE radial families are reported. The quality factors determined experimentally in the far-field detection, as the one used in this study, are representative of the intrinsic quality factors of the optical cavity [255].

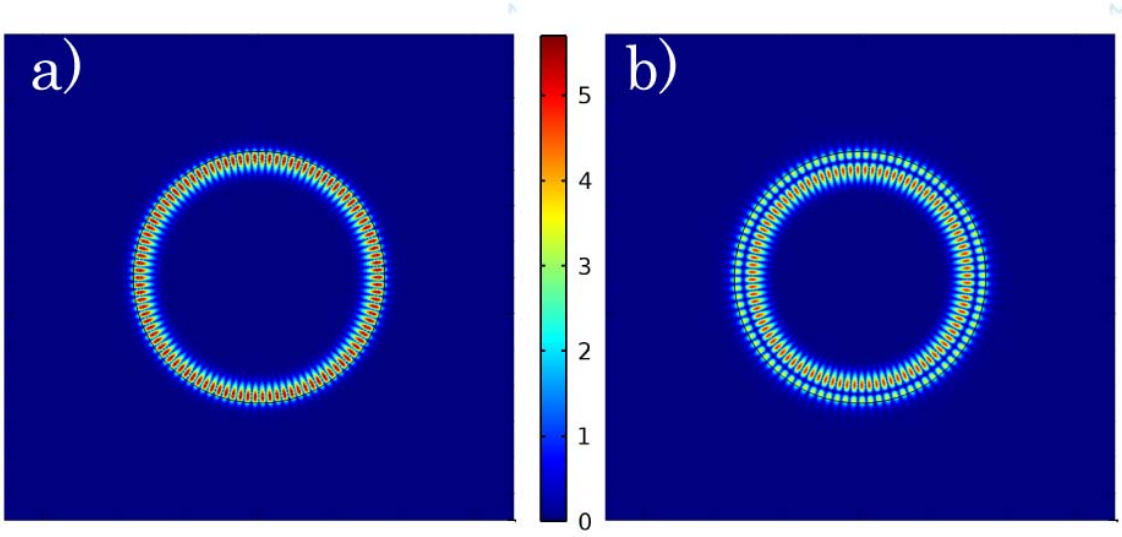

Figure 29 *– Distribution of the electric field modulus for the (**a**) 1st and the (**b**) 2nd TE radial family in the micro-disk resonators of 7 μm diameter. Electric field distributions have been obtained by commercial FEM solver in 2D. For the micro-disks material real refractive index of* n *= 1.69 was used while imaginary part of refractive index was set to zero (transparent material). The air was used as a surrounding ambient with the real part of refractive index set to* n *= 1. The imaginary part of refractive index was again set to zero. Micro-disk surface was modeled as perfectly smooth (no scattering contribution was considered). Silicon pedestal was not accounted for.*

While the intrinsic quality factor depends on the sum of the all loss contributions [232], resonant mode visibility in the far-field is mainly given by the radiative bending losses [255]. Additional factors that influence the visibility of the WGM's are material absorption and scattering [232,256]. As discussed in section 2.6.1, scattering seems not to be the dominant loss contribution and will not be considered further.

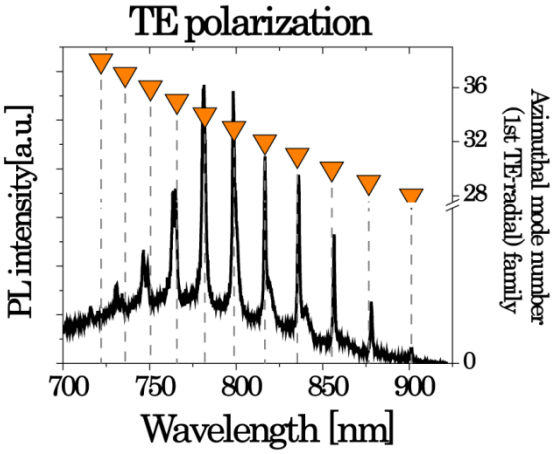

Figure 30 *– PL spectrum of the active micro-disk with a 7 μm of diameter in TE polarization. The azimuthal mode numbers of the 1st radial TE family are associated with the corresponding peaks in PL spectrum. Excitation wavelength was* λ_{exc} *= 532 nm with the excitation photon flux* Φ *= 1.5 x* 10^{21} *ph.*cm*$^{-2}$**s*$^{-1}$*.*

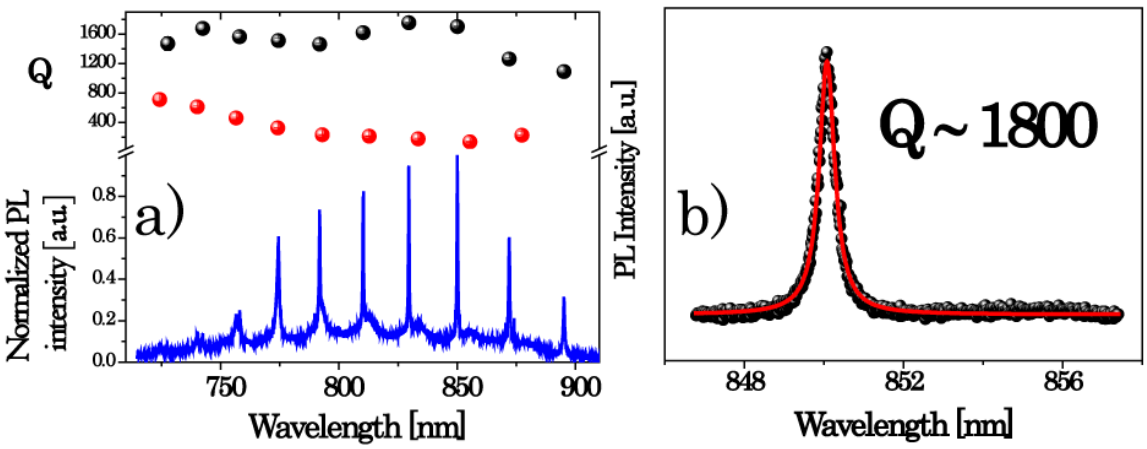

Figure 31 *– (**a**) PL spectrum of the micro-disk with 7 μm diameter obtained in TE polarization (blue solid line). Excitation wavelength was* λ_{exc} *= 532 nm with the excitation photon flux* Φ *= 1.5 x* 10^{21} *ph.*cm*$^{-2}$**s*$^{-1}$*. Quality factors for the two different TE radial families are shown (black spheres for the 1*st *radial family and red spheres for the 2*nd *radial family). (**b**) One of the whispering-gallery modes of the 1*st *TE radial family observed in PL (black spheres) and its fit by Lorentzian function (red solid line) yielding a quality factor of approximately* Q*=1800.*

As can be seen in the **Figure 31a**, the quality factor of the resonant modes of the second radial TE family are increasing continuously from the quality factors values of approximately Q = 300 to the values of Q = 800 towards the shorter wavelengths (λ < 750 nm). From the monotonous increase of the quality factor at shorter emission wavelengths, it can be concluded that the dominant optical losses for the second TE radial family in the spectral region considered (700 – 900 nm) are radiative loss.

Together with the increase of the quality factors, there is as well clear loss of visibility for the whispering gallery modes belonging to the 2nd radial TE family. If the material absorption is responsible for the loss of visibility of WGM's, resonance would get broader and the quality factors would decrease along with resonant modes visibility. As this is not the case, it could be concluded that the lower visibility is a consequence of the lower radiative losses. When the radiative losses become small, it becomes extremely difficult to distinguish the resonant modes from the un-coupled PL background [255].

On the other hand, the first TE radial family shows much higher values of the quality factor (Q ~ 10^3) and more complex spectral dependence (see **Figure 31a**). Lower values of the quality factors on the red side of the PL band could be attributed to the lower confinement and higher radiative losses [230], similar to the case of the second TE radial family. The small decline in the quality factor value, on the far blue side is most probably due to the onset of the material absorption [232].

The material losses due to self-absorption will increase significantly for emission wavelengths below the band-gap of silicon nanocrystals [232]. The band-gap value for silicon nanocrystals depends on their sizes [38]. An average value of the band-gap in the silicon rich oxide material can be matched roughly with its PL band peak position, corresponding to ~1.5 eV for the present samples.

The highest values of the quality factor for the 1st radial TE family were measured around the wavelength of λ = 850 nm (see **Figure 31**). A Q = 1800 was achieved (see **Figure**

31b). In order to investigate the origin of the dominant optical loss for this radial TE family, PL spectrum of the same resonant mode was acquired with decreased excitation photon flux. By lowering the excitation photon flux by 2 orders of magnitude, quality factor of same resonant mode increased to **Q** = 2000. This implies that the maximum quality factors of the 1st radial TE family are limited by free (confined) carrier absorption present at the high excitation photon flux used (see **Figure 31**) [187,230,231].

This is valid for the resonant peaks in the central region of the considered emission wavelengths. The situation changes for shorter/longer wavelengths as discussed previously. Free (confined) carrier absorption losses are not expected to vary drastically in the spectral range considered, explaining the weak spectral dependence of the quality factors for the1st radial TE family [230].

Even though, the quality factor measured are found to be larger than **Q** = 1400 in a broad wavelength range, whispering-gallery modes are almost invisible for wavelengths lower than 700 nm (see **Figure 31a**). This is attributed to the combinations of lower radiative and higher absorption losses for the emission wavelengths lower than 700 nm [255].

From the CW PL analysis presented, it can be deduced a high overall quality of the produced micro-disk optical cavities.

2.7. Time resolved photoluminescence measurements of active micro-disk resonators

2.7.1. Low repetition rate excitation

Time resolved photoluminescence measurements of the active micro-disk resonators were performed using the setup described in section V of the Appendix to Chapter 2. In this section the measurements using low repetition rate laser will be presented. For more details on the experimental conditions see section V of Appendix to Chapter 2.

TR PL measurements with the low repetition rate excitation are very challenging. The PL signal coming from the active micro-disk is extremely weak due to a very low volume of the excited active material (~1 μm^3), while the low repetition rate translates in unreasonably long integration times needed for the PL signal observation. This is a reason why the spectral resolution of the setup was sacrificed, in order to increase overall detection sensibility. PL signal was not even filtered in polarization, to reduce the absorption losses on the polarizer. All this results in higher background and less pronounced cavity peaks respect to the case of CW excitation. The results of these measurements are summarized in **Figure 32**.

The left top panel (**a**) reports the 2D wavelength - time PL map acquired under CW excitation with the same experimental conditions used for the subsequent time resolved measurements. Spectral region of the mutual overlap between the phonon-assisted and zero-phonon PL band was chosen (650 - 900 nm). This is also a spectral region where optical gain has been reported [50,177,180]. In the case of stimulated emission coming from the core states of silicon nanocrystals, the red-shift of the gain band respect to the spectral position of the zero-phonon one was observed [229].

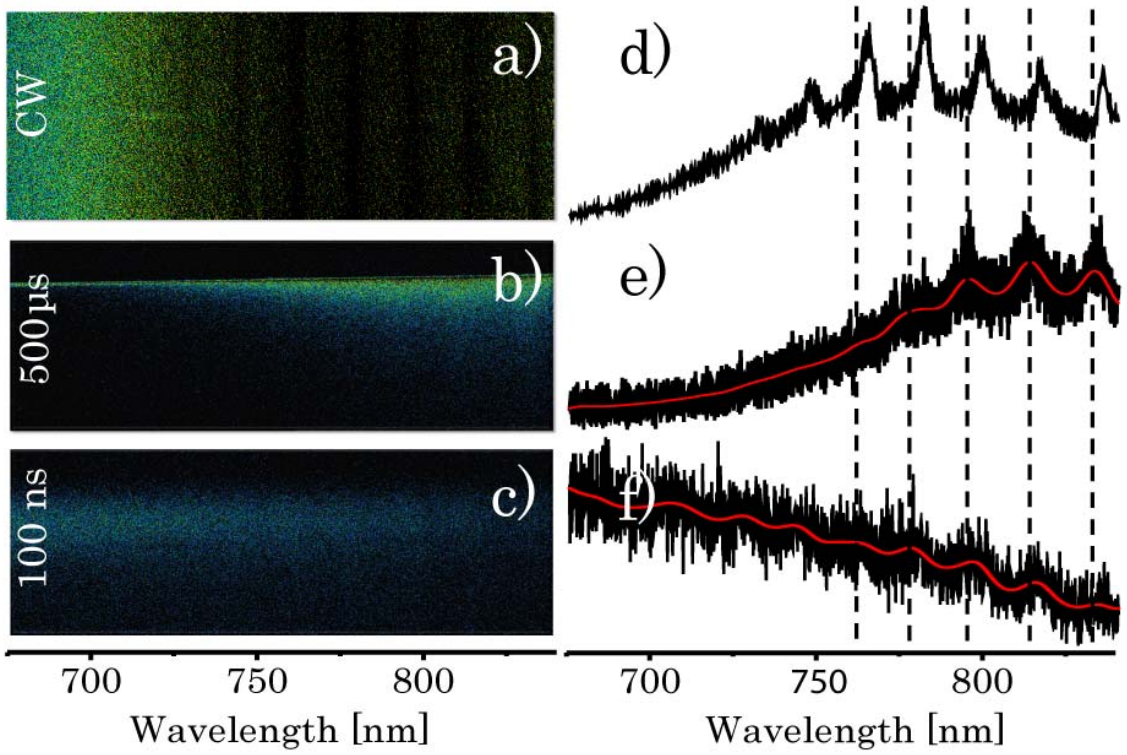

Figure 32 *– (**a-c**) 2D wavelength - time PL maps with (**d-f**) corresponding time-integrated profiles of the cavity embedded silicon nanocrystals on different time-scales and different excitation conditions. The spectral region of the mutual overlap between the phonon-assisted and zero-phonon PL band was chosen (650 - 900 nm). Top panels (**a, d**) have been obtained by CW excitation at* λ_{exc} *= 532nm with an excitation photon flux* Φ *= 1.5 x* 10^{21} *ph.*cm*$^{-2}$**s*$^{-1}$ *while the others have been done with the low repetition rate (10 HZ) pulsed UV excitation at 355 nm (6 ns long pulses) and excitation photon flux* Φ *= 1.78 x* 10^{26} *ph.*cm*$^{-2}$**s*$^{-1}$*. Red lines (**d-f**) are time-integrated profiles on which high frequency filter has been applied in order to remove white noise and put in evidence low frequency modulation due to whispering-gallery modes. Vertical black dashed lines indicate the position of the whispering-gallery modes under pulsed excitation.*

In the panel (**d**) is reported the PL spectrum obtained by integrating in time, the PL map reported in the panel (**a**). It can be noted that under the experimental conditions used, whispering gallery modes are less pronounced and the background from the un-coupled light is much higher. This is a consequence of the lower spectral resolution used and the fact that the PL signal was not filtered in polarization (see also **Figure 28**).

As well, due to a lower spectral resolution the resonant modes appear broader. Moreover, the modes coming from the two radial TE families cannot be distinguished and they emerge as single peaks causing additional broadening of the peaks.

From the panel (**d**), it can be observed that the whispering-gallery modes on the blue side of the PL band are disappearing due to combined effect of smaller radiative losses and increased material losses [232,255], as discussed in section 2.6.2. In addition, resonant modes under CW excitation are red shifted with respect to their position under pulsed excitation due to thermal effects [187,231].

In the middle panel (**b**) of **Figure 32** is presented the 2D wavelength - time PL map acquired under pulsed excitation. In panel (**e**) is reported its time-integrated profile. The time-window used for these TR PL measurements spans 500 μs, with 100 μs prior to laser pulse arrival and 400 μs afterwards. The PL in pulsed conditions resembles closely the one obtained under CW excitation, a part from the thermal shift induced by CW excitation.

It should be noted that an extremely high excitation photon fluxes have been used (see **Figure 32**) in order to detect PL signal, well beyond the damage threshold established in section 2.3.2 of Chapter 2. This was possible as the degradation process was significantly slower due to the low repetition rate of the excitation used. The data presented here are obtained when no visible degradation of micro-disk's PL properties could be observed.

The bottom panel (**c**) represents the 2D wavelength - time PL map obtained under the same excitation conditions as in panel (**b**), only the detection time window was decreased down to 100 ns, with 20 ns prior to laser pulse arrival. In the panel (**f**) it is reported time-integrated profile of the 2D map of the panel (**c**). Already from the panel (**c**) becomes clear that zero-phonon band is completely dominating in the PL signal at this time-scale.

In fact, the PL band completely changes the slope (panel (**f**)). The zero-phonon band is more evident for low excitation rate since the sample relaxes completely between the subsequent laser pulses. That means that there is no slow band that can acts as PL background, allowing for the observation of the zero-phonon emission even when the PL signal is extremely low.

Unfortunately, the PL signal remains very low even under long integration time (~ 7 h) allowing only for qualitative considerations. Nevertheless, some basic conclusions can be drawn. After the filtering of the fast frequency noise in PL spectrum, slow modulations due to whispering-gallery modes can be seen. The modulations are indeed due to WGM's as it was established by their comparison with other two PL spectra (panel (**d,e**)).

Interestingly, the WGM's seem to be visible even in the spectral region where otherwise they cannot be seen. As discussed previously, WGM's are not clearly visible on the blue side (< 750 nm) due to the combination of the low radiative losses and increased absorption related material losses [255]. Thus, their presence, even though small, becomes intriguing.

There are two physical mechanisms that can influence the visibility of WGM's. The radiative losses can be changed for a fixed resonator size and emission wavelength, only if the refractive index of the material is changed. The only mechanism that can change the refractive index on the time-scale in question is free (confined) carrier [231].

However, free carrier absortpion would induce a blue shift of all resonant modes which is not observed [231]. Alternative explanation would be that the material losses of the material have changed. There two types of power dependent losses expected at high excitation photon fluxes. One is a free (confined) carrier absorption which is directly proportional to the excited state population [187] which has its maximum immediately after laser pulse arrival and thus can be safely discarded. The second is the absorption loss bleaching due to presence of the stimulated emission in agreement with our expectations.

From the data reported it seems that there is a partial bleaching of the optical losses that could be related to stimulated emission in the zero-phonon emission band. Nevertheless, it is very difficult to say anything more from the experimental data acquired due to a very

low PL signal. To confirm the presence of the stimulated emission and quantify the amount of optical loss bleaching, additional experiments are needed. Evidently, in order to get more reliable data, experimental conditions have to be changed.

2.7.2. High repetition rate excitation

As previously shown on the thin SRO films, the zero-phonon emission is easier to observe under the high repetition rate excitation, even though the PL background becomes higher as well. In these conditions, contribution from phonon-assisted PL band is impossible to avoid and high excitation photon flux has to be employed in order to enhance the visibility of the fast PL band. Moreover, the zero-phonon PL band is not observable until the multi-exciton regime is reached [200].

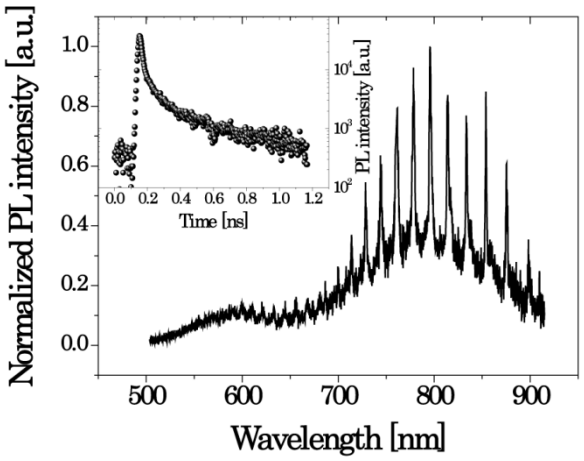

Figure 33 *– Normalized time-integrated PL spectrum of a single active micro-disk resonator of 7 μm diameter under quasi-CW excitation (2 ps pulse duration, 82 MHz repetition rate,* λ_{exc} *= 385 nm) with the excitation photon flux of approximately* Φ *= 1.9 x* 10^{25} *ph.*cm*$^{-2}$**s*$^{-1}$*. Both PL bands, slow and fast can be clearly observed, together with the modulation due to whispering-gallery modes. (**Inset**) The time trace of the zero-phonon PL band showing the multi-exponential nature of the PL decay. PL decay characteristics are the same as observed for the thin films. The time trace was obtained at 580 nm with a spectral window of 90 nm. Quasi-CW excitation was used with the excitation photon flux of* Φ *= 1.9 x* 10^{25} *ph.*cm*$^{-2}$**s*$^{-1}$*. The time decay didn't show any kind of variation with the excitation photon flux in the range of excitation photon fluxes considered (see **Figure 35**).*

In the **Figure 33**, time integrated PL spectrum of a single micro-disc resonator under quasi-CW excitation is reported. Both PL bands, phonon-assisted and zero-phonon, can be clearly seen. Under these excitation conditions, the zero-phonon PL band accounts for 10 % of the total emitted light. That is two orders of magnitude higher than the best result previously reported (~ 0.1 %) [200]. The possibility to observe the zero-phonon emission in the time-integrated spectrum with the contribution significant as this is attributed to a specific excitation conditions and good quality of samples used in this study. WGM's are very well pronounced across the whole phonon-assisted band and they can be observed as well on the red side of the zero-phonon band although with smaller visibility (see **Figure 33**).

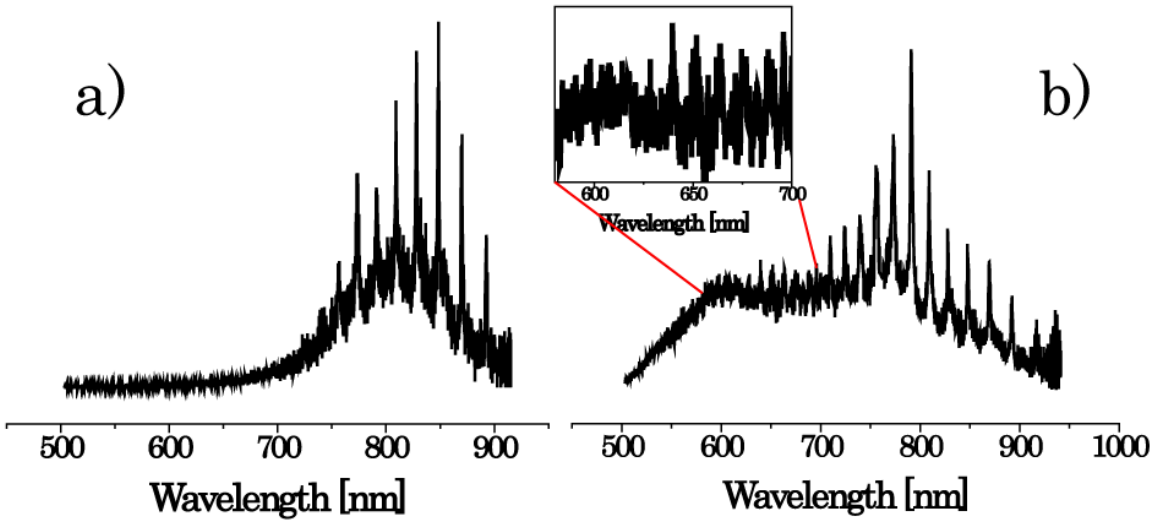

Figure 34 *– Normalized PL spectra for the two different excitation photon fluxes (**a**) **Φ** = 1.5 x 10^{24} ph.*cm^{-2}*s^{-1} and (**b**) **Φ** = 4.9 x 10^{25} ph.*cm^{-2}*$s^{-1}$of the single active micro-disk resonator with the 7 μm diameter. PL spectra are obtained by integrating in time over 1 ns after the laser pulse arrival. Quasi-CW excitation (2 ps pulse duration, 82 MHz repetition rate, λ_{exc} = 385 nm) was used. Excitation photon flux value in panel (**a**) is too low for the observation of a zero-phonon emission. (**Inset**) Part of the PL spectrum on the red side of the zero-phonon emission band. Modulations in PL spectrum due to whispering-gallery modes could be observed.*

The PL lifetime of the zero-phonon component was studied as well (see **Figure 33**). In **Figure 33** only the time trace is reported in order to evidence its multi-exponential nature. The time trace has been obtained in the time window of 1 ns by integrating over the 90 nm wide spectral window. Due to a low visibility of WGM's, and consequently their small contribution to zero-phonon emission, the acquired signal is mostly due to un-coupled light.

Thus it is not surprising that the time decay of the zero-phonon band collected from the edged of the micro-disk resonator showed the same characteristics (mean decay time, stretching parameter, spectral dependence) as in case of the thin SRO films (see section 2.3.2 of the Chapter 2). Moreover, analogously to thin SRO films, the time decay didn't show any kind of variation with the excitation photon flux in the range of excitation photon fluxes considered (see also **Figure 35**).

The zero-phonon PL band is better pronounced if the time window of the 1 ns after the laser pulse arrival is considered (see **Figure 34**). In the **Figure 34** two PL spectra collected from the edge of the micro-disk resonator are reported. They differ by the value of the excitation photon flux used to excite the PL signal. The PL spectrum in the panel (**b**) of the **Figure 34** was excited with excitation photon flux close to the damage threshold while the PL spectrum in panel (**a**) was obtained by exciting with the excitation photon flux approximately 30 times lower.

In this way, the threshold like behavior of the zero-phonon emission could be clearly seen (see **Figure 34**). This behavior is attributed to a different power law dependence of the zero-phonon band on the excitation photon flux respect to excitonic one and its presence in the multi-exciton regime only.

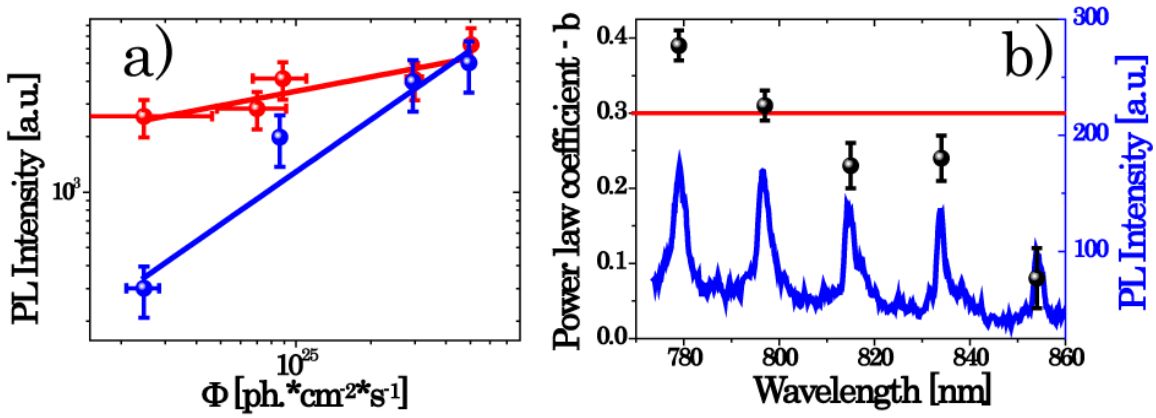

Figure 35 *– (**a**) Log-log plot of the PL intensity dependence on the excitation photon flux of the two PL bands, blue spheres for the zero-phonon emission and red spheres for the phonon-assisted band. Solid lines of the corresponding colors are the best fits by allometric function. For the fast PL band power law coefficient found was* ***b*** *= 0.94 ± 0.12 while for the slow* ***b*** *= 0.3 ± 0.1. For the power law fit of phonon-assisted band, only the contribution from the un-coupled light was considered. Quasi-CW excitation (2 ps pulse duration, 82 MHz repetition rate,* λ_{exc} *= 385 nm) was used. Excitation photon flux was varied from* $\Phi = 2.5 \times 10^{24}$ *ph.*cm^{-2}*s^{-1} to* $\Phi = 4.9 \times 10^{25}$ *ph.*cm^{-2}*s^{-1}. (**b**) Spectral dependence of the power law coefficient for different whispering-gallery modes. Power law coefficients were obtained by fitting the experimental data with allometric function. Only PL contribution integrated over 1 ns after the laser pulse arrival was considered. Same excitation conditions and flux variation were used, as in panel (**a**). Red solid line indicates the power law coefficient obtained for the un-coupled fraction of light in the same spectral region (see panel (**a**). PL spectrum under the highest excitation photon flux is reported as well (blue solid line).*

Interestingly, the fast PL band seems to be more pronounced than in the case of the thin film for the similar excitation photon flux (see **Figure 34**). In addition, a modulation due to whispering gallery modes could be seen across the fast PL band (see **Figure 34**) indicating the possibility of the bleaching of the absorption losses and presence of the stimulated emission as discussed previously in the case of low repetition excitation (see section 2.7.1 of Chapter 2).

In order to get more information on the possible presence of the stimulated emission in zero-phonon band collected from the edge of the active micro-disk resonator, the power dependence of the both PL bands was studied. Only the contribution of the un-coupled light was considered for the phonon-assisted band as the whispering-gallery modes were well pronounced. The results are reported in the **Figure 35**.

As in case of the thin films, different dependencies of the PL intensity on the excitation photon fluxes were found for different PL bands. For slow band a value of the power law coefficient **b** = 0.3 ± 0.1 was found while for the fast PL band power law coefficient was **b** = 0.94 ± 0.12. Both values are in agreement with what found on thin films or under low repetition or CW excitation.

Although, observable as the modulations on the zero-emission PL band, whispering-gallery modes were not visible enough to analyze them quantitatively. Their appearance seems to be compatible with bleaching of optical losses and presence of stimulated emission,

although this was reflected neither in the PL intensity dependence on the excitation photon fluxes nor PL lifetime. However, this is not surprising as both, PL power dependence and the PL lifetime, when integrated over a wide spectral region as in present case, should be dominated by un-coupled portion of the emitted light. Therefore, the values similar to un-patterned film should be found, as actually observed.

Thin films have been already characterized previously without a clear proof of stimulated emission presence in zero-phonon band. Increased sensibility to its presence was expected for whispering-gallery modes but their low visibility impedes any quantification. Thus, measurements are inconclusive again. As a main obstacle to the observation of the WGM's, low radiative losses at short wavelength of the chosen micro-disk resonator are proposed [255].

Visibility of the WGM's in the spectral region of interest (600 - 650 nm) seems to be limited by both material absorption losses and low radiative losses of micro-disk resonator. However, it the WGM's visibility was limited only by the material absorption losses, any bleaching would be clearly visible and stimulated emission presence could be confirmed and quantified.

Nevertheless, some additional conclusions can be drawn. As it can be observed in **Figure 34b**, the zero-phonon PL band is quite broad and its contribution, even small seems to be present on the longer wavelengths as well. Therefore, the power dependence of the clearly visible WGM's on the longer wavelengths was analyzed and reported in the **Figure 35b**. With the spectral resolution used to acquire PL spectra (~1 nm) peaks from the two different TE families appeared as one, and therefore, they were treated as single peaks in the PL power law dependency analysis.

At the high excitation condition used, it is expected that the very high values of free (carrier) absorption will dominate and significantly limit the power law dependence of the WGM's even at the lower excitation photon fluxes [187,231]. In fact, from the **Figure 35b,** it can be seen that power law dependence of the resonant modes on higher wavelengths is very low, much lower than the value found for the un-coupled fraction of light, as expected. However, a very strong spectral dependence of the power law coefficient for different resonant modes could be observed as well.

Previously (see **Figure 19b**), it has been demonstrated that the power law dependence of the phonon-assisted PL band is spectrally flat, thus the strong spectral dependence of the power law coefficient in **Figure 35** has to be a consequence of the presence of the cavity modes. It was demonstrated as well, that although the quality factors in this spectral region were limited by free (confined) carrier absorption, their spectral dependence was very weak as well. If the free (carrier) absorption was the dominant physical mechanism determining the power law dependence of different resonant peaks, rather flat spectral dependence should be expected again.

This is not the case and moreover, the values of power law coefficients of WGM's on the shorter emission wavelengths exceeds the value found for the uncoupled fraction of light, which would be impossible in the case of free (confined) carrier absorption limited process. Thus, the increase of the power law coefficients of whispering-gallery modes towards the shorter emission wavelengths could be attributed to an efficient coupling of the zero-phononPL component.

Although, zero-phonon contribution is expected to be low at emission wavelengths considered, its presence is clearly detected trough the whispering-gallery modes. This shows that the increased sensibility to a change in the PL emission properties in ultrafast dynamics is achieved by using the optical cavity justifying the experimental approach used. However, it seems that the optical resonator used is unsuitable for the study of emission dynamics at the wavelengths of interest.

2.8. Conclusions and future perspectives

In this chapter, it was presented a detailed spectroscopic study of the PL dynamics of the silicon rich oxide thin films produced by PECVD. It was demonstrated the existence of two PL bands of a different origin. The PL band characterized by slow emission dynamics on the timescale of μs, was identified as an excitonic band due to indirect band-gap recombination. The second PL band was characterized with sub-ns dynamics and it was concluded to be due to the zero-phonon recombination originating from the core-states of silicon nanocrystals.

This was the first time that this type of emission has been observed in the samples prepared by CMOS compatible approach. As well, it was the first time this type of emission was observed in the hydrogen passivated silicon nanocrystals.

The ultrafast dynamics of this PL band was thoroughly studied in thin SRO films but no clear evidence of the presence of stimulated emission was found. In order to study further the properties of a zero-phonon emission an optical μ-cavity was used. In particular, micro-disks resonators were produced and studied. Experimental conditions under which the zero-phonon band could be clearly observed were individuated, leading to two orders of magnitude higher visibility of this band, respect the best results ever reported. Moreover, a zero-phonon PL coupling to the resonant modes of an optical cavity was demonstrated.

Although, the coupling was demonstrated, the visibility of the whispering-gallery modes in the spectral region of interest where optical gain was expected was low leading to inconclusive data and qualitative consideration on the presence of stimulated emission in the samples employed. As a major drawback, obstructing the more quantitative analysis, a poor performance of the chosen optical resonator was proposed.

From what presented in this chapter, it becomes evident that this is a work in progress. The first steps have been made by demonstrating the zero-phonon emission and by individuating the experimental conditions under which zero-phonon emission could be clearly observed and studied. In addition, the validity of the approach where active optical cavity is used to probe the ultrafast dynamics has been confirmed.

However, there are as well a few improvements that can be made. First of all, it would be desirable to confirm undoubtedly, the core states of the silicon nanocrystals as the origin of the fast PL band. This could be done by performing the same study presented here on the silicon nanocrystals of different size. Moreover, it would be interesting to see if the zero-phonon emission could be additionally boosted by using smaller nanocrystals. By using smaller nanocrystals the zero-phonon emission could be as well additionally red shifted, bringing it closer to the spectral region where the better performance of used optical resonator is expected, and decreasing at the same time, the absorption losses of material.

Concerning the material properties, the mechanism of photo degradation process should be confirmed. By studying the un-passivated samples under high excitation photon fluxes, it can be determined if the hydrogen bond dissociation is the cause of PL intensity loss. If not, AFM measurements on the thin films should be done to exclude ablation effects. On the other hand, the excitation by the two photon absorption may decrease the degradation phenomena and is surely one route to explore.

As for the optical resonators, the design (resonator dimensions) needs to be improved. The detailed theoretical analysis and modeling are needed to better understand the limiting factors of the resonators used and improve the future design.

There is also an alternative to a far field detection used in this work. Instead of it, an integrated approach could be used where the vertical coupling with the integrated waveguide is used to probe emission of the active micro-disk resonator eliminating the problem of the radiative losses and un-coupled background and thus boosting significantly the sensitivity of detection instruments.

Appendix to Chapter 2

I. Samples production

Samples used in this study were produced in FBK clean-room facilities in a standard CMOS line[6]. Thin films were deposited by using a parallel-plate plasma enhanced chemical vapor deposition (PECVD) technique, on top of crystalline silicon wafers in a mixture of silane (SiH_4, 65 sccm) and nitrous oxide (N_2O, 973 sccm) gases and at chamber temperature of 300°C. As-deposited SiO_x films are 250-nm-thick. Successively, thin films were annealed for one hour in a nitrogen atmosphere at 1100°C resulting in the formation of Si-ncs (through a phase separation process of silicon-rich oxide into Si and SiO_2) embedded in a silica host. During this thermal treatment the SRO layer shrinks down to 200 nm due to the release of hydrogen and micro-voids, present in the as-deposited layer. Si-excess and deposition parameters were chosen in order to yield maximum PL intensity under continuous-wave excitation [257].

Subsequently, a photo-lithographical patterning of the micro-disk arrays is performed and followed by dry (anisotropic, SRO disk definition) and selective wet etching (isotropic, Si pedestal) steps. Finally, the photo-resist is removed in an O_2-plasma chamber. By the end of the described fabrication steps, monolithic Si-nc-based suspended micro-disk resonators are realized (see **Figure 22**). Detailed description of the sample fabrication procedure can found as well in Ref. [230].

II. Continuous-wave photoluminescence characterization of thin films

All PL measurements were performed at room temperature and corresponding spectra were corrected for the spectral response of the detection instruments used. CW PL measurements on thin films were performed in a standard PL configuration with the excitation incident at 30° respect to direction perpendicular on sample surface, while the photoluminescence was collected perpendicularly to the sample surface. As an excitation source two different laser sources were used. For the excitation in UV diode-pumped-solid-state (DPSS) laser emitting at 355 nm was used while for the excitation in visible, another DPSS laser emitting at 532 nm was needed. Spot diameter in both cases was around 500 μm. Detection consisted of visible PMT coupled to SOPRA double monocromator with a maximum spectral resolution of 0.2 nm (spectral resolution of 1 nm was used for experiments in this chapter). The laser power was determined using an Ophir power meter calibrated at 365 nm or 514 nm respectively.

III. Continuous-wave μ-PL measurements in top excitation-top collection configuration

For the CW μ-PL measurements on thin films or μ-discs resonators in top excitation-top collection configuration a LabRAM Aramis μ-Raman system was used (see **Figure 36**), consisting of Zeiss confocal microscope coupled with a 460mm-focal length spectrograph and

air-cooled visible CCD from Andor. As an excitation source DPSS laser emitting at 532 nm was used. Spectral resolution was set to 0.2 nm for the experiments in this chapter. Typical spot size was 2 μm with 100x objective (see **Figure 36**). Focal depth was set to 2 μm. Microscope images of the samples were acquired using the same setup.

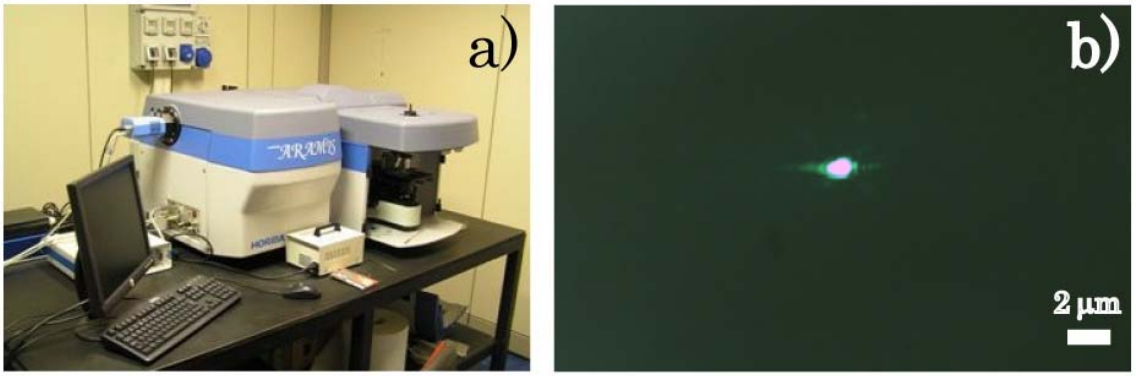

Figure 36 *– (**a**) LabRAM Aramis μ-Raman system. (**b**) DPSS laser (532 nm) spot under 100x objective.*

IV. Time resolved PL measurements on thin films

Time resolved photoluminescence (TR–PL) measurements on thin films were performed using as an excitation source the third harmonic (355 nm, 6 ns pulse width, 10 Hz repetition rate) of a Neodymium doped yttrium aluminium garnet (Nd:YAG) laser with a photon flux of approximately 10^{25} photons $s^{-1}cm^{-2}$ on the sample. Spot size was approximately 500 μm of diameter. As a detection system, a CCD Streak camera interfaced with a spectrometer was used. For the measurements in this chapter, 1 nm of spectral resolution was used while the temporal resolution was set by the particular time window used, being 18 ns or 9 μs for the measurements presented in this chapter.

Additional time resolved photoluminescence on thin films were performed using the μ-PL setup described in section V of Appendix to Chapter 2, in configuration where the excitation was incoming under 45° and photoluminescence light was as well collected on 45°. As excitation, a frequency doubled Ti:Saphire laser was used with 2 ps wide pulses and 82 MHz of repetition rate corresponding to a photon flux of approximately 10^{25} photons $s^{-1}cm^{-2}$ on the sample. As a detection system again streak camera was used with spectral resolution set to 1 nm and temporal to 22 ps. All PL measurements were performed at room temperature and corresponding spectra were corrected for the spectral response of the detection instruments used.

V. Continuous-wave and time resolved PL measurements of active micro-disk resonators in top excitation-edge collection configuration

CW and TR PL measurements on active micro-disk resonators in top excitation-edge collection configuration were done by using the μ-PL experimental setup reported in **Figure 37**. For the CW PL measurements a DPSS laser emitting at λ_{exc} = 532 nm was used as an

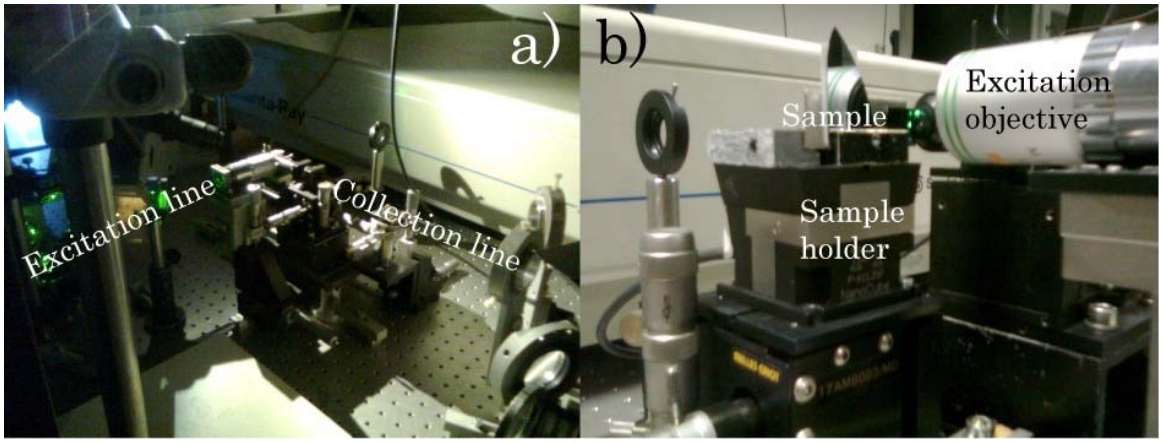

Figure 37 *- μ-PL experimental setup used for the CW and TR PL measurements on the active micro-disk resonators and thin films in top excitation - edge collection configuration. (**a**) Global view of μ-PL setup. (**b**) Close view of the sample holder. Excitation objective can be seen in front, while collection objective is visible in back.*

excitation source. For TR PL measurementsthe third harmonic (355 nm, 6 ns pulse width, 10 Hz repetition rate) of a Neodymium doped yttrium aluminium garnet (Nd:YAG) laser or frequency doubled (385 nm, 2 ps pulse width, 82 MHz of repetition rate) Ti:Saphire laser was used instead. Detection consisted always of the CCD Streak camera interfaced with a spectrometer with minimum values of the spectral resolution of 0.2 nm and temporal 22 ps.

Excitation light was focused trough the infinity corrected long-working distance 20x objective and collected from the edge of the micro-disk resonator with a short working distance 40x objective. If needed collected light could be polarized. Excitation spot size 10 μm of diameter in case of DPSS and Nd:YAG laser and 20 μm for the Ti:Saphire laser.

.

Chapter 3
Silicon nanocrystals as Er^{3+} sensitizers

3.1. Introduction to Er^{3+}

Erbium is a lanthanide trivalent material, a metal belonging to the class of the rare earths. The very name of this class of elements, rare earths, is quite misleading, as the rare earths and erbium along them, are fairly abundantly present in the composition of the Earth's crust. The electronic configuration of the neutral erbium atom could be summarized as :

$$Er = [Xe]\ 4f^{12}\ 6s^{2}$$

where [Xe] represents the xenon core [61]. Interestingly, erbium has its electronic 5s and 5p shells located more externally with respect to the 4f shell due to the physical phenomenon called lanthanide contraction [61,258]. Thanks to that particular electronic configuration, the 4f levels are quite efficiently electro-statically screened from the influence of the external environment.

In the isolated erbium atom, the 4f electronic levels are degenerate and the optical transitions between them are dipole-forbidden by the parity dipole selection rules [61]. When the erbium atoms are embedded in a solid host (crystalline or disordered), they assume their trivalent state by losing the two loosely bound 6s electron and one 4f electron. The trivalent state (3+) is the most stable ionization state in general for the lanthanide ions. They are commonly encountered in this form in most of the solid hosts [258].

In these conditions, orbital shielding of the 5s and 5 p electronic shells starts to be less effective. The electronic crystal field of the host, in which erbium ions are inserted, induces a small perturbation on the 4f levels, lifting the orbital angular momentum degeneracy characteristic of the isolated atom and causing the Stark splitting of the 4f levels. More importantly, the optical transitions among the levels within the 4f shell become possible due to the host perturbation. It is important to notice that the optical activity of the erbium ions is strongly related to that particular ionized state [61].

Nevertheless, thanks to the partial shielding of the outer electronic shells, absorption and emission lines of erbium ions, remain spectrally narrow and similar to the case of isolated atom, with their width determined by the amount of the Stark splitting induced in

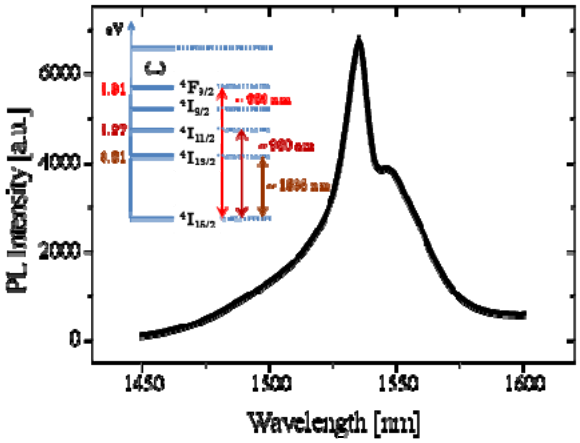

Figure 38 *– PL spectrum of the $^4I_{13/2} - {}^4I_{15/2}$ transition of Er^{3+} ions (transition from the first excited state to the ground state), under non-resonant (λ_{exc} = 476 nm) continuous optical excitation. Approximate width of $\Delta\lambda$ = 30 nm due to host induced Stark splitting can be observed. The excitation wavelength used is called non-resonant, as it does not coincide with any of the internal Er^{3+} optical transitions. In this case photoluminescence of erbium ions is excited trough the energy transfer from the silicon nanoclusters. Sample A from the* ***Table 1*** *was used. (****Inset****): Er^{3+} energy states scheme with Russel-Saunders notation and characteristic radiative transitions of importance to the work presented in this chapter.*

that particular host (see **Figure 38**) [46].

Erbium doped materials are of great interest in optical communications technology as the optical transition of the first excited to ground state ($^4I_{13/2} - {}^4I_{15/2}$) of Er^{3+} ions falls exactly in the third telecom window range, which corresponds to the low propagation loss region of the optical fibers (see **Figure 38**) [61]. This makes the Er^{3+} doped silica fibers perfect gain material for telecom applications which is reflected in the wide use of erbium doped fiber amplifiers (EDFA). Moreover, the Stark splitting is fairly strong for the case of silicate glasses (see **Figure 38**), increasing the material gain bandwidth and allowing for the introduction of the wavelength-division multiplexing (WDM) technology.

Although, the first rare earths doped fiber amplifiers were demonstrated in the 1960's, they remain to be a mainstream technology for the optical amplifications in the telecom applications [258].

However, contrary to its present popularity, erbium doped materials are a cumbersome gain providing material. Although, permitted by a solid host perturbation, optical transitions between electronic levels in the 4f shell remain quasi-forbidden in their nature, resulting in extremely long radiative lifetimes for the erbium ions in silicate glass [259,260]. On the first sight, long radiative lifetime of erbium ions seems beneficial from the point of view of optical amplification, allowing for low pump threshold for population inversion. On the other hand, it makes erbium ions very susceptible to any non-radiative process [261].

One example is ion-dynamic lattice interaction. Multi-phonon relaxation of the Er^{3+} ions is able to decrease significantly the amplifier efficiency, as well as quantum efficiency of erbium doped material [261]. Luckily, due to low-phonon energy of silica glasses [262], this type of non-radiative process is significantly reduced for the $^4I_{13/2} - {}^4I_{15/2}$ transition in silicate

glasses even at room temperature [259], although it remains the dominant relaxation path for the higher excited states [262].

Another common type of quenching center is the –OH group [259,261]. Excited state of Er^{3+} ions couples efficiently trough Förster type of interaction [59] with vibrational levels of –OH group leading to net quenching of photoluminescence [263]. Thus, special care has to be taken in order to reduce the presence of –OH group in erbium doped materials.

In fact, the erbium driven amplification is possible only when good quality matrix with low density of structural defects is achieved and where the occurrence of non-radiative centers is extremely small (low density of impurities) [264].

In addition, erbium ions solubility is very low in silicate glasses [261]. If present in higher concentrations, erbium ions form microscopic metallic clusters which do not contribute to photoluminescence but only to absorption [265,266]. Maximum concentration possible in pure silica while avoiding the erbium clustering has been estimated to be around 10^{-19} ions/cm^3 [261]. This requirement can be partially relaxed in the multi-component glasses where impurities, such as aluminum, allow for easier accommodation of a higher number of Er^{3+} ions in a rigid silica network [261]. However, even when clustering is avoided, an inter-ions interaction still remains possible, which can be avoided only if the concentrations are additionally lowered to values of 10^{-18} ions/cm^3 [261].

The most common type of inter-ion gain limiting interaction is the cooperative up-conversion [267]. In this process, one excited ion de-excites trough energy transfer to another excited ion promoting it to higher excited states. Relaxation from the higher excited states to the fist excited state occurs rapidly and mainly non-radiatively trough multi-phonon relaxation [262], leading to net depletion of excited state population [267]. As two excited ions are needed, this process becomes visible only at high excitation conditions, most commonly trough the shortening of the PL lifetime and increased threshold for the stimulated emission observation [261]. Thus, rather low concentrations of Er^{3+} ions are employed in EDFA.

EDFA's in general are quite bulky devices. The reason for that is the small absorption cross section of erbium ions ($\sigma_{abs} \sim 10^{-21}$ cm^{-2}). Hence, a very long interaction distance inside the fibers (tens of meters) is needed in order to produce optical gain [61]. Due to atomic like transitions, expensive laser excitation sources have to be used instead of flash-lamps and matched with narrow absorption bands, increasing overall price of EDFA. Moreover, only the first and the second excited state can be optically pumped due to very efficient excited state absorption (ESA) [267]. Finally, in optical amplifier erbium ions are embedded in the microns size insulator fiber core, inhibiting any type of electrical excitation [61].

One of the early attempts to overcome these shortcomings of EDFA's, was the doping of silicon with erbium ions [268]. Bulk semiconductors are the natural sensitizers for rare earth ions. When embedded in a semiconductor, the rare earth ions act as point defects that generate defect levels in the semiconductor band-gap. Optically or electrically generated carriers in the semiconductor can then become trapped at these defects to form a bound exciton. As the exciton has strong spatial overlap with the rare earth ion, it can recombine by transferring its energy to the rare earth ion [267].

Particularly, in the case of erbium doping of silicon, this would allow for a broadband optical or electrical excitation, increased excitation cross-section and thus, smaller sizes, CMOS compatibility and on-chip integration [268]. In fact, using this approach, optical amplification has been demonstrated, but unfortunately only at very low temperatures [269].

At room temperatures, quantum efficiency of this material is significantly lower [268]. Reason for that is an extremely efficient Auger back-transfer at room temperatures which seems unavoidable at present, and thus, limits the utility of this approach [270].

Another widely used strategy for the improvement of the erbium doped amplifier performance is co-doping with sensitizers [267]. In this scheme, absorbing specie (sensitizer) is excited easily by very efficient pump photon absorption or electrical excitation. Consequently, the excited sensitizer relaxes giving its energy in non-radiative manner [59,60] to an erbium ion, avoiding the limitations of erbium excitation process and improving overall material performance. To that end, another rare-earth is most commonly used, ytterbium [267]. Work in this chapter will be centered on yet another sensitizer, silicon nanocrystals.

3.2. Silicon nanoparticles as erbium sensitizer

The discovery of the sensitizing action of silicon nanocystals (Si-nc) on erbium ions (Er^{3+}) offered a new material platform where silicon based optical amplifiers and laser sources could be developed [58]. The absorption band edge of the silicon nanocrystals can be easily tailored trough the QCE, however, the density of the resulting electronic states is still large enough that the absorption process could be considered identical to that of the bulk silicon (apart from the band-gap change obviously) [205]. Upon absorption of an incident pump photon a confined exciton is formed. Once created excitons rapidly transfer their energy to the nearby rare-earth ions bringing them to excited state from which they relax radiatively to the ground state with the consequent luminescence at 1.5 μm (see **Figure 38**) [268].

Notice though, that there is a significant difference with respect to the bulk silicon case. In the case of bulk silicon, excitons are free to wonder in large volume (respect to their size) [185] until they get trapped on erbium ion to which they transfer its energy [267]. In the case of silicon nanoparticles, excitons are confined and thus localized. As the energy transfer is characterized by a short range interaction [59,60], it means that erbium ions have to be placed in close proximity to the silicon nanoparticles, which requires a high degree of material engineering [271].

This is usually achieved by optimizing the concentrations of the two species [58,272,273], and controlling their thermally driven diffusion and rearrangement [274–277]. However, the erbium solubility in silicon is even lower than in silica [278], often leading to erbium cluster formation on the silicon nanocrystal / the surrounding matrix boundary, affecting mostly the fraction of erbium ions that should be effectively sensitized by the energy transfer [279–282]. Therefore, lately more advanced fabrication techniques start to be considered [283–285].

The embedded silicon nanoparticles can be produced in two different states differing in a degree of crystallinity: amorphous and crystalline [272]. In the following, amorphous nanoparticles will be referred to as silicon nanoclusters while the crystalline nanoparticles will be called as before, silicon nanocrystals. Both types of silicon nanoparticles can be used for the erbium ions sensitization [58,276]. The main difference is the efficiency of the sensitization of these two species, as it will be shown in the following sections.

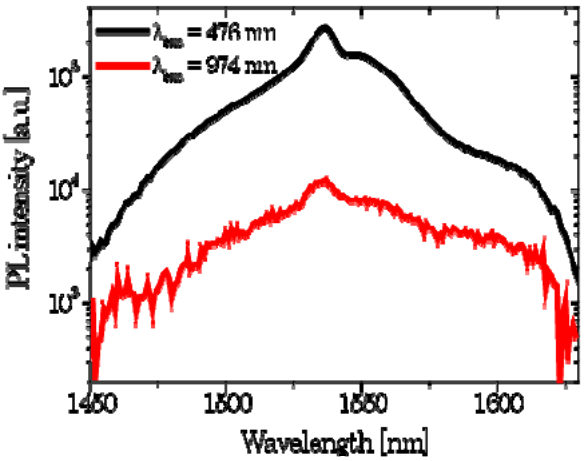

Figure 39 *– PL spectrum of the* $^4I_{13/2} - {}^4I_{15/2}$ *transition of* Er^{3+} *ions (transition from the first excited state to the ground state) under non-resonant (*λ_{exc} *= 476 nm, black solid line) and resonant (*λ_{exc} *= 974 nm, red solid line) CW optical excitation under the same excitation photon flux. In the case of the non-resonant excitation (non-resonant as the excitation wavelength does not overlap with* Er^{3+} *absorption bands) photoluminescence of erbium ions has been excited by the energy transfer from the silicon nanoclusters. Under resonant excitation (which overlaps with* Er^{3+} *absorption band) photoluminescence is excited directly by absorption of the pump photon. For the resonant excitation wavelength used (*λ_{exc} *= 974 nm), the silicon nanoclusters absorption can be considered as negligible. Sample A from the* ***Table 1*** *was used. Orders of magnitude increase of* Er^{3+} *PL intensity (note log scale) is attributed to an increase of effective excitation cross section of* Er^{3+} *ions sensitized by silicon nanoclusters.*

Silicon nanoparticles represent a number of various interesting properties as an erbium sensitizer. CMOS process compatibility combined with convenient light emission in the third telecom window (1.5 μm) has been considered as a particular advantage of this material [16]. Additionally, electrical excitation of the erbium ions becomes possible in this material [63].

The most important property is most certainly, the increase in the Er^{3+} effective excitation cross section from the values of the $\sigma_{exc} \sim 10^{-21}$ cm^{-2} to $\sigma_{exc} \sim 10^{-16}$ cm^{-2} when the Er^{3+} ions are placed in close proximity to the silicon nanocrystals [286]. This is well illustrated in **Figure 39**. When exciting trough the silicon nanoclusters, resulting PL intensity is orders of magnitude higher as a consequence of the increased effective excitation cross section. This is a direct consequence of the energy transfer mechanism. In addition, it was demonstrated that the erbium radiative rate increases in close proximity to silicon nanoparticles due to a change in local density of optical states [287,288].

Another important feature is reported in **Figure 40**. In order to excite Er^{3+} ions efficiently, excitation wavelength has to overlap with one of the absorption bands (see **Figure 40a** and **Figure 40b**). When Er^{3+} ions in pure silica are optically excited, the resulting PL intensity of $^4I_{13/2} - {}^4I_{15/2}$ transition of Er^{3+} ions (transition from the first excited state to the ground state) closely mimics the absorption spectrum of the Er^{3+} ions at the excitation wavelengths (see **Figure 40a** and **Figure 40b**).

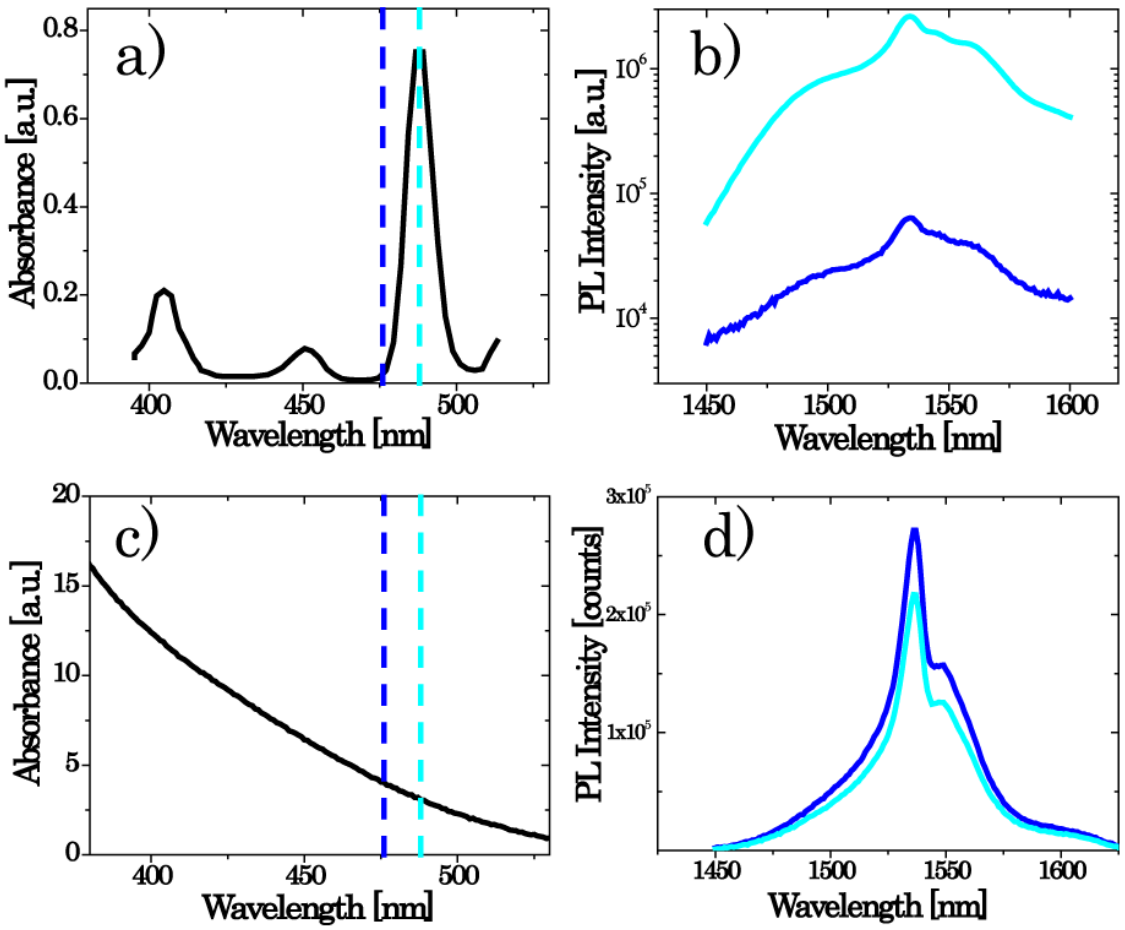

Figure 40 *– (**a**) Absorption spectrum of Er^{3+} ions embedded in pure silica (SiO_2, black solid lines) in the blue-UV (370 - 530 nm) part of the visible spectrum. Blue vertical dashed line corresponds to the wavelength of λ_{exc} = 476 nm which does not overlaps with any of the Er^{3+} absorption bands and thus will be referred to as non-resonant wavelength in the following. Cyan vertical dashed line corresponds to λ_{exc} = 488 nm which overlaps with one of the Er^{3+} absorption bands and therefore is a resonant wavelength. (**b**) PL spectrum the $^4I_{13/2} - {}^4I_{15/2}$ transition (transition from the first excited state to the ground state) of Er^{3+} ions embedded in pure silica (sample from the panel (**a**)) under non-resonant CW excitation (blue solid line) and resonant CW excitation (cyan solid line). PL intensity under non-resonant excitation is two orders of magnitude lower, in accordance with the difference in absorption deduced from the panel (**a**). (**c**) Absorption spectrum of Er^{3+} ions embedded in silica co-doped with silicon nanoclusters (SRO, black solid lines) in the blue-UV (370 - 530 nm) part of the visible spectrum. Blue vertical dashed line corresponds to the wavelength of λ_{exc} = 476 nm, while cyan vertical dashed line corresponds to wavelength λ_{exc} = 488 nm. Monotonic increase of the absorption towards shorter wavelength typical of silicon nanoclusters can be observed* [58,276,289,290]*. Absorption features of Er^{3+} ions cannot be observed as the absorption is dominated by Si-ncl (Si-ncl have orders of magnitude larger absorption cross-section* [286]*) (**d**) PL spectrum of the $^4I_{13/2} - {}^4I_{15/2}$ transition of Er^{3+} ions embedded in SRO film (sample from the panel (**c**)) under the non-resonant CW excitation (blue solid line) and resonant CW excitation (cyan solid line). It can be seen that erbium photoluminescence follows the trend of Si-ncl absorption cross-section.*

However, when the same material is co-doped with silicon nanoclusters PL intensity of $^4I_{13/2} - {}^4I_{15/2}$ transition of Er^{3+} ions follows the absorption spectrum of silicon nanoclusters (see **Figure 40c** and **Figure 40d)**. Therefore, it can be concluded that under these excitation conditions energy transfer is the dominant excitation mechanism and efficient broadband excitation becomes possible.

More detailed experimental characterization of this type can be found as well in the Ref. [58,276,289,290].

As the examples in **Figure 38**, **Figure 39** and **Figure 40** are made on the samples which detailed characterization will be presented in the following sections they demonstrate as well the presence of the energy transfer in the samples studied in this chapter.

Since the first report of the erbium sensitization by silicon nanocrystals [58] and the demonstration of the optical gain in the same material system [62], a large research efforts have been focused towards the understanding of the physical mechanisms behind the energy transfer. In spite of promising initial reports of optical gain [62] and efficient electrical excitation [63], the demonstration of a laser action seems still to be quite challenging.

While a number of limiting factors to stimulated emission have been identified [64,65,271,291], the estimates of their impact on laser action are still imprecise, partially owing to difficulties encountered when modeling the energy transfer mechanism [213,292,293]. Although, the transfer mechanism between Si-nc and Er^{3+} has been thoroughly studied [67,291,293], there is no clear consensus in literature on the more appropriate model to describe this interaction.

Moreover, during the last years, several reports have shown what seems to be an intrinsic limit of the material itself, the low amount of Er^{3+} taking advantage of an efficient indirect transfer mechanism [64,271,294,295]. The fundamental reason of the low excitable percentage is again still under debate and a number of different issues have been proposed as final limiting factors. Among them, the most extended ones have been the finite interaction distance of the coupling strength [271], the presence of Auger back-transfer mechanisms [64], excited state absorption processes [65], cooperative up-conversion [295] and the limited concentration of Er^{3+} ions able to emit light [296].

3.3. Chapter overview

In this chapter, a study of Er^{3+} doped silicon rich oxide (SRO) materials and Er^{3+} doped SRO based devices will be presented. Final objective of the work presented, is the realization of the working devices. However, before the working devices may be manufactured, the properties and drawbacks of the active material and the physical aspects behind them have to be studied and well understood.

In particular, two types of devices will be considered in this work. One will be an optically pumped waveguide amplifier, while the second one will be a novel structure based on the slot waveguides for an electrical pumping of the erbium doped SRO. These different categories of optical amplifying devices require as well different types of material to be used. To that end two types of samples were considered: μm thick Er^{3+}-doped SRO films suitable for

optically pumped amplifiers and tens of nm thin Er^{3+}-doped SRO films suitable for electrically pumped amplifiers and lasers.

The first part of the work presented in this chapter has been realized in the framework of the project LANCER financed by EC. The final objective of this project has been the realization of the optically pumped erbium doped waveguide amplifier (EDWA) based on Si-nc sensitized erbium co-doped silica as a replacement technology for the existing EDFA, relaxing the size and pumping requirements of the existing technology solutions.

My participation in this project started near its end, when the material optimization and waveguide modeling were already largely done. This is the reason why the material optimization and devices modeling has been omitted in this part. Nevertheless, the main guidelines of that work will be shortly summarized.

In order to optimize an optical performance of the active material, knowledge of the underlying physics becomes essential. Thus, attention in the first part of this chapter will be focused on the study of the energy transfer, quantification of the optical performance of optimized material and device characterization. By means of pump& probe experiments an internal gain has been measured in optically pumped Er^{3+}-doped SRO active waveguide, measured values being still too low for a working device.

The second part of the work in this chapter has been done in the framework of another EC funded project HELIOS. The main goal is the realization of integrated, CMOS compatible, electrically pumped laser and optical amplifier based on SRO:Er material. In the first part vast material characterization will be presented of very thin films suitable for electrical injection. By employing extensive optical, electrical and structural characterization a pressing drawback in this material has been identified and possible remedy to low performance of Er^{3+} doped SRO devices has been proposed. Considering a set of optimized samples, quantitative optical experiments are reported and optical performance of optimized material quantified.

In order to achieve an electrical pumping of erbium doped thin SRO novel opto-electronic structures are proposed, modeled and manufactured. Moreover, a preliminary result of their performance is also presented.

3.4. Thick Er^{3+} doped SRO films suitable for optically pumped EDWA[7]

3.4.1. Material optimization

The samples under study have been fabricated by a RF reactive magnetron co-sputtering under argon-hydrogen mixture of 2-inches confocal pure SiO_2 and Er_2O_3 targets [275]. To form nanoparticles, a sub-stochiometric silicon rich silicon oxide (SRO) has

[7] Samples were produced by F. Gourbilleau, R. Rizk and their co-workers in Caen, France.

Table 1 – Samples specifications

Deposition method:		RF reactive magnetron sputtering	
Sample name	**Si excess (%)**	**Er^{3+} ($x10^{20}$ cm^{-3})**	**Annealing Temperature (°C)**
A	5 ± 2	3.4 ± 0.2	900
B	6 ± 2	---	900
A1	5 ± 2	3.4 ± 0.2	900 + 1100
B1	6 ± 2	---	900 + 1100
C	---	0.5 ± 0.1	---

been deposited followed by an annealing treatment to promote phase separation between silicon and its oxide. In order to perform comparative spectroscopic characterization, the deposition parameters employed to obtain the best sample in terms of high PL intensity (under non-resonant pumping – λ_{exc} = 476 nm) and long lifetime of the $^4I_{13/2} \rightarrow {}^4I_{15/2}$ Er^{3+} transition, have been used to fabricate a set of different samples with and without Er^{3+} and with different annealing treatments (see **Table 1**).

Detailed description of fabrication details and optimization procedure can be found in section I of appendix to Chapter 3 and Ref. [272,275,297].

RF-co-sputtering technique has been preferred over other techniques, as it is particularly suitable for Er^{3+} doping of glass, allowing for the deposition of homogeneous films up to several micrometers of thickness of controlled composition [277]. Er^{3+} ions are incorporated in the SRO films during the deposition process [272], avoiding the ion implantation process needed to introduce them in SRO films deposited by other CMOS compatible approaches (PECVD, LPCVD). Thus, non-radiative recombination channels due to implantation induced damage are avoided leading to higher matrix quality [264].

Recently there have been raised certain doubts that silicon excess presence in the SiO_2 matrix, apart from the nanoclusters formation, is responsible of increased non-radiative relaxation of erbium ions [273,298]. On that regard, co–sputtering shows superior characteristic regarding the more complete phase separation of deposited films for the same silicon excess and annealing temperature [226], with the better stochiometry of surrounding matrix and consequent reduction in silicon excess related defects [226,298] respect to other CMOS compatible approaches.

In this study 5 different samples have been used. Their specifications are summarized in **Table 1**. The first four samples in the (A, B, A1 and B1) are deposited over a 5 μm SiO_2 cladding layer placed above a silicon substrate. Samples A and A1 have silicon excess of 5% and Er^{3+} content of 3.4×10^{20} cm^{-3}, as determined from the secondary ion mass spectrometry (SIMS) and Rutherford backscattering spectroscopy (RBS). For the samples B and B1 same deposition conditions were used but without erbium target. Thickness of all four samples was fixed to $\mathbf{d} = 1.2$ μm.

Samples A and B were annealed at $\mathbf{T_{annealing}} = 900$°C for 1 h under pure nitrogen flow and they likely contain amorphous silicon nanoclusters due to the low annealing temperature used which does not allow a complete phase separation [299] and nanocluster crystallization [271,272]. Samples A1 and B1 have been annealed for the second time at $\mathbf{T_{annealing}} = 1100$°C for 1 h under pure nitrogen flow in order to induce complete phase separation and nanoclusters crystallization [226]. As reference sample, Er^{3+} doped soda-lime glass fabricated by Corning was used (sample C).

3.4.2. Energy transfer under high-energy optical excitation

The spectroscopic experiments have been performed both in visible (VIS) and infrared (IR) range, with CW and pulsed laser excitation sources. The CW source was an Ar^+ laser of which two different laser lines were employed, one which was resonant ($\lambda_{exc} = 488$ nm) with Er^{3+} internal transitions and other non-resonant ($\lambda_{exc} = 476$ nm) [61].

The pulsed source was the third harmonic ($\lambda_{exc} = 355$ nm) of a Nd:YAG laser with 10 ns pulse width, a repetition rate of 10 Hz and a photon flux of $\Phi = 1 \times 10^{25}$ ph /(cm^2s) during the pulse. For detection in the visible a CCD streak camera coupled to a spectrometer was used, with a variable time-resolution going down to 22 ps and a monochromator coupled with a GaAs-photo-multiplier (PMT), respectively for time resolved (TR) and CW measurements. In the infrared, the signal was spectrally resolved with a monochromator and subsequently detected with InGaAs IR-PMT. All measurements have been performed at room temperature and corrected for the spectral response of the detecting instruments.

A typical PL spectrum of the samples A and B, measured with an excitation wavelength non-resonant with any Er^{3+} internal transition ($\lambda_{exc} = 476$ nm), is shown in **Figure 41a**. Interference fringes that appear in the PL spectrum are due to multiple reflection in SiO_2 bottom cladding. It is possible to recognize several spectral features: around 980 nm and 1535 nm, the characteristic transitions of Er^{3+} in SiO_2 appear, related respectively to the first ($^4I_{13/2} - {}^4I_{15/2}$) and second excited ($^4I_{11/2} - {}^4I_{15/2}$) to the fundamental state optical transitions.

The wide band centred at 700 nm is related to silicon nanoparticles emission, while the emission band centred at 1100 nm is due to the silicon substrate. The silicon nanoparticles PL band is very broad which is characteristic of the amorphous nanoparticles [300]. This is further demonstrated in **Figure 41b.** Under UV excitation $\lambda_{exc} = 355$ nm with higher photon energy, PL band attributed to silicon nanoclusters, significantly blue-shifts pointing out to incomplete phase separation [299] and significant population of small and amorphous clusters [300].

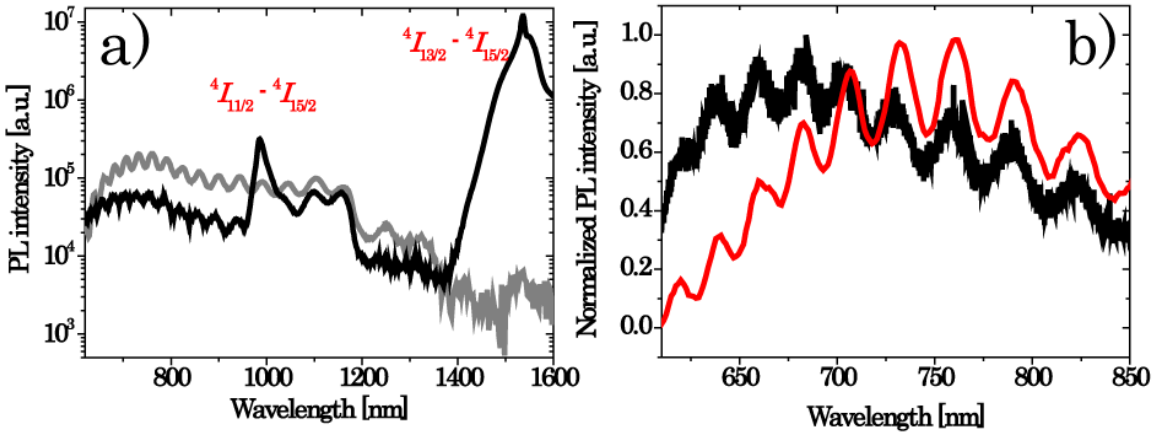

Figure 41 *– (**a**) PL spectra of samples A (black solid line) and B (grey solid line) under non-resonant excitation (λ_{exc} = 476 nm) and same excitation photon flux. Small modulations visible in both PL spectra are interference fringes due to multiple reflections in SiO_2 bottom cladding. Broad PL band centered on λ = 700 nm present in both sample is PL coming from the amorphous silicon nanoclusters. Nanocluster's PL emission is stronger in sample without Er^{3+} ions (sample B). Small feature at λ = 1150 nm is PL coming from the silicon substrate. Narrow PL features at λ = 980 nm and λ = 1535 nm in PL spectrum of sample A (Er^{3+} doped) are due to $^4I_{11/2} - {}^4I_{15/2}$ and $^4I_{13/2} - {}^4I_{15/2}$ radiative transitions respectively. (**b**) Time integrated PL spectrum of sample B (without Er^{3+} ions) in VIS-NIR spectral region (600 – 850 nm) under pulsed UV excitation (λ_{exc} = 355 nm) compared with PL spectrum of the same sample under non-resonant CW excitation (λ_{exc} = 476 nm). PL spectrum is blue shifted under UV excitation.*

Since the optical excitation used is non-resonant with any of the internal Er^{3+} transitions, Er^{3+} related radiative transitions are due to energy transfer from the silicon nanoparticles. This has been previously confirmed in the **Figure 40** by demonstrating that Er^{3+} related PL emission intensity reflects the changes in the silicon nanoclusters absorption cross-section and in **Figure 39** by showing increased excitation efficiency when non-resonant excitation is used.

Respect to sample B the CW measurement reveals that the PL of sample A in the visible region is quenched as a whole, without showing any apparent spectral features. This decrease is only about a factor of 3, so a clear residual VIS-PL emission is still present in the sample with Er^{3+}. Energy transfer from the silicon nanoclusters to Er^{3+} ions is competing process to exciton radiative recombination. As the Er^{3+} ions have been introduced in the samples during the deposition phase [272,275] avoiding the implantation damage [264], quenching of the visible PL could be attributed to an energy transfer [58].

In the **Figure 42** is reported a comparison between the once and doubled annealed samples. In the double annealed samples (with erbium or without) the visible PL band is red-shifted, narrower and significantly stronger indicating increased crystallinity of the samples and silicon nanocrystals formation [226]. Interestingly, Er^{3+} related transitions are quenched in sample A1 respect to sample A.

The possibility of Er^{3+} clusterization during the annealing procedure has been discarded by analyzing the Er^{3+} ions first excited state decay at different excitation photon fluxes (not shown) [271,297]. As the PL lifetime found is similar to that reported for sample A

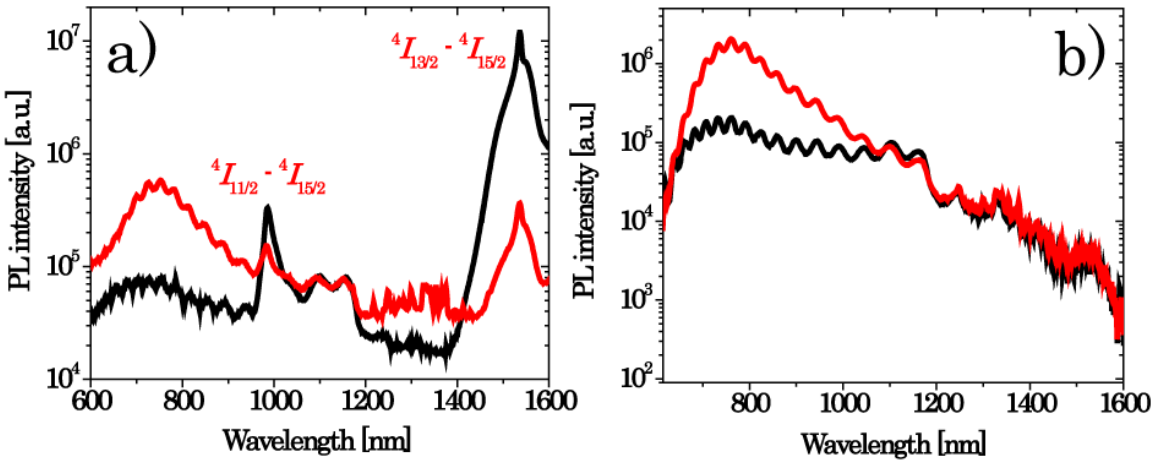

Figure 42 *– (**a**) PL spectra of samples A (black solid line) and A1 (red solid line) under non-resonant excitation (**λ**$_{exc}$ = 476 nm) and same excitation photon flux. Small modulations visible in both PL spectra are interference fringes due to multiple reflections in SiO_2 bottom cladding. Broad PL band centered at **λ** = 750 nm present in both sample is PL coming from the silicon nanoparticles. This PL band is red-shifted, narrower and much more intense in double annealed sample (A1) indicating formation of silicon nanocrystals. Small feature at **λ** = 1150 nm is PL coming from the silicon substrate. Narrow PL features at **λ** = 980 nm and **λ** = 1535 nm in PL spectra of both samples (A and A1) are due to $^4I_{11/2} - {}^4I_{15/2}$ and $^4I_{13/2} - {}^4I_{15/2}$ radiative transitions respectively. Er^{3+}ions related radiative transitions are less pronounced in doubled annealed sample (A1). (**b**) PL spectra of samples B (black solid line) and B1 (red solid line) under non-resonant excitation (**λ**$_{exc}$ = 476 nm) and same excitation photon flux. Broad PL band centered on **λ** = 750 nm present in both sample is PL coming from the silicon nanoparticles. This PL band is red-shifted, narrower and more intense in double annealed sample (B1) indicating formation of silicon nanocrystals.*

(**τ** = 5.5 ms) [291], and since the non-resonant excitation was used, decrease in erbium related PL is attributed to a lower energy transfer efficiency for the crystalline samples. This is further confirmed by smaller decrease of visible PL of sample A1 respect to sample B1 for a factor of 2.8, which is less than a factor of 3 observed for annealed once samples.

In order to investigate further the nature of silicon nanoparticles and degree of crystallinity of different samples, TR PL measurements have been performed in the visible. The results of these measurements for samples B and B1 are reported in **Figure 43**. It can be seen that both samples show multi-exponential nature of the time decay typical of silicon nanoparticles [160,172,301].

These type of time decays can be well fitted by stretched exponential function [109]. Sample B1 (see **Figure 43b)** shows strong dependence of the lifetime on the observation wavelength pointing out to the crystalline nature of the silicon nanocrystals [110]. On the other hand, sample B shows shorter lifetime and smaller stretching parameter with no spectral dependence of the lifetimes, which can be associated with amorphous nature of silicon nanoclusters. Identical results have been obtained as well in erbium doped samples A and A1. For the sample A amorphous nature of nanoparticles is confirmed, while the results on sample A1 are consistent with the presence of silicon nanocrystals.

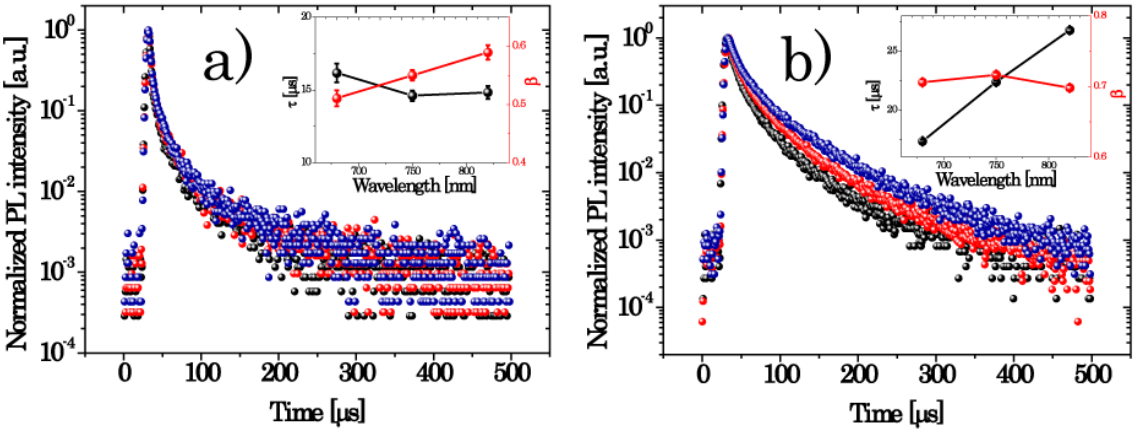

Figure 43 *– (**a**) Visible PL time traces of the sample B observed at* λ *= 680 nm (black spheres),* λ *= 750 nm (red spheres) and* λ *= 820 nm (blue spheres). Time decays show strong multi-exponential nature. Time traces have been obtained by integrating over 90 nm wide spectral windows. (**Inset**) Time decays from the main panel have been fitted with the stretched exponential function and fitting parameters are reported. PL lifetimes (black spheres) of approximately 15 μs are observed for all observation wavelengths. Lack of the spectral dependence of the lifetimes points out to an amorphous nature of silicon nanoclusters* [38]*. This is further confirmed by a low value of stretching parameter* β *= 0.55 (red spheres). (**b**) Visible PL time traces of the sample B1 observed at* λ *= 680 nm (black spheres),* λ *= 750 nm (red spheres) and* λ *= 820 nm (blue spheres). Time decays show strong multi-exponential nature. Time traces have been obtained by integrating over 90 nm wide spectral windows. (**Inset**) Time decays from the main panel have been fitted with the stretched exponential function and fitting parameters are reported (black spheres for lifetimes and red spheres for stretching parameters). Strong wavelength dependence of the lifetimes point out to a crystalline nature of the silicon nanocrystals* [38,110]*. Pulsed UV excitation was used in both cases (*λ_{exc} *= 355 nm, 6 ns pulses, 10 Hz repetition rate) with excitation photon flux* Φ *= 1 x* 10^{25} *ph./(*cm^2**s).*

Visible PL intensity dependence was also studied as a function of the excitation photon flux for the sample A (with erbium) and B (without erbium). Results were fitted with the allometric function. In both cases, sub-linear dependence on the excitation photon flux was found. For the sample B, the power law coefficient is found to be very close to 2/3 (**b** = 0.72 ± 0.01), which is the signature of a three particle Auger recombination mechanism [54]. Although emission from sample B is more intense, the power law coefficient is higher for sample A (**b** = 0.83 ± 0.05).

Difference between exponents can be explained by the existence of different mechanism in sample A that reduces the exciton population of the emitting level to a values where Auger process is weaker and thus exponent is closer to unity (notice that this is true only in well passivated, high quality samples).

The only difference between the two samples is the erbium presence in sample A. Therefore this competitive process to Auger recombination is attributed to an energy transfer. This implies as well that the energy transfer has to be a very fast process, as the Auger recombination is active on the ns timescale [54].This means that when Er^{3+} ions are introduced in the sample, the visible PL lifetime gets reduced. To investigate this possibility, time decays of the sample B and A are reported in **Figure 44**.

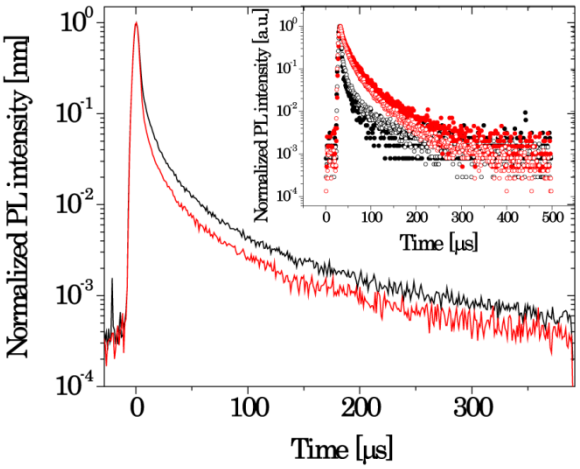

Figure 44 *– PL time decay of the sample B (black solid line, without Er^{3+}) and sample A (red solid line, with Er^{3+}). Shortening in the initial decay can be observed for the sample A. Time trace were obtained by integration over 90 nm wide spectral windows centered at* λ *= 700 nm. (**Inset**) PL time decay of the sample A (solid black circles), sample B (empty black circles), sample A1 (solid red circles) and sample B1 (empty red circles). Time trace were obtained by integration over 90 nm wide spectral windows centered at* λ *= 680 nm. Pulsed UV excitation was used (*λ_{exc} *= 355 nm, 6 ns pulses, 10 Hz repetition rate) with excitation photon flux* Φ *= 1 x 10^{25} ph./(cm^2*s).*

As can be seen in **Figure 44**, the PL decay only speeds up for sample A during the first tens of ns as a consequence of the transfer process, while afterwards the temporal evolution of the PL signal is roughly the same (although lower in the intensity). The situation does not differ in the case of the double annealed samples (see **Inset** of **Figure 44**).

Thus, only initial dynamics of silicon nanocluster PL is influenced. This is a consequence of different initial exciton population in accordance with what inferred from CW measurements. Moreover, the decay of sample B can be divided in two parts: first, characterized by a slow process with a stretched exponential line shape (tens of μs) that is typical of the spontaneous emission process in Si-nc; and second, a fast decay (tens of ns) that can be associated with Auger recombination mechanisms within the silicon nanoclusters [54], hot carrier emission [200] or silicon excess related defects [67,302].

Since the intrinsic recombination lifetime for excitons within Si-nc is of the order of tens of μs, in a case of a transfer mechanism related to inter-band recombination, the energy transfer to Er^{3+} would be expected to be quite inefficient and slow, which is not the case. Moreover, the slow component of the time decay should be affected as well. Therefore, it can be concluded that energy transfer is a very fast process competitive to Auger (~ns timescale) [54] and not related to a inter-band transition of excitons in silicon nanoparticles or at least not in its dominant part.

Interestingly, as shown in **Figure 41**, only two erbium related transitions could be observed in sample A, $^4I_{11/2}$ - $^4I_{15/2}$ and $^4I_{13/2}$ - $^4I_{15/2}$. Based on this one could tentatively conclude that the energy transfer does not occur for higher energy state of erbium. To get more insight, PL spectrum of sample A and C are compared in **Figure 45**. PL spectra have been obtained by exciting with λ_{exc} = 488nm. Under these conditions, sample C is excited trough the higher excited erbium states, while in sample A energy transfer remains dominant excitation mechanism (see **Figure 40**).

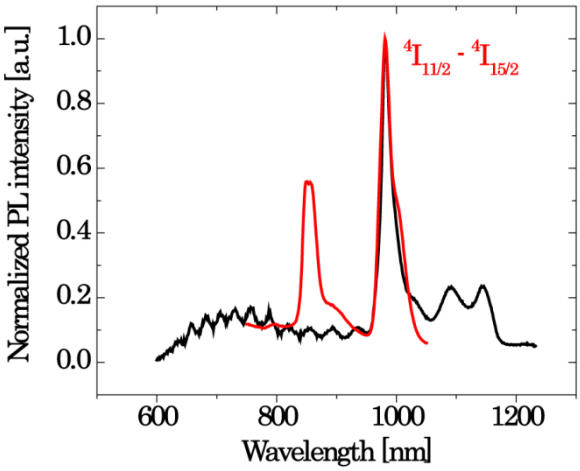

Figure 45 *– Visible PL spectra of sample A (black solid line) and sample B (red solid line) under resonant excitation (λ_{exc} = 488 nm).*

Sample C shows an additional peak situated at λ = 850 nm. However, peak due to $^4I_{9/2}$ - $^4I_{15/2}$ transition should be situated around λ = 800 [61]. Thus it can be concluded that this peak is not due to $^4I_{9/2}$ - $^4I_{15/2}$ transitions but due to radiative relaxation between excited erbium states [61]. In fact, in sample C there is a strong cooperative up-conversion process present, boosting the visibility of higher excited states under high photon flux or high energy excitation. Nevertheless, the visibility of these peaks is much less intense than the $^4I_{11/2}$ - $^4I_{15/2}$ and $^4I_{13/2}$ - $^4I_{15/2}$ transitions.

The reason for a better visibility of $^4I_{11/2}$ and $^4I_{13/2}$ levels related optical transitions is that they are separated by a large energy gap from other energy levels, inhibiting effectively multi-phonon relaxation [262]. Moreover, transitions from the higher excited states of erbium ions, if present in the PL spectrum of sample A would be very difficult to observe as sample A does not suffer from up-conversion process [297] and in addition have strong PL band of nanocrystals that may hinder the small emission from the excited states of erbium. That implies that even though the higher excited states of erbium are not visible in the PL spectrum of sample A it does not mean that energy transfer is not occurring at the higher excited states as well.

Therefore, in order to get more insight on the energy transfer, the dynamic of only these two transitions was studied (see **Figure 46**). The analysis of the IR emission reveals that the signal at 980 nm ($^4I_{11/2}$ - $^4I_{15/2}$ transition) after a steep rise that lasts less than 100 ns is constantly decreasing as a single exponential function, with a time constant of τ = 4.6 ± 0.5 µs. On the other hand, the 1 535 nm signal ($^4I_{13/2}$ - $^4I_{15/2}$ transition) is rising with almost the same time constant (τ = 4.2 ± 0.5 µs). The whole decay of the $^4I_{13/2}$ - $^4I_{15/2}$ transition is not shown as it is very long (τ = 5.5 ms) and it is characterized by a single exponential decay [291], which is independent of the excitation photon flux or wavelength [296,297]. It is not possible to compare directly the populations in the two levels, since the PL intensities are inversely proportional to the unknown radiative lifetimes.

However, it seems that part of the energy transfer process involves the level $^4I_{11/2}$ in agreement with CW PL spectrum. The level $^4I_{13/2}$ is populated through the internal relaxation processes from $^4I_{11/2}$ (decay constant of $^4I_{11/2}$ transition and rise time of $^4I_{13/2}$ transitions are fairly similar) as well as directly, both being the same order of magnitude.

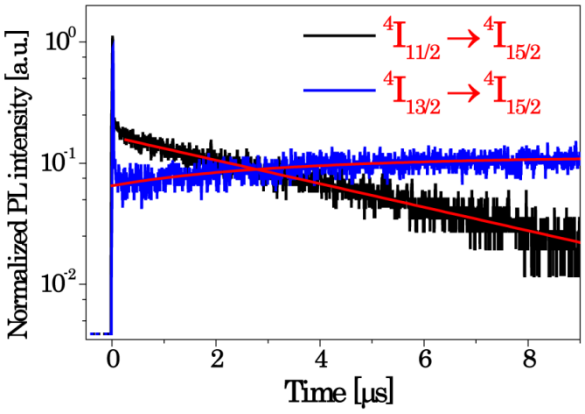

Figure 46 *– Initial PL dynamics of the $^4I_{11/2}$ - $^4I_{15/2}$ (black solid line) and $^4I_{13/2}$ - $^4I_{15/2}$ (blue solid line) Er^{3+} transitions. Time traces were fitted with the single exponential function (red solid lines) yielding decay time τ = 4.6 ± 0.5 μs for 980 nm signal ($^4I_{11/2}$ - $^4I_{15/2}$) and rise time of τ = 4.2 ± 0.5 μs for 1535 nm signal ($^4I_{13/2}$ - $^4I_{15/2}$). Pulsed UV excitation was used (λ_{exc} = 355 nm, 6 ns pulses, 10 Hz repetition rate) with excitation photon flux Φ = 1 x 10^{25} ph./(cm^2*s).*

The single exponential function observed in the 980 nm decay suggests that the main contribution to this level is direct at these excitation conditions, and not trough the internal excitation of higher excited levels, although it's small contributions cannot be completely excluded.

Another striking features is the appearance of a very fast (tens of ns) signal immediately after the laser pulse. The nature of this component has been thoroughly studied on the samples A and B and the results have been reported in Ref. [291]. Here it will be shortly summarized the findings reported in Ref. [291] concerning this component.

A similar component was observed previously and it was associated with Auger back-transfer mechanisms from excited Er^{3+} to excited carriers within the Si-nc [64]. The Auger back-transfer is the main limiting process for the erbium luminescence in erbium doped silicon [268,270] and it was proposed to be main limiting factor for erbium luminescence in silicon nanoparticles co-coped material as well [64].

In the **Figure 47a**[8] is reported the spectral dependence of the PL signal from the sample A after pulsed UV excitation, integrated over the first 200 ns after the laser pulse arrival and after 200 ns from the pulse arrival. It can be seen that the initial fast component is spectrally broad and that the erbium related transitions are only weakly pronounced which is not the case in the slower component. The time decay of the same fast component is reported in the inset of the same figure for the wavelengths coinciding or not with erbium related transitions. In both cases the same fast dynamic is present, excluding the Auger back-transfer as its origin [64].

In the **Figure 47b**[8] the spectral dependence of the PL signal integrated over the first 200 ns after the pulse arrival for sample A (with erbium) and sample B (without erbium) is reported. Moreover, it is reported the dynamics of this fast component for the same two wavelengths previously considered. It can be seen that the same dynamics as in previous case

[8] PL measurements of the fast PL component have been performed by D. Navarro-Urrios and A. Pitanti.

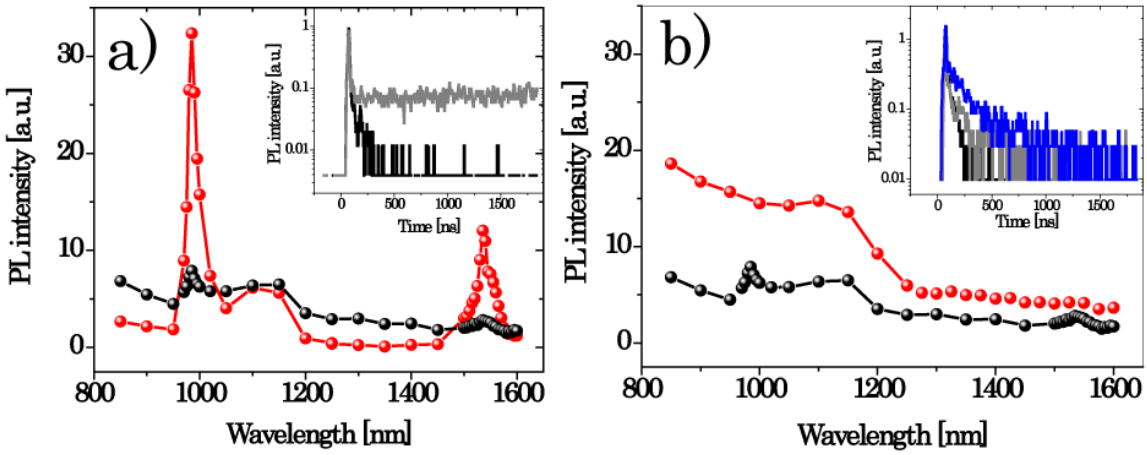

Figure 47[8] *– (**a**) PL spectrum of the sample A integrated over the first 200 ns from the laser pulse arrival (black spheres) and from 200 ns to 2μs (red spheres). (**Inset**) Time decay of PL signal of sample A recorded at* λ *= 1300 nm (black solid line) and* λ *= 1535 nm (grey solid line). (**b**) PL spectrum of the samples A (black spheres) and sample B (red spheres) integrated over the first 200 ns from the laser pulse arrival. (**Inset**) Time decay of PL signal of sample B recorded at* λ *= 1300 nm (black solid line),* λ *= 1535 nm (grey solid line) and* λ *= 1100 nm (blue solid line). Pulsed UV excitation was used (*λ_{exc} *= 355 nm, 6 ns pulses, 10 Hz repetition rate) with excitation photon flux* Φ *= 1 x* 10^{25} *ph./(*cm^2**s).*

is present. In the same figure it is reported also the PL signal dynamics recorded at 1100 nm coming from the silicon substrate. As it can be seen this signal is decaying slower and thus fast PL component does not have origin in the substrate.

The samples A1 and B1 were as well considered and the same behavior of the fast component has been found (data not shown)[8]. These findings are very similar to what reported in [303], where samples with amorphous nanoclusters have been considered. This PL component was attributed to a silicon excess related states situated at the nanocluster surface [302].

As this component is slightly quenched when the erbium ions are introduced (see **Figure 41** and **Figure 47**, spectral region around 1300 nm), it was proposed that they have a role in erbium ions excitation [67,302]. However, recently it has been demonstrated that in highly crystalline samples, the fast component at λ = 1535 nm could be partially due to fast erbium de-excitation trough the erbium related trap states [304].

Independently on the exact origin of this fast PL component, the presence of the Auger back-transfer mechanism can be ruled out in the samples under the study.

3.4.3. Semi – empirical model for energy transfer under high-energy optical excitation

A detailed model of the electronic and optical properties of a single Si-nc can only be built with extreme difficulty. Moreover, due to the specific deposition characteristics of the studied samples the most probable situation is that, within the active material, an ensemble of Si-nc of different sizes and geometries is present. For this reason, the dynamics of the

system can be easier modelled by a phenomenological set of rate equations. A simplified description of the system allows simulating the overall experimental picture described in the previous paragraphs.

One example of this type of modeling is presented in section II of Appendix to Chapter 3. It is worth to note that this model is valid only for the first hundreds of nanoseconds after the excitation, where Auger and the transfer mechanism dominate the dynamics of the carriers within the Si-nc (intrinsic and bimolecular-like recombination mechanisms are neglected) and, consequently, the Er^{3+} excitation. This model describes very well the system in the high excitation regime, although it fails in certain aspect for the lower-energy excitation as it will be presented in next section.

Although simplified, this model provides with some new insight in energy transfer physics. There are basically three important aspects that can be deduced from the comparison of simulations with experiments. First is that the inter-band transitions could not be responsible for the dominant part of energy transfer, although their small contribution cannot be excluded. Second one is that the energy transfer is extremely fast with the upper limit of $\tau_{transfer} \leq 36$ ns as estimated by comparison of simulations with experimental results. The third one is that the interaction distance between the two interacting species would have to scale exponentially with the distance in order to describe well experimental data. This is in agreement with what found in Ref. [66,305,306].

Exponential decay of the interaction efficiency with distance is characteristic for the so-called Dexter type of interaction, whose efficiency is given by the degree of overlap of the wavefunctions [60]. Recent theoretical study demonstrated that this should be the dominant type of interaction between indirect band-gap quantum dots [153]. This type of excitation has been found as well to be responsible for efficient interaction between silicon nanocrystals and oxygen molecules [307]. Moreover, it has been demonstrated that the energy transfer mechanism between silicon nanoparticles and erbium ions could be controlled by a change in local density of optical states [308], which is contrary to what expected from the case of dipole-dipole type of interaction [266].

However, there are as well some works that model silicon nanoparticles – erbium ion interaction as a dipole-dipole kind of interaction [64,293,309] in analogy with excitation mechanism in bulk silicon [267,268,270,278] and mutual interaction between erbium ions [61,266].

Recently, it has been demonstrated that the dipole – dipole interaction can appear as exponential under certain conditions [310] and as well that $Er^{3+} - Er^{3+}$ interaction (which is dipole – dipole type of interaction) could play significant part in energy transfer [306]. Thus, exponential decay of interaction alone is not sufficient to distinguish between dipole [59] or exchange interaction [60].

3.4.4. Energy transfer under low-energy optical excitation

Most of the energy transfer studies have been performed with optical excitation in the high energy spectral region (blue, UV) where the absorption cross section of silicon nanoparticles is dominating that of the Er^{3+} ions [117,286]. Excitation at longer wavelengths (lower energies), where the absorption cross section of these two materials becomes

comparable, may provide with valuable insight in the energy transfer mechanism [233,290,293,311,312].

In this section a photoluminescence (PL) study of silicon rich oxide thin films co-doped with Er^{3+} ions (SRO:Er^{3+}), under low–energy optical excitation. In particular, samples A and B were used (see **Table 1**). The general features of the PL dynamics are studied by time resolved photoluminescence (TR PL) measurements, performed both in the visible and in the infrared.

Photoluminescence measurements were done using, as an excitation source, the optical pulses (6 ns pulse length, 10 Hz repetition rate) of an optical parametric oscillator (OPO) pumped with the third harmonic of a Nd:YAG laser. The excitation photon flux ($\Phi \sim 10^{24}$ ph * cm^{-2} * s^{-1}) was maintained constant over the whole used spectral range. Detection consisted of a spectrograph (Chromex) coupled to a streak camera (Hamamatsu, visible) or of a monocromator (Chromex) coupled to an InGaAs photomultiplier (Hamamatsu, infrared) with overall time resolution of 2 ns (visible) and 40 ns (infrared), respectively. All measurements were performed at room temperature. All spectra were corrected for the spectral response of the instruments.

When optically exciting this material (with energy not matching any of the possible internal transitions of Er^{3+} ions, **Figure 38**), the pump photons are absorbed by the silicon nanoclusters and the energy is subsequently transferred to the Er^{3+} ions. In section 3.4.2, it was demonstrated that this energy transfer occurs on a very short temporal scale in agreement with what reported recently in literature [64,67]. As a consequence of the energy transfer, the exciton population in silicon nanoclusters is decreased, leading to a quenching of the visible PL (originating from silicon nanoclusters) in the Er^{3+} doped sample (sample A, see **Figure 41**).

As reported in **Figure 44**, only the initial part of the visible PL dynamics is influenced by the energy transfer. Thus, the visible PL dynamic is monitored at λ = 750 nm in the first 400 ns after the laser pulse arrival, by using a 50 ns time gate (see **Figure 48**) in order to filter out any initial fast contribution that might not be due to radiative inter-band exciton recombination in silicon nanoclusters [54,67,200,291,303]. We observe that although there is a clear difference in the emission dynamic for the two samples (A and B, see **Table 1**) with a "blue" pump (λ_{exc} = 470 nm), the difference disappears moving towards the "red" (λ_{exc} = 640 nm) (**Figure 48**). Slow emission dynamics was checked as well, and as in the case of the UV excitation (λ_{exc} = 355 nm, **Figure 44**), it was independent on the erbium presence and in addition, it was insensitive to an excitation wavelength change.

It is important to underline that the difference in the emission dynamic of the two samples under "blue" pump condition does not necessary imply that the energy transfer from silicon nanoclusters to Er^{3+} is still occurring on the timescale of observation ($\tau_{obs} \approx 100$ ns). In fact, it was demonstrated recently that the energy transfer could be a very fast process [64,67], taking place typically on the timescale shorter than 100 ns [64] ($\tau_{transfer} < 36$ ns in sample A, see **Figure 82b**).

On the other hand, the exciton recombination dynamics in silicon nanoparticles depends heavily on the exciton population itself, due to effects such as Auger recombination [54] and inter-nanocluster transport [115,159]. This is well illustrated in the **Figure 48**, if the emission dynamic of the *same* sample under two *different* excitation conditions ("blue" and "red") is considered. Although, approximately, the same excitation photon fluxes were used ($\Phi \sim 10^{24}$ ph * cm^{-2} * s^{-1}), the wavelength dependence of the

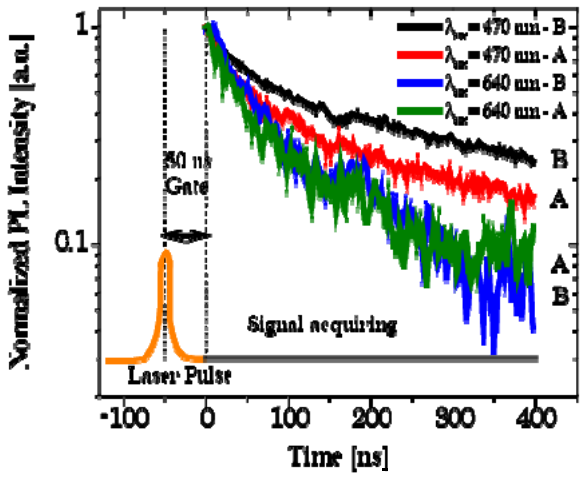

Figure 48 *- Fast decay dynamics of the visible PL of samples A (red and green solid line) and B (black and blue solid line) under* λ_{exc} *= 470 nm excitation (upper two lines, black solid line for sample B and red solid line for sample A) and* λ_{exc} *= 640 nm (lower two lines, blue solid line for sample B and green solid line for sample A). The time decay traces were recorded at* λ *= 750 nm using a 90 nm wide spectral window. (**Inset**)* Δt *= 50 ns time gate was used in order to filter out any initial fast contribution that might not be due to radiative inter-band exciton recombination in silicon nanoclusters.*

absorption cross-section [117] of the Si-nc leads to different exciton populations and different fast (< μs) emission dynamics.

The difference in emission dynamics observed between *different* samples (A and B) under the *same* ("blue" pump) excitation condition is an indicator of a different exciton population in the two samples. This difference is not related to a change in the absorption cross-section (as the same pump conditions are used), but to the Er^{3+} ions presence [117,286]. As already mentioned previously, Er^{3+} ions are introduced during the deposition phase [275], minimizing therefore the occurrence of non-radiative quenching centers [264,278]. Hence, the difference in emission dynamics (exciton population) is associated with the energy transfer mechanism present in erbium co-doped sample in analogy with what presented in **Figure 44**.

However, if the *different* samples (A and B) are considered under the *same* "red" pump condition (**Figure 48**) the emission dynamics (exciton populations) observed are practically the same. As it is rather unlikely that non-radiative recombination due to Er^{3+} related defect states show such a strong dependence on excitation wavelength in this range of energies [270,304], we attribute this distinct behavior to a *change* in the energy transfer process.

In order to investigate further this phenomenon the initial PL dynamics of the $^4I_{13/2} - {}^4I_{15/2}$ transition of Er^{3+} ions (at λ = 1535 nm, transition from the first excited to fundamental state) is monitored, while changing the excitation wavelength in the spectral range (λ_{exc} = 540 nm – 680 nm) around the value of the "red" pump previously used (λ_{exc} = 640 nm).

In the literature, the dynamics of the $^4I_{13/2} - {}^4I_{15/2}$ transition is frequently described by an initial microseconds PL rise followed by a very slow PL decay (on millisecond time scale, τ = 5.5 ms in sample A) (see **Figure 49**) [64,291]. The later is due to the radiative $^4I_{13/2} - {}^4I_{15/2}$ transition and, in the absence of detrimental effects such as cooperative up-conversion, it is independent on the excitation photon flux [297].

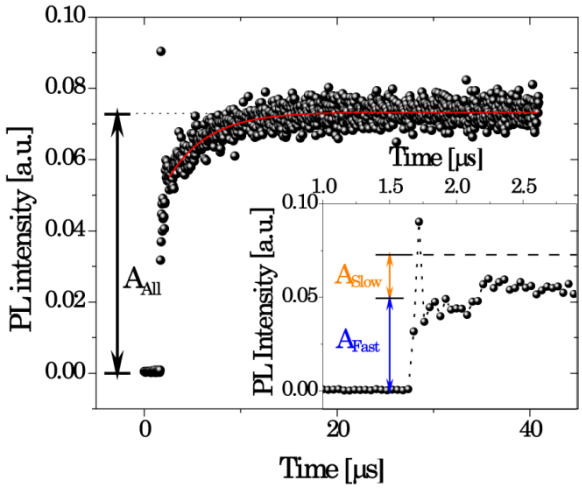

Figure 49 *- Initial PL dynamics of the* $^4I_{13/2}$ - $^4I_{15/2}$ *transition of* Er^{3+} *ions under* λ_{exc} *= 560 nm pulsed excitation (black spheres). The best fit by Eq. 9 (red line) of the experimental data is also shown. The meaning of the fit parameter* A_{All} *is illustrated as well. (**Inset**) Zoom on the first μs of the initial PL dynamics. Graphical interpretation of the fit parameters* A_{Slow} *and* A_{Fast} *are shown.*

On the other hand, the initial microseconds rise dynamic is considered to be due to the internal relaxation from high energy states of Er^{3+} to the $^4I_{13/2}$ state [291,293,313]. The higher energy states of Er^{3+} are indirectly populated by the energy transfer process.

Although, the first tens of ns are hidden by a very fast PL decay contribution (**Figure 49**, Inset, discussed as well in section 3.4.2 , see **Figure 45**), it is evident that the μs PL rise does not start from a zero level. This implies that a fraction of the Er^{3+} ions have been excited through the energy transfer process directly to the first excited state [291,293,313].

In order to quantify the relative contributions of the direct and higher state energy transfer contributions to the total PL we fit the experimental data with the equation (see section III of Appendix to Chapter 3 for more details):

$$I_{PL}(t) = I_{Background} + A_{All}\exp[-(t-t_0)/t_2] - A_{Slow}\exp[-(t-t_0)/t_1] \qquad (9)$$

Where $I_{Background}$ (background level) and t_0 (laser pulse arrival time) are fit parameters, t_1 = 4.2 μs and t_2 = 5.5 ms have been measured previously (rise and decay of $^4I_{13/2}$ - $^4I_{15/2}$ transition, see section 3.4.2). The other fit parameters are A_{Slow} and A_{All} (A_{Fast} being A_{All} – A_{Slow}). Their graphical interpretation is presented in **Figure 49**. A_{Slow} weights the electronic contribution to the first excited state coming from the internal relaxation from higher energy states, while A_{Fast} represents the direct contribution to the first excited state. A_{All} is simply the sum of the two, or in other words, the total contribution to the first excited state.

More insight on the underlying physics could be gained by the plot of the ratio A_{Fast}/A_{All} (see **Figure 50**), which yields an estimate of the "fast" direct contribution (given by A_{Fast}) to the total excited Er^{3+} population, as a function of the excitation wavelength. The same dependence is found even when t_1 is assumed to be a fit parameter. In this case values of t_1 of the order of few μs are found as well.

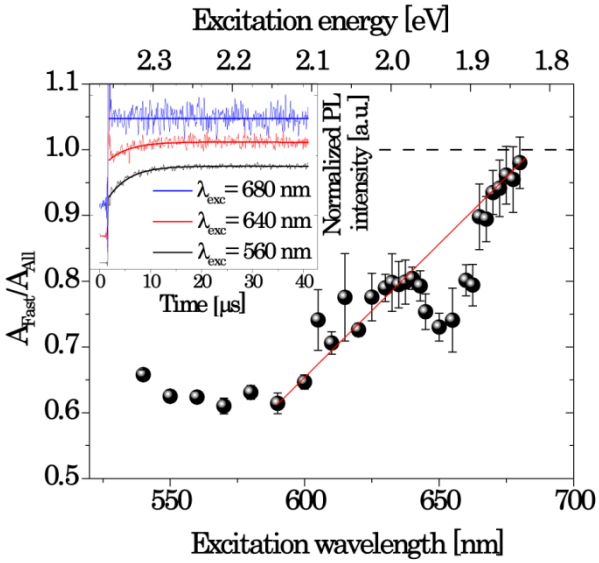

Figure 50 *- Variation of the* A_{Fast}/A_{All} *ratio (black spheres) with the excitation wavelength. The black dashed line represents the value at which no contribution from higher excited state of* Er^{3+} *ions is present. The red solid line is only a guideline for the eyes.* ***(Inset)*** *Initial PL dynamics of the* $^4I_{13/2}$ *-* $^4I_{15/2}$ *transition of* Er^{3+} *ions under* λ_{exc} *= 560 nm (thin black bottom curve),* λ_{exc} *= 640 nm (thin red middle curve) and* λ_{exc} *= 680 nm (thin blue upper curve) pulsed excitation. The best fits by Eq. 9 (thick lines of corresponding color) of the experimental data are also shown. The data and fit curves have been normalized and offset by 0.2 for clarity.*

A non-monotonic dependence of the A_{Fast}/A_{All} ratio upon excitation wavelength could be observed in **Figure 50**. For excitation wavelength shorter than λ_{exc} < 600 nm a saturation region where the ratio is almost independent of the excitation photon wavelength is found. On the contrary, for longer excitation wavelengths, the ratio is increasing, and reaches a value of one for λ_{exc} = 680 nm, independently of the photon flux (within the limits imposed by experimental setup). The anti-resonant feature at λ_{exc} = 650 nm is related with the direct resonant excitation of Er^{3+} ions to $^4F_{9/2}$ energy state (see **Figure 38**). Indeed, in this an increase of the "slow" contribution (given by A_{Slow}) case is observed, leading to a decrease of the ratio A_{Fast}/A_{All}. Note that resonant features at shorter wavelengths are not observed, since the energy transfer to high Er^{3+} states becomes more efficient than the direct excitation.

A ratio of one corresponds to a complete absence of the contribution from higher lying states to the Er^{3+} $^4I_{13/2}$ state. In other words, energy transfer from silicon nanoclusters to higher excited states of Er^{3+} is not allowed any more at the excitation energy of E_{exc} = 1.82 eV, where the excess energy with the respect to the second excited state of Er^{3+} is approximately ΔE = 0.55 eV. It is worth noticing that transition to this state is rather smooth, taking place for excitation energies in the range between 2.1 and 1.8 eV (see **Figure 50**). Moreover, a part from the change in its initial dynamics (**Figure 48**), visible PL coming from the silicon nanoclusters is still observable.

These observations could be associated with the intra-band model for the energy transfer [293] (see section 3.4.3 and section II of Appendix to Chapter 3). In this model, intra-band electronic transitions are responsible for the energy transfer to Er^{3+} and, in particular, they require a minimum excess energy corresponding to a band-gap value of silicon nanoclusters.

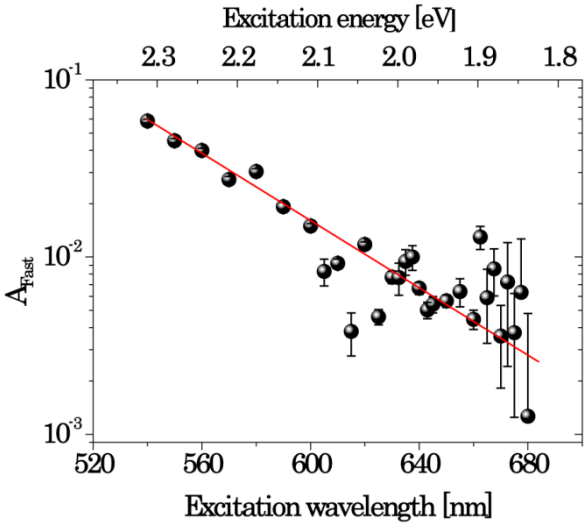

Figure 51 *- A_{Fast} (direct contribution to the first excited state of Er^{3+} ions) dependence on the excitation wavelength (black spheres). The red solid line is only a guideline for the eyes.*

However, it comes as a surprise the relatively small amount of the measured excess energy values needed for the transfer to occur towards the $^4I_{11/2}$ state ($\mathbf{\Delta E}$ = 0.8 - 0.55 eV).

These values are lower than the expected band-gap energy of silicon nanoclusters in sample A ($\mathbf{E_{Band\text{-}gap}} \approx 1.6$ eV, as estimated from PL peak [314]) and even lower than the bulk crystalline silicon band-gap ($\mathbf{E_{Band\text{-}gap}} \approx 1.1$ eV), indicating a participation of a sub-band-gap state in the energy transfer process.

Sub-band-gap states have been theoretically predicted in amorphous silicon nanoclusters with low hydrogen content [37]. In addition, a modest spread in energy has been suggested to occur for weakly localized states due to limited effects of quantum confinement [37].

It should be mentioned, that recently, it has been postulated, as well, the possible existence of deep trap states related with presence of Er^{3+} ions in the bulk silicon [270].

An alternative explanation to these experimental observations would be that two different types of sensitizers are present in sample A. As the absorption cross-section of the silicon nanoclusters is decreasing with wavelength [117], the effective cross-section of Er^{3+} ions sensitization through the silicon nanoclusters may reach a lower value, where the contribution from another sensitizer type could become significant.

The influence of Er^{3+} related matrix defects on Er^{3+} photoluminescence has been demonstrated recently, but in very different energy range [304]. On the other hand, the silicon excess related states erbium sensitization has been well established in a wide range of excitation energies [302,311]. However, an evenly distribution in the energy of these defect states is expected [311,313], with wavelength dependence of effective cross-section for erbium sensitization mirroring the one of silicon nanoclusters [311]. Moreover, the energy transfer to higher energy states of Er^{3+} ions would be still possible for this sensitizing mechanism at the excitation energies used, in contrast to what we observe.

To address this issue, $\mathbf{A_{Fast}}$ (direct contribution to the first excited state) is reported in **Figure 51** as a function of the excitation energy (wavelength). A continuous monotonic

decrease can be observed across the whole excitation range suggesting the existence of only one erbium sensitizer which is related to Si-nc.

The presence of a saturation region below 600 nm (see **Figure 50**) with a value of A_{Fast}/A_{All} ratio equal to 0.6 implies that direct energy transfer to the first excited state remains to be a dominant excitation mechanism even under short wavelength excitation.

Recently, it has been reported an experimental work where the sensitizing action of the silicon nanoclusters has been done under low-energy optical excitation [312]. In this work, it was found that the PL intensity ratio of $^4I_{13/2}$ - $^4I_{15/2}$ Er^{3+} related transitions with respect to the $^4I_{11/2}$ - $^4I_{15/2}$ transitions is increasing with the increase of excitation energy from 1.9 eV to 2.2 eV where it suddenly saturates.

This was attributed to an increased quantum yield of the $^4I_{13/2}$ - $^4I_{15/2}$ transition in this range of energies. As a physical mechanism behind this phenomenon a photon cutting between two neighboring erbium ions was evoked [312], wher one of these two erbium ions gets excited to higher energetic states via virtual-Auger process [315].

Photon cutting has the advantage that it can also explain the immediate non-resonant excitation of Er^{3+} ions to different excited states. However, in the case of photon cutting, the non-monothonical increase in the direct contribution to the first excited state with decreased excitation wavelength would be expected [312]. From the data presented (see **Figure 50** and **Figure 51**), it becomes clear that the direct contribution increases monotonically following the silicon nanoclusters absorption cross-section [117] while additional increase in erbium related PL emission comes from the Er^{3+} excitation through the higher excited states.

Moreover, the quantum cutting mechanism proposed [312] depends heavily on the inter-ion interaction which has proved to be negligible in the samples under study [297]

In order to get more insight on the processes involved, the study of the dynamics of the second excited state would be rather helpful. However, the analysis of this last is complicated by the weak signal under “red” excitation and by the high background noise due to residual Si-nc emission. Thus, these measurements are inconclusive and, as such, were not reported here.

In conclusion, a systematic study of the energy transfer process in silicon nanoclusters and Er^{3+} co-doped thin films under low energy optical excitation was reported in this section. Profound differences in the fast dynamic of the visible PL with respect to the high energy optical excitation regime were found.

We attribute them to a decrease of the energy transfer efficiency and/or decrease of excitation to higher (than first) excited states of Er^{3+}. We explain this behavior in the framework of the intraband model in terms of sub-bandgap states participation in the energy transfer.

We confirm that the energy transfer to the first excited state of Er^{3+} remains to be a dominant excitation mechanism in the range of considered excitation energies, implying that even with the opening of the new excitation channels, through the higher Er^{3+} excited states, only modest improvements in the efficiency of the Er^{3+} ions excitation should be expected.

3.4.5. Quantitative optical measurements of Er^{3+} doped SRO films

The samples that have been previously studied represent optimized samples (see section I of Appendix to Chapter 3). The energy transfer efficiency in the samples has been monitored by comparative analysis with different samples deposited under different deposition parameters. As a figure of merit high PL intensity (large number of emitters) and long PL lifetime (low number of defect) under non-resonant excitation were considered [275].

The most promising sample in terms of transfer efficiency is chosen as active layer in samples to be studied (sample A).

However, once the optimized material is reached, question arises on how well can this material perform in an actual device. To determine this, a quantitative optical characterization of the optimized sample is needed. An estimate of the optical performance of the material can be obtained by a set of standard PL measurements and comparative analysis with the reference samples with known absolute characteristics. To that end in the present case the sample C from **Table 1** was used. The exact procedure is reported in section IV and V Appendix to Chapter 3. As in the optimized sample there were no traces of cooperative up-conversion [297], a simplified procedure was used (see section IV of Appendix to Chapter 3).

Erbium ions are very sensitive to a number of non-radiative processes (see section 3.1) [264]. Thus, the main question that has to be answered in the case of any erbium doped material is: how many of the incorporated erbium ions are optically active after their incorporation in the host [61,278,296]? Obviously, only the optically active ions may contribute to optical amplification making their quantification essential, prior to the realization of any working device [261,265].

In principle, the estimation of optically active Er^{3+} can be performed by absorption measurements. However, in this case an exact value of Er^{3+} absorption cross section in silicon-rich oxide is required, since the technique allows one to obtain the product $\sigma_{dir}*N_{Er}$ (σ_{dir} is absorption cross-section for the resonant excitation and N_{Er} is the active erbium concentration). Er^{3+} optical transitions are controlled by the host crystal and a modification of σ_{dir} is expected in SRO material with respect to the pure SiO_2. Hence, PL measurements were preferred for initial estimate.

A very thorough characterization of the optically active fraction of erbium ions in sample A is reported in Ref. [296]. It was found in fact a two-fold enhancement of the direct excitation cross-section (at 975 nm) of erbium ions in sample A with respect to the case of pure silica. In addition only 19% of the total erbium content was found to be optically active.

In sensitized material, as the one under study, it is of importance as well to know, how many of the erbium ions can be effectively sensitized? Following the procedure described in the section V of Appendix to Chapter 3, it was found that only 8% of total erbium content in the sample A could be effectively sensitized by silicon nanoclusters.

With the obtained values becomes clear that the potential gain of the waveguide amplifier would be at least 5 times lower than what initially expected, based on the total erbium content.

It is worth to note that the fraction of Er^{3+} sensitized by Si-ncl should not be evaluated only on the base of the total erbium content but as well as a fraction of the

optically active ions. In this case, it is found that 42% of optically active ions can be sensitized. This is not sufficient for the realization of a working device, although it is much higher than what initially considered comparing with the total erbium content.

Thus, it can be hoped that with further material optimisation gain may be achieved if the non-active fraction (81 % of total content) of the erbium ions is not absorbing.

In silica, Er^{3+} do not show optical activity when they are coupled to a quenching centres, but they continue to absorb light even when clusterized [265,266]. On the contrary to the silica case, there haven't been similar characterization works performed on the silicon rich oxide films co-doped with erbium. This is the reason why it becomes important to reveal the role of the non-optically active fraction of erbium ions.

3.4.6. The optical role of non-emitting ions

In order to determine the optical role of non-emitting ions, rib waveguides were produced (see **Figure 52**) and material was studied directly in the waveguide amplifier configuration. The samples under study are similiar to sample A. In addition, a top cladding layer of 1 μm of SiO_2 has been grown. In order to produce mono-modal rib-loaded waveguides with high confinement factor (see **Figure 52**), a dry etching of the top SiO_2 cladding was performed down to 200 nm over the active layer. In this study 5 μm wide waveguides were used (see **Figure 52**).

The optical losses of the waveguides have been determined by means of the cut-back technique (see section VI of Appendix to chapter 3), in the spectral range from 1460 to 1580 nm. A tapered fiber was used to butt-couple the input light, leading to coupling losses of about 4 dB.

The evaluation of the cross section at λ = 1480 nm from the time resolved μPL measurements has been performed following exactly the procedure described in Ref. [296] and thus will not be reported here. The measurements were performed as well at λ = 980 nm and compared with what reported in Ref. [296] in order to assure its accuracy and reproducibility.

Pump and probe experiments were carried out to evaluate the signal enhancement (SE) of a probe signal coupled to the waveguides, when a pump signal is also present [316]. As a probe signal a tunable laser was used and as a pump signal a high power diode laser emitting at λ_{exc} = 1.48 μm (far away from the absorption spectrum of silicon nanoclusters). Both lasers have been combined in a wavelength-division-multiplexer (WDM) fiber, connected to a tapered fiber and finally butt-coupled into the active waveguide. In order to filter out the contribution of the amplified spontaneous emission (ASE) signal related to the pump we have modulated the probe signal and used a lock-in at the detection stage.

As an initial step spectral losses of the waveguide have been quantified. The raw insertion loss spectrum showed the Er^{3+} related absorption peak superimposed to a background that decreases by increasing the wavelength. These background losses values were about 3.0 ± 0.5 dB/cm at λ = 1535 nm and 4.0 ± 0.5 dB/cm at λ = 1480 nm and are associated to passive scattering losses from the Si nanostructures present in the matrix and the matrix itself [317].

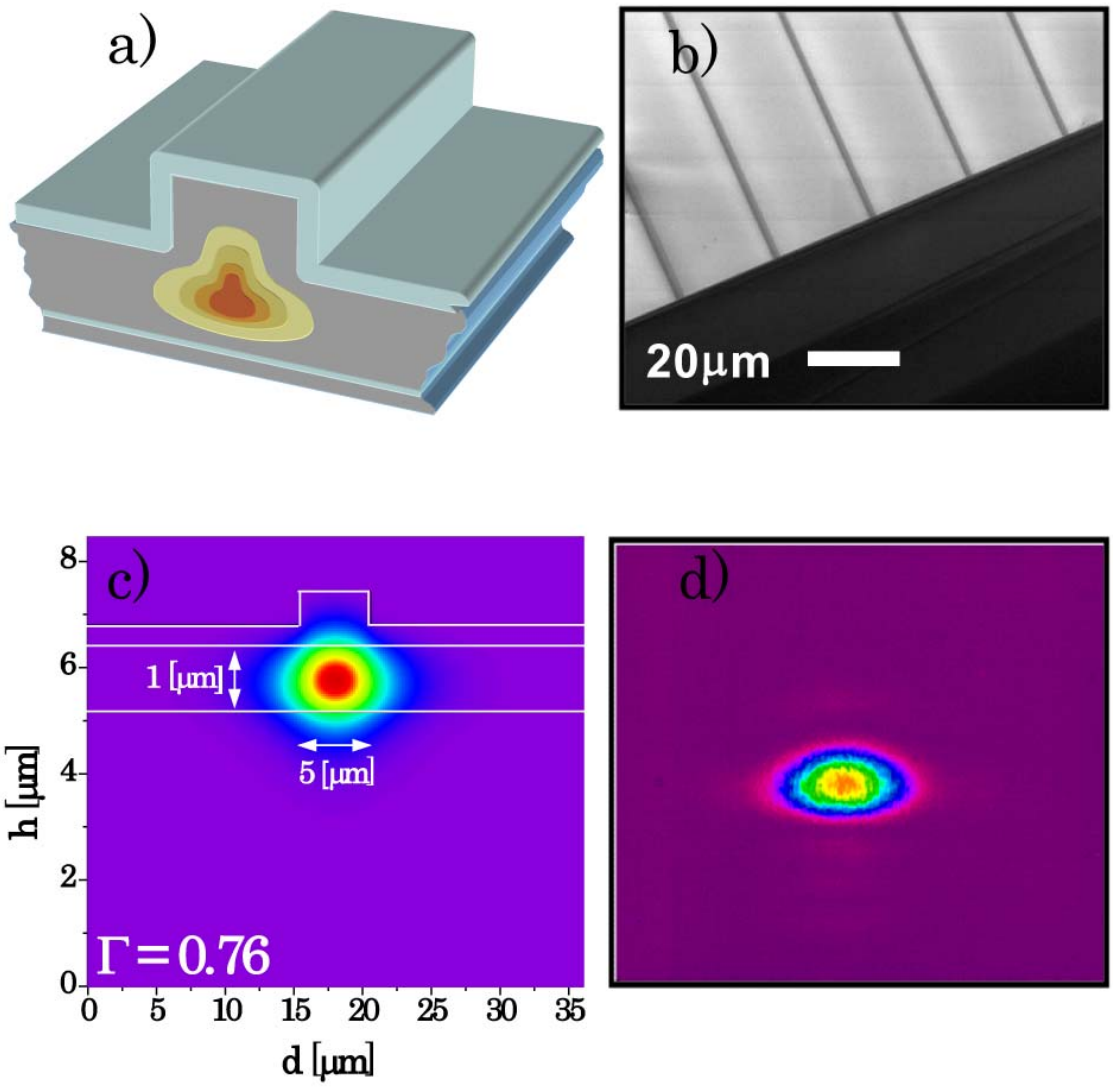

Figure 52 *– (**a**) Example of the rib waveguide structure. From Ref.* [318]. *(**b**) Photo of the sample with defined waveguide structures. (**c**) Simulated mode profile at* λ *= 1535 nm. 2D FMM solver was used. (**d**) Photo of the mode profile at* λ *= 1535 nm.*

In **Figure 53** is shown the result of subtracting these passive losses from the propagation losses, the remaining contribution being that associated to the direct absorption losses (α_{abs}) of Er^{3+}. It is worth to mention that α_{abs} is related to the total Er^{3+} absorbing content (N_{abs}) by the following relation:

$$\alpha_{abs}(dB/cm) = 4.34 * \sigma_{abs} * N_{abs} * \Gamma \qquad (10)$$

where Γ is the confinement factor of the waveguides (Γ = 0.8 as extracted from beam propagation method (BPM) simulations) and σ_{abs} is the absorption cross section at the tested wavelength. It is important to note that the maximum of absorption losses is about 3.5 ± 0.2 dB/cm at λ = 1534 nm. Therefore, if full population inversion is achieved, the internal gain values would compensate for the passive losses and net optical gain of about 0.5 dB/cm would be possible.

It is possible to extract the spectral shape of σ_{abs} by estimating it at a certain wavelength and then using the spectral shape of the absorption losses. This procedure has

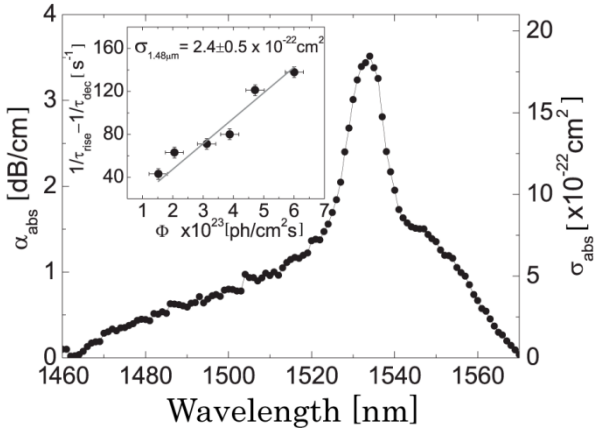

Figure 53 *- Spectral dependence of the absorption losses (left axis) and of the absorption cross section (right axis). (**Inset**) The difference of the inverses of the rise and decay lifetimes, as a function of the excitation photon flux. The gray curve corresponds to the linear fit used to extract* σ_{abs}.

been done at λ = 1.48 μm with high photon flux by time resolved PL measurements following the procedure reported in Ref. [296].

The difference of the inverses of the lifetimes as a function of excitation photon flux is a linear curve whose slope is proportional to σ_{abs} at the pumping wavelength. In the inset of **Figure 53**, these data are presented, providing a value of σ_{abs} (1.48 μm) = 2.4 ± 0.5 x 10^{22} cm^2.

By applying the McCumber theory [61], the emission cross section σ_{em} can be calculated from the absorption cross-section σ_{abs} using:

$$\sigma_{em}(\nu) = \sigma_{abs}(\nu)\exp\left(\frac{\varepsilon - h\omega}{kT}\right) \tag{11}$$

where ε is the average energy of the transition, **k** the Boltzmann constant, and **T** the temperature. The values of emission cross-section σ_{em} (1.48 μm) found is about 4 times lower than σ_{abs} (1.48 μm).

Moreover, from σ_{abs} and Eq. (10) the concentration of absorbing Er^{3+} can be calculated to be N_{abs} = 4.9 ± 1.0 10^{20} cm^3. N_{abs} is slightly higher than the total content measured by SIMS (see **Table 1**), but compatible with this value. Even though there is a sizeable error bar derived from the entire experimental procedure, we can state that most of Er^{3+} absorbs. To determine the concentration of emitting Er^{3+} (N_{em}), pump and probe measurements have been performed. Since excitation is performed at λ = 1.48 μm, it can be assumed an effective two level system to describe the population of $^4I_{13/2}$ level (**N2**) and $^4I_{15/2}$ level (**N1**), being **N1**+**N2** = N_{em}.

In **Figure 54** is shown the profile of the TE mode in the horizontal (**Figure 54a**) and vertical (**Figure 54b**) directions for λ = 1.48 μm (pump) and λ = 1.54 μm (probe) wavelengths as extracted from the beam propagation method (BPM) simulations. The overlap between the pump and the probe optical modes is higher than 98%.

The ratio between the probe signal with the pump on $I_{pump\&probe}$ and the probe signal with the pump off I_{probe} is defined as the SE measured at the output of the waveguide. It will be assumed that the emission and absorption cross sections (σ_{em} and σ_{abs} respectively) are equal, which is reasonable around the maximum of the emission-absorption spectrum [61],

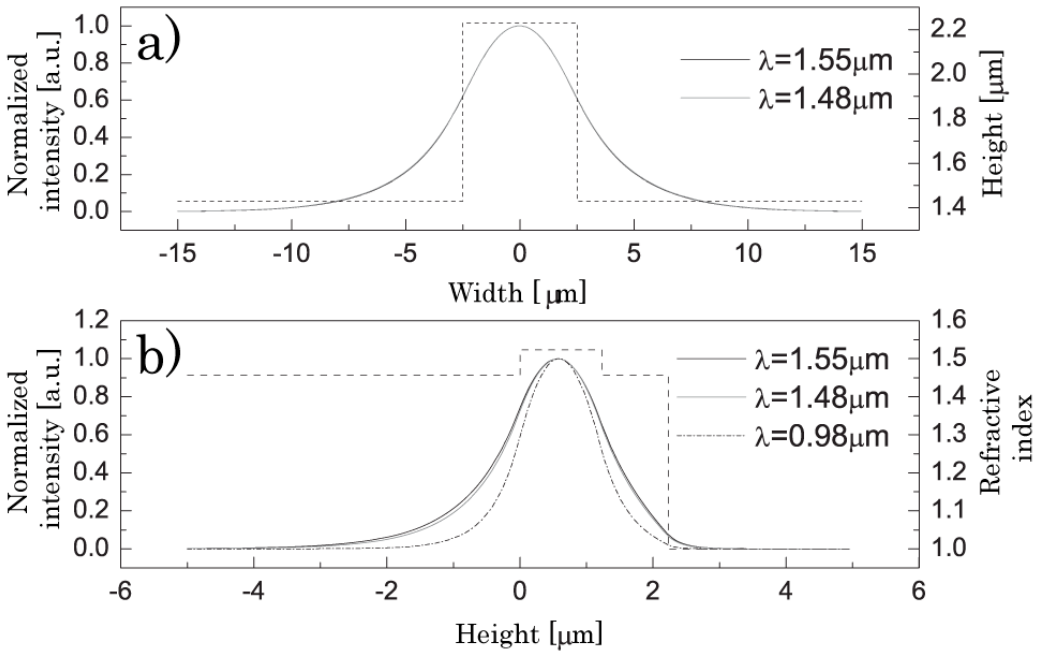

Figure 54 *– (**a**) Horizontal shape of the supported modes at* λ *= 1.54 μm (black) and* λ *= 1.48 μm (gray). The horizontal profile of the waveguide is also shown (dashed line). (**b**) Vertical shape of the supported modes at* λ *= 1.54 μm (solid black), at* λ *= 1.48 μm (gray) and at* λ *= 0.98 μm (dash dotted black). The vertical profile of the refractive index of the waveguide is also shown (dashed line).*

and take into account the stimulated emission contribution at the pump wavelength. Under those conditions SE and internal gain g_{int} are:

$$\begin{aligned} SE &= \frac{\exp((N_2 * \sigma_{em} - N_1 * \sigma_{abs}) * \Gamma * L)}{\exp(-N_{em} * \sigma_{abs} * \Gamma * L)} \\ &\approx \exp(2 * \sigma_{abs} * \frac{\sigma_{exc} * N_{em} * \Phi}{\frac{1}{\tau_d} + 1.25 * \sigma_{exc} * \Phi} * \Gamma * L) \\ &= \exp(2 * g_{\text{int}} * L) \end{aligned} \tag{12}$$

$$g_{\text{int}}(dB/cm) = 4.34 * \sigma_{abs} * \frac{\Phi * \sigma_{exc} * N_{em}}{\frac{1}{\tau_d} + 1.25 * \Phi * \sigma_{exc}} * \Gamma = \frac{G_{\text{int}}}{L} \tag{13}$$

where G_{int} is the total internal gain, τ_d is the decay lifetime of the ${}^4I_{13/2} - {}^4I_{15/2}$ transition, $\sigma_{exc} = \sigma_{abs}$ (1.48 μm) and L is the length of the waveguide. Note that excitation photon flux is reported at the input waveguide facet and decays along the waveguide with approximately 4 dB/cm of loss. For low excitation flux, $\tau_d^{-1} >> \Phi\sigma_{exc}$ and:

$$g_{\text{int}} = \tau_d * \sigma_{abs} * N_{em} * \sigma_{exc} * \Gamma * \Phi \tag{14}$$

is linear in excitation flux.

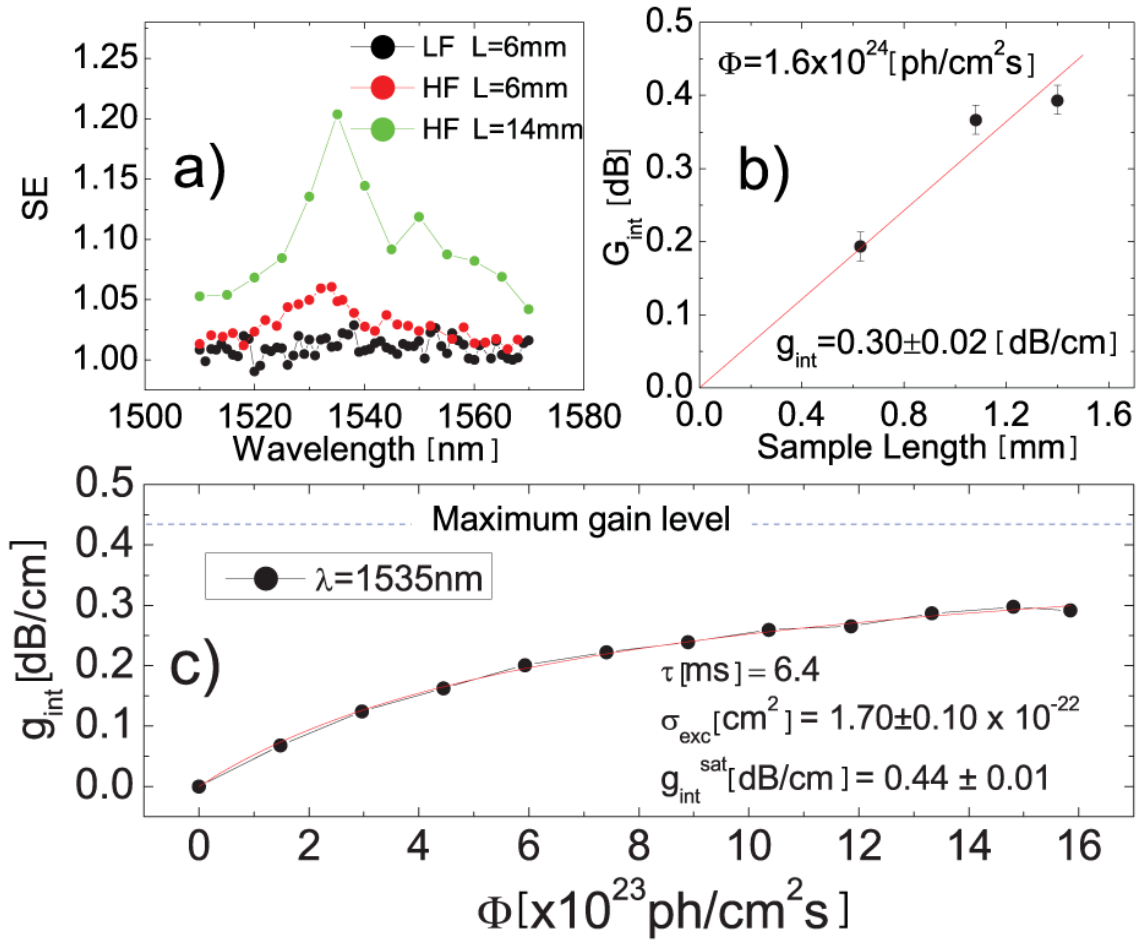

Figure 55[9] *– (**a**) SE of **L** = 6 mm long waveguide at low and high excitation photon flux **Φ** (black and red solid circles respectively) and of **L** = 14 mm long waveguide at high excitation photon flux (green solid circles). (**b**) **G_{int}** for different waveguide lengths at high excitation photon fluxes **Φ**. A linear fit to the data is also shown. (**c**) **g_{int}** as a function of excitation photon flux **Φ** for a waveguide length of **L** = 6mm. A fit using Eq. 13 is also shown.*

In **Figure 55**[9], the spectral dependences of SE for low and high excitation photon fluxes are reported for **L** = 6mm long waveguide (black and red solid circles respectively). By comparing these two measurements it is clear how SE increases with excitation photon flux. For a **L** = 14 mm long waveguide (green solid circles), it is possible to enhance further SE in an almost exponential way, revealing very clearly the Er^{3+} signature.

Figure 55[9] shows **G_{int}** as a function of the waveguide length for the high excitation photon flux. From the linear fit of the data, a **g_{int}** of about 0.3 dB/cm can be extracted. The deviation from the linear behavior is due to pump depletion.

Finally, in **Figure 55[9]** is shown **g_{int}** at **λ** = 1535nm as a function of excitation photon flux for the shortest waveguide. The experimental data present a sub-linear behavior, which

[9] The measurements were performed at University of Barcelona by D. Navarro-Urrios and F. Ferrarese-Lupi.

is a clear indication that saturation is close to be achieved although not yet reached due to pump power limitations. A maximum value of g_{int} = 0.3 dB/cm at Φ =1.6 x 10^{24} ph/(cm^2*s), with an error of less than 5% is found. The experimental points are fitted with Eq. 13, where τ_d = 6.4 ms was extracted from the pure exponential behavior of the $^4I_{13/2} - {}^4I_{15/2}$ PL decay. This value is slightly longer than the one of sample A from **Table 1**.

The fit yields two parameters: σ_{exc} and g_{int} at saturation, g_{int}^{sat}. The best fit is shown in **Figure 55**[9] as a red solid line. For the first fit parameter was found σ_{exc} = 1.7 ± 0.1 10^{-22} cm^2, which is similar to the one derived by the analysis presented in **Figure 53**. The second fit parameter is g_{int}^{sat} = 0.44 ± 0.01 dB/cm, which could be 0.55 dB/cm in the absence of the pump induced stimulated emission. The latter value is just 16 ± 2% of the absorption at the same wavelength **Figure 53**. This is very similar to a value of 19% reported for sample A [296].

From this result, it is straightforward to conclude that most of the Er^{3+} within the matrix is able to absorb but cannot emit light efficiently. Even more, within the approximation of equal absorption and emission cross sections, we could conclude that 84% of the Er^{3+} population cannot be inverted. Moreover, the emitting Er^{3+} population does not suffer from strong cooperative up-conversion mechanisms [297].

Therefore, based on all the previous observations, it can be postulated the existence of two types of Er^{3+} ions: one able to recombine radiatively with long PL lifetime and another surrounded by quenching centers where the radiative recombination probability is extremely small. Reasons for that may be that a big fraction may be placed within the silicon nanoclusters and suffer an efficient Auger back-transfer [270], although this seems less probable in light of presented results and low solubility of Er^{3+} in silicon [278]. Another probability is that they clusterize and suffer from quenching effects.

Indeed, it has already been reporte that erbium ions tend to clusterize in the vicinity of silicon nanoparticle [279–282]. It remains puzzling why this clusterization is not followed by other effects such as cooperative up-conversion [261,265]. This indicates or very inhomogeneous local distribution of erbium ions or very inhomogeneous distribution of the quenching centers.

In any case, the fact that more than 80% of the Er^{3+} acts as absorber is the first indispensible step of knowledge towards a clear understanding of this material, which may allow optimizing the emitting and coupled content beyond the threshold of transparency.

3.4.7. Optical amplification of sensitized erbium ions

As demonstrated in previous section, the main drawback of the studied material is a large fraction of non-optically active ions. These ions contribute to the absorption of light but they do not contribute to the optical amplification. The previous study has been performed under resonant excitation. If the erbium ions are excited trough the silicon nanoclusters even lower fraction of ions should be involved in the optical amplification process, as the fraction of sensitized ions found was even lower than the optically active ones (see section 3.4.5).

In this section, it will be presented the results that confirm this hypothesis, assuring that the most pressing issue of this material is optical activity of erbium ions.

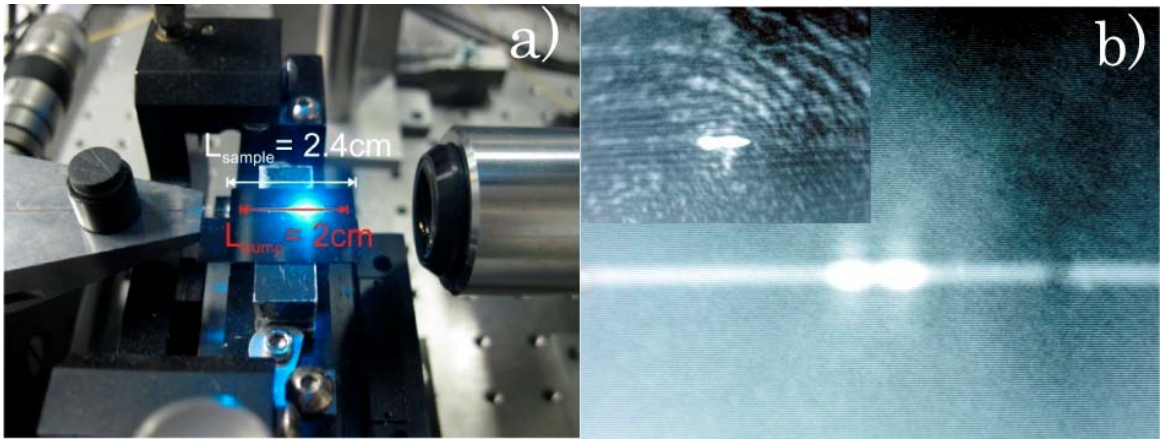

Figure 56 *– (**a**) Photograph of the pump and probe setup. Pumping beam in the form of a long stripe has been aligned along the rib waveguide. (**b**) Amplified spontaneous emission (ASE) under intense excitation (λ_{exc} = 488 nm) can be observed at the output of the waveguide. Double spot indicates multi-mode waveguiding. (**Inset**) Photograph of the probe signal at the output of the rib waveguide.*

Optical amplification measurements have been again performed using the pump and probe measurements on the rib waveguide samples [297,316,317]. Samples were prepared in way analogous to what described in previous section. For the measurements the 20 μm wide waveguides were used. On contrary to the rib waveguides previously used, these waveguides are multimode (see **Figure 56**). Wider waveguide were used in order to facilitate alignment with a pump beam as the measurements configuration has been changed (see **Figure 56**).

When exciting the Er^{3+} trough the silicon nanoclusters, visible or UV pump beam is used. These excitation wavelengths are not suitable for the co-propagating configuration due to different mode overlaps of pump and probe beams and a very strong depletion of the pump flux due to absorption of silicon nanocluster. More suitable configuration is the one where the sample is excited vertically, similar to PL measurements.

To that end, the laser beam is transformed with help of cylindrical lens in a long stripe and focused and aligned along the waveguide, providing uniform excitation along the whole length (see **Figure 56a**). Active films are only μm thick, thus the pump depletion can be considered as negligible. In this configuration, stripe alignment with waveguide becomes an issue, as μm precision has to be maintained over a few cm of length (sample length, **L** = 2.4 cm in present case) justifying the choice of the wider waveguides.

As an excitation, the λ_{exc} = 488nm line of an argon laser was used. This excitation wavelength is resonant with erbium transition but under the photon fluxes used, the main contribution comes from the excitation trough the silicon nanoclusters. As a probe a tuneable laser was used as in previous section. In detection an InGaAs PMT coupled with double monocromator was used in order to spectrally resolve the signal.

When exciting the Er^{3+} ions trough the energy transfer from the silicon nanoclusters, an additional source of optical loss arises originating from excited state population of silicon nanoclusters [297,316]. Study of carrier absorption losses on this material have been performed in Ref. [297,319] and it will not be considered here.

Confinement factor Γ in the multimode waveguide is difficult to estimate as the specific mode excitation depends on the exact input position (input spot size is 2 - 3 μm). In

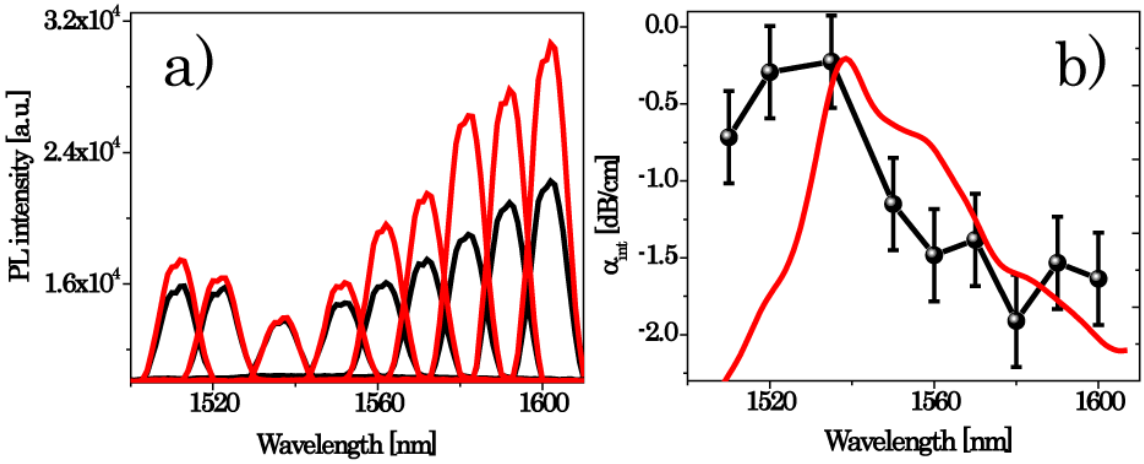

Figure 57 *– (**a**) Spectrally resolved pump and probe measurements with the pump off (red solid line) and pump on (black solid line). Probe signal (probe laser FWHM is* $\Delta\lambda \approx 1pm$*) appears very broad due to a low spectral resolution of detecting instruments used. Excitation photon flux* $\Phi = 2.7 \times 10^{20}$ *ph./(cm²*s) and excitation wavelength* $\lambda_{exc} = 488$ *nm were used. (**b**) Spectrally resolved internal losses (black spheres) measured for excitation photon flux* $\Phi = 2.9 \times 10^{20}$ *ph./(cm²*s) and excitation wavelength* $\lambda_{exc} = 488$ *nm. ASE spectrum is superimposed (red solid line).*

order to maximize the overlap of the probe signal with excited population of erbium ions, probe position was adjusted until the transmitted signal mimicked the amplified spontaneous emission (ASE) output (**Figure 56b**), assuring similar coupling to the waveguided modes. Probe intensity was regulated to match the ASE intensity as well.

For the sake of internal loss estimates, same value of confinement factor as in previous section was used leading to slight overestimate of internal gain value.

Internal (pump induced losses) were define in an empirical way [316,317] as:

$$\alpha_{\text{int}}(dB/cm) = 2 * g_{\text{int}}(dB/cm) = \frac{4.34}{L_{pump}(cm) * \Gamma} * \ln\left(\frac{I_{Pump\&\ probe} - I_{ASE}}{I_{probe}}\right) \qquad (15)$$

Where $\mathbf{L_{pump}}$ is a pump stripe length and $\mathbf{I_{ASE}}$ is ASE intensity. In previous section ASE was eliminated by the use of lock-in amplifier but here it has to be considered as lock-in is not used.

The results of the spectrally resolved pump and probe measurements are reported in **Figure 57**. It can be observed that the probe signal decrease when the pump signal is on. This pump induced optical loss is attributed to carrier absorption [186,297,316]. Obviously, this is a detrimental effect in view of optical amplification that this material should provide.

However, optical losses associated with confined carrier absorption do not show spectrally flat profile, while rather a spectral dependence that resembles the emission shape of erbium ions. This indicates erbium related bleaching of the optical losses and the presence of a modest optical gain.

From **Figure 58**, for the high excitation photon fluxes, it can be estimated approximate internal gain of $\mathbf{g_{int}} = 0.35 \pm 0.2$ dB/cm. At the excitation photon fluxes used,

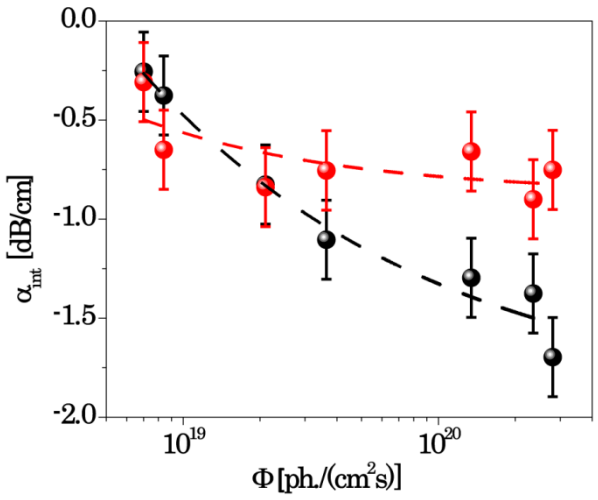

Figure 58 *– Internal loss as a function of the excitation photon flux at* λ *= 1600 nm (black spheres) and* λ *= 1535 nm (red spheres). Dashed lines are guidelines for the eyes.*

Er^{3+} excitation trough the energy transfer could be considered to be already in saturation, thus the value found could be considered as a rough estimate of the maximum internal gain under non-resonant excitation. This value should be scaled down for the correct value of confinement factor Γ which is somewhere between 0.8 and 1, giving approximately half of the value found in previous section, in agreement with the ratio of coupled to optically active fraction of erbium ions (see section 3.4.5). This is additional confirmation that the main drawback in this material is a low fraction of optically active erbium ions.

3.5. Thin Er^{3+} doped SRO films suitable for electrically pumped waveguide amplifiers and lasers

3.5.1. Electrical injection and slot waveguides

One of the main drawbacks of current EDFA technology is that the erbium ions in erbium doped fibers cannot be excited by electrical injection. The reason is that erbium ions are dispersed in the fiber core of typically **d** = 5 μm diameter made of insulating material (silicon dioxide) [61]. Electrical injection in the insulating material is a very challenging task and becomes literary impossible for the μm thick silicate glass.

However, recently there has been a significant progress in the charge injection in SRO [52]. In SRO the charge transport is assisted by the silicon nanoparticles. Interestingly, it was demonstrated that even bipolar injection can be achieved in thin multilayer SRO films where the silicon nanocrystals size is precisely controlled [52]. By co-doping the same material with Er^{3+}, electroluminescence of erbium ions was achieved [63].

However, in order to achieve electrical injection in this material, active films have to be very thin with a typical thickness lower than **d** < 50 nm [52,63]. This is not a problem if the fabrication of the light emitting diodes (LED) is of interest [63], but it is a big issue for

the realization of the waveguide amplifiers and lasers. The main problem is that SRO films of this thickness does not support any guided modes due to the low refractive index (typically **n** = 1.5 - 2.0 [320]). Moreover, in order to achieve electrical injection, thin SRO film has to be in contact with the electrode material characterized with a high refractive index (typically silicon **n** = 3.4 [125]), causing the leaking of light toward the high refractive index material with high optical losses due to doping.

Luckily, optical waveguiding in this configuration can be accomplished by the use of slot waveguides [321,322]. Slot waveguides are a particular type of waveguide structures where thin layer of low refractive index (tens of nm of thickness) material is embedded between two thicker layers of high refractive index material (hundred of nm of thickness) like in a sandwich.

Guided mode is mainly supported by the presence of the two high refractive index layers similarly to a silicon channel waveguide. In addition, due to refractive index mismatch between the central low and the surrounding high refractive index layers, field component perpendicular to the interface between these, is greatly enhanced in the low refractive index part [321].

This structure naturally allows for both electrical injection and optical guiding in very thin films of low-refractive index material [323,324]. However, devices of this type require differently prepared active material with respect to what have been considered previously. Active films have to be very thin (**d** ≈ 50 ns). Thus, the films that were previously considered are incompatible for their higher thickness (**d** ≈ μm). Additional advantage would be if the films could be deposited by any of the more common employed CMOS compatible deposition methods (CVD or ion implantation).

This means that the material optimization has to be redone, as the active material properties can significantly differ when the deposition technique [226,298] or, even, only the thickness is changed [325].

In the following, different deposition techniques will be evaluated firstly on single layers of thin films. Once the optimum deposition technique is individuated, multilayer structure will be studied. The multi-layer films are expected to have the advantage to allow bipolar injection and, consequent, better power efficiency [52], leading to better amplifier performance.

Throughout, the rest of this chapter, thin films made by PECVD, LPCVD, and Silicon ion implantation deposition techniques will be studied[10]. In all cases thin films (single or multi-layer) are deposited directly on the silicon substrate with approximate thickness of **d** = 50 nm. Sometimes, they will be as well capped by a thin layer (~ 150 nm) of poly-silicon in order to mimic slot-like environment.

In this configuration top poly-silicon layer can be used as well as an electrode, allowing for the retrieval of the information of the behaviour of the studied thin film under the electrical injection. In all cases erbium ions are incorporated in films by means of the ion implantation technique.

---

[10] Samples were produced by J.M. Fedeli and his co-workers in LETI facilities, France.

1.1.1. Single layer thin films – reference samples[10]

In this section, it will be presented a short study performed on three reference samples. These samples were produced in order to demonstrate the presence of the energy transfer from silicon nanoclusters to erbium ions in thin samples, evaluate the influence of the silicon excess on erbium concentration profiles and suitability of implantation parameters. Having in mind the very small thickness of the considered films, when ion implantation is used there is a high probability that part of the erbium ions will be present even in the silicon substrate. Thus, the evaluation of the optical role of these ions becomes important as well.

General characteristics of these three reference samples are shortly summarized in the **Table 2**. The reference sample R1 consists only of the crystalline silicon substrate on which no active film was deposited. Active film (SRO) of sample R2 was deposited by PECVD deposition technique, while the thin film deposited on sample R3 is pure silica deposited by LPCVD.

All three samples were shortly annealed following the rapid thermal processing protocol (RTP) at **T** = 900°C for **t** = 5 minutes. RTP is commonly used for the activation and diffusion control of dopants, in manufacturing of electrical devices. In this case RTP annealing served as promoter of partial phase separation in sample R2 and silicon nanoclusters creation. Other two reference samples were treated as well in order to allow direct comparison of sample properties.

As the final goal of this study is realization of the electrically pumped devices, the RTP annealing is very appealing as a possible phase separation promoter in SRO films, since it would greatly simplify the fabrication process. Thus, this type of annealing was tested as well on reference samples in order to evaluate its suitability.

Table 2 *– Reference samples specifications*

Reference samples				
Sample name	**Deposition method**	**Si excess [at. %]**	**Annealing type**	**Post -annealing type**
R1	---	100 %	RTP T = 900°C t = 5 min	RTP T = 900°C t = 5 min
R2	PECVD	13 %	RTP T = 900°C t = 5 min	RTP T = 900°C t = 5 min
R3	LPCVD	0 %	RTP T = 900°C t = 5 min	RTP T = 900°C t = 5 min

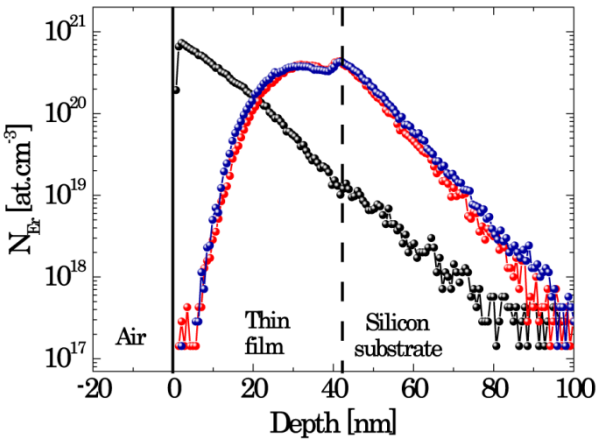

Figure 59[11] *– Er^{3+} ions concentration profiles of samples R1 (black spheres), R2 (red spheres) and R3 (blue spheres). Black solid line represents the samples surface, while the vertical dashed black line represents the position of silicon substrate in samples R2 and R3. Concentration profiles have been obtained by means of SIMS.*

After the thermal treatment, all three samples were implanted with Er^{3+} ions. Ion energy of 40 keV and fluence of 1 x 10^{15} at./cm^2 were used. Finally, all the samples have been thermally treated for a second time using the same thermal treatment in order to partially recover ion implantation damage and optically activate erbium ions [278].

Sample composition was characterized by XPS[11]. Silicon excess determination was done using:

$$Si_{exc} = \frac{[Si] - \frac{1}{2}[O] - \frac{3}{4}[N]}{[Si] + [O] + [N]} \qquad (16)$$

where [Si], [O] and [N] are atomic concentration of silicon, oxygen and nitrogen respectively, as determined from XPS measurements. It was found that the composition of the samples R1 and R3 correspond to composition of pure silicon and pure silica, respectively. For the sample R2 silicon excess of 13 % was found very close to the nominal value of 16 %. Contrary to what expected for PECVD deposited sample, no measurable nitrogen contents was detected in sample R2. Nitrogen was not detected either in samples R1 and R3.

Erbium concentration profiles were analyzed in all three samples by means of SIMS[11] and are reported in **Figure 59**. Erbium concentrations were determined by using a calibration sample of known erbium concentration. For the samples R2 and R3 a thickness **d** = 43 nm was found, a value that is slightly smaller than the nominal one (**d** = 50 nm). Moreover, significant part of implanted erbium was detected in the silicon substrate. Thus, the ion energy has been lowered for the ion implantation of the subsequent samples. Contrary to samples previously studied (thick films), as a consequence of ion implantation of erbium ions, the resulting concentration profiles are not flat.

[11] Structural characterization was performed at University of Barcelona by O. Jambois, B. Garrido and P. Pellegrino.

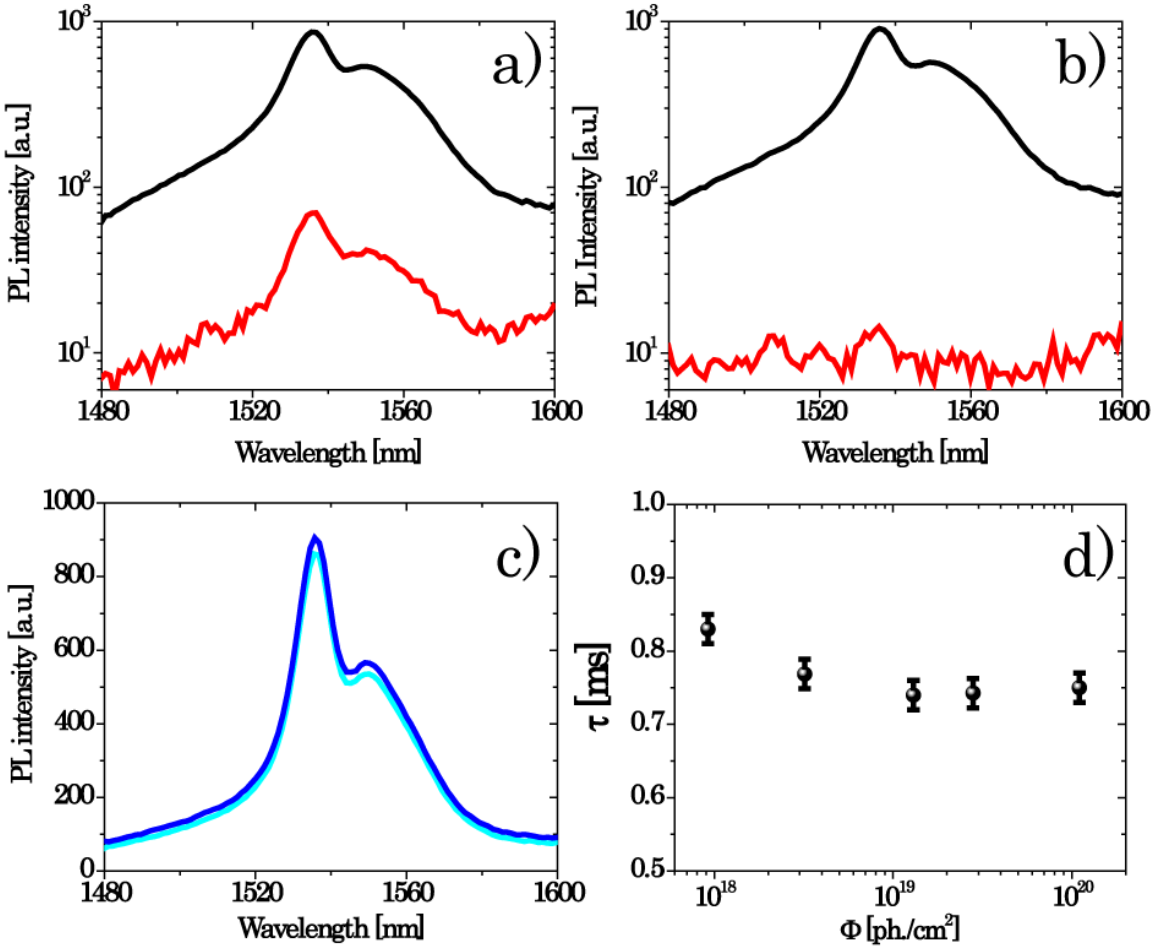

Figure 60 *– (**a**) PL spectra of sample R2 (black solid line) and sample R3 (red solid line) under resonant* λ_{exc} *= 488 nm excitation. Excitation photon flux used was* Φ *= 1.7 x 10¹⁹ ph./cm² (**b**) PL spectra of sample R2 (black solid line) and sample R3 (red solid line) under non-resonant* λ_{exc} *= 476 nm excitation. Excitation photon flux used was* Φ *= 1.7 x 10¹⁹ ph./cm². (**c**) PL spectra of sample R2 under the resonant* λ_{exc} *= 488 nm excitation (cyan solid line) and non-resonant* λ_{exc} *= 476 nm excitation (blue solid line). Excitation photon flux used was* Φ *= 1.7 x 10¹⁹ ph./cm². (**d**) PL lifetime dependence on the excitation photon flux for the sample R2. Non-resonant excitation wavelength* λ_{exc} *= 476 nm excitation was used.*

The maximum of the Er^{3+} concentration has been found in both cases (sample R2 and R3) approximately 10 nm above the silicon substrate. The peak concentration was n_{peak} = 3.9 x 10^{20} at./cm³ for the sample R2 and n_{peak} = 3.8 x for 10^{20} at./cm³ for sample R3. These values of peak concentrations are very similar to erbium concentration used in thick samples (see **Table 1**). However, average concentrations are lower than in previous case being $n_{average}$ = 1.8 x 10^{20} at./cm³. More importantly, by comparing the erbium profiles of sample R2 and R3, it can be observed that the concentration profile is independent of the silicon excess.

Optical properties of these three samples were studied a well. As an excitation source two laser lines of Argon laser were used λ_{exc} = 488 nm (resonant excitation) and λ_{exc} = 476 nm (non-resonant excitation). Detection consisted of InGaAs PMT coupled with a monocromator. Spectral resolution was set to 5 nm due to low signal coming from the very thin samples.

Time resolved measurements were performed with the same setup modulating the laser beam with a mechanical chopper.

Results of PL measurements for samples R2 and R3 are reported in **Figure 60**. Sample R1 is not reported as it didn't show any detectable light for any value of the excitation photon flux (in the limits of experimental setup used) independently of excitation wavelength. This implies that all the erbium ions situated in silicon, including the parts of Er^{3+} ions implanted in the silicon substrate in samples R2 and R3, can be considered as optically inactive and do not contribute to PL emission.

From the **Figure 60a,** it can be seen that under resonant excitation there is only a very weak signal coming from the sample R3, which completely disappears when the excitation wavelength is changed to non-resonant (see **Figure 60b**). Therefore, Er^{3+} related PL emission under non-resonant excitation is completely due to excitation trough the energy transfer from silicon nanoparticles.

This is nicely illustrated in **Figure 60a** where sample R2 shows orders of magnitude higher PL intensity respect to sample R3 under the same excitation conditions. Moreover, Er^{3+} related PL intensity is not disappearing when the excitation wavelength is changed to non-resonant (see **Figure 60b)**, but it is rather growing (see **Figure 60c)**, a characteristic of the energy transfer mediated PL emission (see also **Figure 40**).

PL lifetimes were also monitored for the sample R2 in a range of excitation photon fluxes. The results of these measurements are reported in **Figure 60a**. Very small values for PL lifetime was found $\tau_{PL} \approx 0.75$ ms. Smaller values of PL lifetimes in these samples respect to the thick ones are expected, as the silicon excess is larger changing the refractive index of material [259,260,320] and nanoparticle density [287,288]. Moreover, erbium ions in these films are situated very close to a plane of high refractive index material which provides with a modest Purcell enhancement of radiative rate [326–329]. However, the very low values observed are most probably due to the low matrix quality. This is a consequence of applied thermal treatment which was not sufficient to cure the implantation damage [278].

Small dependence of the PL lifetime was detected as well, indicating possible presence of the cooperative up-conversion process. This is a very different behaviour with respect to previously studied thick films where for similar erbium concentration no signs of cooperative up-conversion were detected.

Summarizing, from this short study of reference samples, it can be concluded that erbium ions in silicon are optically inactive, PL emission under non-resonant excitation is entirely due to energy transfer, erbium concentration profiles are independent of silicon excess and although, the average erbium concentrations are lower than in case of thick films cooperative up-conversion is probably present.

1.1.2. Single layers – deposition technique comparison[10]

The aim of the work presented in this section is a detailed spectroscopic, structural and electrical characterization of thin erbium implanted SRO films with a special emphasis on comparison between different deposition techniques and evaluation of optimum thermal treatment.

To this end a series of samples were prepared[10] by using three different deposition techniques: Plasma Enhanced Chemical Vapor Deposition (PECVD), Low Pressure Chemical Vapor Deposition (LPCVD) and Silicon ion implantation in stoichiometric silicon oxide produced by LPCVD. All the thin films were deposited on p-type CZ silicon substrate (1-50 Ω·cm) while deposition parameters were adjusted in order to produce different silicon excess in the SRO films (see **Table 3**).

After the deposition, all samples were thermally treated to yield phase separation, silicon precipitation and nanocluster formation. The type, temperature and duration of the thermal treatments were varied. In the erbium co-doped samples, erbium was introduced using ion implantation (Dose: 1 x 10^{15} at./cm^2, Energy: 25 keV). Implantation energy was lowered in order to move the concentration maximum towards the sample surface and decrease the percentage of erbium ions in silicon substrate.

Table 3 *– Single layer samples specifications*

Single layer samples				
Sample name	**Deposition method**	**Nominal Si excess [at. %]**	**Annealing type**	**Post annealing type**
SA	LPCVD	12	RTP T = 1100°C t = 5 min	Furnace T = 800°C t = 6 h
SB	Si I. I.	12	RTP T = 1100°C t = 5 min	Furnace T = 800°C t = 6 h
SC	PECVD	12	RTP T = 1100°C t = 5 min	Furnace T = 800°C t = 6 h
SA1	LPCVD	12	Furnace T = 900°C t = 1 h	Furnace T = 800°C t = 6 h
SC1	PECVD	12	Furnace T = 900°C t = 1 h	Furnace T = 800°C t = 6 h
SA2	LPCVD	16	Furnace T = 900°C t = 1 h	Furnace T = 800°C t = 6 h
SC2	PECVD	16	Furnace T = 900°C t = 1 h	Furnace T = 800°C t = 6 h

Resulting erbium concentration profiles should be very similar to what will be presented in following section for multi-layer samples (conclusion based on simulated profiles [12] and TEM images, actual SIMS characterization was not performed on these samples).

After implantation, samples were additionally annealed to recover implantation induced defects and to activate implanted erbium ions [278]. The temperature of the post-annealing process was kept constant among the different samples. Based on the results presented in previous section on the reference samples (see **Table 2**), RTP annealing was discarded and instead furnace post-annealing treatment was applied. Relatively high temperature and long duration was chosen in order to assure as complete matrix recovery as possible after ion implantation, whilst still not interfering with the matrix property (silicon nanoparticles size and crystallinity) defined by the first thermal treatment.

Recently, it was demonstrated that light emitting properties of erbium based material could significantly change inside slot waveguide [328–331] or close to a plane of high refractive index material [259,287,327,332]. This might cause discrepancies between optimization of thin films when they are inserted into slot waveguide. In order to avoid this problem, all samples were covered by a 150 nm thick poly-silicon layer in order to provide a "slot like" dielectric environment.

Another advantage of this approach is that top poly-silicon layer can serve as an electrode allowing for realization of very simple electrical devices such as capacitors. This permits the electrical characterization on the same thin film. An example of this structure is reported as an Inset in **Figure 61b**[13] .

The slot thickness of 50 nm has been chosen as a trade-off between the maximum value for which efficient bipolar injection has been demonstrated [333] and the optimum value for the minimum laser threshold [334]. The maximum net gain (minimum lasing threshold) for single mode operation has been found for a slot thickness of 50-60 nm [334]. The net gain decreases drastically by decreasing the slot thickness imposing the lower limit on the slot thickness considered. Consequently, a thickness of 50 nm seems a suitable choice.

For this slot thickness, the Purcell enhancement [326] of radiative rate should be modest and have only minor effect on the radiative lifetime of the emitters in active film [328–330]. Nevertheless, it has been considered in an empirical way by capping the active region.

The determination of the percentage of the silicon excess was done by means of XPS[11] measurements on monitor samples (data not shown). It was found that in case of silicon ion implantation and PECVD the actual silicon excess agreed with the nominal one within experimental error of XPS technique (± 1%). In the case of LPCVD deposited samples agreement was good for low silicon excess although there might be a few percent of deviation for high silicon excess.

From XPS data obtained on monitor samples it was found as well that the presence of nitrogen in our PECVD samples could be as high as 5-6 at. % while not detectable in the samples deposited by the other two techniques. The presence of nitrogen could offset the

[12] Erbium concentration profile simulations were performed by A. Marconi.
[13] Photograph of capacitor device was taken by E. Rigo.

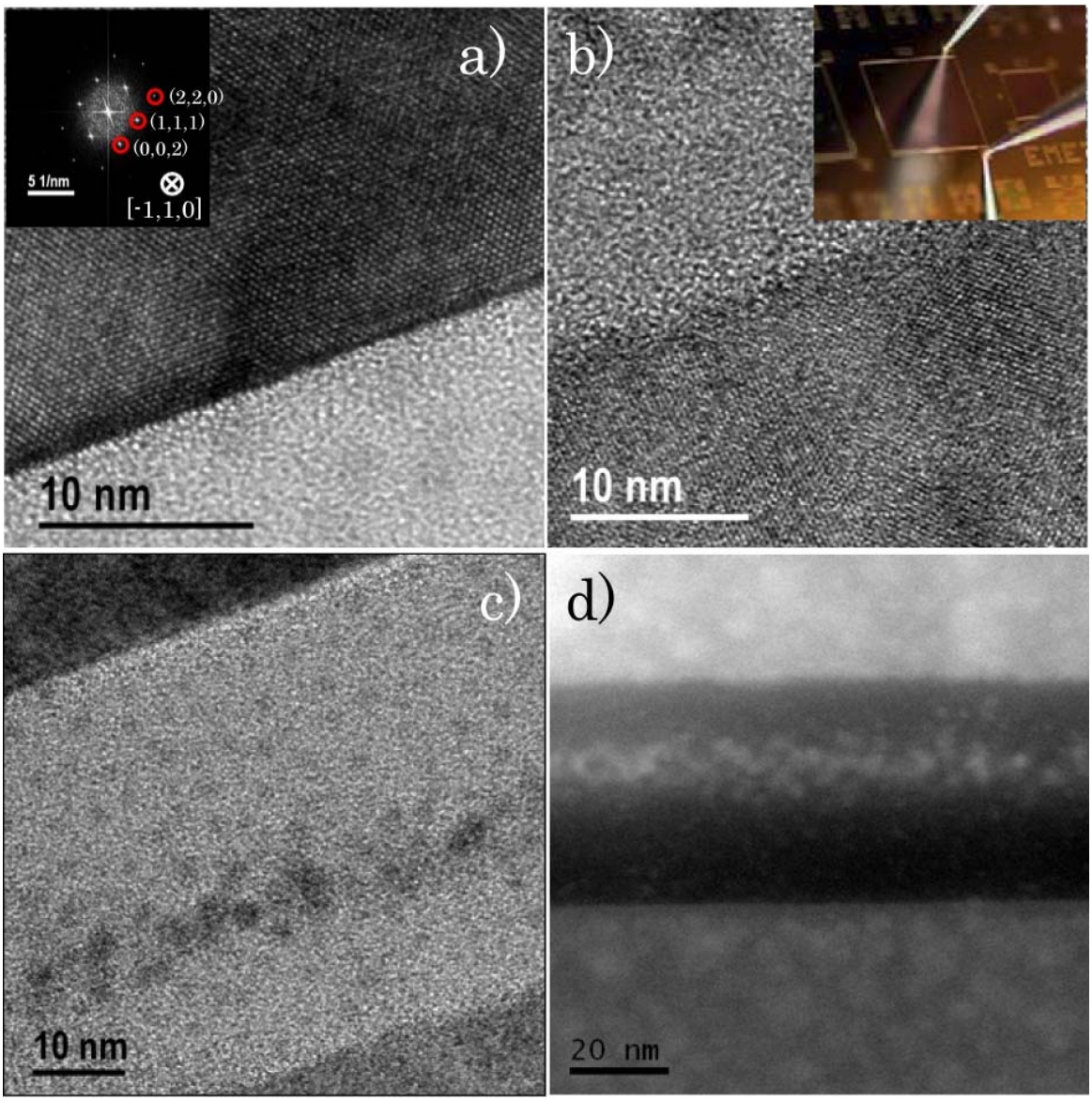

Figure 61[14] *– (**a**) Bright field transmission electron microscope (BF-TEM) image of sample SA2. Sharp interface between the crystalline silicon substrate and the SRO active layer can be observed. Darker spots in SRO layer are silicon nanoparticles. (**Inset**) Diffraction pattern of the crystalline silicon substrate. The observation was done along [-1,1,0] zone axis. (**b**) BF-TEM image of interface between the SRO active layer and the poly-silicon top layer. Increased roughness with respect to panel (**a**) can be observed.(**Inset**)*[13] *Photograph of the un-biased capacitor device formed by poly-silicon cladding of the active layer. (**c**) High resolution TEM (HR-TEM) image of SRO active layer. Silicon nanoclusters can be observed as darker spots. Very dark spots in the bottom part are due to erbium cluster formation. (**d**) High-angle annular dark field scanning transmission electron microscope image (HAADF-STEM) of SRO active layer confirming the origin of the very dark spots observed in panel (**c**) as erbium clusters.*

silicon mobility thus requiring higher annealing temperatures to form the silicon nanoparticles and slowing down the matrix restructuring [226,335].

Although, the exact knowledge of the size, density and fraction of clustered silicon is certainly of great help in order to study the energy transfer efficiency, and micro-structural evolution of deposited films, studies of this type become impractical when a large number of samples is considered. Thus, in this section a more phenomenological approach will be employed.

It has been shown recently [226,273,276,300] that the size, density and percentage of clustered silicon in samples produced by different deposition techniques influence strongly the light emitting properties of silicon nanoclusters. Therefore, spectroscopic methods can be used to evaluate the quality of the produced materials. This is reasonable as the optical performance of active material is of main interest.

Detailed structural analysis will be performed on one sample, in order to determine the basic structural properties. Then samples that differ only for the local environment of erbium ions will be compared. As a figure of merit, it will be monitored the erbium ions emission excited by non-resonant excitation, i. e. via energy transfer from the Si-nc.

Results of TEM imaging of sample SA2 is reported in **Figure 61**[14]. It can be observed a very sharp interface between active layer and silicon substrate (see **Figure 61a**), while the roughness is higher on the interface between SRO and poly-silicon (see **Figure 61b**). Low interface roughness is important as it may be source of significant optical losses [324,336].

Thickness of approximately **d** = 52 nm was estimated for sample SA2, a value very close to a nominal value of **d** = 50 nm. Silicon nanoclusters presence in active material could be observed in **Figure 61c** with quite uniform density across the whole layer depth. Observed nanoclusters are probably amorphous in nature, having in mind the low temperature annealing of this sample. In order to infer more information on the crystallinity degree of the observed nanoparticles, energy filtered TEM imaging was performed on the same sample. However, due to a low contrast, these measurements were inconclusive.

In **Figure 61c** and **Figure 61d** very dark spots can be observed, attributed to a presence of erbium clusters in the active material. This was confirmed as well by EFTEM and electron energy loss spectroscopy (EELS) (data not shown). Visible erbium clustering layer begins approximately 15 nm from the SRO/poly-silicon interface and spans for ~11 nm in depth.

The appearance of the erbium clusterization is also detrimental effect and it will most certainly influence negatively the material performance. The presence of erbium clustering is usually accompanied with inter-ion interaction and cooperative up-conversion [61,261,264–266,278] explaining the PL lifetime dependence observed on reference sample R2 (see **Table 2**).

Continuous photoluminescence (CW PL) measurements were performed using the lock-in technique, with the λ_{exc} = 476 nm line of an Argon ion laser, which is not resonant with any erbium optical transition. Time resolved photoluminescence (TR PL) measurements were done by modulating a laser beam with a mechanical chopper at high frequency. The detection system consisted of: spectrograph coupled to InGaAs PMT and photon counting

[14] TEM imaging was performed by J.M. Rebled, Ll. López, S. Estradé and F. Peiró at LENS, MIND-IN2UB, University of Barcelona, Spain.

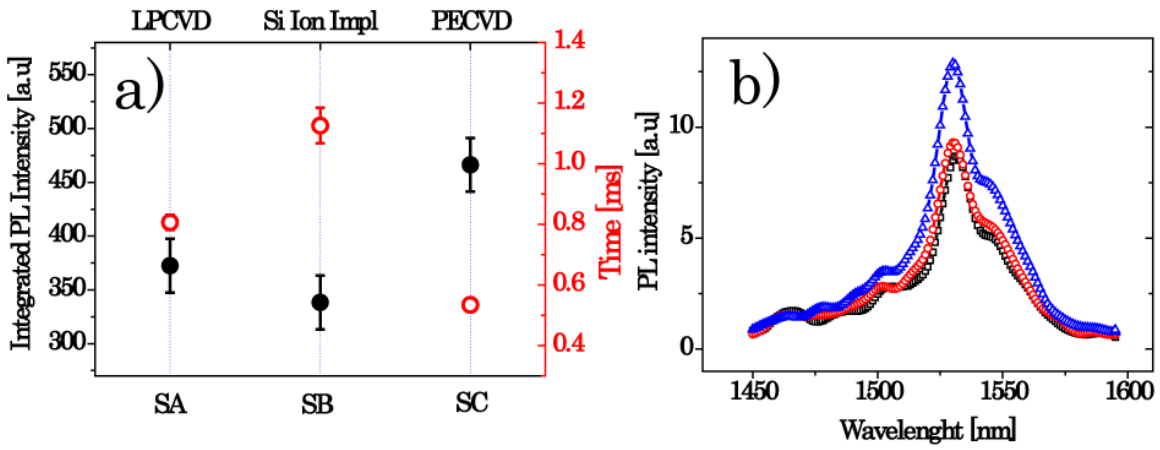

Figure 62 *– (**a**) Integrated PL intensity (solid black circles) and PL lifetime (empty red circles) of $^4I_{13/2} - {}^4I_{15/2}$ erbium transition for the samples SA, SB and SC (see **Table 3**) under non-resonant (λ_{exc} = 476 nm) excitation and excitation photon flux Φ_{exc} = 4 x 10^{20} ph./cm^2.(**b**) PL spectra of the $^4I_{13/2} - {}^4I_{15/2}$ erbium transition of samples SA (empty black squares), SB (empty red circles) and SC (empty blue triangles) under same excitation conditions as in panel (**a**).*

unit. CW and TR PL measurements were performed at the same photon fluxes (Φ_{exc} = 4 x 10^{20} photons/cm^2).

In order to evaluate the suitability of different deposition technique in producing high quality thin films, three nominally equal samples were produced by different techniques and analyzed (sample SA, SB and SC in **Table 3**). All of three samples were implanted by the same erbium dose and thermally treated in the same way (RTP annealing). Higher temperature RTP annealing was chosen as lower temperature RTP annealing yielded quite poor reference sample. A lower Si excess was chosen (12 at. %).

Typical IR PL spectra and decay constants are shown in **Figure 62**. Decay constants are of the order of milliseconds, somewhat shorter than what reported previously for thick samples.The best sample in terms of PL intensity is the one deposited by PECVD. The same sample shows also the fastest decay and highest sensibility to a change in annealing conditions (**Figure 63a, Figure 62a** and **Figure 63b** were obtained under same conditions and can be mutually compared). This could be an indication of a partial phase separation and consequent lower matrix quality due to incorporation of nitrogen during the deposition process [226,335] .

Most of the difference in the PL intensity between these three samples could be simply attributed to a difference in the decay constants.The longest decay time is observed for samples deposited by silicon ion implantation. Although, this sample was twice implanted (first by silicon ions and subsequently by erbium ones) the post-annealing treatments applied was sufficient for the complete matrix recovery.

Since for electrical injection, multilayer Si-nc/SiO_2 films have better properties in terms of low turn-on voltage of electroluminescence [52,333] and since silicon ion implantation is not suitable for multilayer sample production, additional attention is focused only on PECVD and LPCVD samples. In particular, another type of annealing (furnace annealing) was studied while varying the Si excess in the samples.

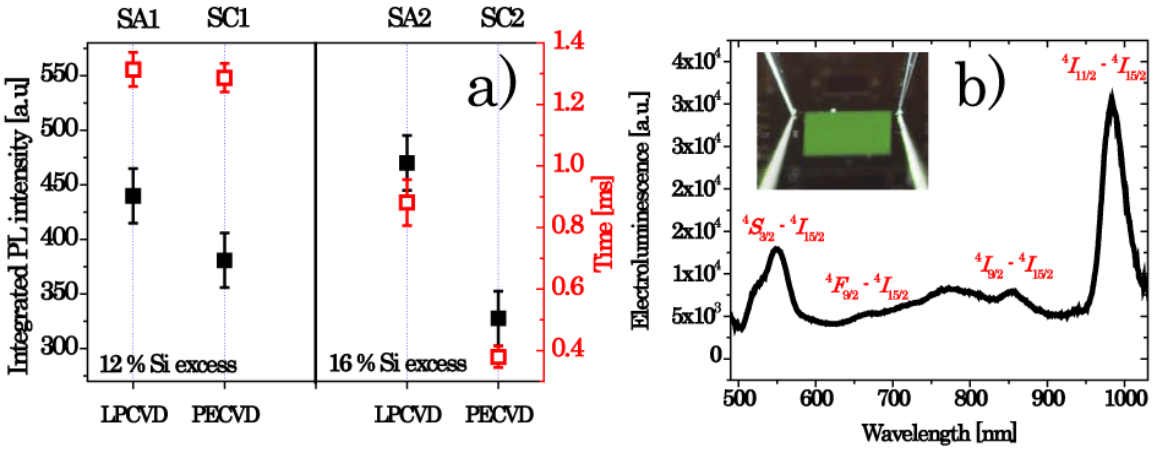

Figure 63 *– **(a)** Integrated PL intensity (solid black squares) and PL lifetime (empty red squares) of $^4I_{13/2}$ – $^4I_{15/2}$ erbium transition for the samples SA1, SC1, SA2 and SC2 (see **Table 3**) under non-resonant (λ_{exc} = 476 nm) excitation and excitation photon flux Φ_{exc} = 4 x 10^{20} ph./cm². **(b)**[15] Visible EL spectrum of sample SA1 capacitor under bias voltage of 38 V. Series of erbium related transition could be observed. **(Inset)**[13] Photograph of the biased device.*

The results presented in previous section on the reference samples on the influence of silicon excess on erbium concentration distribution, suggests that the difference in light emitting properties among the different samples is mainly due to a different silicon and erbium clusterization , erbium ions – Si-nc interaction and local environment of erbium ions.

The furnace annealing at 900°C for 1 h was found to be the most suitable annealing for the thick samples studied previously. In the case of the thin samples with 12 at. % of silicon excess, furnace annealing at 900°C seems to be beneficial with respect to RTP annealing especially in the case of the LPCVD sample (SA1) (see **Figure 62** and **Figure 63**). Both, SA1 and SC1 samples show similar PL intensities while decay constant reached the level of the sample SB indicating much better matrix quality. With the same annealing and increased silicon excess, degradation in light emitting properties is observed. The decay constants diminish in both samples (SA2 and SC2), while in sample SC2 PL intensity decreases as well.

Based on the results presented, oxide matrix quality is of key importance. The decay constants in our samples indicate good oxide quality and weak non-radiative recombinations. Best results are found for samples where erbium ions are in impurities free (nitrogen-free) stoichiometric SiO_2, which is the case of silicon ion implantation and LPCVD; LPCVD being more suited for multilayer approach.

It seems that higher silicon cluster densities impact negatively on light emitting properties of erbium ions. These results agree well with what was recently found on similar materials [298]. The same decrease in performances is observed when the partial phase separation is less complete which is probably the case of RTP annealing. For this reason, furnace annealing (on a longer time scale) looks more appropriate with respect to rapid

[15] Electroluminescence measurements were performed by A. Marconi, A. Tengattini, A. Anopchenko, O. Jambois, Y. Berencén and J.M. Ramiréz.

thermal annealing to get a complete phase separation.

This was confirmed as well by the analysis of emission properties of active films under electrical excitation[15]. Furnace annealing and lower silicon excess were found beneficial for erbium emission under electrical excitation.

As reported in **Figure 61**, erbium clusters were observed in the sample SA2 implying a good possibility of cooperative up-conversion in these samples. However, no visible peaks due to erbium related transitions were observed in visible under optical pumping. Quantitative optical measurements were not possible as the poly-silicon tope cladding does not allow for a precise excitation photon flux estimate.

However, under DC electrical excitation (see **Figure 63b**[15]) erbium related transition become visible across the visible range indicating the possible presence of cooperative up-conversion. Under the electrical bias conditions in question (V_{bias} = 38 V) erbium ions are excited by impact ionization of injected carriers with possible large energy (few eV) and, consequently, can be excited to a very high excited states from which they de-excite radiatively similarly to what happens in cathodo-luminescence [277,302]. Thus, the observation of erbium related visible peaks across the visible range still cannot be taken as a definitive proof of cooperative up-conversion presence in the samples.

1.1.3. Multi-layer samples

There are basically two different physical mechanisms that could be exploited for the erbium ions excitation in the SRO material under electrical bias. Er^{3+} ions can be excited directly by the impact ionization of "hot" (energetic) carriers injected in SRO matrix [63] or by an energy transfer from the excited silicon nanoparticles [298,337]. The second mechanism is especially attractive when bipolar injection (carrier tunnelling) in silicon nanoparticles is achieved [52,175].

If the impact ionization is considered as a principle Er^{3+} excitation mechanism, energy transfer properties of the active material become largely irrelevant as the excitation cross-section for the erbium ions under these excitation conditions is of the same order of magnitude as the one of silicon nanoparticles [338–340]. Thus, the silicon nanoparticles could lose their role as sensitizers and serve mostly to increase the conductivity of the surrounding matrix, allowing also for improved device stability under "hot" carrier injection with respect to a pure oxide.

In the single layer samples under DC electrical injection impact ionization could be the dominant excitation mechanism [63,340], making the optical study of energy transfer efficiency of secondary importance. Although, the presence of the energy transfer opens an additional route to erbium ions excitation, net improvement would probably be of the same order of magnitude.

Situation is very different when the multi-layer samples are considered, since in the multi-layer samples bipolar injection has been demonstrated [52,333]. The main advantage of this type of electrical injection is that the carriers are injected by tunnelling with a very low onset voltage for electroluminescence and consequently high power efficiency [333]. That translates in low device degradation and long term stability of performance of the device which is the main requirements for commercial use.

In the multi-layer samples, carriers tunnel in silicon nanoparticles, while the injection in surrounding insulating matrix (SiO_2) is mostly inhibited by their low energy (low voltages). Under these conditions, erbium ions excitation by means of impact ionization becomes negligible, leaving the energy transfer as the only remaining excitation path. This situation becomes practically the electrical analogue of the non-resonant optical excitation. Evidently, given the peculiarity of ions excitation in these circumstances, optical study of the energy transfer efficiency provides crucial information on the optical performance of the active material.

In this section, it will be presented detailed study of the erbium doped multi-layer SRO/SiO_2 samples. The main accent will be focused on the results obtained by spectroscopic means which will be combined with additional information gathered from structural and electrical analysis.

For the sake of clarity, a study of only four multi-layer samples (see **Table 4**) will be reported in this section similarly to the case of thick samples (see section 3.4). One type of multi-layer structure (see **Figure 64a**) and two different annealing treatments (see **Table 4**) were chosen resulting in amorphous and crystalline nanoparticles. In addition, samples not implanted with erbium were provided as reference.

Multi-layer samples considered here were deposited by LPCVD[10]. LPCVD was found to be the most suitable deposition technique for multi-layer samples based on a study presented in section 1.1.2.

Table 4 *– Multi-layer samples specifications*

Multi-layer samples				
Sample name	**Deposition method**	**Erbium implantation**	**Annealing type**	**Post annealing type**
MA	LPCVD	Yes	Furnace T = 900°C t = 1 h	Furnace T = 800°C t = 6 h
MB	LPCVD	Yes	Furnace T = 1000°C t = 1 h	Furnace T = 800°C t = 6 h
MA1	LPCVD	No	Furnace T = 900°C t = 1 h	Furnace T = 800°C t = 6 h
MB1	LPCVD	No	Furnace T = 1000°C t = 1 h	Furnace T = 800°C t = 6 h

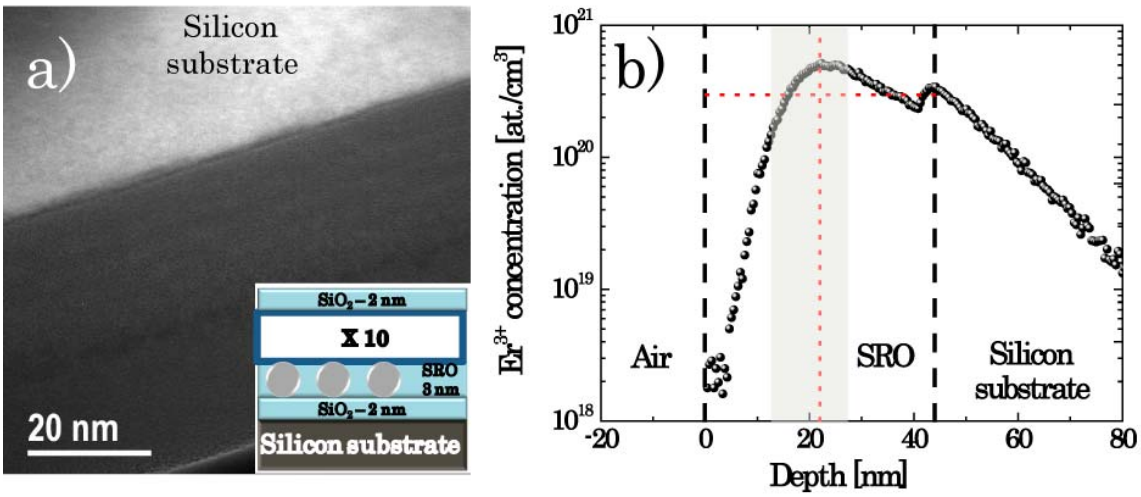

Figure 64 *– (**a**)[14] BF-TEM image of the sample MA (see **Table 4**). Multi-layer structure can be observed in the SiO_x layer. Bright lines correspond to SRO layers. Dark spots in the middle of SiO_x layer are clusterized erbium ions. (**Inset**) Schematic of the multi-layer structure. Thin (**d** = 2 nm) SiO_2 is deposited on silicon substrate and top of multi-layer stack, serving as buffer and top cladding layer respectively. In between, **d** = 3 nm thin SRO (20 at. % of nominal silicon excess) layers are alternated with **d** = 2 nm SiO_2 layers. Total of 10 periods was used resulting in overall nominal thickness of **d** = 52 nm. (**b**)[11] Semi-log plot of erbium concentration profile in sample MB (see **Table 4**) obtained by SIMS. Implantation dose of 1 x 10^{15} at./cm^2 and ion energy of 20 keV were used. Erbium concentration profile is clearly asymmetric, although better centered in active material with respect to the high energy implant reported in **Figure 59**. Thick vertical dashed lines indicate interfaces between air/SRO and SRO/ silicon substrate. Vertical dotted red line corresponds to peak Er^{3+} concentration (n_{peak} = 5.2 x 10^{20} at./cm^3) and horizontal dotted red line to an average Er^{3+} concentration in active layer ($n_{average}$ = 2.9 x 10^{20} at./cm^{-3}). Shaded area corresponds to a layer in which erbium clusterization is visible in TEM images.*

Multi-layer structures consist of a **d** = **2** nm thin silicon dioxide layer deposited on crystalline silicon wafer on top of which is deposited a **d** = 3 nm thick SRO layer with nominal silicon excess of 20 at. % forming the first period of the multi-layer structure (see **Figure 64a**). This particular combination of silicon excess and layer thicknesses for the multi-layer samples was chosen in order to mimic structures in which high power efficiency and bipolar injection was demonstrated [52,333].

The structure period was repeated 10 times in order to reach the desired thickness of **d** ≈ 50 nm for optimum performance in slot waveguide amplifier, as discussed in previous section [334]. Finally, the multi-layer structures were capped with **d** = 2 nm of silicon dioxide in order to make them symmetric.

The multi-layer samples considered in this were not capped with polycrystalline silicon top cladding while the nominally equal samples with top poly-silicon electrode were produced for electrical characterization. Samples without the top cladding allow for quantitative spectroscopic analysis.

After the active material deposition, samples were thermally treated in order to induce the phase separation and nanoparticle growth and formation. Based on the results presented in previous section, samples MA and MA1 were thermally at $T_{annealing}$ = 900°C for **t**

= 1 h which was found to be the optimum annealing treatment in terms of maximum erbium PL intensity and longest PL lifetime under non-resonant excitation (confirmed on the series of multi-layer samples, data not shown). This type of thermal treatment is expected to lead to the formation of amorphous nanoclusters, similarly to the case of thick samples [271,300].

The samples MB and MB1 were treated at higher temperature. This allows for comparison of energy transfer efficiency as a function of nanoparticle crystalllinity degree (see section 3.4.2).

Subsequently, the samples MA and MB were implanted with erbium ions and thermally treated for the second time. Post-annealing treatment analogue to the single layer samples was employed. Samples without erbium (MA1 and MB1) were thermally treated in same manner, in order to allow for direct comparison with erbium implanted samples.

Photoluminescence measurements were done employing the three different lines of Argon ion laser: λ_{exc} = 488 nm (resonant), λ_{exc} = 476 nm (non-resonant) and additional line in UV λ_{exc} = 361 nm for the CW visible PL measurements. For the resonant excitation, laser diode emitting at λ_{exc} = 974 nm was used as well. At this wavelength silicon nanoparticles absorption could be considered as negligible. TR PL measurements in infrared were performed by modulating the laser beam with mechanical chopper in the case of excitation with the Argon ion laser, or by modulating the diode driving current by an external function generator in the case of excitation with the laser diode.

TR PL in visible were done using as the excitation the third harmonic of a Nd:YAG laser (λ_{exc} = 355 nm, 6 ns pulses, 10 Hz). As detection in visible, GaAs PMT (CW PL) or streak camera (TR PL) were used and InGaAs PMT for the IR (both CW and TR PL measurements). In the case of TR PL measurements in IR InGaAs PMT was interfaced with multichannel scalar. In all cases before detection, optical signal was spectrally filtered with monocromator.

The TEM[14] image of sample MA is reported in **Figure 64a**. Multi-layer structure in active layer can be seen, although the contrast between the SRO (bright lines) and oxide layer is quite weak. Moreover, it seems that the structure is better expressed closer to the silicon substrate.

The two multi-layer samples (MA and MB) were implanted with erbium (Dose: 1 x 10^{15} at./cm^2 and Energy: 20 keV). Erbium concentration profile for the sample MB is reported in **Figure 64b**. The peak concentration of n_{peak} = 5.2 x 10^{20} at./cm^3 is located approximately **d** = 22 nm from the sample surface. The concentration profile is clearly asymmetric due to vicinity of the silicon substrate which acts as effective stopper layer for the ion energies in question (see **Figure 59**), but the maximum of concentration is quite precisely positioned in the centre of active layer, in contrast to what observed for the single layer reference samples implanted with higher energy (see **Figure 59**).

Maximum Er^{3+} concentration in these samples is higher than the one found in the thin reference samples with higher energy implantation (see section 1.1.1 and **Figure 59**) or thick samples (see **Table 1**). Average erbium concentration was determined to be $n_{average}$ = 2.9 x 10^{20} at./cm^{-3}, a value slightly lower than the one of thick samples (see **Table 1**). Influence of the matrix state determined by the first annealing treatment and the type of post-annealing treatment on the erbium concentration profiles was monitored as well (data not shown). No visible differences were found in agreement with expected low erbium diffusivity in this type of matrix [274,341]. This implies as well that in different samples only the local environment of erbium ions changes [277,342,343].

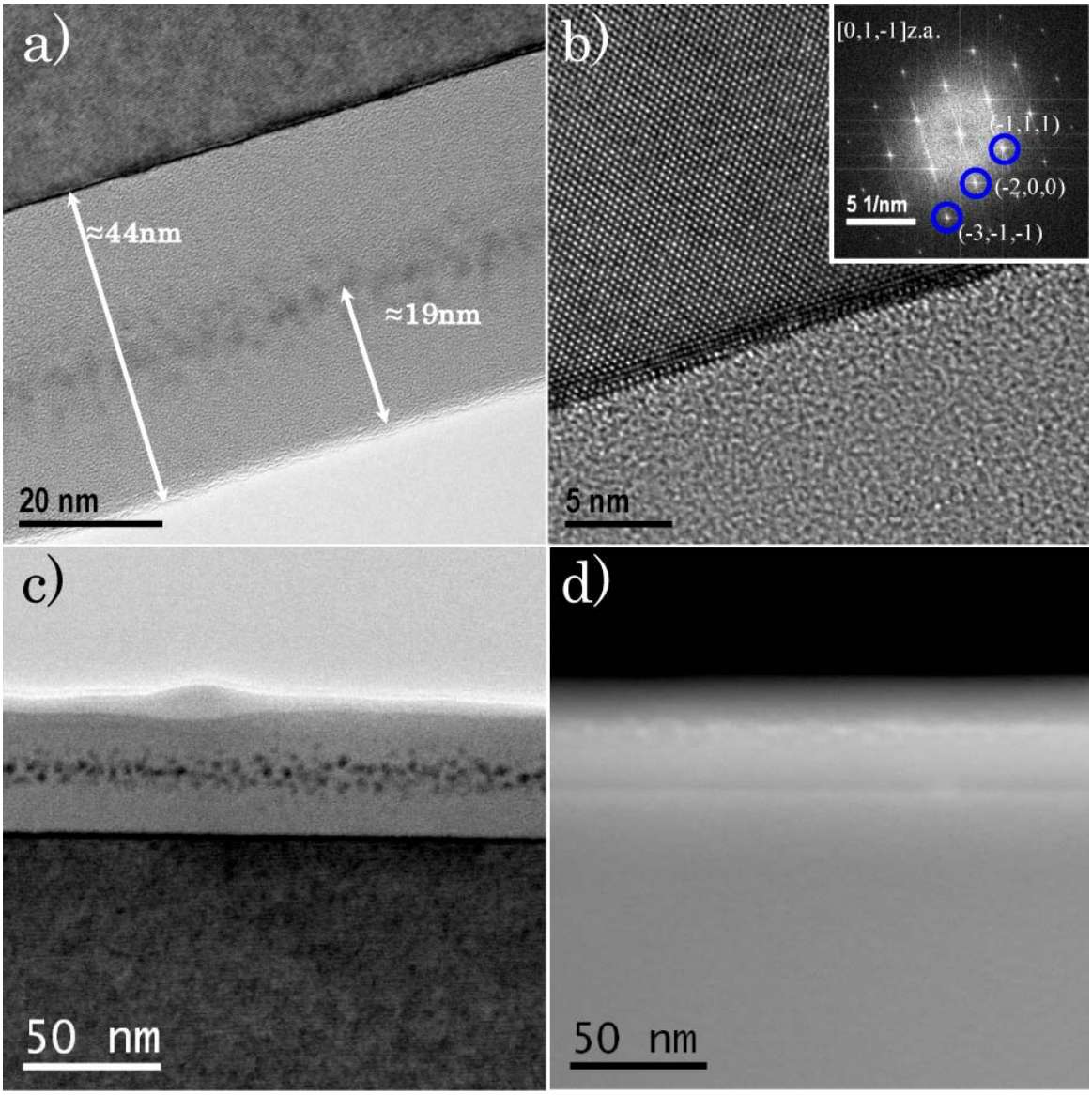

Figure 65[14] *– (**a**) BF-TEM image of sample MA. SRO layer thickness is approximately **d** ≈ 44 nm. Dark spots situated in the approximate centre of SRO layer are erbium nanoclusters. Erbium cluster layer is situated at **d** ≈ 19 nm under the sample surface and extends for 10-15 nm. (**b**) HR-TEM image of the interface between SRO layer and crystalline silicon substrate in sample MA. Smooth interface with low roughness between two materials can be observed. (**Inset**): Diffraction pattern of the crystalline silicon substrate. The observation was done along [0,1,-1] zone axis. (**c**) BF-STEM image of sample MA. Erbium clustering (dark spots) is evident in the central part of SRO layer. (**d**) HAADF-STEM image of the same sample confirming the origin of dark spots in centre of active layer as erbium clusters.*

The average silicon excess was controlled with XPS measurements performed on the sample MB. From the composition of the multi-layer structure, a nominal silicon excess of 11 at. % was expected while the actual silicon excess was slightly lower (9 at. %).

Thickness of the active material was determined by TEM imaging. For the sample MA approximate thickness of **d** ≈ 44 nm was found, while for sample MB thickness was **d** ≈ 40

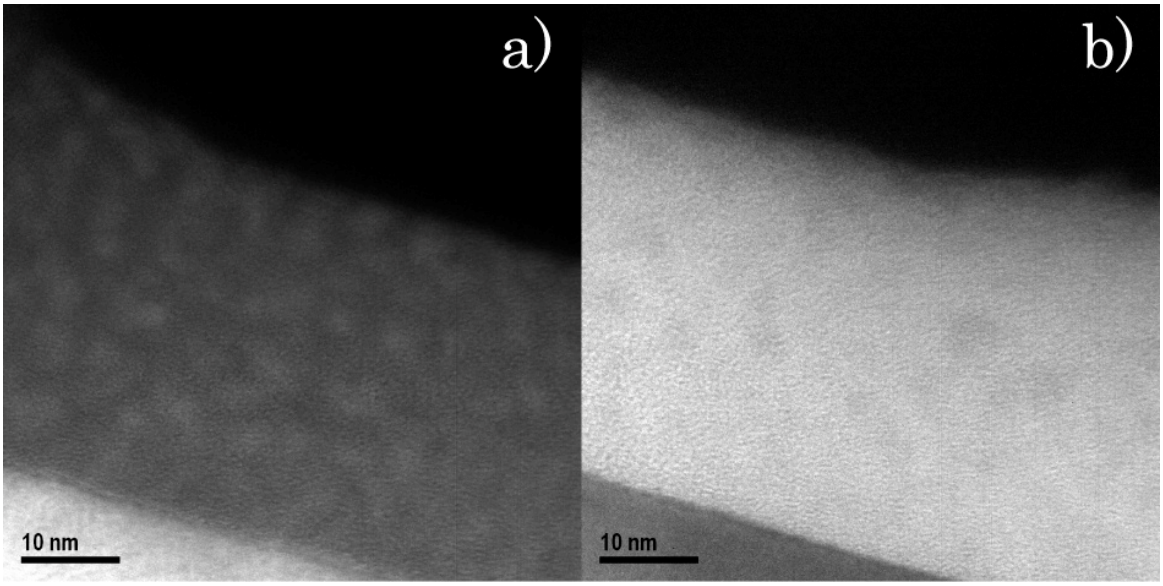

Figure 66 *– (**a**) EF-TEM image of sample MB. Image was filtered at 15 eV (crystalline silicon plasmon peak) with 5eV wide energy window. Bright spots are silicon nanocrystals. (**b**) EF-TEM image of the same sample. Image was filtered at 23 eV (SiO_x plasmon peak) with 5 eV wide energy window. Bright spots are due to amorphous silicon nanoclusters. Darker spots in both panels are due to erbium clusters.*

nm (see **Figure 65a**). These values are very similar and slightly lower than the nominal ones. The difference is attributed to compacting of the SRO multi-layer structure upon annealing [52,333,344].

Interface between SRO layer and crystalline silicon substrate was found to be very smooth in all cases (see **Figure 65b**) similarly to the case of single layer samples (see **Figure 61**). This is very important as the roughness at the interface may be source of significant optical losses when optical waveguiding is considered [345–348] .

In both samples (MA and MB), erbium clusters are clearly visible (see **Figure 65**). Their origin has been confirmed in both samples by EF-TEM (**Figure 66**), HAADF-STEM (see **Figure 65d**) and EELS (not shown). In sample MA cluster layer is positioned at approximately **d** ≈ 19 nm under the sample surface (see **Figure 65a**), while in sample MB it

was at **d** ≈ 14 nm. Interestingly, the position of erbium cluster layer does not coincide with the maximum of erbium concentration determined from SIMS. The origin of this discrepancy is not known at the present.

Visible erbium clustering layer in both cases extends for 10 – 15 nm in the active material as deduced from TEM imaging (see for example **Figure 65**). Erbium agglomeration could be a big drawback from the point of view of optical performance of the device. Clustering is usually accompanied by a very strong cooperative up-conversion [61,261,278], which is obviously unwanted effect when the stimulated emission is considered. Presence of clustering implies as well, that a big part of erbium ions should be optically inactive [265].

From the TEM images it could be estimated a fraction of erbium ions that should be optically inactive. Assuming the 15 nm wide cluster region centred at 20 nm from the sample surface (see **Figure 65**), and knowing the SIMS concentration profile (see **Figure 64b**) and by

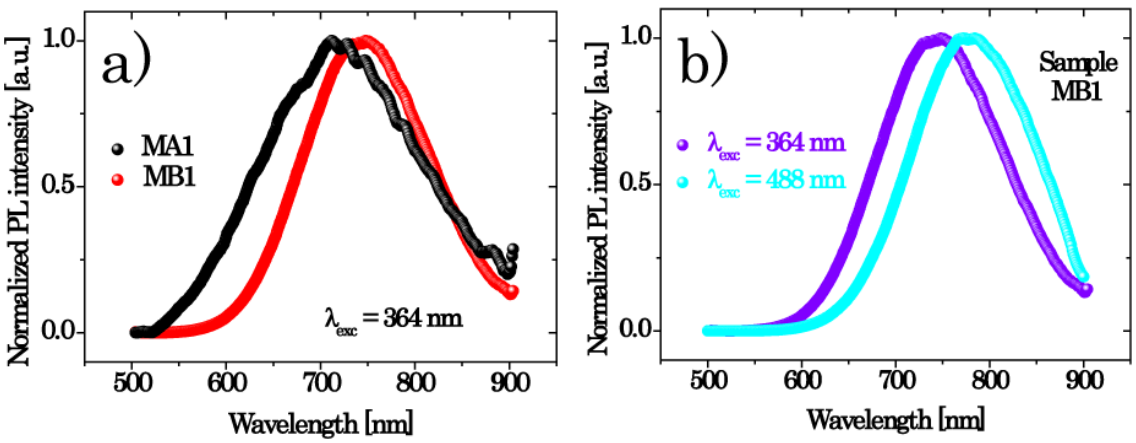

Figure 67 *– (**a**) Normalized visible PL spectra of the samples MA1 (black spheres) and MB1 (red spheres). PL intensity of sample MA1 is 13.5 times less intense than the one of the sample MB1. In addition, PL spectrum of sample MA1 is broader and blue-shifted, indicating less phase separation and presence of amorphous silicon nanoclusters. On other hand, PL band properties of the sample MB1 are consistent with the presence of mostly crystalline silicon nanoparticles population. Excitation wavelength in UV (**λ_{exc}** = 364 nm) was used in both cases, with the excitation photon flux of **Φ** = 3 x 10^{18} ph./cm^2. (**b**) PL spectra of sample MB1 under UV (**λ_{exc}** = 364 nm, violet spheres) and visible (**λ_{exc}** = 488 nm, cyan spheres) excitation. PL spectrum is red-shifting when the excitation wavelength is changed from UV to visible indicating the presence of small nanocrystals and amorphous nanoclusters.*

postulating that all the erbium ions in that region of sample are optically inactive, it is found that 55 ± 5 % of total number of erbium ions should be optically inactive (absorbing but not emitting).

This is a significant fraction of erbium ions and it is sufficient by itself to prevent any possible net gain and population inversion. Evidently, in order to provide with optimized gain material this issue has to be solved. The most straightforward way to achieve this goal is to reduce the erbium concentration with the direct penalty on the maximum achievable optical gain value. This translates as well in more rigid device design and fabrication requirements (lower optical losses) and larger device footprint.

Nevertheless, even at this stage, it is instructive to correlate these findings with the results of the spectroscopic analysis.

Apart from the study of erbium clusterization, EF-TEM imaging can be used for the study of silicon nanoparticle crystallinity degree. The results of EF-TEM imaging of sample MB are reported in (**Figure 66**). Images were filtered at 15 eV (crystalline silicon plasmon peak) or 23 eV (SiO_x plasmon peak) with 5 eV wide energy windows (see **Figure 66**). For the sample MA amorphous clusters were found, while for the sample MB nanoparticles

population was dominated mostly by crystalline nanocrystals. In both samples smaller population of different crystallinity was observed (crystalline for MA and amorphous for MB, see **Figure 66**).

In **Figure 67** the visible PL spectra of samples MA1 and MB1 (samples without erbium, see **Table 4**) are reported. PL spectrum of sample MA1 is broader, blue shifted and less intense (13.5 times) when compared to the PL band of sample MB1. Considering the

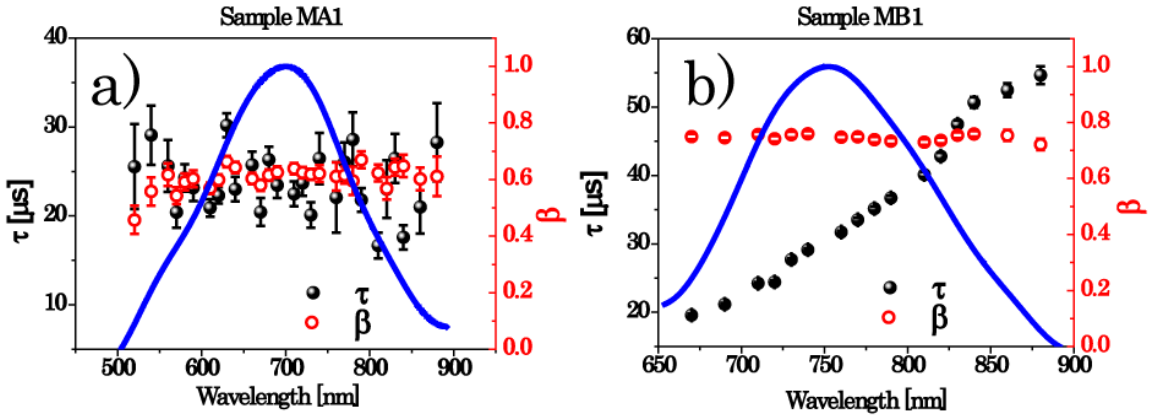

Figure 68 *– (**a**) Spectral dependence of PL lifetimes (**τ**, black spheres) and stretching parameters (**β**, empty red circles) for the sample MA1. PL lifetimes and stretching parameters were obtained by fitting the experimental data with stretched exponential function* [109]*. Experimental data were obtained by integrating over 20 nm wide spectral windows. Normalized time integrated PL spectrum obtained under the same excitation conditions is reported as well (blue solid line). No spectral dependence of the lifetimes (**τ**) could be observed, while the values of stretching parameters (**β**) are quite low indicating amorphous silicon nanoclusters as origin of the visible PL. Pulsed UV excitation was used (**λ_{exc}** = 355 nm, 6 ns, 10 Hz). (**b**) Spectral dependence of PL lifetimes (**τ**, black spheres) and stretching parameters (**β**, empty red circles) for the sample MB1. PL lifetimes (**τ**) and stretching parameters (**β**) were obtained by fitting the experimental data with stretched exponential function* [109]*. Experimental data were obtained by integrating over 20 nm wide spectral windows. Normalized time integrated PL spectrum obtained under the same excitation conditions is reported as well (blue solid line). Strong spectral dependence of lifetimes (**τ**) can be observed. Together with the high values of stretching parameters (**β**), it is consistent with the presence of silicon nanocrystals in sample MB1. Pulsed UV excitation was used (**λ_{exc}** = 355 nm, 6 ns, 10 Hz).*

annealing treatments that were applied on these samples, it indicates that the silicon nanoparticles in sample MA1 are mostly amorphous while in sample MB1 mostly crystalline, in agreement with the results of EF-TEM imaging (see **Figure 66**).

Amorphous nature of silicon nanoparticles in sample MA1 is further confirmed by a large red-shift of PL peak position when excitation is changed from UV to visible (not shown). Interestingly, PL band of sample MB1 shows the similar red shift under the change of excitation wavelength, indicating the presence of smaller amorphous population as deduced from EF-TEM images (see**Figure 67b**).

More insight on the crystallinity degree of silicon nanoparticles in different samples is given by time resolved measurements. Experimental data are obtained by integrating the PL signal over a 20 nm wide spectral window. Subsequently the data are fitted with a stretched exponential function [109] and the results are reported in **Figure 68**.

Quite long lifetimes were found for the sample MA1 (**τ** ≈ 15 μs) indicating a high quality matrix [37]. In addition, stretching parameters (**β**) were quite low and no spectral dependence of the lifetimes could be observed. This indicates that amorphous nanoclusters are mostly responsible for observed visible PL in sample MA1, in agreement with what concluded from TEM imaging. On the other hand, sample MB1 shows higher values of

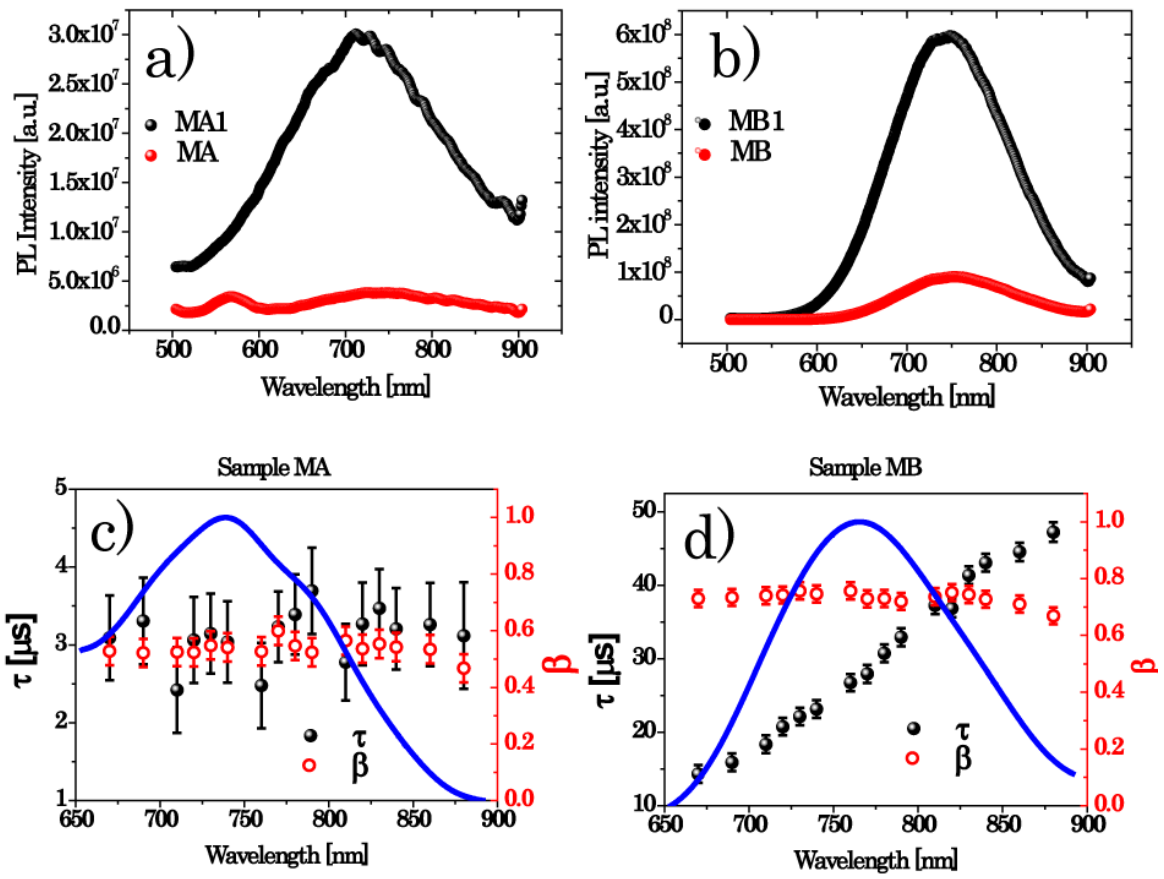

Figure 69 *– (**a**) Visible PL spectra of sample MA1 (black spheres) and sample MA (red spheres) under CW UV (**λexc** = 364 nm) excitation. Excitation photon flux used was **Φ** = 3 x 10¹⁸ ph./cm². (**b**) Visible PL spectra of sample MB1 (black spheres) and sample MB (red spheres) under CW UV (**λexc** = 364 nm) excitation. Excitation photon flux used was **Φ** = 3 x 10¹⁸ ph./cm².(**c**) Spectral dependence of PL lifetimes (**τ** , black spheres) and stretching parameters (**β**, empty red circles) for the sample MA. PL lifetimes and stretching parameters were obtained by fitting the experimental data with stretched exponential function* [109]*. Experimental data were obtained by integrating over 20 nm wide spectral windows. Normalized time integrated PL spectrum is reported as well (blue solid line). No spectral dependence of the lifetimes (**τ**) could be observed, while the values of stretching parameters (**β**) are quite low indicating amorphous silicon nanoclusters as origin of the visible PL. Pulsed UV excitation was used (**λexc** = 355 nm, 6 ns, 10 Hz). (**d**) Spectral dependence of PL lifetimes (**τ**, black spheres) and stretching parameters (**β**, empty red circles) for the sample MB. PL lifetimes and stretching parameters were obtained by fitting the experimental data with stretched exponential function* [109]*. Normalized time integrated PL spectrum is reported as well (blue solid line). Strong spectral dependence of lifetimes (**τ**) can be observed. Together with the high values of stretching parameters (**β**), it is consistent with the presence of silicon nanocrystals in sample MB. Pulsed UV excitation was used (**λexc** = 355 nm, 6 ns, 10 Hz).*

stretching parameters (**β**) and strong spectral dependence of PL lifetimes (**τ**, see **Figure 68**) indicating the presence of silicon nanocrystals .

Both type of samples, annealed at high (1000°C) or low (900°C) temperature, show significant visible PL quenching (see **Figure 69a** and **Figure 69b**) when the erbium is

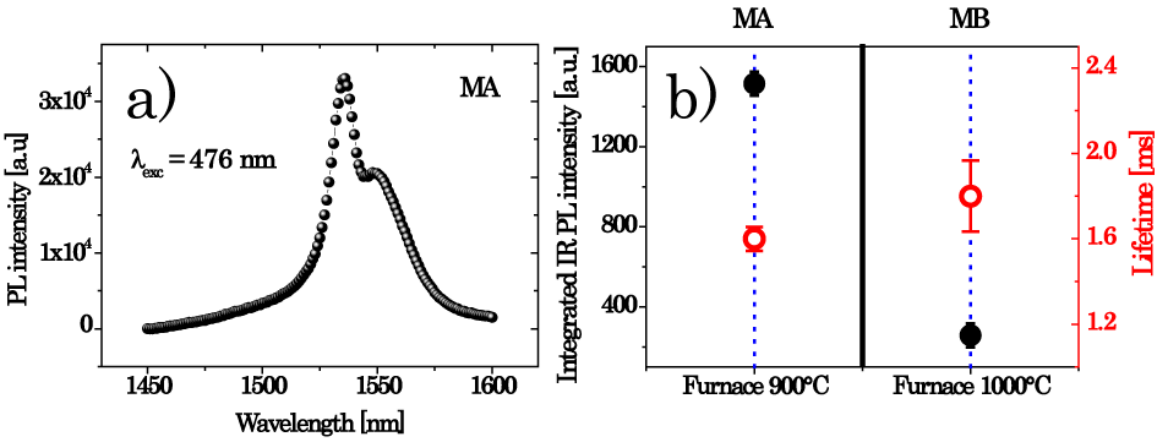

***Figure 70** – (**a**) PL spectrum of $^4I_{13/2}$ – $^4I_{15/2}$ erbium transition in sample MA under non-resonant excitation (λ_{exc} = 476 nm) with excitation photon flux Φ = 3 x 10^{20} ph./cm². (**b**) Integrated PL intensities (black solid circles) of $^4I_{13/2}$ – $^4I_{15/2}$ erbium transition and PL lifetimes (red empty circles) of the same transition for the samples MA (annealed at 900°C) and MB (annealed at 1000°C). Non-resonant excitation (λ_{exc} = 476 nm) with excitation photon flux Φ = 3 x 10^{20} ph./cm² was used.*

incorporated in the active material. In the case of samples annealed at lower temperature (MA1 and MA, annealed at 900°C, see **Table 4**) quenching is approximately 6.5 times, while in the case of the samples annealed at higher temperatures (MB1 and MB, annealed at 1000°C, see **Table 4**) quenching is higher (7 times). This is different with respect to what observed in thick samples studied before. In the case of thick samples, samples annealed at higher temperature showed less visible PL quenching in the erbium presence (see section 3.4.2 and **Figure 42**).

A part from the loss of the PL intensity, these samples show shortening of PL lifetimes independently of the nanoparticles crystallinity degree. Lifetime shortening is more pronounced in the case of sample MA, annealed at 900°C. This is very different with respect to the case of thick samples prepared by RF co-sputtering, where only the initial fast part of PL dynamics was influenced by the erbium ions presence.

However, in the thick samples erbium ions were incorporated in the matrix during the film deposition phase followed by the subsequent annealing [272,275]. In the case of thin samples considered, SRO properties were mainly determined by the first annealing treatment after which the films were implanted with erbium ions.

Ion implantation induces significant damage to the implanted matrix, creating a number of non-radiative recombination sites [264,278], which could be responsible for the observed shortening of the PL lifetimes. In the pure silica very high thermal budget is necessary to recover completely the implantation damage (T = 1200°C, t = 1 h) [264,278]. Thus, it may be that applied post annealing treatment is not sufficient to recover completely the matrix.

The results of IR PL (CW and TR) under non-resonant excitation (λ_{exc} = 476 nm) are reported in the **Figure 70**. Both samples, MA and MB, show very long PL lifetimes for $^4I_{13/2}$ – $^4I_{15/2}$ erbium transition. Considering the high silicon excess [287,288,349] and the fact that these samples are very thin and deposited upon high refractive index material (silicon substrate) [259,326,327,332] the observed lifetimes are exceptionally long indicating the very

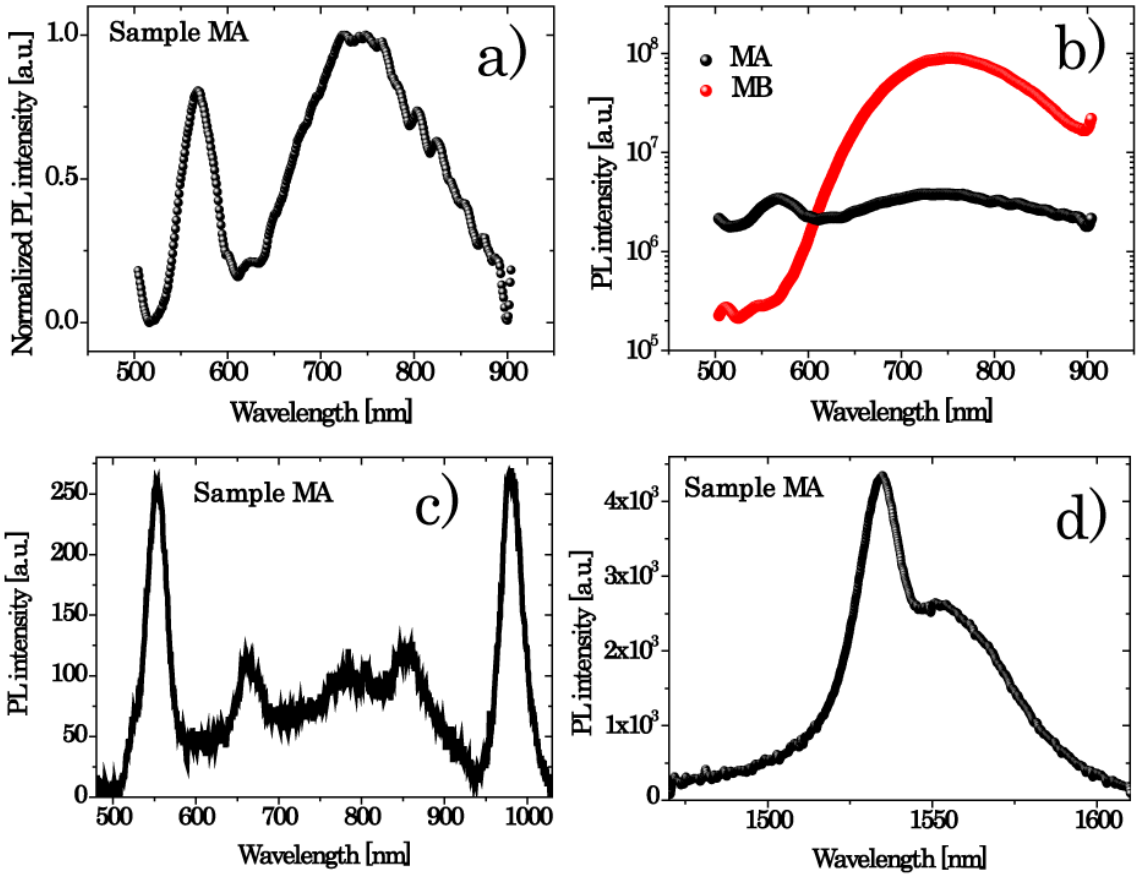

***Figure 71** – (**a**) Normalized visible PL spectrum of sample MA under CW UV excitation (λ_{exc} = 364 nm, Φ = 3 x 10^{18} ph./cm^2). Additional peak at approximately λ = 550 nm could be observed. (**b**) Visible PL spectra of samples MA (black solid line) and MB (red solid line) under CW UV excitation (λ_{exc} = 364 nm, Φ = 3 x 10^{18} ph./cm^2). (**c**)[15] Visible EL spectrum of the sample MA. (**d**)[15] EL spectrum of $^4I_{13/2}$ – $^4I_{15/2}$ erbium transition of sample MA.*

good matrix quality. These observations are contrary to what concluded from the visible TR PL, indicating that at least part of the observed visible PL shortening is not due to implantation damage.

From the **Figure 70**, it can be seen that the erbium related PL is more intense in the sample annealed at low temperature, analogously to the case of thick samples. Both erbium implanted samples have similar erbium PL lifetimes but sample MB shows almost six times less PL intensity respect to sample MA under the same non-resonant excitation. As the PL lifetimes are very similar, it can be concluded that in sample MB there are less emitters (lower energy transfer efficiency).

Under the electrical injection these samples showed as well strong erbium related electroluminescence (see **Figure 71d**) and high power efficiency (> 0.05 %)[15]. However, onset voltages for the electroluminescence are quite high (around 30 V) meaning that under electrical injection erbium is mainly excited by impact ionization. Reasons for high operating voltages are not known at present.

Based on long PL lifetimes under non-resonant excitation and high power efficiency under electrical excitation it can be tentatively concluded that the sample MA is an optimized

sample.

However, as shown previously by TEM imaging there is an erbium clustering in this sample which should influence the optical performance of active material. Moreover, cooperative up conversion should be fairly strong.

In fact, if the visible PL spectrum of sample MA is considered apart from the visible PL band coming from the silicon nanoclusters there is an additional peak that can be correlated to a cooperative up-conversion presence (see **Figure 71a**). Interestingly, this peak is not present neither in sample MB under the same CW UV excitation (see **Figure 71b**) nor in sample MA when is excited resonantly with λ_{exc} = 488 nm (data not shown). That means that the cooperative up-conversion is influencing heavily the coupled erbium fraction and that very high excitation photon fluxes are needed for its observation.

The presence of this peak is as well responsible for less visible PL quenching after erbium incorporation in sample MA with respect to sample MB. If this peak is not considered quenching is similar to the case of sample MB.

Cooperative up-conversion in the sample MA could be observed only when the excitation photon energy was increased, corresponding to higher pumping condition (higher absorption cross section) [117]. When pumping electrically, resulting pumping conditions could be considered as even more energetic than UV excitation [338]. In the **Figure 71c it** is reported the visible EL spectrum of active material corresponding to sample MA. A number of Er^{3+} related transitions can be observed across the whole visible/NIR region. This implies that a significant part of visible erbium related EL is due to cooperative up-conversion. This is valid as well for the single layer samples considered previously.

In order to evaluate the impact of cooperative up-conversion on performance of active material, it is important to quantify it. For the determination of the coefficient of cooperative up-conversion it was used the procedure described in section IV of Appendix to Chapter 3 and Ref. [271]. Cooperative up-conversion estimate was done by exciting resonantly (λ_{exc} = 974 nm) and non-resonantly (λ_{exc} = 476 nm). As reference sample, sample C from **Table 1** was used.

However, before any quantitative evaluation is done, it is very important to estimate approximately the radiative lifetime of erbium ions in sample MA. In a bulk silica erbium radiative lifetime was measured to be τ_{rad} = 18 ms [260]. However, in the presence of silicon nanoparticles refractive index of material is changing [349], influencing as well the radiative lifetime of Er^{3+}. Having in mind the silicon excess in this sample (9 at.%) and comparing with the literature [63,271,294,316,349], radiative lifetime of τ_{rad} = 10 ms can be deduced.

This is in good agreement with what expected for bulk samples when accounting for near field enhancement of radiative rate in vicinity of silicon nanoparticles (τ_{rad} = 10 ms [287]. τ_{rad} = 7 ms [288]). However, sample MA is a thin sample deposited on top of the high refractive index material (silicon substrate), thus a certain enhancement of the radiative rate is expected [259,287,326–329,332]. Taking into account the asymmetric profile of the erbium ions in this sample (see **Figure 64**) a value of τ_{rad} = 7 ms was estimated.

Quantitative optical measurements on these samples are very difficult due to a very weak signal which is a consequence of the very small excited volume (very thin samples). This is the reason why the quantitative measurements are performed only on the brightest sample in terms of erbium related PL (MA). Estimate of optical performance of other samples

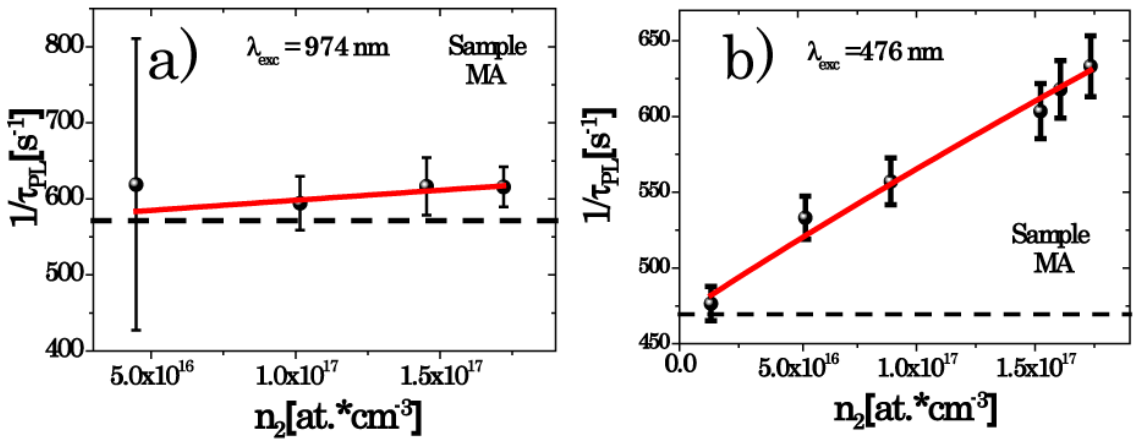

Figure 72 *– (**a**) Cooperative up-conversion estimate on sample MA using resonant excitation (**λ_{exc}** = 974 nm). Excitation photon flux was varied from **Φ** = 2.3 x 10^{21} ph./cm² to 2.2 x 10^{22} ph./cm². Experimental data (black spheres) have been fitted with Eq. 31 (red solid line, see section IV of Appendix to Chapter 3) yielding **C_{up}** = 5 ±13 x 10^{-16} cm^3 * s^{-1}. Dashed horizontal line represents the time decay in absence of cooperative up-conversion estimated from the fit (red solid line) to be **τ_0** = 1.8 ± 0.3 ms. (**b**) Cooperative up-conversion estimate on sample MA using non-resonant excitation (**λ_{exc}** = 476 nm). Excitation photon flux was varied from **Φ** = 2.8 x 10^{18} ph./cm² to 2.7 x 10^{02} ph./cm². Experimental data (black spheres) have been fitted with Eq. 31 (red solid line, see section IV of Appendix to Chapter 3) yielding **C_{up}** = 2.1 ± 0.3 x 10^{-15} cm^3 * s^{-1}. Dashed horizontal line represents the time decay in absence of cooperative up-conversion estimated from fit (red solid line) to be **τ_0** = 2.13 ± 0.05 ms.*

can be obtained by comparison with the sample MA.

Results of the measurements performed for the determination of cooperative up-conversion coefficient are reported in **Figure 72**. In both cases (resonant and non-resonant excitation) same results (within experimental error) were found. As in the case of non-resonant excitation effective excitation cross section is significantly larger (see **Figure 73a**), the results obtained by non-resonant excitation are less noisy and it will be used in following.

For the cooperative up-conversion coefficient it was found **C_{up}** = 2.1 ± 0.3 x 10^{-15} cm^3 * s^{-1}, which is a pretty high value in agreement with what expected from previous analysis. For the limit PL decay time in the absence of cooperative up-conversion a value of **τ_0** = 2.13 ± 0.05 ms was found.

Using the resonant excitation (**λ_{exc}** = 974 nm) the absorption cross-section for direct excitation can be found following the procedure described in the section V of Appendix to Chapter 3. The value found is **σ_{dir} (974 nm)** = 1.9 ± 1.3 x 10^{-21} cm^2. This value is in agreement (within the experimental error) with the value previously reported in Ref. [296] (**σ_{dir} (974 nm)** = 3.1 ± 0.5 x 10^{-21} cm^2). It is very difficult to obtain more accurate estimate of direct erbium cross-section in sample MA due to a low PL signal. Therefore, in the following the value from the Ref. [296] will be used instead.

Knowing cooperative up-conversion coefficient and direct erbium absorption cross-section [296], the fraction of optically active erbium ions can be estimated following the procedure described in section IV of Appendix to Chapter 3.

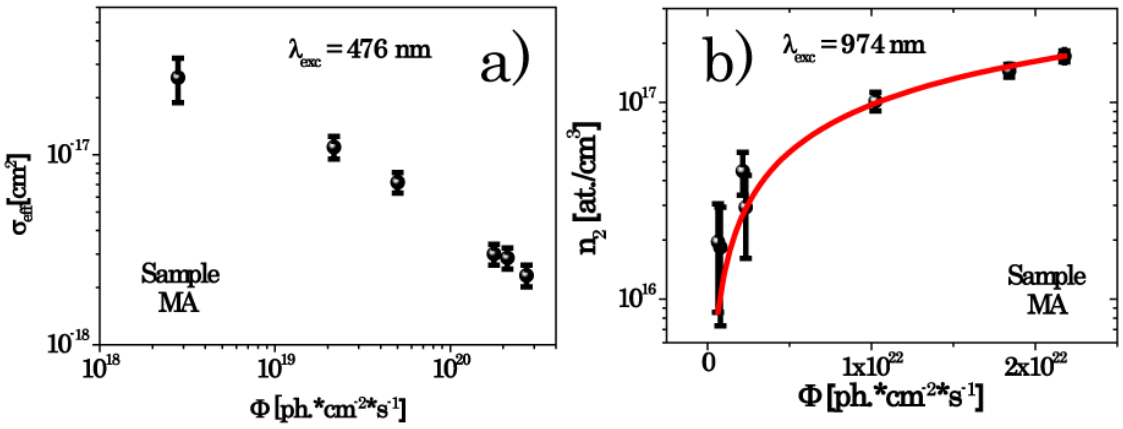

Figure 73 *– (**a**) Effective excitation cross-section dependence on excitation photon flux of Er^{3+} of sample MA under non-resonant excitation (λ_{exc} = 476 nm). (**b**) Determination of optically active fraction of erbium ions in sample MA. Experimental data (black spheres are fitted with Eq. 30 (red solid line, see section IV of Appendix to Chapter 3) giving the total active erbium concentration in sample MA of n_{active} = 2.1 ± 0.2 x 10^{18} at./cm³. Resonant excitation wavelength was used λ_{exc} = 974 nm.*

It is found that the total active erbium concentration in sample MA is n_{active} = 2.1 ± 0.2 x 10^{18} at./cm³. This counts for approximately 0.75 ± 0.11 % of total erbium content. The same procedure can be applied for the sensitized fraction of erbium ions obtaining 0.1 %. However, in the case of sensitized fraction Eq. 30 does not fit the data nicely as in case of optically active fraction implying that there are additional factors that were not considered and that the applied procedure is not adequate for the estimate of sensitized fraction.

The estimated value of optically active erbium fraction is very low, much lower than what estimated from TEM imaging. This is reasonable as in the TEM images only a clusters of certain size can be imaged (few nm of size). Thus, if erbium clusters are smaller consisting of only few erbium ions they will not be observed with TEM but they will influence heavily the optical properties of active material.

Again as a limiting factor in this material, loss of optical activity of erbium ions was found. However, in this case there is strong evidence that behind the loss of optical activity of erbium ions there is erbium clustering. Erbium clustering is probably the main limiting factor at current erbium concentration in thin samples (~10^{20} at./cm³) and it is probably responsible as well for the loss of optical activity in thick samples.

Moreover, it becomes clear that the sample optimization procedure used is not adequate. Nice results in terms of erbium PL, lifetime and power efficiency can be obtained even when the main fraction of erbium ions is optically inactive. Main figure of merit when optimising this material should be the optical activity of erbium. Once the optimized erbium concentration is achieved silicon nanoparticles should be tailored to increase sensitized fraction while maintaining optical activity of the erbium ions.

1.1.4. Waveguide amplifier design

Slot waveguides have been proposed as a possible solution to optical waveguiding in very thin films of low refractive index [321,322]. Moreover, this novel structures provide a straightforward way to get electrical injection in erbium doped active thin films made of insulating material [323,324]. There have been a few designs proposed for actual electrically driven devices, however they were not suitable for mass production exploiting the CMOS process or in particular, were not suitable for the use with erbium doped active insulating materials [323,324,350,351].

In this section it will be presented the design of a novel structure that can be exploited for production of electrically pumped waveguide amplifier based on erbium doped material. The main advantage of the proposed approach is that it can be produced in standard CMOS line using optical lithography.

In the case of the erbium doped material the design of the waveguide amplifier is the design of suitable waveguide configuration in which electrical injection can be achieved [323].

There are basically two possible designs that can be considered: vertical and horizontal slot waveguide [323]. Vertical slot waveguides are very interesting from the sensing point of view as they permit interaction with external ambient [352–355]. However, a big drawback of the vertical design is the etch induced roughness of the slot walls, responsible for significant optical losses in vertical configuration [323,356], although significant progress have been made recently in suppression of roughness induced optical losses [351,357]. Moreover, usually only the limited filling of slot region by active material is possible [356].

However, the main reason for the choice of horizontal configuration is a simple fact that the multi-layer material in slot region is very difficult to deposit in vertical configuration even by conformal growth (see **Figure 74a**).

When designing this type of structures, there are few points that need special care if the modelled structure is to be actually feasible.

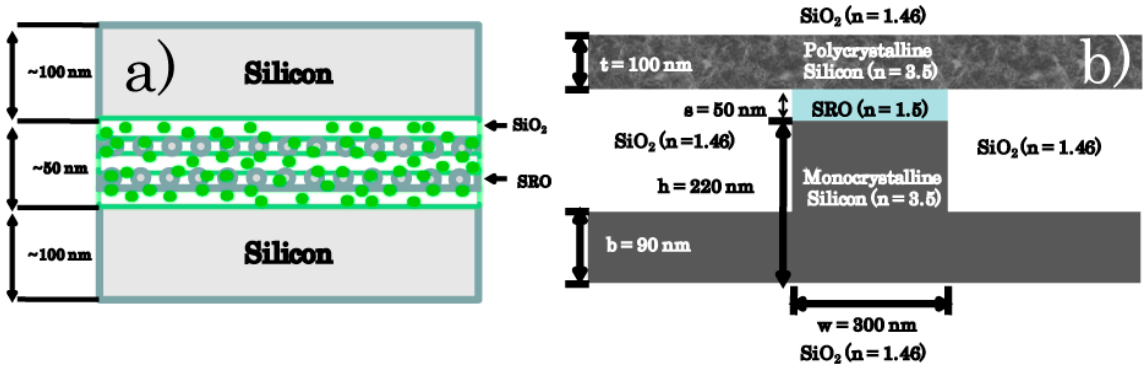

***Figure 74** – (**a**) Schematic of typical configuration of the horizontal slot waveguide, where the multi-layer erbium (green spots) doped SRO (grey spheres) material of approximate thickness of **d** = 50 nm is sandwiched between two layers of silicon. (**b**) Schematic of the optimized novel structure which provides with optical waveguiding and permits the electrical injection in erbium doped SRO material.*

The most important are fabrication issues. Very precise control of device dimensions can be achieved by using the electron beam lithography [356], however fot industrial applications and mass production, optical lithography has to be used. The devices that allow for electrical excitation are usually of complex design, involving the structures that have to be defined with multiple overlapping levels by different lithographic masks [358].

However, when optical lithography is used (even in the case of deep UV), the typical realignment error of optical mask on different structure levels is of the order of magnitude of typical single mode slot waveguide [321,352,356]. Thus, when designing this type of structures, a special attention has to be addressed in order to relax optical alignment conditions between different mask levels. As well, small features have to be defined in a single etch procedure as the subsequent realignment becomes impossible (an example being the central part of slot waveguide).

Even though the main part of the structure has to be defined in a single etch, an access to a top and bottom cladding have to be present for electrical connections. Whole slot structure has to have as well limited volume of high refractive index material, in order to avoid leaking of the field from the low refractive index area of the slot. Moreover, slot waveguides have to be well isolated from the silicon substrate for the same reason.

Another serious issue is the choice of materials. As discussed previously, active material consists of low refractive index material with 50 nm thickness build by subsequent deposition of multilayer structure of erbium doped SRO. As top and bottom claddings which build the slot waveguide and provide with electrical contacts, silicon is material of choice due to the good electrical conductivity, easy processing and CMOS compatibility.

Silicon on the other hand can be found in three main forms: as monocrystalline, polycrystalline and amorphous. Monocrystalline silicon has superior electrical and optical properties when compared to other two forms. Unfortunately, monocrystalline silicon films cannot be grown in CMOS process and is only available as a substrate or as device layer in SOI.

Some additional flexibility is offered by the silicon-on-insulator (SOI) technology. SOI allows for good separation from the silicon substrate and reduced light leakage and provides with a single monocrystalline layer that can be used for the definition of the bottom cladding.

However, the top cladding has to be made of polycrystalline or amorphous silicon. There have been trials to bond two SOI wafers in order to define horizontal slot waveguides made completely out of monocrystalline silicon [359]. However, bonding procedure is expensive and complicated process and has never been demonstrated with SRO as bonding layer. Thus, it will be disregarded from further considerations.

Very nice results in terms of optical losses have been achieved in horizontal slot waveguides by using the hydrogenated amorphous silicon top cladding [336]. Unfortunately, amorphous silicon is characterized by poor electrical conductivity. On other hand, polysilicon is commonly used as a conductive material in microelectronics. Slot structures with polycrystalline silicon have been already demonstrated, although with very high optical losses [331]. Optical losses in polysilicon based slot waveguide have been reduced lately reaching the present record value of 7 dB/cm for propagation losses [324].

The reasons for high optical losses in polysilicon are scattering from inherently large surface roughness, grain boundaries and absorption due to silicon dangling bonds formed on

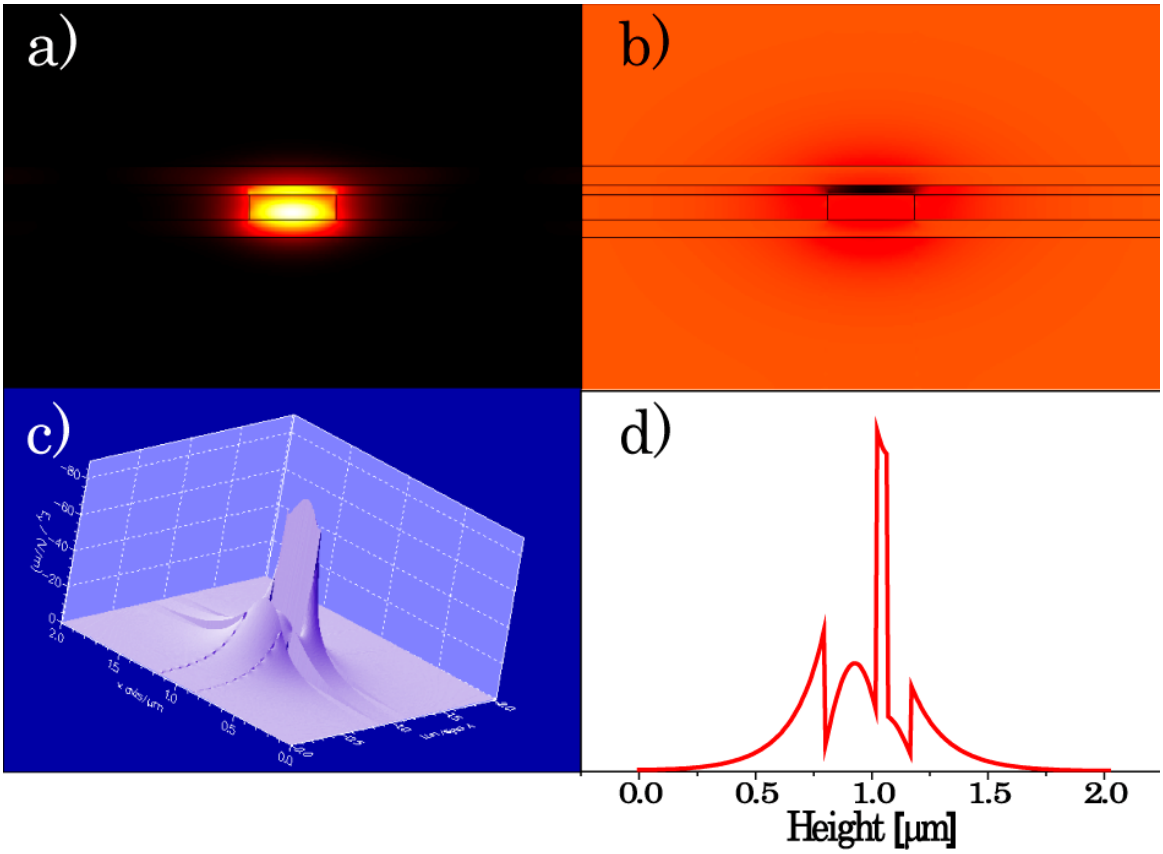

Figure 75 *– (**a**) Optical power distribution of the first TM mode in an optimized novel structure whose cross-section is reported in **Figure 74b**. (**b**) $|E^2|$ distribution of the E_y (vertical) component of the electric field for the first TM mode. Strong enhancement in slot region can be observed (dark region). (**c**) 3D image of $|E^2|$ distribution of the E_y (vertical) component of electric field for the first TM mode reported in panel (**b**). Z – axis corresponds to electric field strength. (**d**) The relative magnitude of the electric field for the first TM mode along the vertical directions of panels (**a**) and (**b**) and y-axis of panel (**c**). Strong enhancement in slot region can be observed.*

the grain boundaries [345–348,360–362]. These losses can be reduced by long high temperature annealing procedures in presence of forming gas where hydrogen passivates silicon dangling bonds. However, this is impractical in electrically active type of devices as it may cause dopant out-diffusion and may interfere with optimum thermal budget for SRO.

Therefore, it is more attractive to minimize the fraction of light guided in polycrystalline part of slot waveguide, while still maintaining high fraction of field in slot region.

Silicon based electrical devices has to be additionally doped with impurity atoms in order to increase the material conductivity. However, doping is a significant source of additional optical losses due to free carrier absorption [363]. By using the polysilicon, doping and consequently optical losses due to free carrier absorption can be significantly reduced. Nevertheless, the dopant presence should be avoided in parts of the structure where the light confinement is significant.

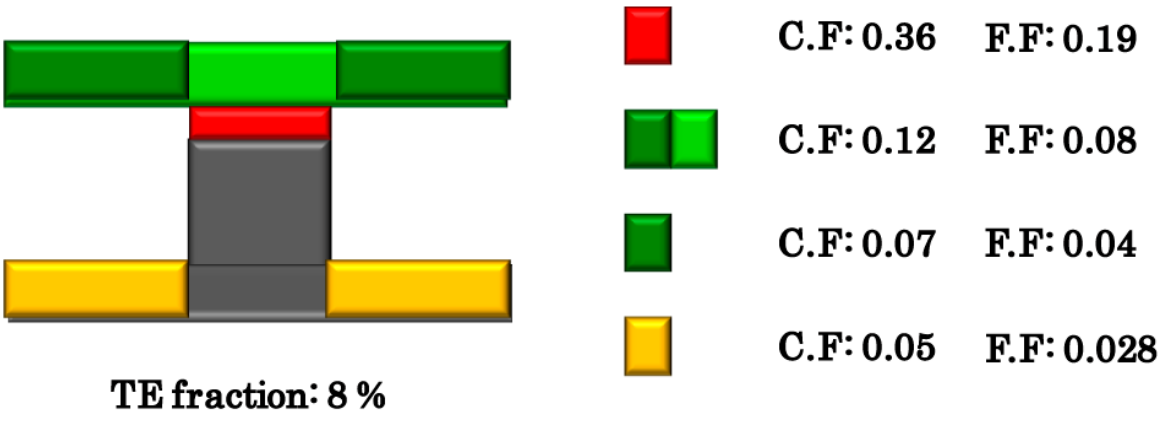

Figure 76 *– Schematic of the optimized asymmetric slot waveguide with the color legend of its different parts. Slot region where the active material is situated is indicated in red, polycrystalline part is colored in green (with the dark green parts representing heavily doped region of polysilicon for electrical contacts), and monocrystalline part is grey (with yellow parts indicating the heavily doped part for electrical contacts). C.F. stands for confinement factors and gives the $|E^2|$ fraction of the first TM mode (fraction of the electric field) in a given region while F.F. is fill factor and gives the fraction of the optical power. The first TM mode is characterized as well by small presence of opposite polarization of 8%.*

These requirements can be achieved by asymmetric design of slot waveguides (see **Figure 74**). Asymmetric design has been used in vertical slot waveguides in order to allow for sharp bends [364] and single mode operation [351,357]. The main reason for the use of the asymmetric design here is to account for fabrication issues and minimized the fraction of electric field situated in the polysilicon part while at the same time maximizing the fraction of the electric filed inside of the slot region (see **Figure 75** and **Figure 76**).

Optimized waveguide parameters are reported in **Figure 74**. This design has a number of advantages. By using the SOI technology good confinement can be achieved while the leaking of the light towards the substrate is strongly suppressed by a few microns of buried oxide (see **Figure 75**). Commercially available SOI wafer with 220 nm of silicon thickness on the top of buried oxide was used as a substrate. Slot thickness was defined previously and fixed at50 nm.

With this design central part of the slot can be defined in a single etch procedure (etch of slot region and partial etch of monocrystalline ridge structure). Height of **b** = 90 nm of bottom wings is enough to maintain good electrical conductivity while optimizing the fraction of the field in the slot region (see **Figure 76** and **Figure 77a**).

Polysilicon top cladding can be deposited and lithographically patterned with extremely relaxed precision in the µm range as the top polysilicon "wings" length does not influence the optical waveguiding in the TM polarization. Top cladding thickness was chosen in order to have good electrical conductivity, and maximise the field in slot region, while still maintaining the low fraction of the field in the cladding itself.

Waveguide width is chosen in order to achieve the single mode behaviour. However, wider multi-mode waveguides were considered as well (width 500 nm and 1 µm).

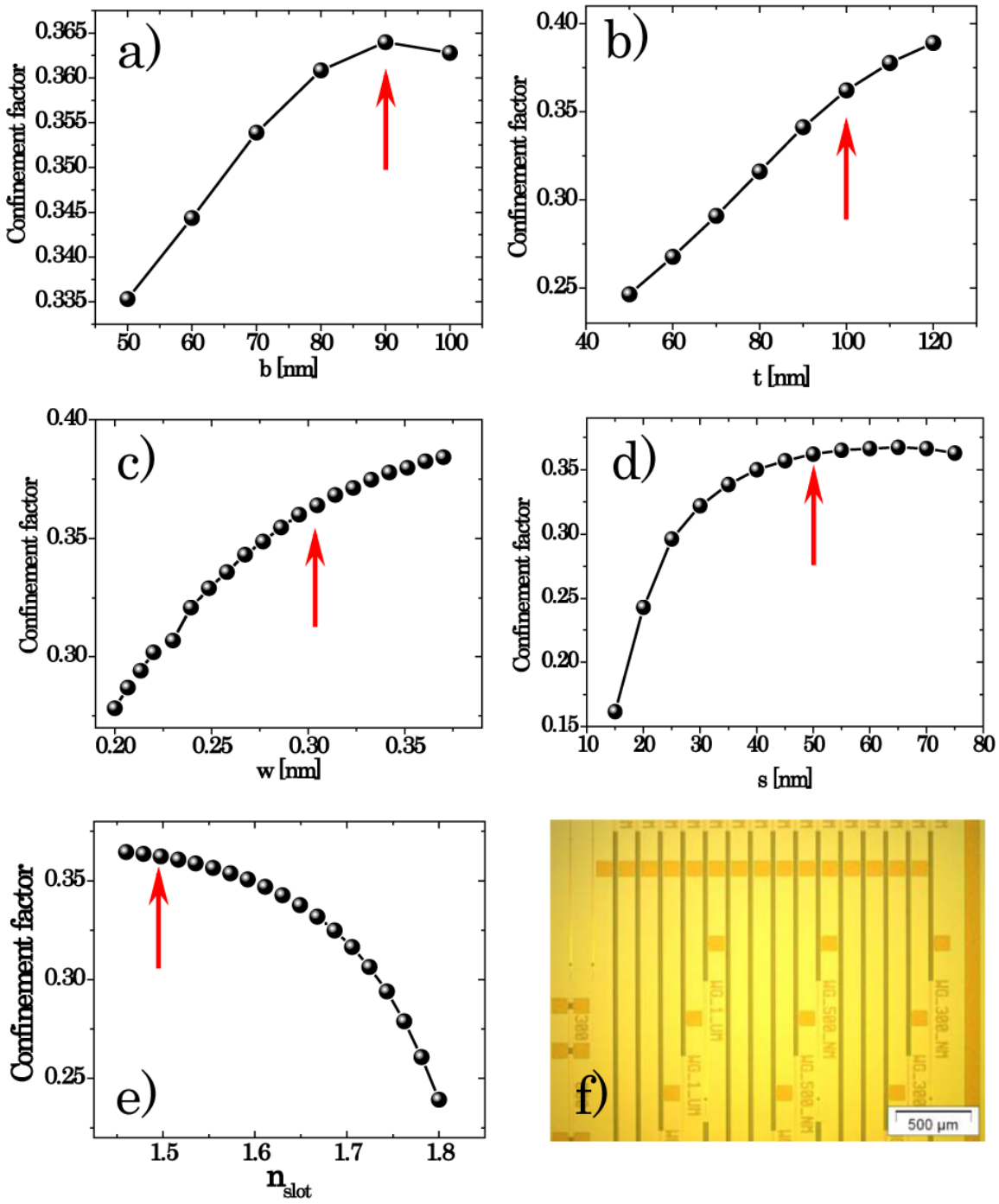

Figure 77 *– Dependence of the confinement factor in the slot region of the optimized asymmetric slot structure on: (**a**) the bottom "wings" height **b**, (**b**) top polysilicon cladding thickness **t**, (**c**) the slot width **w**, (**d**) the slot thickness **s** and (**e**) the slot material refractive index* n_{slot}*. Results were obtained by commercial FMM solver. (**f**)*[10] *Microscope image of produced electrically pumped waveguide amplifier. Thick lines in the image represent the active region of the waveguide amplifier that can be electrically biased. Small orange squares are contact pads. Graphical interpretation of the slot waveguide parameters is reported in* ***Figure 74b****. Red arrows indicate optimized parameters which were used as nominal parameters in waveguide manufacturing process.*

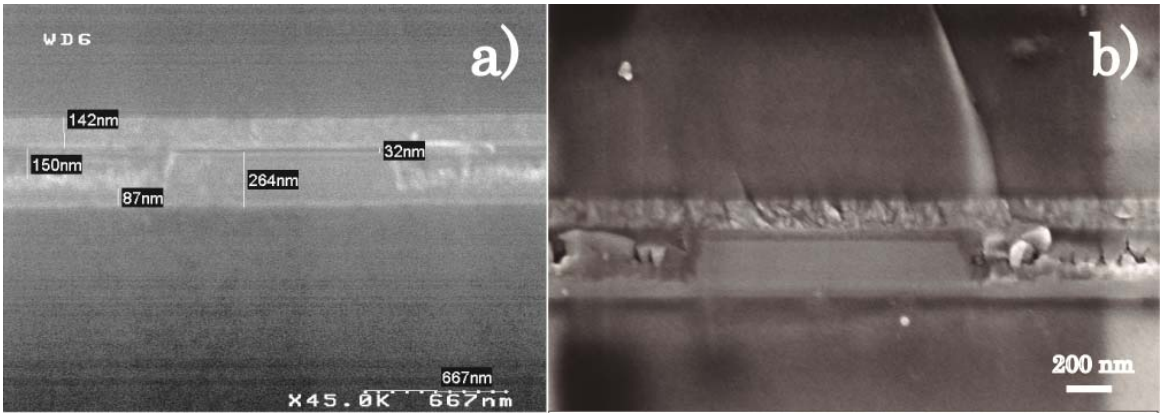

***Figure 78** – (**a**) SEM image of the produced slot waveguide. Produced structure shows good agreement with optimized modeled parameters. (**b**) SEM image of the produced slot waveguide. Grain structure of the top polycrystalline silicon cladding is clearly visible.*

As it can be seen in **Figure 77**, slot parameters are quite robust for fabrication variations, including the changes of slot thickness or slot refractive index change (different silion excess, different thermal treatments).

Although the doping has to be limited close to the active material it can be increased significantly in the waveguides "wings" (see **Figure 76**) providing with good electrical contacts. Bottom part can be doped gradually with lower dopant concentration under active film as monocrystalline silicon is characterized by fairly good conductivity. Due to small thickness of upper and bottom wings and relatively large separation between them no waveguiding occurs in the waveguide "wings". SRO is deposited directly on the silicon substrate leading to smooth interface and low scattering contribution. It is possible that scattering could be more expressed at the vertically etched slot walls, however this surface is significantly smaller than in regular slot waveguide.

In **Figure 78** an SEM image of one of the produced slot waveguides is reported. Wider multimode waveguide was imaged (**w** ≈ 1 μm). This waveguide can be electrically biased showing good conductivity and electroluminescence. However, the first run of waveguide amplifiers showed quite high passive optical losses (~ 30 dB/cm). Unfortunately, due to fabrication errors on reference structures, the origin of these high passive losses is still not established.

1.1.5. Resonant structures design

Waveguide amplifiers are not the only active elements that are of interest when the erbium doped material is considered. Erbium doped materials attracted primarily significant attention as they can be used as a material platform for the realization of a silicon based laser.

The main difference between optical amplifier and the laser, is that laser has one additional element, an optical cavity which re-circulates the emitted light. There are a number of different resonant structures that can be defined and realized in this material.

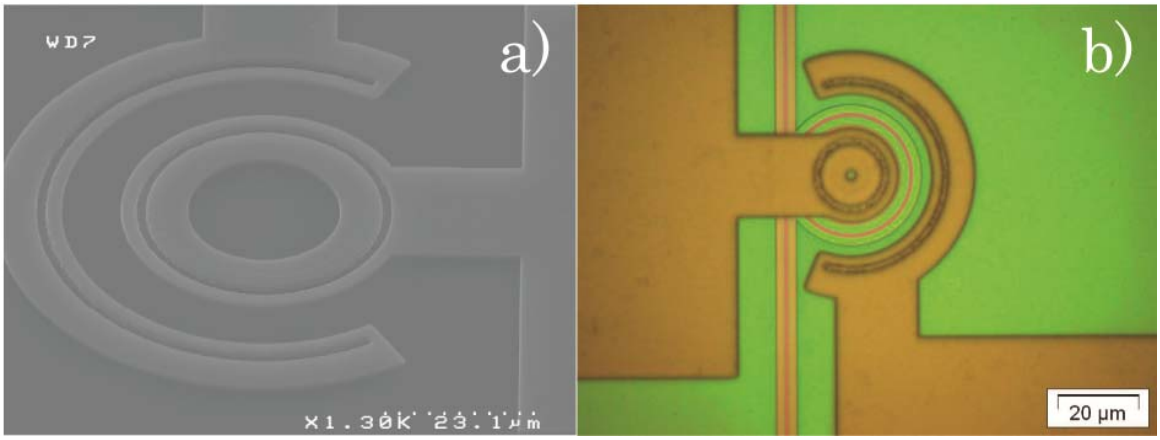

Figure 79[10] *– (**a**) SEM image of the ring resonator based on the design of electrically pumped asymmetric slot waveguide amplifier. (**b**) Microscope image of the ring resonator.*

There are several resonant structures that can be defined directly on the waveguides. The simplest is to use a WGM type of resonator in the form of ring or disc resonator, advantage of the ring resonator being that can be produced completely following the waveguide amplifier design [323,324,336,359].

For the disc resonators contact definition similar to capacitor design previously shown may be used. However in the first steps of evaluation of feasibility, the ring resonators have an additional advantage of having smaller number of radial families that may out-couple leading to consequently easier transmission/emission spectrum interpretation.

An example of the ring resonator[10] defined using the waveguide amplifier design is reported in **Figure 79**. In a preliminary characterization Q factors of approximately Q ~ 25 000 were measured on these devices. Moreover, an electroluminescence from the same device has been observed. Cavity influence on the light emitting properties of the erbium doped SRO is still under investigation.

Another simple optical cavity that can be defined on the waveguides is the Fabry-Pérot type of cavity [323]. This type of optical cavity can be defined by simply cleaving the waveguide facets, although resulting reflectivity of the facets will be very low. Thus, it is desirable to have the mirrors of the optical cavity defined in a different manner. To that purpose distributed Bragg reflectors (DBR) may be used. By using two DBR mirrors on the waveguide amplifier Fabry-Pérot cavity can be easily realized.

However, in the case of periodic structure definition on these waveguides, special care has to be paid to DBR design, in order to minimize the scattering contribution while still maintaining the minimal feature size in the domain of optical lithography. An example of the Fabry-Pérot cavity with the optimized design for the DBR mirrors is reported in **Figure 80**. Again electroluminescence from these devices has been demonstrated while the optical and electro-optical characterization is under way.

In this initial phase, only these two types of optical cavities have been considered due to their inherent simplicity of production. On the other hand Fabry-Pérot allows for the testing of the manufacturing process of gratings. If proven successful these two approaches can be easily enlarged by incorporation of a number of different optical cavity designs such as: WGM resonators (disc and racetrack resonators) with in plane or vertical coupling,

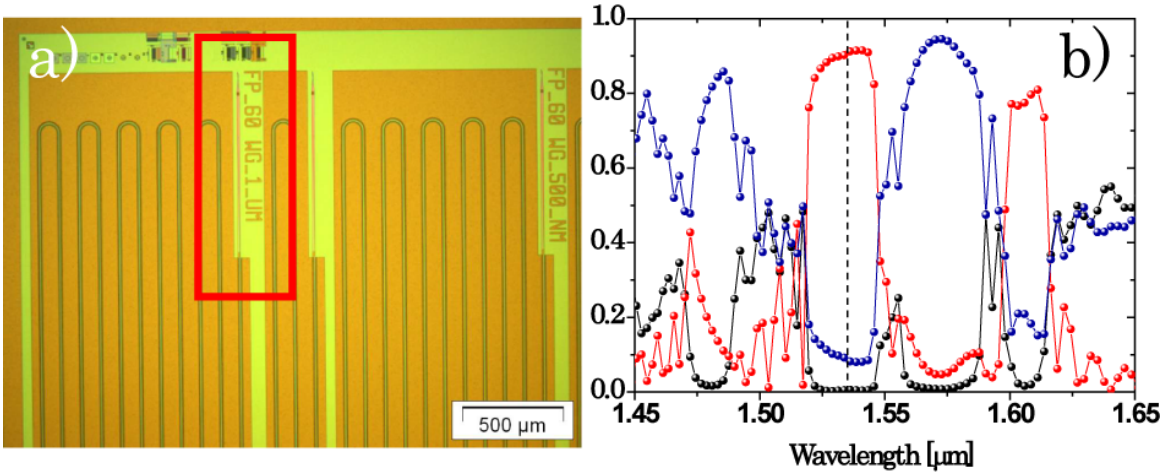

Figure 80[10] *– (**a**) Microscope image of Fabry-Pérot cavity defined on the slot waveguide. Distributed Bragg (DBR) mirror is evidenced with red frame. (**b**) Simulated transmitted (black spheres), reflected (red spheres) and scattered (blue spheres) contribution of the optimized DBR mirror as a function of wavelength. Vertical black dashed line indicates erbium emission peak (**λ** = 1535 nm). Different contributions are obtained by 3D-FDTD simulation. Mirrors parameters used are: number of periods is 80, period length is 395 nm, duty cycle is 50 %, trench depth 150 nm (to the bottom cladding).*

photonic crystal cavities, vertical emitting resonant structures, distributed feedback resonators (DFB) etc .

1.2. Conclusions and future perspectives

In this chapter a detailed study of Er^{3+}-doped silicon-rich-oxide (SRO) materials was presented. In particular, optical properties and possible drawbacks of this active material have been studied and the physical aspects behind them analyzed. As the data set has been acquired on large set of samples deposited by different deposition techniques (RF co-sputtering, PECVD, LPCVD, Silicon Ion implantation) of different thickness, erbium ion concentration, silicon excess and thermal treatments, results obtained could be easily generalized.

It was shown that a major drawback of this material is the loss of optical activity of erbium ions when inserted in a SRO matrix due to erbium clustering for concentrations higher than 10^{20} at./cm^3. As a possible remedy, lowering of the erbium concentration is proposed with the direct penalty on the optical performance of active material in the terms of optical gain.

From the results presented in this chapter it becomes evident that further material optimization is needed. Moreover, it becomes clear that the sample optimization technique used is not adequate. Good results in terms of erbium PL, lifetime and power efficiency can be obtained even when the main fraction of erbium ions is optically inactive.

Therefore, the main figure of merit when optimising this material should be optical activity of erbium. Once the optimized erbium concentration is achieved silicon nanoparticles

should be tailored to increase sensitized fraction while maintaining optical activity of erbium ions. Although, not discussed in this work, there are certain number of issues correlated with the presence of silicon nanoparticles of which the most important is free (confined) absorption. However, in optimized material, depletion of excited silicon nanocrystals population is naturally achieved via energy transfer to erbium ions reducing significantly free (confined) carrier absorption. Another issue may be a very short Er^{3+} - Si-nc interaction distance which probably could be addressed with advanced fabrication techniques.

Interestingly, in this work, it was shown that a common belief that only a few percent of erbium ions in SRO matrix is actually sensitized is a simple artifact of erbium ion deactivation when clustered. In fact, the sensitized fraction of Er^{3+} ions which maintain their optical activity is actually high (close to 50%), although not sufficient for the population inversion even in the ideal case where all erbium ions maintain their optical activity. While this number is of secondary importance until the erbium clusterization is resolved, it shows clearly that a very high sensitized fraction of erbium ions could be achieved by standard deposition techniques.

The sensitization mechanism between silicon nanoparticles and erbium ions was studied and its complex nature illustrated as well. Unfortunately, at the present point is still not possible to formulate a complete working theory of the energy transfer process although some important physical aspects of this process have been elucidated in this work. In particular, one set of samples was thoroughly studied with both high and low energy optical excitation. Additional study with an excitation in an intermediate range of photon energies combined with a similar study on the samples with a slightly different deposition parameters (annealing temperature, silicon excess, erbium concentration) would probably be sufficient for accurate theoretical modelling of energy transfer process. Obviously, the studies of this type are very time consuming and would require a significant effort.

Finally, a possibility of electrical injection in this material has been considered. Even if the achieved values of net gain are very low requiring very large footprint of working device, electrical injection would represent a net advantage respect to any existing EDFA technology. To that end, novel opto-electronic structures were proposed, modeled and manufactured and preliminary results of their performance wer presented.

Appendix to Chapter 3

I. Production of the thick films for EDWA[7]

The silicon oxide samples co-doped with Er^{3+} ions and silicon nanoparticles have been fabricated with a radiofrequency (RF) reactive magnetron co-sputtering technique by CIMAP-Ensicaen research institute (Caen - France). The deposition has been performed in a controlled argon-hydrogen mixture environment employing pure SiO_2 and Er_2O_3 targets. The non-stoichiometric silicon oxide deposition made possible the formation of silicon nanoparticles by a post-deposition annealing treatment, which has been performed at different temperatures, in order to selectively grow amorphous for annealing temperatures $\mathbf{T_{annealing}} \leq 900°C$ or crystalline nanoparticles for $\mathbf{T_{annealing}} \geq 1000°C$. More details on the material deposition can be found in Ref. [272,275].

In order to properly analyze the effects of energy transfer, a wide set of samples has been prepared, modifying the deposition parameters (substrate temperature, RF power on targets and the hydrogen rate in the hydrogen-argon mixture) [272]. The silicon excess content and Er^{3+} concentration have been chosen in order to minimize confined carrier absorption effect [297]. The energy transfer efficiency has been monitored by comparative analysis of samples deposited under different deposition parameters. As a figure of merit high PL intensity (large number of emitters) and long PL lifetime (low number of defects) under non-resonant excitation was considered [275].

The most promising sample in terms of transfer efficiency has been chosen as active layer in rib or rib-loaded waveguides, which have then been tested in pump & probe experiments. The lithographic processing has been performed at FBK-APP.

Before optical characterization, the deposition technique has been tested for reproducibility and sample homogeneity within the 4-inches wafer. This last check has been performed by multi-points m-line measurements [365], in which refractive indices and thickness have been checked for consistency.

II. Semi-empirical model of energy transfer[16]

In this section, it will be presented a modeling of the transfer mechanism through a set of coupled rate equations involving the carrier populations of a number of effective levels within the silicon nanocrystals and the Er^{3+} ions. This model includes several recombination and excitation mechanisms, and is based on several evidences observed in continuous wave and time-resolved photoluminescence measurements presented in section 3.4.2.

In this scheme (see **Figure 81**), a silicon nanocluster is represented by an effective

[16] Numerical simulations have been performed by A. Pitanti.

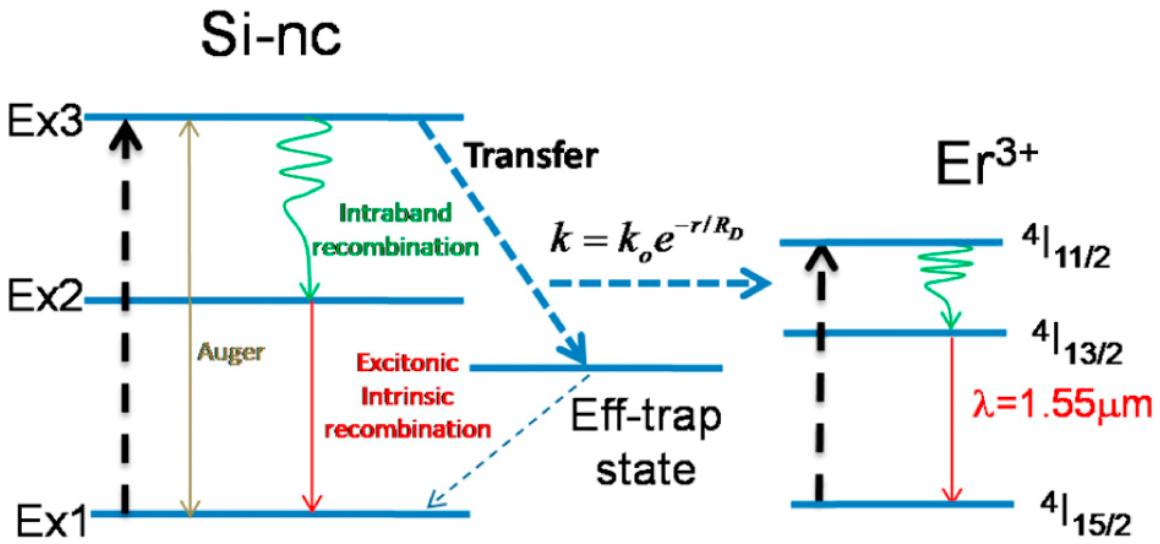

Figure 81 *– Scheme of the levels and transitions involved in energy transfer mechanism.*

three level system (which could be constituted by manifolds), consisting of two band edge levels that account for the fundamental ground state (Ex1) and the radiative level that originates the PL emission (Ex2) and high-lying level which absorbs the incoming 355nm radiation (Ex3) [110,292]. Hot carrier PL emission has not been considered.

On the other hand Er^{3+} is schematized as a three levels system: $^4I_{11/2}$ (N_{Er3}), $^4I_{13/2}$ (N_{Er2}) and $^4I_{15/2}$ (N_{Er1}). This is justified by a very fast relaxation from higher excited states [262]. This does not mean that energy transfer does not occur on higher energy states. However, as this higher states relax fast non-radiatively to lower ones without observable PL contribution, overall system can be simplified [271].

The following six coupled-equation system has been considered to model the silicon nanoparticle/Er^{3+} interaction:

$$\frac{d}{dt}N_{Exc1} = -\sigma_{Si-np} * \Phi_{Exc}(t) * N_{Si-np} + \frac{1}{2} * C_A (N_{Exc2})^3 \tag{17}$$

$$\frac{d}{dt}N_{Exc2} = \omega_{32} * N_{Exc3} - C_A (N_{Exc2})^3 \tag{18}$$

$$\frac{d}{dt}N_{Exc3} = \sigma_{Si-np} * \Phi_{Exc}(t) * N_{Si-np} - \omega_{32} * N_{Exc3} - k * N_{Exc3} * N_{Er1} + \frac{1}{2} * C_A (N_{Exc2})^3 \tag{19}$$

$$\frac{d}{dt}N_{Er1} = -k * N_{Exc3} * N_{Er1} + \frac{1}{\tau_{21}} * N_{Er2} \tag{20}$$

$$\frac{d}{dt}N_{Er2} = \frac{1}{\tau_{32}} * N_{Er3} - \frac{1}{\tau_{21}} * N_{Er2} \tag{21}$$

$$\frac{d}{dt} N_{Er3} = k * N_{Exc3} * N_{Er1} - \frac{1}{\tau_{32}} * N_{Er3} \quad (22)$$

Where:

- σ_{Si-np} is silicon nanoparticle absorption cross section ($\sigma_{Si-np} \sim 1 \times 10^{15}$ cm^2 [117]),
- Φ_{Exc} (t) is the excitation photon flux at the excitation wavelength λ_{exc} = 355 nm. Gaussian temporal shape with FWHM = 10 ns was used, in accordance with the actual laser pulse shape and width.
- C_A is the Auger coefficient.
- ω_{ij} is the probability of the i →j transitions while τ_{ij} is the inverse of the transition probability.
- **k** is the coupling constant for the energy transfer process between silicon nanoparticles and Er^{3+} ions. It was assumed that the coupling constant scales with distance following an exponential decay [66,305,306].

Only one type of energy transfer has been considered, intra-band energy transfer from the highest excitonic level. Direct transfer to the first excited erbium state has not been taken in account. Radiative or non-radiative transitions from the second excited to the ground erbium state have not been considered. Only relaxation path for the second excited erbium state is trough the first excited erbium state.

The model is valid only for the initial dynamics after the pulsed excitation, thus the radiative recombination of excitons (slow component, see **Figure 43** and **Figure 44**) has been neglected. The inter-nanocluster transport could be a very fast process [157,159] but it was not considered either. Up-conversion mechanism was not detected in sample [297], therefore it was not included.

Once an exciton has been formed in level Ex3, it can relax either to level Ex2 or to an internal effective-trap-state transferring the energy difference to an Er^{3+} nearby, which gets excited. If relaxation to level Ex2 occurs, the carrier can be re-excited back to level Ex3 by an Auger or alternatively can radiatively recombine to the level Ex1, emitting photons responsible for the Si-nc emission band reported in **Figure 41a**. Thus, Auger mechanisms could be considered more as a feedback than a detrimental process, similar to a case of zero-phonon emission [200].

Excitons from the effective trap level cannot recombine radiatively so they are considered totally inactive in terms of visible PL emission. This has been indicated with a dashed arrow in **Figure 81**. The existence of a "trap-like" state, through which silicon nanoparticles sensitize Er3+ ions, has been a recurring idea in several models of energy exchange mechanism [292,366].

The existence of a "trap-like" state through which the Si-nc could sensitize Er^{3+} ions is necessary to explain the decrease of the whole VIS-PL spectra when Er^{3+} ions are introduced in the SRO matrix. This state is assumed in the model as an effective level (correlated with the presence of Si-nc in the matrix) of undefined origin [37,67,270,302].

It is worth to note that a good selection of the different parameters (keeping the values related with experimental constraints) allows reproducing the experimental dynamics of both samples just by "switching on" the transfer mechanism. An example of the fits of experimental data for samples A and B is reported in **Figure 82.** Double annealed samples

can be fitted nicely as well using the same model, leading similar values. More details on the modeling can be found elsewhere [319].

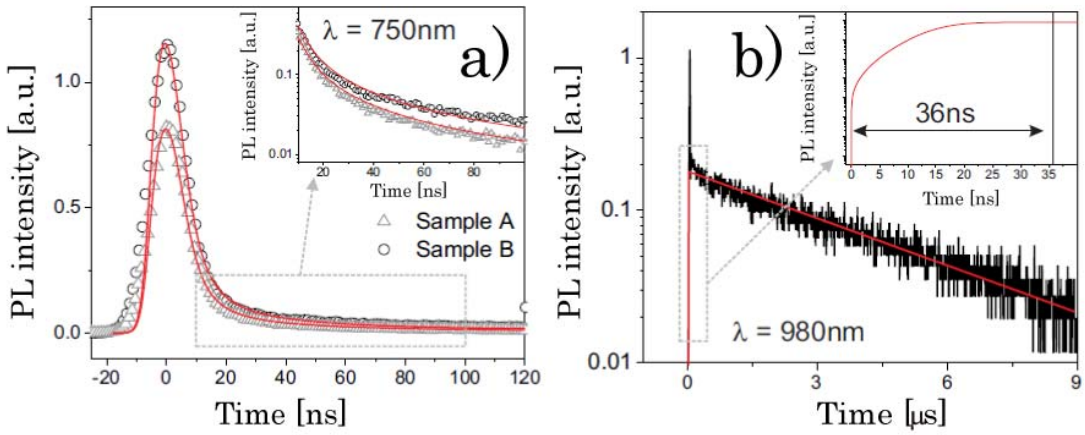

***Figure 82** – (**a**) Comparison of experimental and simulated decays for sample A and B. The intra-band recombination probability found is $w_{32} = 1 \pm 2 \times 10^{10}\ s^{-1}$, while the Auger coefficient $C_A = 2 \pm 3 \times 10^{32}\ cm^6/s$. (**b**) Fit of $^4I_{11/2} - {}^4I_{15/2}$ decay. From the fit a transfer time $\tau_{transfer} = 36 \pm 10$ ns is estimated.*

III. Derivation of the Equation 9

The PL dynamics of the $^4I_{13/2} - {}^4I_{15/2}$ transition of Er^{3+} ions (at **λ** = 1535 nm, transition from the first excited to fundamental state, see **Figure 38**) is characterized by two contributions (**Figure 49**): a very fast direct one (on ≈ ns timescale) and a slow (on ≈ μs timescale) process caused by the internal relaxation from the higher excited states of Er^{3+} ions. The very fast decaying initial PL contribution is not considered, since regardless of its origin, its contribution to the total PL intensity is insignificant.

Therefore, the time evolution of the PL signal can be described by the following equation:

$$I_{PL}(t) = I_{Background} + A_{Fast}\exp[-(t-t_0)/t_2] + A_{Slow}\{1-\exp[-(t-t_0)/t_1]\}\exp(-[t-t_0]/t_2) \quad (23)$$

where $\mathbf{I_{Background}}$ (background level) and $\mathbf{t_0}$ (laser pulse arrival time) are fit parameters, $\mathbf{t_1}$ = 4.2 μs and $\mathbf{t_2}$ = 5.5 ms are fixed quantities (rise and decay of $^4I_{13/2} - {}^4I_{15/2}$ transition under pulsed UV excitation (see **Figure 46** and **Figure 49**)), and have been independently measured (see section 3.4.2 and Ref. [213]). $\mathbf{t_2}$ is the decay constant of the first excited state while $\mathbf{t_1}$ is the measure of the internal relaxation time. The other fit parameters are $\mathbf{A_{Slow}}$ and $\mathbf{A_{Fast}}$. $\mathbf{A_{Fast}}$ is the direct contribution to the total PL while $\mathbf{A_{Slow}}$ gives the contribution by the internal relaxation from higher energy states.

The first exponential term describes the PL signal evolution coming from the fraction of the Er^{3+} ions population that has been directly excited to the first excited state while the second term gives the PL signal of the Er^{3+} ions that has been excited to higher states. In this last case, PL follows an internal relaxation from the higher states to the first excited state. On the timescale of the observation, the amplitude of the later one is a function of time as the

internal relaxation continues (Eq. 23)) causing the complex exponential dependence of the PL signal in time.

It is assumed that the direct excitation to the first (and higher) excited states is instantaneous (faster than the time resolution of our detection system ≈ 40 ns) and that the relaxation from the higher excited states to the $^4I_{13/2}$ state can be well described by a decaying single exponential function with a characteristic time $\mathbf{t_1}$ = 4.2 μs. Note that Eq. 23 and parameter physical interpretation is different with respect to what can be found in similar works [110,290].

By introducing the parameter $\mathbf{A_{All}}$, which is the sum of the previous two contributions, or in other words, the total contribution to the first excited state:

$$A_{All} = A_{Fast} + A_{Slow} \tag{24}$$

Eq. 23 could be rewritten as:

$$\begin{aligned} I_{PL}(t) &= I_{Background} + A_{Fast}\exp[-(t-t_0)/t_2] + A_{Slow}\exp[-(t-t_0)/t_2] \\ &\quad -A_{Slow}\exp[-(t-t_0)/t_1]\exp[-(t-t_0)/t_2] \\ &= I_{Background} + A_{All}\exp[-(t-t_0)/t_2] - A_{Slow}\exp\{[t_2(t-t_0)+t_1(t-t_0)]/[t_1t_2]\} \end{aligned} \tag{25}$$

Knowing that $\mathbf{t_1}$ is more than three orders of magnitude smaller than $\mathbf{t_2}$, Eq. 25 can be simplified to:

$$I_{PL}(t) = I_{Background} + A_{All}\exp[-(t-t_0)/t_2] - A_{Slow}\exp[-(t-t_0)/t_1] \tag{26}$$

This form is the one used for the fitting procedure.

IV. Quantification of the optically active fraction of erbium ions in Er^{3+} doped SRO films

An estimate of the optically active fraction of the erbium ions in Er^{3+} doped SRO film can be deduced with good accuracy from a series of standard PL measurements. For more accurate determination, data obtained in the procedure described in following, need to be combined with μ-PL measurements following the procedure in Ref. [296], obtaining a data set that spans a very broad range of excitation photon fluxes.

Quantification of the optically active fraction of erbium ions is done, using a comparative analysis with a sample whose absolute characteristics are known. In this work as a reference sample it was used sample C from **Table 1**. In the first step detection has to be calibrated with the help of a reference sample. Absolute value of emitted photon flux $\mathbf{\Phi_{em}}$ can be expressed as a function of the excited state population of erbium ions in reference sample $\mathbf{N_2^{ref}}$:

$$\Phi_{em} = \frac{V_{exc}^{ref} * N_2^{ref}}{\tau_{rad}^{ref}} \tag{27}$$

Where V_{exc} is excited volume of reference sample and τ_{rad}^{ref} is the radiative lifetime of the erbium ions in the reference sample. τ_{rad}^{ref} = 18 ms for sample C from **Table 1** was assumed, being the value reported for erbium doped bulk silica [260]. For the soda-lime glass (as in case of sample C) reports of erbium radiative lifetime vary between 16 ms [266] and 22 ms [259], making the value of bulk silica a good approximation.

Sample C and all other samples characterized in this work were thinner than the focal depth of lenses used to focus the resonant excitation light (λ_{exc} = 980 nm) on the samples, thus the excitation photon flux across the samples could be considered as constant. Under resonant λ_{exc} = 980 nm excitation, absorption due to silicon nanoclusters was considered as negligible and all the erbium related photoluminescence was attributed to direct excitation.

Excited state population of reference sample N_2^{ref} can be found knowing the excitation conditions from:

$$N_2^{ref} \approx \sigma_{abs}^{ref}(980nm) * \Phi_{exc} * \tau_{PL}^{ref} * N_{total}^{ref} \tag{28}$$

Where σ_{abs}^{ref} is the absorption cross-section for erbium ions for resonant λ = 980 nm excitation in a reference sample (soda-lime glass in case of sample C, σ_{abs}^{ref} = 1.02 x 10^{-21} cm^2, taken from the Ref. [261]). PL lifetime for the reference sample was measured to be τ_{PL}^{ref} = 7.7 ms.

It was assumed that all erbium ions in reference sample are optically active and a value of a total content from **Table 1** was used in equation 28.

Eq. 28 is a simplified version of:

$$N_2^{ref} = N_{total}^{ref} * \frac{\sigma_{abs}^{ref}(980nm) * \Phi_{exc}}{\sigma_{abs}^{ref}(980nm) * \Phi_{exc} + \frac{1}{\tau_{PL}^{ref}}}. \tag{29}$$

Eq. 29 is derived for the excited state population under the assumption of quasi-two level where the relaxation probability is given by $(\tau_{PL}^{ref})^{-1}$. Quasi-two level system is a good approximation for erbium ions as the typical recombination times for $^4I_{13/2} - {}^4I_{15/2}$ transition are orders of magnitude longer than any other internal relaxation time [271]. In the limit of low excitation photon flux regime when $(\tau_{PL}^{ref})^{-1} >> \sigma_{abs}^{ref} * \Phi_{exc}$ Eq. 29 reduces to Eq. 28.

If the cooperative up-conversion is considered, more complex form is found:

$$N_2^{ref} = \frac{\left[\left(\sigma_{abs}^{ref}(980nm) * \Phi_{exc} + \frac{1}{\tau_0}\right)^2 + 4 * \sigma_{abs}^{ref}(980nm) * C_{up}^{ref} * N_{total}^{ref} * \Phi_{exc}\right]^{1/2}}{2 * C_{up}^{ref}} - \frac{\left(\sigma_{abs}^{ref}(980nm) * \Phi_{exc} + \frac{1}{\tau_0}\right)}{2 * C_{up}^{ref}} \tag{30}$$

where C_{up}^{ref} is cooperative up-conversion coefficient for the reference sample and τ_0 would be a decay time in the absence of the cooperative up-conversion. C_{up}^{ref} and τ_0 have to be determined independently by fitting the experimental data with [271]

$$\frac{1}{\tau_{PL}^{ref}(\Phi_{exc})} = \frac{N_2^{ref} * C_{up}^{ref}}{\ln(1+\tau_0 * N_2^{ref} * C_{up}^{ref})} \quad (31)$$

For more accurate modelling of cooperative up-conversion see Ref. [61,367,368]. In the limit of low excitation photon fluxes Eq. 30 reduces to Eq. 28 as well.

Detection calibration was always performed in the limit of low excitation photon fluxes where Eq. 28 could be applied.

Once the detection is calibrated the excited state population of the samples can be easily determined inverting Eq. 27 and using the samples parameters. For sample A from **Table 1** τ_{rad} = 16 ms was used. Choice of radiative value of lifetime used for the thin films has been discussed in section 1.1.3.

For the determination of the optically active fraction of erbium ions in the samples one of the Eq. 28, 29 or 30 can be used for fitting the experimental data, depending on the excitation conditions and presence or absence of the cooperative up-conversion. For sample A from **Table 1**, Eq. 29 was used [296], while for the thin films for the electrical excitation Eq. 30 was used.

V. Quantification of the sensitized fraction of erbium ions in Er^{3+} doped SRO films

Calibration of the detection system is done in a manner analogous to what described in section IV of Appendix to Chapter 3. In order to quantify the sensitized fraction of erbium ions samples are excited in visible. For experimental simplicity reference sample (sample C) can be excited in visible as well. In this case σ_{abs}^{ref} (488 nm) = 2 x 10^{-21} cm^2 or σ_{abs}^{ref} (476 nm) = 5 x 10^{-23} cm^2 are used in Eq. 28 for calibration purposes [261].

Experimental data obtained from the samples can be fitted by Eq. 29 or Eq. 30. In both cases excitation cross section σ_{eff} for erbium ions for that particular sample has to be used. Excitation cross section is a function of excitation photon flux and needs to be determined independently for all values of excitation photon flux used.

For a quasi-two level system it can be demonstrated that [271]:

$$\frac{1}{\tau_r} - \frac{1}{\tau_d} = \sigma_{eff} * \Phi_{exc} \quad (32).$$

where τ_r and τ_d are rise and decay times respectively, of PL for that particular excitation photon flux Φ_{exc}. This relationship can be used to for the determination of the σ_{eff}.

VI. Cut-back method

To evaluate passive propagation losses of a single mode channel like optical waveguides, the cut-back method is often employed [369]. In this method light is injected into the waveguide employing a tapered optical fiber or objective with sub-micrometric position

control. At the opposite edge of the waveguide, the transmitted signal is collected by detection instruments.

Propagation losses inside of the waveguide are a function of the travelled distance (**L**) according to the Beer-Lambert law:

$$\frac{I_{out}}{I_{in}} = A_0 * \exp(-\alpha_{propagation} * L) \tag{33}$$

Where $\mathbf{I_{out}}$ and $\mathbf{I_{in}}$ are light intensity at the output and input of the waveguide respectively, $\mathbf{A_0}$ is a constant term, $\boldsymbol{\alpha_{propagation}}$ are propagation losses and **L** is the waveguide length. All the other losses are represented by the constant factor $\mathbf{A_0}$. The main contribution to this class is given by the mismatch between the input beam and the waveguide field modal shape (coupling losses).

Using waveguides of different lengths it is possible to separate propagation (distance dependent) and coupling losses (distance independent) contributions.

In the single mode waveguide there is only one transmission maximum as a function of exact input position, corresponding to a maximum overlap of the input and guided mode spatial profiles allowing for the reproducible alignment procedure. In the multimode waveguides this is not true anymore, making the cut-back method unreliable.

Conclusions

The work in this thesis has been centered on the light emitting properties of silicon nanocrystals and the possible applications of this particular material platform to various topics ranging from bio-imaging to erbium ion sensitization.

Silicon nanocrystals as bio-imaging agent have been investigated by employing colloidal dispersion of individual silicon nanocrystals where surface properties could be controlled to a great extent. By using a suitable functionalization scheme, high quality hydrophilic luminescent nanoparticles were produced. Importantly, very stable PL characteristics in ethanol suspension have been demonstrated allowing for easy storage.

In particular, it was demonstrated that a limited agglomeration occurs on nanoscale leading to increased scattering of light by dynamic agglomeration, undermining the optical performance of this colloidal system. The agglomeration impact on light emitting performance of this system has been studied and established in this work and alternative approach to mitigate this phenomenon was individuated and tested. As the more complete surface coverage by functionalizing molecules is rather challenging to achieve from the chemical point of view, the effect of surfactants as a physical coating was explored successfully to decrease agglomeration.

Using the improvements in the physical coating, bio-imaging on living cells (*in vitro*) was demonstrated showing that silicon nanocrystals have a great potential in bio-imaging and offer a promising alternative to commonly used fluorescence dyes.

A part from being good light emitters, silicon nanocrystals could also amplify the light. This is a reason why the part of the work in this thesis has been dedicated to the investigation of silicon nanocrystals as a gain material. While most of the studies on this topic are concentrated on the nanocrystal surface as a driving mechanism behind the optical amplification, the work presented in this thesis concerns the study of a zero phonon (direct) optical transition as a possible source of optical amplification in this material system. To this scope, investigation of the dynamics of the system on a nanosecond time-scale and under high excitation conditions has been employed.

For the first time this type of emission has been observed in samples prepared by a PECVD. As well, it was the first time this type of emission was observed in hydrogen passivated silicon nanocrystals.

Additional insight on ultrafast dynamics has been obtained by using optical cavities in the form of optically active free-standing micro-disk resonators. Extensive characterization of photoluminescence properties from the cavity-embedded Si-ncs from a single micro-disk resonator has been explored. Experimental conditions under which the zero-phonon band could be clearly observed were individuated, leading to two orders of magnitude higher visibility of this band, respect the best results ever reported. Moreover, the zero-phonon PL coupling to the resonant modes of an optical cavity was demonstrated.

Although, the coupling was demonstrated, the visibility of the whispering-gallery modes in the spectral region of interest, where optical gain was expected, was low leading to inconclusive data and qualitative consideration on the presence of stimulated emission in the samples. As a major drawback, obstructing the more quantitative analysis, a poor performance of the chosen optical resonator was proposed.

The first steps towards optical amplification exploiting the zero-phonon emission have been made by demonstrating the zero-phonon emission in samples used and by individuating the experimental conditions under which zero-phonon emission could be clearly observed and studied. In addition, the validity of the approach where active optical cavity is used to probe the ultrafast dynamics has been confirmed. Results obtained indicate that zero-phonon emission could be exploited for optical amplification in this system although further analysis is needed to determine to what extent (laser action?).

To that end a new series of micro-disk resonators have been produced and are waiting to be characterized. In particular, resonator size have been varied from 4 to 10 μm of diameter with different silicon excess as well (different refractive index and spectral position of zero-phonon band) allowing for precise tuning of radiative losses. In addition, a series of resonators with an integrated bus waveguide have been produced in order to mitigate drawbacks of far field collection. Moreover, novel coupled asymmetric micro-disc resonators have been produced. Preliminary simulations show directional in plane emission from this structure allowing for more efficient far field collection.

Finally, in the last part of this thesis a study of Er^{3+}-doped Silicon-Rich-Oxide (SRO) materials and Er^{3+}-doped SRO based devices is presented. This part of the work differs from the rest of the work reported in this thesis as is not focused on the light emitting properties of silicon nanocrystals but mostly on their non-radiative process engineering (energy transfer to erbium ions).

Er^{3+} doped SRO opens the route towards compact waveguide amplifiers and lasers and allows for the possibility of electrical injection schemes, which are not realizable in standard erbium amplifiers used in EDFA for telecom applications.

The sensitization mechanism between silicon nanoparticles and erbium ions was studied and its complex nature was illustrated. Although, the acquired knowledge of physics involved was not sufficient for formulation of a complete working theory of the energy transfer process, some important physical aspects of this process have been elucidated paving the way towards its complete understanding.

By employing extensive optical, electrical and structural characterization a pressing drawback in this material has been identified. Clustering induced loss of optical activity of erbium ions has been shown to be responsible for low optical performance of active material in all cases considered. As a possible remedy to low performance of Er^{3+} doped SRO devices, lowering of erbium concentration has been proposed with direct penalty on expected device

performance and more rigid device design and fabrication requirements (lower optical losses) and larger device footprint.

However, even in material suffering from the above mentioned downsides by means of pump& probe experiments an internal gain has been measured in optically pumped Er^{3+}-doped SRO active waveguide, demonstrating the feasibility of the approach although further optimization is still needed.

A particular advantage of this approach is the possibility of electrical pumping of erbium ions. To that end, novel opto-electronic structures were proposed, modeled and manufactured and preliminary results of their performance were presented while the complete characterization is under way.

While the results obtained so far are most certainly interesting, additional characterization is necessary in order to evaluate the suitability of proposed design.

In this thesis I've tried to assess suitability of silicon nanocrystals as a material platform in a number of various applications departing from the basic physical properties governing the behavior of this system. While only a few potential applications and physical aspects behind them were discussed in detail in this thesis, a complete list of possible applications is far from being complete.

A part from previously mentioned, appealing properties of silicon nanocrystals as light emitter, gain medium and rare earth sensitizer, silicon nanocrystals could offer other functionalities. The development of highly nonlinear integrated devices is a key step towards the achievement of ultra-fast and low–power consumption optical signal processing in silicon.

It has been shown that Si-nc/SiO_2 displays a high Kerr nonlinearity at telecom wavelengths as a consequence of both quantum confinement and dielectric mismatch effects [370]. This makes silicon nanocrystals one of the key materials for future silicon-based nonlinear optical devices such as all optical switches and modulators. The possibility of realization of all optical switching has been already successfully realized by means of ring resonators based on Si:nc slot waveguides [371]. Equally exciting is the possibility of performing wavelength conversion in the telecom communication band by exploiting the four-wave-mixing, as recently demonstrated [372].

My current work deals as well with the non-linear optical properties of silicon nanocrystals and their possible use as a basis for a new generation of integrated non-linear devices. In order to explore the feasibility of this approach a new geometry for optical coupling (vertical coupling) has been used for coupling with active high Q factors optical cavities. In this way, simplified on-chip light distribution, more controllable manufacturing and easy characterization of devices are achieved.

This work is still in its initial phase and therefore it was not included as a separate chapter in this thesis, however for the sake of completeness it is mentioned here.

List of publications

Journal publications (in international peer-reviewed journals) :

1. **N. Prtljaga**, D. Navarro-Urrios, A. Pitanti, F. Ferrarese Lupi, B. Garrido and L. Pavesi "Silicon nanoclusters sensitization of erbium ions under low-energy optical excitation" submitted to ***J. Appl. Phys.*** ;
2. J. M. Ramirez, F. Ferrarese Lupi, O. Jambois, Y. Berencén, D. Navarro-Urrios, A. Anopchenko, A. Marconi, **N. Prtljaga**, A. Tengattini, L. Pavesi, J. P. Colonna, J. M. Fedeli and B. Garrido "Erbium emission in MOS light emitting diodes: from energy ions to direct impact excitation" ***Nanotechnology*** **23** (2012) 125203 (8 pp);
3. A. Anopchenko, A. Tengattini, A. Marconi, **N. Prtljaga**, N. Daldosso, , J. M. Ramirez, O. Jambois, Y. Berencén, D. Navarro-Urrios, B. Garrido, F. Milesi, J. P. Colonna, J. M. Fedeli and L. Pavesi "Bipolar pulsed excitation of erbium doped silicon LEDs" accepted to ***J. Appl. Phys.***;
4. O. Jambois, J. M. Ramirez, Y. Berencén, D. Navarro-Urrios, A. Anopchenko, A. Marconi, **N. Prtljaga**, A. Tengattini, P. Pellegrino, N. Daldosso, L. Pavesi, J. P. Collona, J. M. Fedeli and B. Garrido "Effect of the annealing treatments on the electroluminescence efficiency of SiO_2 layers doped with Si and Er" ***J. Phys. D: Appl. Phys*** . **45** (2012) 045103 (5 pp);
5. J. M. Ramirez, O. Jambois, Y. Berencén, D. Navarro-Urrios, A. Anopchenko, A. Marconi, **N. Prtljaga**, N. Daldosso, L. Pavesi, J. P. Collona, J. M. Fedeli and B. Garrido "Polarization strategies to improve the emission of Si based light sources emitting at 1.55 μm" ***Mater. Sci. Eng., B*** (2011) in press (5 pp);
6. S. Manna, **N. Prtljaga**, S. Das, R. K. Singha, N. Daldosso, S. K. Ray and L. Pavesi "Growth and photoluminescence characteristics of Er doped Ge nanowires" ***Nanotechnology*** **23** (2012) 065702 (7 pp);
7. D. Navarro-Urrios, F. Ferrarese Lupi, **N. Prtljaga**, A. Pitanti, O. Jambois, J. M. Ramirez, Y. Berencén, N. Dalsosso, B. Garrido and L. Pavesi "Copropagating pump and probe experiments on Si-nc in SiO_2 rib waveguides doped with Er: the role of "dark" ions" ***Appl. Phys. Lett.*** **98** (2011) 231114 (3 pp);
8. O. Jambois, J. M. Ramirez, Y. Berencen, D. Navarro-Urrios, S. Hernandez, A. Anopchenko, A. Marconi, **N. Prtljaga**, N. Daldosso, L. Pavesi, J. P. Colonna, J. M. Fedeli and B. Garrido "Effect of the annealing treatments on the transport and electroluminescence properties of SiO2 layers doped with Er and Si nanoclusters" ***MRS Proceedings*** **1289** (2011) mrsf10-1289-h05-11 (7 pp)

9. **N. Prtljaga**, E. D'Amato, A. Pitanti, R. Guider, E. Froner, S. Larcheri, M. Scarpa and L. Pavesi "Photoluminescence of hydrophilic silicon nanocrystals in aqueous solutions" ***Nanotechnology*** **22** (2011) 215704 (9 pp);
10. E. Froner, E. D'Amato, R. Adamo, **N. Prtljaga**, S. Larcheri, L. Pavesi, A. Rigo, C. Potrich and M. Scarpa "Deoxycholate as an efficient coating agent for hydrophilic silicon nanocrystals" ***J. Colloid. Interf. Sci.*** **358** (2011) 86-92 (7 pp);
11. **N. Prtljaga**, D. Navarro-Urrios, A. Marconi, A. Anopchenko, J. P. Colonna, F. Milesi, N. Daldosso, O. Jambois, B. Garrido, J. M. Fedeli and L. Pavesi "Erbium implanted silicon rich oxide thin films suitable for slot waveguides applications" ***Opt. Mat.*** **33** (2011) 1083-1085 (3 pp);
12. D. Navarro Urrios, O. Jambois, F. Ferrarese Lupi, P. Pellegrino, B. Garrido A. Pitanti, **N. Prtljaga**, N. Daldosso and L. Pavesi "Si nanoclusters coupled to Er3+ ions in a SiO2 matrix for optical amplifiers" ***Opt. Mat.*** **33** (2011) 1086-1090 (5 pp);
13. A. Pitanti, D. Navarro-Urrios, **N. Prtljaga**, N. Daldosso, F. Gourbilleau, R. Rizk, B. Garrido and L. Pavesi "Energy transfer mechanism and Auger effect in Er^{3+} coupled silicon nanoparticle samples" ***J. Appl. Phys.*** 108 (2010) 053518 (8 pp);

Journal publications (in national journals):

1. Anopchenko, F. J. Aparicio Rebollo, P. Bettotti, F. Bianco, P. Belluti, M. Cazzanelli, K. Fedus, E. Froner, D. Gadolfi, M. Ghuliniyan, N. Kumar, Y. Jestin, P. Ingenhoven, S. Larcheri, L. Lunelli, M. Mancinelli, A. Marconi, E. Moser, L. Pasquardini, C. Pederzolli, C. Potrich, **N. Prtljaga**, G. Pucker, F. Ramiro Manzano, E. Rigo, M. Scarpa, F. Sgrignuoli, A. Tengattini and L. Pavesi "La nanofotonica in silicio e la fotonica con il nanosilicio" accepted to ***Il Nuovo Saggiatore***;

Acknowledgments

I would like to thank my supervisor, Prof. Lorenzo Pavesi, for introducing me to the world of scientific research and the patient guidance and advice he has provided throughout my time as his PhD student.

I am grateful to everyone who directly or indirectly supported and contributed to the writing of this dissertation. To all NL group members, current and past, for their help and shared knowledge. To all the members of research groups that I had opportunity to visit and collaborate with for enriching my research experience. To the administrative staff, for their help, support and patience.

I would like to thank to the committee members for reading this thesis. Special thanks to the University of Trento and the European Commission (HELIOS project) for financing my PhD.

I am grateful to my fellow PhD students, for their encouragements and friendship. To many more for making the part of this period of my life.

To my friends and loved ones for their support and love.

Bibliography

[1] F. K. Lutgens and E. J. Tarbuck, *Essentials of Geology (7th Edition)*, 7th ed. (Prentice Hall College Div; 7th edition, 2000), p. 449.

[2] F. H. Nielsen, Annual Review of Nutrition **4**, 21-41 (1984).

[3] C. Exley, Journal of Inorganic Biochemistry **69**, 139-144 (1998).

[4] R. L. Cowie, J. Murray, and M. R. Becklake, in *Murray and Nadel's Textbook of Respiratory Medicine - Volume 2/PART III* , edited by J. F. Murray, J. A. Nadel, R. J. Mason, C. V. Broaddus, T. R. Martin, T. E. J. King, and D. E. Schraufnagel, 5th ed. (Elsevier, Philadelphia, 2010).

[5] V. Castranova, Environmental Health Perspectives **102**, 65 (1994).

[6] X. Shi, Y. Mao, L. N. Daniel, U. Saffiotti, N. S. Dalal, and V. Vallyathan, Environmental Health Perspectives **102**, 149 (1994).

[7] J. Bardeen and W. Brattain, Physical Review **75**, 1208 (1949).

[8] P. Siffert and E. Krimmel, editors, *Silicon: Evolution and Future of a Technology* (Springer, Berlin, 2004), p. 534.

[9] E. Haller, Materials Science in Semiconductor Processing **9**, 408–422 (2006).

[10] A. Saxena, *Invention of Integrated Circuits: Untold Important Facts* (World Scientific Pub Co Inc, Singapore, 2009), p. 564.

[11] G. E. Moore, Electronics Magazine **38**, 82–85 (1965).

[12] S. Borkar, P. Dubey, K. Kahn, D. Kuck, H. Mulder, S. Pawlowski, and J. Rattner, Technology @ Intel Magazine 1-10 (2005).

[13] R. S. Chau, Technology @ Intel Magazine 1-7 (2004).

[14] D. A. B. Miller, Applied Optics **49**, F59-70 (2010).

[15] G. Chen, H. Chen, M. Haurylau, N. A. Nelson, D. H. Albonesi, P. M. Fauchet, and E. G. Friedman, in *Interconnect Technology Conference, 2006 International* (IEEE, 2006), pp. 39–41.

[16] D. Liang and J. E. Bowers, Nature Photonics **4**, 511-517 (2010).

[17] H. Park, A. Fang, S. Kodama, and J. Bowers, Optics Express **13**, 9460-4 (2005).

[18] A. W. Fang, H. Park, O. Cohen, R. Jones, M. J. Paniccia, and J. E. Bowers, Optics Express **14**, 9203-10 (2006).

[19] J. Van Campenhout, P. Rojo Romeo, P. Regreny, C. Seassal, D. Van Thourhout, S. Verstuyft, L. Di Cioccio, J.-M. Fedeli, C. Lagahe, and R. Baets, Optics Express **15**, 6744-9 (2007).

[20] M. E. Groenert, C. W. Leitz, A. J. Pitera, V. Yang, H. Lee, R. J. Ram, and E. A. Fitzgerald, Journal of Applied Physics **93**, 362 (2003).

[21] L. Cerutti, J. B. Rodriguez, and E. Tournie, IEEE Photonics Technology Letters **22**, 553-555 (2010).

[22] J. Liu, X. Sun, R. Camacho-Aguilera, L. C. Kimerling, and J. Michel, Optics Letters **35**, 679–681 (2010).

[23] D. Liang and J. E. Bowers, Journal of Vacuum Science & Technology B: Microelectronics and Nanometer Structures **26**, 1560 (2008).

[24] D. Liang, J. E. Bowers, D. C. Oakley, A. Napoleone, D. C. Chapman, C.-L. Chen, P. W. Juodawlkis, and O. Raday, Electrochemical and Solid-State Letters **12**, H101 (2009).

[25] J. M. Fedeli, L. Di Cioccio, D. Marris-Morini, L. Vivien, R. Orobtchouk, P. Rojo-Romeo, C. Seassal, and F. Mandorlo, Advances in Optical Technologies **2008**, 1-15 (2008).

[26] X. Sun, J. Liu, L. C. Kimerling, and J. Michel, Optics Letters **34**, 1198-200 (2009).

[27] O. Boyraz and B. Jalali, Optics Express **12**, 5269-73 (2004).

[28] H. Rong, A. Liu, R. Jones, O. Cohen, D. Hak, R. Nicolaescu, A. Fang, and M. Paniccia, Nature **433**, 292-4 (2005).

[29] H. Rong, R. Jones, A. Liu, O. Cohen, D. Hak, and A. Fang, Nature **433**, 725-8 (2005).

[30] S. G. Cloutier, P. A. Kossyrev, and J. Xu, Nature Materials **4**, 887-91 (2005).

[31] M. J. Chen, J. L. Yen, J. Y. Li, J. F. Chang, S. C. Tsai, and C. S. Tsai, Applied Physics Letters **84**, 2163 (2004).

[32] S. Saito, Y. Suwa, H. Arimoto, N. Sakuma, D. Hisamoto, H. Uchiyama, J. Yamamoto, T. Sakamizu, T. Mine, S. Kimura, T. Sugawara, and M. Aoki, Applied Physics Letters **95**, 241101 (2009).

[33] A. D. Yoffe, Advances in Physics **50**, 1-208 (2001).

[34] D. Kovalev, H. Heckler, G. Polisski, and F. Koch, Physica Status Solidi (B) **215**, 871-932 (1999).

[35] M. Fujii, in *Silicon Nanocrystals: Fundamentals, Synthesis and Applications*, edited by L. Pavesi and R. Turan (Wiley-VCH Verlag GmbH & Co. KGaA, Weinheim, Germany, 2010), pp. 43-68.

[36] G. Hadjisavvas and P. Kelires, Physical Review Letters **93**, 1-4 (2004).

[37] G. Allan, C. Delerue, and M. Lannoo, Physical Review Letters **78**, 3161-3164 (1997).

[38] M. S. Hybertsen, Physical Review Letters **72**, 1514–1517 (1994).

[39] O. Lehtonen and D. Sundholm, Physical Review B **72**, 27-29 (2005).

[40] M. Luppi and S. Ossicini, Physical Review B **71**, 1-15 (2005).

[41] A. A. Konakov and V. A. Burdov, Journal of Physics. Condensed Matter : an Institute of Physics Journal **22**, 215301 (2010).

[42] Y. Niquet, C. Delerue, and G. Allan, Physical Review B **62**, 5109-5116 (2000).

[43] M. Wolkin, J. Jorne, P. Fauchet, G. Allan, and C. Delerue, Physical Review Letters **82**, 197-200 (1999).

[44] A. Saar, Journal of Nanophotonics **3**, 032501 (2009).

[45] D. Jurbergs, E. Rogojina, L. Mangolini, and U. Kortshagen, Applied Physics Letters **88**, 233116 (2006).

[46] M. L. Mastronardi, F. Maier-Flaig, D. Faulkner, E. J. Henderson, C. Kübel, U. Lemmer, and G. A. Ozin, Nano Letters **12**, 337-42 (2012).

[47] D. Kovalev, H. Heckler, M. Ben-Chorin, G. Polisski, M. Schwartzkopff, and F. Koch, Physical Review Letters **81**, 2803–2806 (1998).

[48] O. Bisi, S. Ossicini, and L. Pavesi, Surface Science Reports **38**, 1–126 (2000).

[49] L. Pavesi, L. Dal Negro, C. Mazzoleni, G. Franzò, and F. Priolo, Nature **408**, 440-4 (2000).

[50] K. Luterová, K. Dohnalová, V. Švrček, I. Pelant, J.-P. Likforman, O. Crégut, P. Gilliot, and B. Hönerlage, Applied Physics Letters **84**, 3280 (2004).

[51] M. H. Nayfeh, S. Rao, N. Barry, J. Therrien, G. Belomoin, A. Smith, and S. Chaieb, Applied Physics Letters **80**, 121 (2002).

[52] A. Anopchenko, A. Marconi, M. Wang, G. Pucker, P. Bellutti, and L. Pavesi, Applied Physics Letters **99**, 181108 (2011).

[53] H. Schweizer, M. Jetter, and F. Scholz, in *Topics in Applied Physics*, edited by P. Michler (Springer Berlin Heidelberg, Berlin, Heidelberg, 2003), pp. 185-236.

[54] H. M'ghaieth, H. Maaref, I. Mihalcescu, and J. C. Vial, Physical Review B **60**, 4450-4453 (1999).

[55] C. Delerue, M. Lannoo, G. Allan, E. Martin, I. Mihalcescu, J. Vial, R. Romestain, F. Muller, and A. Bsiesy, Physical Review Letters **75**, 2228–2231 (1995).

[56] C. Garcia, B. Garrido, P. Pellegrino, R. Ferre, J. A. Moreno, J. R. Morante, L. Pavesi, and M. Cazzanelli, Applied Physics Letters **82**, 1595 (2003).

[57] L. Pavesi, Advances in Optical Technologies **2008**, 1-12 (2008).

[58] M. Fujii, M. Yoshida, Y. Kanzawa, S. Hayashi, and K. Yamamoto, Applied Physics Letters **71**, 1198-1200 (1997).

[59] T. Förster, Radiation Research Supplement **2**, 326 (1960).

[60] D. L. Dexter, The Journal of Chemical Physics **21**, 836 (1953).

[61] P. Becker, N. Olsson, and J. R. Simpson, *Erbium-doped Fiber Amplifiers: Fundamentals and Technology* (Academic press, San Diego, 1999), p. 464.

[62] H.-S. Han, S.-Y. Seo, and J. H. Shin, Applied Physics Letters **79**, 4568 (2001).

[63] O. Jambois, F. Gourbilleau, A. J. Kenyon, J. Montserrat, R. Rizk, and B. Garrido, Optics Express **18**, 2230-5 (2010).

[64] I. Izeddin, a. Moskalenko, I. Yassievich, M. Fujii, and T. Gregorkiewicz, Physical Review Letters **97**, 2-5 (2006).

[65] C. J. Oton, W. H. Loh, and a. J. Kenyon, Applied Physics Letters **89**, 031116 (2006).

[66] B. Garrido, C. García, P. Pellegrino, D. Navarro-Urrios, N. Daldosso, L. Pavesi, F. Gourbilleau, and R. Rizk, Applied Physics Letters **89**, 163103 (2006).

[67] O. Savchyn, F. Ruhge, P. Kik, R. Todi, K. Coffey, H. Nukala, and H. Heinrich, Physical Review B **76**, 1-10 (2007).

[68] C. L. Amiot, S. Xu, S. Liang, L. Pan, and J. X. Zhao, Sensors **8**, 3082-3105 (2008).

[69] N. O'Farrell, A. Houlton, and B. R. Horrocks, International Journal of Nanomedicine **1**, 451-72 (2006).

[70] S. Sengupta, D. Eavarone, I. Capila, G. Zhao, N. Watson, T. Kiziltepe, and R. Sasisekharan, Nature **436**, 568-72 (2005).

[71] K. Welsher, Z. Liu, S. P. Sherlock, J. T. Robinson, Z. Chen, D. Daranciang, and H. Dai, Nature Nanotechnology **4**, 773-80 (2009).

[72] D. Kim, S. Park, J. H. Lee, Y. Y. Jeong, and S. Jon, Journal of the American Chemical Society **129**, 7661-5 (2007).

[73] E. B. Voura, J. K. Jaiswal, H. Mattoussi, and S. M. Simon, Nature Medicine **10**, 993-8 (2004).

[74] Z. Liu, C. Davis, W. Cai, L. He, X. Chen, and H. Dai, Proceedings of the National Academy of Sciences of the United States of America **105**, 1410-5 (2008).

[75] C. Kirchner, T. Liedl, S. Kudera, T. Pellegrino, A. Muñoz Javier, H. E. Gaub, S. Stölzle, N. Fertig, and W. J. Parak, Nano Letters **5**, 331-8 (2005).

[76] M. Green and E. Howman, Chemical Communications (Cambridge, England) 121-3 (2005).

[77] C. A. Poland, R. Duffin, I. Kinloch, A. Maynard, W. A. H. Wallace, A. Seaton, V. Stone, S. Brown, W. Macnee, and K. Donaldson, Nature Nanotechnology **3**, 423-8 (2008).

[78] J. F. Popplewell, S. J. King, J. P. Day, P. Ackrill, L. K. Fifield, R. G. Cresswell, M. L. di Tada, and K. Liu, Journal of Inorganic Biochemistry **69**, 177-80 (1998).

[79] J.-H. Park, L. Gu, G. von Maltzahn, E. Ruoslahti, S. N. Bhatia, and M. J. Sailor, Nature Materials **8**, 331-6 (2009).

[80] S. C. Bayliss, R. Heald, D. I. Fletcher, and L. D. Buckberry, Advanced Materials **11**, 318-321 (1999).

[81] J. Frangioni, Current Opinion in Chemical Biology **7**, 626-634 (2003).

[82] R. C. Benson and H. A. Kues, Physics in Medicine and Biology **23**, 159-163 (1978).

[83] L. T. Canham, Applied Physics Letters **57**, 1046 (1990).

[84] Z. Yuan, A. Anopchenko, N. Daldosso, R. Guider, D. Navarro-Urrios, A. Pitanti, R. Spano, and L. Pavesi, Proceedings of the IEEE **97**, 1250–1268 (2009).

[85] S. Godefroo, M. Hayne, M. Jivanescu, A. Stesmans, M. Zacharias, O. I. Lebedev, G. Van Tendeloo, and V. V. Moshchalkov, Nature Nanotechnology **3**, 174-8 (2008).

[86] M. J. Sailor and E. C. Wu, Advanced Functional Materials **19**, 3195-3208 (2009).

[87] J. G. C. Veinot, Chemical Communications (Cambridge, England) 4160-8 (2006).

[88] S. Zhang, J. Li, G. Lykotrafitis, G. Bao, and S. Suresh, Advanced Materials **21**, 419–424 (2009).

[89] Y. Li, X. Chen, and N. Gu, The Journal of Physical Chemistry. B **112**, 16647-53 (2008).

[90] S. Sato and M. T. Swihart, Chemistry of Materials **18**, 4083–4088 (2006).

[91] D. A. Eckhoff, J. N. Stuart, J. D. B. Sutin, J. V. Sweedler, and E. Gratton, The Journal of Chemical Physics **125**, 081103 (2006).

[92] H. S. Choi, W. Liu, P. Misra, E. Tanaka, J. P. Zimmer, B. Itty Ipe, M. G. Bawendi, and J. V. Frangioni, Nature Biotechnology **25**, 1165-70 (2007).

[93] F. Erogbogbo, K.-T. Yong, I. Roy, G. Xu, P. N. Prasad, and M. T. Swihart, ACS Nano **2**, 873-8 (2008).

[94] Y. He, Y. Su, X. Yang, Z. Kang, T. Xu, R. Zhang, C. Fan, and S.-T. Lee, Journal of the American Chemical Society **131**, 4434-8 (2009).

[95] Z. F. Li, E. T. Kang, K. G. Neoh, and K. L. Tan, Biomaterials **19**, 45-53 (1998).

[96] Z. Kang, Y. Liu, C. H. A. Tsang, D. D. D. Ma, X. Fan, N.-B. Wong, and S.-T. Lee, Advanced Materials **21**, 661-664 (2009).

[97] D. Gräf, M. Grundner, and R. Schulz, Journal of Vacuum Science & Technology A: Vacuum, Surfaces, and Films **7**, 808 (1989).

[98] X. Li, Y. He, S. S. Talukdar, and M. T. Swihart, Langmuir **19**, 8490–8496 (2003).

[99] X. Li, Y. He, and M. T. Swihart, Langmuir : the ACS Journal of Surfaces and Colloids **20**, 4720-7 (2004).

[100] A. Gupta and H. Wiggers, Nanotechnology **22**, 055707 (2011).

[101] Z. Zhou, L. Brus, and R. Friesner, Nano Letters **3**, 163-167 (2003).

[102] A. Puzder, A. J. Williamson, J. C. Grossman, and G. Galli, Journal of the American Chemical Society **125**, 2786-91 (2003).

[103] L. Koponen, L. Tunturivuori, M. Puska, and R. Nieminen, Physical Review B **79**, 1-6 (2009).

[104] Q. S. Li, R. Q. Zhang, S. T. Lee, T. A. Niehaus, and T. Frauenheim, The Journal of Chemical Physics **128**, 244714 (2008).

[105] M. E. Ahmed, J. P. Goss, R. J. Eyre, P. R. Briddon, and M. A. Taylforth, Journal of Physics: Conference Series **245**, 012046 (2010).

[106] R. J. Clark, M. K. M. Dang, and J. G. C. Veinot, Langmuir : the ACS Journal of Surfaces and Colloids **26**, 15657-64 (2010).

[107] P. M. Fauchet, Journal of Luminescence **70**, 294–309 (1996).

[108] B. Gelloz and N. Koshida, Applied Physics Letters **94**, 201903 (2009).

[109] C. Lindsey and G. Patterson, The Journal of Chemical Physics **73**, 3348-57 (1980).

[110] M. Fujii, K. Imakita, K. Watanabe, and S. Hayashi, Journal of Applied Physics **95**, 272 (2004).

[111] T. Takagahara and K. Takeda, Physical Review B **46**, 15578 (1992).

[112] J. Valenta, A. Fucikova, F. Vácha, F. Adamec, J. Humpolíčková, M. Hof, I. Pelant, K. Kůsová, K. Dohnalová, and J. Linnros, Advanced Functional Materials **18**, 2666-2672 (2008).

[113] I. Sychugov, R. Juhasz, J. Valenta, and J. Linnros, Physical Review Letters **94**, 4-7 (2005).

[114] A. Pitanti, M. Ghulinyan, D. Navarro-Urrios, G. Pucker, and L. Pavesi, Physical Review Letters **104**, 1-4 (2010).

[115] L. Pavesi and M. Ceschini, Physical Review B **48**, 17625-17628 (1993).

[116] G. Credo, M. Mason, and S. K. Buratto, Applied Physics Letters **74**, 1978-1980 (1999).

[117] D. Kovalev, J. Diener, H. Heckler, G. Polisski, N. Künzner, and F. Koch, Physical Review B **61**, 4485-4487 (2000).

[118] J. Rheims, J. Köser, and T. Wriedt, Measurement Science and Technology **8**, 601-605 (1997).

[119] G. M. Hale and M. R. Querry, Applied Optics **12**, 555 (1973).

[120] Y. He, Z.-H. Kang, Q.-S. Li, C. H. A. Tsang, C.-H. Fan, and S.-T. Lee, Angewandte Chemie **121**, 134-138 (2008).

[121] A. B. Sieval, B. van den Hout, H. Zuilhof, and E. J. R. Sudhölter, Langmuir **17**, 2172-2181 (2001).

[122] G. Mie, Annalen Der Physik **330**, 377-445 (1908).

[123] C. F. Bohren and D. R. Huffman, *Absorption and Scattering of Light by Small Particles* (Wiley-VCH Verlag GmbH, Weinheim, Germany, 1998), p. 544.

[124] Http://www.philiplaven.com/, (n.d.).

[125] M. A. Green and M. J. Keevers, Progress in Photovoltaics: Research and Applications **3**, 189-192 (1995).

[126] G. Ledoux, J. Gong, F. Huisken, O. Guillois, and C. Reynaud, Applied Physics Letters **80**, 4834 (2002).

[127] M. I. Mishchenko, L. D. Travis, and A. A. Lacis, *Scattering, Absorption and Emission of Light by Small Particles*, First (Cambridge University Press, Cambridge, UK, 2002), p. 445.

[128] S. Chattopadhyay and P. W. Bohn, Analytical Chemistry **78**, 6058-64 (2006).

[129] V. Chirvony, A. Chyrvonaya, J. Ovejero, E. Matveeva, B. Goller, D. Kovalev, A. Huygens, and P. de Witte, Advanced Materials **19**, 2967-2972 (2007).

[130] M. Balaguer, E. Pastor, L. Bychto, P. Atienzar, M. A. Miranda, E. Matveeva, and V. S. Chirvony, Physica Status Solidi (a) **205**, 2585-2588 (2008).

[131] C. A. Canaria, M. Huang, Y. Cho, J. L. Heinrich, L. I. Lee, M. J. Shane, R. C. Smith, M. J. Sailor, and G. M. Miskelly, Advanced Functional Materials **12**, 495 (2002).

[132] R. J. Hunter, *Zeta Potential in Colloid Science: Principles and Applications* (Academic Press Inc, New York, 1981), p. 386.

[133] Y. Li and N. Gu, The Journal of Physical Chemistry. B **114**, 2749-54 (2010).

[134] E. S. Pagac, D. C. Prieve, and R. D. Tilton, Langmuir **14**, 2333-2342 (1998).

[135] E. Fuguet, C. Ràfols, M. Rosés, and E. Bosch, Analytica Chimica Acta **548**, 95-100 (2005).

[136] M. Kulakci, U. Serincan, R. Turan, and T. G. Finstad, Nanotechnology **19**, 455403 (2008).

[137] H. Jang, L. E. Pell, B. A. Korgel, and D. S. English, Journal of Photochemistry and Photobiology A: Chemistry **158**, 111-117 (2003).

[138] S. Caamaño, A. Shiori, S. H. Strauss, and E. C. Orton, The Journal of Heart Valve Disease **18**, 101-5 (2009).

[139] A. N. Bashkatov, E. A. Genina, V. I. Kochubey, and V. V. Tuchin, Journal of Physics D: Applied Physics **38**, 2543-2555 (2005).

[140] A. M. Smith, M. C. Mancini, and S. Nie, Nature Nanotechnology **4**, 710-1 (2009).

[141] F. Erogbogbo, K. T. Yong, I. Roy, R. Hu, W. C. Law, W. Zhao, H. Ding, F. Wu, R. Kumar, M. T. Swihart, and others, ACS Nano **5**, 413-423 (2010).

[142] F. Erogbogbo, K.-T. Yong, R. Hu, W.-C. Law, H. Ding, C.-W. Chang, P. N. Prasad, and M. T. Swihart, ACS Nano **4**, 5131-8 (2010).

[143] J. W. Aptekar, M. C. Cassidy, A. C. Johnson, R. A. Barton, M. Lee, A. C. Ogier, C. Vo, M. N. Anahtar, Y. Ren, S. N. Bhatia, C. Ramanathan, D. G. Cory, A. L. Hill, R. W. Mair, M. S. Rosen, R. L. Walsworth, and C. M. Marcus, ACS Nano **3**, 4003-8 (2009).

[144] J. Choi, N. S. Wang, and V. Reipa, Bioconjugate Chemistry **19**, 680-5 (2008).

[145] F. De Angelis, A. Pujia, C. Falcone, E. Iaccino, C. Palmieri, C. Liberale, F. Mecarini, P. Candeloro, L. Luberto, A. de Laurentiis, G. Das, G. Scala, and E. Di Fabrizio, Nanoscale **2**, 2230-6 (2010).

[146] K. Fujioka, M. Hiruoka, K. Sato, N. Manabe, R. Miyasaka, S. Hanada, A. Hoshino, R. D. Tilley, Y. Manome, K. Hirakuri, and K. Yamamoto, Nanotechnology **19**, 415102 (2008).

[147] A. Karakuscu, R. Guider, L. Pavesi, and G. D. Sorarù, Journal of the American Ceramic Society **92**, 2969-2974 (2009).

[148] A. Gupta and H. Wiggers, Physica E: Low-dimensional Systems and Nanostructures **41**, 1010-1014 (2009).

[149] L. Mangolini, D. Jurbergs, E. Rogojina, and U. Kortshagen, Journal of Luminescence **121**, 327-334 (2006).

[150] M. R. Linford, P. Fenter, P. M. Eisenberger, and C. E. D. Chidsey, Journal of the American Chemical Society **117**, 3145-3155 (1995).

[151] H. Takagi, H. Ogawa, Y. Yamazaki, A. Ishizaki, and T. Nakagiri, Applied Physics Letters **56**, 2379 (1990).

[152] A. Filonov, S. Ossicini, F. Bassani, and F. D'Avitaya, Physical Review B **65**, 1-9 (2002).

[153] G. Allan and C. Delerue, Physical Review B **75**, 1-8 (2007).

[154] V. A. Belyakov and V. A. Burdov, Journal of Surface Investigation. X-ray, Synchrotron and Neutron Techniques **4**, 588-590 (2010).

[155] V. A. Belyakov, V. A. Burdov, R. Lockwood, and A. Meldrum, Bulletin of the Russian Academy of Sciences: Physics **74**, 1080-1082 (2010).

[156] A. Meldrum, R. Lockwood, V. A. Belyakov, and V. A. Burdov, Physica E: Low-dimensional Systems and Nanostructures **41**, 955-958 (2009).

[157] L. Titova, T. Cocker, D. Cooke, X. Wang, A. Meldrum, and F. Hegmann, Physical Review B **83**, 1-9 (2011).

[158] R. Lockwood and A. Meldrum, Physica Status Solidi (a) **206**, 965-968 (2009).

[159] R. Lockwood, A. Hryciw, and A. Meldrum, Applied Physics Letters **89**, 263112 (2006).

[160] C. Delerue, G. Allan, C. Reynaud, O. Guillois, G. Ledoux, and F. Huisken, Physical Review B **73**, 1-4 (2006).

[161] A. Yurtsever, M. Weyland, and D. A. Muller, Applied Physics Letters **89**, 151920 (2006).

[162] B. Goller, S. Polisski, H. Wiggers, and D. Kovalev, Applied Physics Letters **97**, 041110 (2010).

[163] D. Prendergast, J. C. Grossman, A. J. Williamson, J. L. Fattebert, and G. Galli, Journal of American Chemical Society **126**, 13827-13837 (2004).

[164] F. Trani, D. Ninno, and G. Iadonisi, Physical Review B **75**, 1-4 (2007).

[165] K. Seino, F. Bechstedt, and P. Kroll, Nanotechnology **20**, 135702 (2009).

[166] O. Guillois, Journal of Applied Physics **95**, 3677 (2004).

[167] R. Guerra, I. Marri, R. Magri, L. Martin-samos, O. Pulci, E. Degoli, and S. Ossicini, Physical Review B **75**, 1-9 (2010).

[168] K. Dunn, J. Derr, T. Johnston, M. Chaker, and F. Rosei, Physical Review B **80**, 1-9 (2009).

[169] K. Sato and K. Hirakuri, Journal of Applied Physics **100**, 114303 (2006).

[170] G. Zatryb, A. Podhorodecki, J. Misiewicz, J. Cardin, and F. Gourbilleau, Nanoscale Research Letters **6**, 106 (2011).

[171] J. Rowlette, R. Kekatpure, M. Panzer, M. Brongersma, and K. Goodson, Physical Review B **80**, 1-6 (2009).

[172] J. Linnros, N. Lalic, A. Galeckas, and V. Grivickas, Journal of Applied Physics **86**, 6128-6134 (1999).

[173] A. Meldrum, P. Bianucci, and F. Marsiglio, Optics Express **18**, 10230-46 (2010).

[174] R. Walters, J. Kalkman, A. Polman, H. Atwater, and M. de Dood, Physical Review B **73**, 2-5 (2006).

[175] R. J. Walters, G. I. Bourianoff, and H. a Atwater, Nature Materials **4**, 143-6 (2005).

[176] S. Ossicini, L. Pavesi, and F. Priolo, *Light Emitting Silicon for Microphotonics* (Springer-Verlag, Berlin, 2003), p. 282.

[177] L. D. Negro, M. Cazzanelli, N. Daldosso, Z. Gaburro, L. Pavesi, F. Priolo, D. Pacifici, G. Franzò, and F. Iacona, Physica E: Low- **16**, 297-308 (2003).

[178] M. Cazzanelli, D. Kovalev, L. Dal Negro, Z. Gaburro, and L. Pavesi, Physical Review Letters **93**, 1-4 (2004).

[179] K. Dohnalová, K. Žídek, L. Ondič, K. Kůsová, O. Cibulka, and I. Pelant, Journal of Physics D: Applied Physics **42**, 135102 (2009).

[180] P. M. Fauchet, J. Ruan, H. Chen, L. Pavesi, L. Dal Negro, M. Cazzaneli, R. G. Elliman, N. Smith, M. Samoc, and B. Luther-Davies, Optical Materials **27**, 745-749 (2005).

[181] H. Chen, J. H. Shin, P. M. Fauchet, J.-Y. Sung, J.-H. Shin, and G. Y. Sung, Applied Physics Letters **91**, 173121 (2007).

[182] V. A. Belyakov, V. A. Burdov, R. Lockwood, and A. Meldrum, Advances in Optical Technologies **2008**, 1-32 (2008).

[183] F. Zhou and J. D. Head, The Journal of Physical Chemistry B **104**, 9981-9986 (2000).

[184] B. M. Monroy, O. Crégut, M. Gallart, B. Hönerlage, and P. Gilliot, Applied Physics Letters **98**, 261108 (2011).

[185] L. Pavesi, Materials Today **8**, 18–25 (2005).

[186] D. Navarro-Urrios, a. Pitanti, N. Daldosso, F. Gourbilleau, R. Rizk, G. Pucker, and L. Pavesi, Applied Physics Letters **92**, 051101 (2008).

[187] R. D. Kekatpure and M. L. Brongersma, Nano Letters **8**, 3787-93 (2008).

[188] W. P. Dumke, Physical Review **127**, 1559-1563 (1962).

[189] C.-Y. Tsai, Journal of Applied Physics **99**, 053506 (2006).

[190] T. Trupke, M. a. Green, and P. Würfel, Journal of Applied Physics **93**, 9058 (2003).

[191] S. Imhof and A. Thränhardt, Physical Review B **82**, 1-6 (2010).

[192] M. J. Chen, C. S. Tsai, and M. K. Wu, Japanese Journal of Applied Physics **45**, 6576-6588 (2006).

[193] X. Sun, J. Liu, L. C. Kimerling, and J. Michel, Applied Physics Letters **95**, 011911 (2009).

[194] M. L. Cohen and J. R. Chelikowsky, *Electronic Structure and Optical Properties of Semiconductors* (Sprineger-Verlag, Berlin, 1988), p. 264.

[195] J. Valenta, a Fucikova, I. Pelant, K. Kůsová, K. Dohnalová, a Aleknavičius, O. Cibulka, a Fojtík, and G. Kada, New Journal of Physics **10**, 073022 (2008).

[196] J. P. Wilcoxon and G. A. Samara, Applied Physics Letters **74**, 3164-3166 (1999).

[197] D. S. English, L. E. Pell, Z. Yu, P. F. Barbara, and B. a. Korgel, Nano Letters **2**, 681-685 (2002).

[198] K. Kůsová, O. Cibulka, K. Dohnalová, I. Pelant, J. Valenta, A. Fucíková, K. Zídek, J. Lang, J. Englich, P. Matejka, P. Stepánek, and S. Bakardjieva, ACS Nano **4**, 4495-504 (2010).

[199] K. Dohnalová, K. Kůsová, O. Cibulka, L. Ondič, and I. Pelant, Physica Scripta **T141**, 014011 (2010).

[200] W. D. a M. de Boer, D. Timmerman, K. Dohnalová, I. N. Yassievich, H. Zhang, W. J. Buma, and T. Gregorkiewicz, Nature Nanotechnology **5**, 878-84 (2010).

[201] J. P. Wolfe, Physics Today **35**, 46 (1982).

[202] A. L. Efros and M. Rosen, Annual Review of Materials Science **30**, 475–521 (2000).

[203] M. V. Rama Krishna and R. a. Friesner, The Journal of Chemical Physics **96**, 873 (1992).

[204] D. Babic, Superlattices and Microstructures **22**, (1997).

[205] a. Moskalenko, J. Berakdar, a. Prokofiev, and I. Yassievich, Physical Review B **76**, 1-9 (2007).

[206] A. A. Prokofiev, A. S. Moskalenko, I. N. Yassievich, W. D. A. M. Boer, D. Timmerman, H. Zhang, W. J. Buma, and T. Gregorkiewicz, JETP Letters **90**, 758-762 (2010).

[207] P. Schmidt, R. Berndt, and M. Vexler, Physical Review Letters **99**, 1-4 (2007).

[208] A. Nozik, Annual Review of Physical Chemistry 193-231 (2001).

[209] a Sa'ar, Y. Reichman, M. Dovrat, D. Krapf, J. Jedrzejewski, and I. Balberg, Nano Letters **5**, 2443-7 (2005).

[210] E. Hendry, M. Koeberg, F. Wang, H. Zhang, C. de Mello Donegá, D. Vanmaekelbergh, and M. Bonn, Physical Review Letters **96**, 1-4 (2006).

[211] V. Klimov, A. Mikhailovsky, D. McBranch, C. Leatherdale, and M. Bawendi, Science (New York, N.Y.) **287**, 1011-3 (2000).

[212] M. C. Beard, K. P. Knutsen, P. Yu, J. M. Luther, Q. Song, W. K. Metzger, R. J. Ellingson, and A. J. Nozik, Nano Letters **7**, 2506-12 (2007).

[213] a. Pitanti, D. Navarro-Urrios, N. Prtljaga, N. Daldosso, F. Gourbilleau, R. Rizk, B. Garrido, and L. Pavesi, Journal of Applied Physics **108**, 053518 (2010).

[214] F. Trojánek, K. Neudert, M. Bittner, and P. Malý, Physical Review B **72**, 1-6 (2005).

[215] D. Timmerman, I. Izeddin, and T. Gregorkiewicz, Physica Status Solidi (a) **207**, 183-187 (2010).

[216] V. I. Klimov, C. J. Schwarz, D. W. McBranch, and C. W. White, Applied Physics Letters **73**, 2603 (1998).

[217] M. Sykora, L. Mangolini, R. Schaller, U. Kortshagen, D. Jurbergs, and V. Klimov, Physical Review Letters **100**, 1-4 (2008).

[218] F. Trojánek, K. Neudert, P. Malý, K. Dohnalová, and I. Pelant, Journal of Applied Physics **99**, 116108 (2006).

[219] K. Žídek, F. Trojánek, P. Malý, L. Ondič, I. Pelant, K. Dohnalová, L. Šiller, R. Little, and B. R. Horrocks, Optics Express **18**, 25241-9 (2010).

[220] E. Luppi, F. Iori, R. Magri, O. Pulci, S. Ossicini, E. Degoli, and V. Olevano, Physical Review B **75**, 033303 (2007).

[221] L. Ramos, J. Furthmüller, and F. Bechstedt, Physical Review B **71**, 1-7 (2005).

[222] N. Daldosso, M. Luppi, S. Ossicini, E. Degoli, R. Magri, G. Dalba, P. Fornasini, R. Grisenti, F. Rocca, L. Pavesi, S. Boninelli, F. Priolo, C. Spinella, and F. Iacona, Physical Review B **68**, 1-8 (2003).

[223] I. F. Crowe, M. P. Halsall, O. Hulko, A. P. Knights, R. M. Gwilliam, M. Wojdak, and A. J. Kenyon, Journal of Applied Physics **109**, 083534 (2011).

[224] G. Zatryb, A. Podhorodecki, X. J. Hao, J. Misiewicz, Y. S. Shen, and M. a Green, Nanotechnology **22**, 335703 (2011).

[225] a. La Magna, G. Nicotra, C. Bongiorno, C. Spinella, M. G. Grimaldi, E. Rimini, L. Caristia, and S. Coffa, Applied Physics Letters **90**, 183101 (2007).

[226] G. Franzò, M. Miritello, S. Boninelli, R. Lo Savio, M. G. Grimaldi, F. Priolo, F. Iacona, G. Nicotra, C. Spinella, and S. Coffa, Journal of Applied Physics **104**, 094306 (2008).

[227] C. Spinella, C. Bongiorno, G. Nicotra, E. Rimini, A. Muscarà, and S. Coffa, Applied Physics Letters **87**, 044102 (2005).

[228] R. Lockwood, S. McFarlane, J. R. Rodríguez Núñez, X. Y. Wang, J. G. C. Veinot, and a. Meldrum, Journal of Luminescence **131**, 1530-1535 (2011).

[229] K. Žídek, I. Pelant, F. Trojánek, P. Malý, P. Gilliot, B. Hönerlage, J. Oberlé, L. Šiller, R. Little, and B. Horrocks, Physical Review B **84**, 1-9 (2011).

[230] M. Ghulinyan, D. Navarro-Urrios, A. Pitanti, A. Lui, G. Pucker, and L. Pavesi, Optics Express **16**, 13218-24 (2008).

[231] M. Xie, A. Pitanti, M. Ghulinyan, D. Yang, G. Pucker, and L. Pavesi, Physical Review B **84**, 1-6 (2011).

[232] R. Kekatpure and M. Brongersma, Physical Review A **78**, 1-13 (2008).

[233] D. Timmerman, I. Izeddin, P. Stallinga, I. N. Yassievich, and T. Gregorkiewicz, Nature Photonics **2**, 105-109 (2008).

[234] O. B. Gusev, a. a. Prokofiev, O. a. Maslova, E. I. Terukov, and I. N. Yassievich, JETP Letters **93**, 147-150 (2011).

[235] J. Diener, D. Kovalev, G. Polisski, and F. Koch, Optical Materials **17**, 117-120 (2001).

[236] L. Negro, Optics Communications **229**, 337-348 (2004).

[237] R. Pereira, D. Rowe, R. Anthony, and U. Kortshagen, Physical Review B **83**, 1-9 (2011).

[238] D. Pierreux and a. Stesmans, Physical Review B **66**, 1-9 (2002).

[239] J. A. Kelly and J. G. C. Veinot, ACS Nano **4**, 4645-56 (2010).

[240] L. a Huck and J. M. Buriak, Journal of the American Chemical Society **134**, 489-97 (2012).

[241] J. A. Kelly, A. M. Shukaliak, M. D. Fleischauer, and J. G. C. Veinot, Journal of the American Chemical Society **133**, 9564-71 (2011).

[242] R. Elliman, M. Lederer, N. Smith, and B. Lutherdavies, Nuclear Instruments and Methods in Physics Research Section B: Beam Interactions with Materials and Atoms **206**, 427-431 (2003).

[243] P. Blood, Quantum Electronics, IEEE Journal Of **36**, 354–362 (2000).

[244] K. L. Shaklee, R. E. Nahory, and R. F. Leheny, Journal of Luminescence **7**, 284-309 (1973).

[245] J. Valenta, I. Pelant, and J. Linnros, Applied Physics Letters **81**, 1396 (2002).

[246] F. Trojánek, K. Žídek, K. Neudert, I. Pelant, and P. Malý, Journal of Luminescence **121**, 263-266 (2006).

[247] K. J. Vahala, Nature **424**, 839-46 (2003).

[248] A. B. Matsko and V. S. Ilchenko, Selected Topics in Quantum Electronics, IEEE Journal Of **12**, 3–14 (2006).

[249] L. Rayleigh, Philosophical Magazine Series 6 **20**, 1001-1004 (1910).

[250] D. Armani, T. Kippenberg, S. Spillane, K. Vahala, and others, Nature **421**, 925–928 (2003).

[251] Y. Akahane, T. Asano, B. S. Song, S. Noda, and others, Nature **425**, 944–947 (2003).

[252] T. J. Kippenberg, S. M. Spillane, D. K. Armani, and K. J. Vahala, Applied Physics Letters **83**, 797 (2003).

[253] M. Ghulinyan, R. Guider, G. Pucker, and L. Pavesi, IEEE Photonics Technology Letters **23**, 1166-1168 (2011).

[254] R.-J. Zhang, S.-Y. Seo, A. P. Milenin, M. Zacharias, and U. Gösele, Applied Physics Letters **88**, 153120 (2006).

[255] B. Redding, E. Marchena, T. Creazzo, S. Shi, and D. W. Prather, Optics Letters **35**, 998-1000 (2010).

[256] F. Ferrarese Lupi, D. Navarro-Urrios, J. Monserrat, C. Dominguez, P. Pellegrino, and B. Garrido, Physica Status Solidi (C) **8**, 1060-1065 (2011).

[257] L. Ferraioli, M. Wang, G. Pucker, D. Navarro-Urrios, N. Daldosso, C. Kompocholis, and L. Pavesi, Journal of Nanomaterials **2007**, 1-5 (2007).

[258] M. J. F. Digonnet, editor, *Rare-earth-doped Fiber Lasers and Amplifiers*, Second Edi (Marcel Dekker Inc., New York, 2001), p. 777.

[259] E. Snoeks and A. Lagendijk, Physical Review Letters **74**, 2459–2462 (1995).

[260] M. de Dood, L. Slooff, A. Polman, A. Moroz, and A. van Blaaderen, Physical Review A **64**, 1-7 (2001).

[261] W. J. Miniscalco, Lightwave Technology, Journal Of **9**, 234–250 (1991).

[262] C. Layne and W. Lowdermilk, Physical Review B **16**, 10-22 (1977).

[263] L. H. Slooff, a. van Blaaderen, a. Polman, G. a. Hebbink, S. I. Klink, F. C. J. M. Van Veggel, D. N. Reinhoudt, and J. W. Hofstraat, Journal of Applied Physics **91**, 3955 (2002).

[264] A. Polman, Physica B: Condensed Matter **300**, 78–90 (2001).

[265] R. S. Quimby, W. J. Miniscalco, and B. Thompson, Journal of Applied Physics **76**, 4472 (1994).

[266] M. de Dood, J. Knoester, a. Tip, and a. Polman, Physical Review B **71**, 1-5 (2005).

[267] A. Polman and F. C. J. M. van Veggel, Journal of the Optical Society of America B **21**, 871 (2004).

[268] A. J. Kenyon, Semiconductor Science and Technology **20**, R65-R84 (2005).

[269] N. N. Ha, K. Dohnalová, and T. Gregorkiewicz, Physical Review B **81**, 1-6 (2010).

[270] I. Izeddin, M. Klik, N. Vinh, M. Bresler, and T. Gregorkiewicz, Physical Review Letters **99**, 1-4 (2007).

[271] B. Garrido, C. García, S.-Y. Seo, P. Pellegrino, D. Navarro-Urrios, N. Daldosso, L. Pavesi, F. Gourbilleau, and R. Rizk, Physical Review B **76**, 1-15 (2007).

[272] K. Hijazi, L. Khomenkova, J. Cardin, F. Gourbilleau, and R. Rizk, Physica E: Low-dimensional Systems and Nanostructures **41**, 1067-1070 (2009).

[273] G. Franzò, E. Pecora, F. Priolo, and F. Iacona, Applied Physics Letters **90**, 183102 (2007).

[274] Y.-W. Lu, B. Julsgaard, M. C. Petersen, R. V. S. Jensen, T. G. Pedersen, K. Pedersen, and a. N. Larsen, Applied Physics Letters **97**, 141903 (2010).

[275] L. Khomenkova, F. Gourbilleau, J. Cardin, and R. Rizk, Physica E: Low-dimensional Systems and Nanostructures **41**, 1048-1051 (2009).

[276] G. Franzò, S. Boninelli, D. Pacifici, F. Priolo, F. Iacona, and C. Bongiorno, Applied Physics Letters **82**, 3871 (2003).

[277] F. Gonella, G. Battaglin, . Cattaruzza, . Trave, a. Leto, and G. Pezzotti, Thin Solid Films (2011).

[278] A. Polman, Journal of Applied Physics **82**, 1 (1997).

[279] I. F. Crowe, R. J. Kashtiban, B. Sherliker, U. Bangert, M. P. Halsall, A. P. Knights, and R. M. Gwilliam, Journal of Applied Physics **107**, 044316 (2010).

[280] R. J. Kashtiban, U. Bangert, I. F. Crowe, M. Halsall, a J. Harvey, and M. Gass, Journal of Physics: Conference Series **241**, 012097 (2010).

[281] R. J. Kashtiban, U. Bangert, I. Crowe, M. P. Halsall, B. Sherliker, a J. Harvey, J. Eccles, a P. Knights, R. Gwilliam, and M. Gass, Journal of Physics: Conference Series **209**, 012043 (2010).

[282] X. Wang, P. Li, M. Malac, R. Lockwood, and A. Meldrum, Physica Status Solidi (C) **8**, 1038-1043 (2011).

[283] H. Rinnert, G. W. Adeola, and M. Vergnat, Journal of Applied Physics **105**, 036101 (2009).

[284] J. Rodríguez and J. G. C. Veinot, Journal of Materials Chemistry **21**, 1713 (2011).

[285] S. Núñez-Sánchez, P. M. Roque, R. Serna, and a. K. Petford-Long, Applied Physics Letters **98**, 151109 (2011).

[286] F. Priolo, G. Franzò, D. Pacifici, V. Vinciguerra, F. Iacona, and A. Irrera, Journal of Applied Physics **89**, 264 (2001).

[287] P. Horak, W. H. Loh, and A. J. Kenyon, Optics Express **17**, 906-911 (2009).

[288] L. Borowska, S. Fritzsche, P. G. Kik, and A. E. Masunov, Journal of Molecular Modeling **17**, 423-8 (2011).

[289] F. Enrichi, G. Mattei, C. Sada, E. Trave, D. Pacifici, G. Franzò, F. Priolo, F. Iacona, M. Prassas, and M. Falconieri, Optical Materials **27**, 904-909 (2005).

[290] M. Falconieri, E. Borsella, F. Enrichi, G. Franzò, F. Priolo, F. Iacona, F. Gourbilleau, and R. Rizk, Optical Materials **27**, 884-889 (2005).

[291] D. Navarro-Urrios, a. Pitanti, N. Daldosso, F. Gourbilleau, R. Rizk, B. Garrido, and L. Pavesi, Physical Review B **79**, 2-5 (2009).

[292] a. Kenyon, M. Wojdak, I. Ahmad, W. Loh, and C. Oton, Physical Review B **77**, 1-9 (2008).

[293] I. Izeddin, D. Timmerman, T. Gregorkiewicz, a. Moskalenko, a. Prokofiev, I. Yassievich, and M. Fujii, Physical Review B **78**, (2008).

[294] M. Wojdak, M. Klik, M. Forcales, O. Gusev, T. Gregorkiewicz, D. Pacifici, G. Franzò, F. Priolo, and F. Iacona, Physical Review B **69**, 1-4 (2004).

[295] P. G. Kik and A. Polman, Journal of Applied Physics **88**, 1992 (2000).

[296] D. Navarro-Urrios, Y. Lebour, O. Jambois, B. Garrido, a. Pitanti, N. Daldosso, L. Pavesi, J. Cardin, K. Hijazi, L. Khomenkova, F. Gourbilleau, and R. Rizk, Journal of Applied Physics **106**, 093107 (2009).

[297] D. Navarro-Urrios, a. Pitanti, N. Daldosso, F. Gourbilleau, L. Khomenkova, R. Rizk, and L. Pavesi, Physica E: Low-dimensional Systems and Nanostructures **41**, 1029-1033 (2009).

[298] A. Irrera, F. Iacona, G. Franzò, M. Miritello, R. Lo Savio, M. E. Castagna, S. Coffa, and F. Priolo, Journal of Applied Physics **107**, 054302 (2010).

[299] M. Roussel, E. Talbot, F. Gourbilleau, and P. Pareige, Nanoscale Research Letters **6**, 164 (2011).

[300] F. Iacona, C. Bongiorno, C. Spinella, S. Boninelli, and F. Priolo, Journal of Applied Physics **95**, 3723 (2004).

[301] L. Pavesi and M. Ceschini, Physical Review. B, Condensed Matter **48**, 17625 (1993).

[302] S. Cueff, C. Labbé, B. Dierre, F. Fabbri, T. Sekiguchi, X. Portier, and R. Rizk, Journal of Applied Physics **108**, 113504 (2010).

[303] a. Al Choueiry, a. M. Jurdyc, B. Jacquier, F. Gourbilleau, and R. Rizk, Journal of Applied Physics **106**, 053107 (2009).

[304] S. Saeed, D. Timmerman, and T. Gregorkiewicz, Physical Review B **83**, 1-5 (2011).

[305] F. Gourbilleau, C. Dufour, R. Madelon, and R. Rizk, Journal of Luminescence **126**, 581-589 (2007).

[306] I. Y. Kim, J. H. Shin, and K. J. Kim, Applied Physics Letters **95**, 221101 (2009).

[307] D. Kovalev and M. Fujii, Advanced Materials **17**, 2531-2544 (2005).

[308] T. Nakamura, M. Fujii, S. Miura, M. Inui, and S. Hayashi, Physical Review B **74**, 1-6 (2006).

[309] K. Imakita, M. Fujii, and S. Hayashi, The European Physical Journal D **34**, 161-163 (2005).

[310] K. Choy, F. Lenz, X. X. Liang, F. Marsiglio, and a. Meldrum, Applied Physics Letters **93**, 261109 (2008).

[311] O. Savchyn, R. M. Todi, K. R. Coffey, L. K. Ono, B. R. Cuenya, and P. G. Kik, Applied Physics Letters **95**, 231109 (2009).

[312] N. N. Ha, S. Cueff, K. Dohnalová, M. T. Trinh, C. Labbé, R. Rizk, I. N. Yassievich, and T. Gregorkiewicz, Physical Review B **84**, 1-5 (2011).

[313] O. Savchyn, R. M. Todi, K. R. Coffey, and P. G. Kik, Applied Physics Letters **94**, 241115 (2009).

[314] E. G. Barbagiovanni, D. J. Lockwood, P. J. Simpson, and L. V. Goncharova, Journal of Applied Physics **111**, 034307 (2012).

[315] A. A. Prokofiev, A. S. Moskalenko, A. N. Poddubny, and I. N. Yassievich, Physica Status Solidi (C) **8**, 1033-1037 (2011).

[316] N. Daldosso, D. Navarro-Urrios, M. Melchiorri, L. Pavesi, F. Gourbilleau, M. Carrada, R. Rizk, C. García, P. Pellegrino, B. Garrido, and L. Cognolato, Applied Physics Letters **86**, 261103 (2005).

[317] N. Daldosso, D. Navarro-Urrios, M. Melchiorri, C. Garcia, P. Pellegrino, B. Garrido, C. Sada, G. Battaglin, F. Gourbilleau, R. Rizk, and others, Selected Topics in Quantum Electronics, IEEE Journal Of **12**, 1607–1617 (2006).

[318] B. J. Luff, D. Feng, D. C. Lee, W. Qian, H. Liang, and M. Asghari, Advances in Optical Technologies **2008**, 1-6 (2008).

[319] A. Pitanti, Light-matter Interaction in Silicon Nanophotonic Structures, Università degli studi di Trento, 2010.

[320] J. a. Moreno, B. Garrido, P. Pellegrino, C. Garcia, J. Arbiol, J. R. Morante, P. Marie, F. Gourbilleau, and R. Rizk, Journal of Applied Physics **98**, 013523 (2005).

[321] V. R. Almeida, Q. Xu, C. a Barrios, and M. Lipson, Optics Letters **29**, 1209-11 (2004).

[322] Q. Xu, V. R. Almeida, R. R. Panepucci, and M. Lipson, Optics Letters **29**, 1626-8 (2004).

[323] C. A. Barrios and M. Lipson, Optics Express **13**, 10092-101 (2005).

[324] K. Preston and M. Lipson, Optics Express **17**, 1527-34 (2009).

[325] S. Cueff, C. Labbé, O. Jambois, B. Garrido, X. Portier, and R. Rizk, Nanoscale Research Letters **6**, 395 (2011).

[326] E. M. Purcell, Physical Review **69**, 681 (1946).

[327] H. Urbach and G. Rikken, Physical Review A **57**, 3913-3930 (1998).

[328] C. Creatore, L. C. Andreani, M. Miritello, R. Lo Savio, and F. Priolo, Applied Physics Letters **94**, 103112 (2009).

[329] C. Creatore, L. C. Andreani, M. Galli, M. Miritello, R. Lo Savio, and F. Priolo, Journal of Optics A: Pure and Applied Optics **11**, 114011 (2009).

[330] Y. C. Jun, R. M. Briggs, H. A. Atwater, and M. L. Brongersma, Optics Express **17**, 7479-90 (2009).

[331] M. Galli, D. Gerace, a. Politi, M. Liscidini, M. Patrini, L. C. Andreani, a. Canino, M. Miritello, R. L. Savio, a. Irrera, and F. Priolo, Applied Physics Letters **89**, 241114 (2006).

[332] C. Creatore and L. Andreani, Physical Review A **78**, 1-15 (2008).

[333] A. Anopchenko, A. Marconi, E. Moser, S. Prezioso, M. Wang, L. Pavesi, G. Pucker, and P. Bellutti, Journal of Applied Physics **106**, 033104 (2009).

[334] J. T. Robinson, K. Preston, O. Painter, and M. Lipson, Optics Express **16**, 16659-69 (2008).

[335] N. Daldosso, G. Das, S. Larcheri, G. Mariotto, G. Dalba, L. Pavesi, a. Irrera, F. Priolo, F. Iacona, and F. Rocca, Journal of Applied Physics **101**, 113510 (2007).

[336] R. Guider, N. Daldosso, A. Pitanti, E. Jordana, J.-M. Fedeli, and L. Pavesi, Optics Express **17**, 20762-70 (2009).

[337] F. Priolo, C. Presti, G. Franzò, a. Irrera, I. Crupi, F. Iacona, G. Di Stefano, a. Piana, D. Sanfilippo, and P. Fallica, Physical Review B **73**, 2-5 (2006).

[338] A. Irrera, D. Pacifici, M. Miritello, G. Franzò, F. Priolo, F. Iacona, D. Sanfilippo, G. Di Stefano, and P. G. Fallica, Applied Physics Letters **81**, 1866 (2002).

[339] S. Lombardo, S. Campisano, G. N. Van den Hoven, and A. Polman, Journal of Applied Physics **77**, 6504-6510 (1995).

[340] F. Iacona, D. Pacifici, A. Irrera, M. Miritello, G. Franzò, F. Priolo, D. Sanfilippo, G. Di Stefano, and P. G. Fallica, Applied Physics Letters **81**, 3242 (2002).

[341] A. Polman, D. Jacobson, D. Eaglesham, R. Kistler, and J. Poate, Journal of Applied Physics **70**, 3778–3784 (1991).

[342] C. Maurizio, F. Iacona, F. D'Acapito, G. Franzò, and F. Priolo, Physical Review B **74**, 1-7 (2006).

[343] P. Noé, H. Okuno, J.-B. Jager, E. Delamadeleine, O. Demichel, J.-L. Rouvière, V. Calvo, C. Maurizio, and F. D'Acapito, Nanotechnology **20**, 355704 (2009).

[344] M. Wang, a. Anopchenko, a. Marconi, E. Moser, S. Prezioso, L. Pavesi, G. Pucker, P. Bellutti, and L. Vanzetti, Physica E: Low-dimensional Systems and Nanostructures **41**, 912-915 (2009).

[345] Q. Fang, J. Song, S. Tao, M. Yu, G. Lo, and D. Kwong, Optics Express **16**, 6425–6432 (2008).

[346] S. Zhu, Q. Fang, M. B. Yu, G. Q. Lo, and D. L. Kwong, Optics Express **17**, 20891-9 (2009).

[347] L. Liao, D. Lim, A. Agarwal, X. Duan, K. K. Lee, and L. C. Kimerling, Journal of Electronic Materials **29**, 1380-1386 (2000).

[348] K. K. Lee, D. R. Lim, H. C. Luan, A. Agarwal, J. Foresi, and L. C. Kimerling, Applied Physics Letters **77**, 1617–1619 (2000).

[349] N. Daldosso, D. Navarro-Urrios, M. Melchiorri, L. Pavesi, C. Sada, F. Gourbilleau, and R. Rizk, Applied Physics Letters **88**, 161901 (2006).

[350] P. Muellner, N. Finger, and R. Hainberger, Optics Express **16**, 287–294 (2008).

[351] R. Ding, T. Baehr-Jones, W.-J. Kim, B. Boyko, R. Bojko, A. Spott, A. Pomerene, C. Hill, W. Reinhardt, and M. Hochberg, Applied Physics Letters **98**, 233303 (2011).

[352] J. T. Robinson, L. Chen, and M. Lipson, Optics Express **16**, 4296-301 (2008).

[353] T. Claes, J. G. Molera, K. De Vos, E. Schacht, R. Baets, and P. Bienstman, IEEE Photonics Journal **1**, 197-204 (2009).

[354] A. H. J. Yang, T. Lerdsuchatawanich, and D. Erickson, Nano Letters **9**, 1182-8 (2009).

[355] A. H. J. Yang, S. D. Moore, B. S. Schmidt, M. Klug, M. Lipson, and D. Erickson, Nature **457**, 71-5 (2009).

[356] E. Jordana, J. M. Fedeli, P. Lyan, J. Colonna, P. Gautier, N. Daldosso, L. Pavesi, Y. Lebour, P. Pellegrino, B. Garrido, and others, in *Group IV Photonics, 2007 4th IEEE International Conference On* (IEEE, 2007), pp. 1–3.

[357] A. Spott, T. Baehr-Jones, R. Ding, Y. Liu, R. Bojko, T. O'Malley, A. Pomerene, C. Hill, W. Reinhardt, and M. Hochberg, Optics Express **19**, 10950-8 (2011).

[358] T. N. Theis, IBM Journal of Research and Development **44**, 379-390 (2000).

[359] R. M. Briggs, M. Shearn, A. Scherer, and H. a. Atwater, Applied Physics Letters **94**, 021106 (2009).

[360] A. Säynätjoki, J. Riikonen, H. Lipsanen, and J. Ahopelto, Journal of Materials Science: Materials in Electronics **14**, 417–420 (2003).

[361] J. Orcutt, S. Tang, S. Kramer, and H. Li, in *CLEO: Science and Innovations* (2011), pp. 5-6.

[362] K. Preston, B. Schmidt, and M. Lipson, Optics Express **15**, 17283-90 (2007).

[363] R. Soref and B. Bennett, IEEE Journal of Quantum Electronics **23**, 123-129 (1987).

[364] P. A. Anderson, B. S. Schmidt, and M. Lipson, Optics Express **14**, 9197-202 (2006).

[365] R. Ulrich and R. Torge, Applied Optics **12**, 2901-8 (1973).

[366] S.-Y. Seo and J. H. Shin, Applied Physics Letters **78**, 2709 (2001).

[367] G. Franzo, D. Pacifici, V. Vinciguerra, F. Priolo, and F. Iacona, Applied Physics Letters **76**, 2167 (2000).

[368] S. V. Sergeyev and B. Jaskorzynska, Physical Review B **62**, 628-633 (2000).

[369] O. A. Vlasenko, E. M. Zolotov, and R. F. Tavlykaev, Soviet Journal of Quantum Electronics **19**, 681-682 (1989).

[370] R. Spano, N. Daldosso, M. Cazzanelli, L. Ferraioli, L. Tartara, J. Yu, V. Degiorgio, E. Giordana, J. M. Fedeli, and L. Pavesi, Optics Express **17**, 3941-50 (2009).

[371] A. Martínez, J. Blasco, P. Sanchis, J. V. Galán, J. García-Rupérez, E. Jordana, P. Gautier, Y. Lebour, S. Hernández, R. Guider, N. Daldosso, B. Garrido, J. M. Fedeli, L. Pavesi, J. Martí, and R. Spano, Nano Letters **10**, 1506-11 (2010).

[372] a. Trita, C. Lacava, P. Minzioni, J.-P. Colonna, P. Gautier, J.-M. Fedeli, and I. Cristiani, Applied Physics Letters **99**, 191105 (2011).